

Thesis presented to the Instituto Tecnológico de Aeronáutica, in partial fulfillment of the requirements for the degree of Doctor of Science in the Program of Physics, Atomic and Molecular.

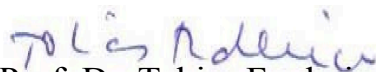
Kamyar Mohseni

**APPLICATION OF FADDEEV TECHNIQUE: FROM
THREE-BODY NUCLEAR SYSTEMS TO 2D SEMICONDUCTOR
MATERIALS**

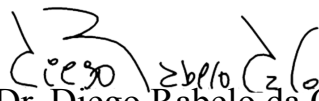
Thesis approved in its final version the signatories below:



Prof. Dr. André Jorge Carvalho Chaves
Advisor



Prof. Dr. Tobias Frederico
Co-advisor



Prof. Dr. Diego Rabelo da Costa
Co-advisor

Instituto Tecnológico de Aeronáutica – ITA
São José dos Campos, SP – Brazil
2024

Cataloging-in Publication Data
Documentation and Information Division

Mohseni, Kamyar
Application of Faddeev Technique: From Three-Body Nuclear Systems to 2D Semiconductor Materials / Kamyar Mohseni.
São José dos Campos, 2024.
169f.

Thesis of Doctor of Science –Course of Physics.Area of Atomic and Molecular Physics –Instituto Tecnológico de Aeronáutica, 2024.Advisor: Prof. Dr. André Jorge Carvalho Chaves.

1. Faddeev equation. 2. Zero range. 3. Universality. 4. Two dimensions. 5. Exciton. 6. Trion.
7. Few-body. I.Instituto Tecnológico de Aeronáutica. II. Title.

BIBLIOGRAPHIC REFERENCE

MOHSENI, Kamyar. **Application of Faddeev Technique: From Three-Body Nuclear Systems to 2D Semiconductor Materials**. 2024. 169f. Thesis of Doctor of Science – Instituto Tecnológico de Aeronáutica, São José dos Campos.

CESSION OF RIGHTS

AUTHOR'S NAME: Kamyar Mohseni

PUBLICATION TITLE: Application of Faddeev Technique: From Three-Body Nuclear Systems to 2D Semiconductor Materials.

PUBLICATION KIND/YEAR: Thesis / 2024

It is granted to Instituto Tecnológico de Aeronáutica permission to reproduce copies of this thesis and to only loan or to sell copies for academic and scientific purposes. The author reserves other publication rights and no part of this thesis can be reproduced without the authorization of the author.

Kamyar Mohseni
R. Abolição, Apto 44, Bl 4 - Vila Sanches,
12245-500 – São José dos Campos–SP

APPLICATION OF FADDEEV TECHNIQUE: FROM THREE-BODY NUCLEAR SYSTEMS TO 2D SEMICONDUCTOR MATERIALS

Kamyar Mohseni

Thesis Committee Composition:

Prof. Dr. Marcelo Marques	Chairperson	-	ITA
Prof. Dr. André Jorge Carvalho Chaves	Advisor	-	ITA
Prof. Dr. Tobias Frederico	Co-advisor	-	ITA
Prof. Dr. Diego Rabelo da Costa	Co-advisor	-	UFC
Prof. Dr. Wayne Leonardo Silva de Paula	Internal member	-	ITA
Prof. Dr. Andrey Chaves	External memeber	-	UFC
Prof. Dr. Marcelo Takeshi Yamashita	External memeber	-	UNESP

To my Family.

Acknowledgments

My doctoral journey began with a thrilling sense of adventure as I left Iran to pursue my academic dreams abroad. This adventure led me to a world of new and unique experiences, pushing me beyond my comfort zone and broadening my horizons in ways I never imagined. This journey not only expanded my academic horizons but also transformed me as a person, introducing me to inspiring individuals from around the world who have shaped my perspectives and enriched my life.

One of the most fortunate encounters of my PhD journey was with Dr. Hadizadeh. Dr. Hadizadeh is not only an exceptional professor with a unique perspective, but also an incredibly kind and professional person. His guidance extended beyond my academic pursuits, offering invaluable support and wisdom that also shaped my personal development. I am particularly grateful for his encouragement to explore unconventional ideas, patience in explaining complex concepts, and support during challenging times. I am forever grateful for the opportunity to have learned from and worked alongside him.

Dear Dr. Hadizadeh;

Thank you from the bottom of my heart. Every moment of our conversations has been a lesson in life and in my profession.

I was incredibly fortunate to have the opportunity to learn from and work alongside Professor Tobias. His expertise in few-body and atomic physics, combined with his supportive and encouraging nature, made him an exceptional mentor. He not only helped me develop my research skills but also instilled in me a deep appreciation for the beauty and complexity of this field. I am truly grateful for his guidance and inspiration.

My PhD journey could have been much more daunting if I hadn't had a supervisor like Dr. Andre. Andre's incredibly kind nature and constant support, both academic and personal, were invaluable, and I will always be grateful for them. I am deeply grateful to both my advisors, Dr. Andre and Dr. Diego, for their support and guidance throughout this journey. Their expertise in the field of condensed matter was invaluable, and besides this, it was their kindness, patience, and belief in me that truly made the difference.

One of the most beautiful things in my life happened during my doctoral studies:

meeting and marrying Flavia. Flavia's understanding and unwavering support not only made my PhD journey easier but also showed me that *"happiness is only real when shared"*¹.

My dearest Flavia;

Thank you for being you. Your love, support, and understanding have been my constant throughout this journey. I am eternally grateful to have you by my side, and I can't wait to see what adventures await us in the future.

Finally, words cannot express my gratitude and love for my mother, father, sister Zahra, and brother Erfan. Without their encouragement and unconditional love, neither starting this journey nor completing it would have been possible.

I am also grateful for the friendships that sustained me throughout this journey. I especially want to thank Sergio Piling, Carla Osmarin, Estevao Teixeira, Renata Fraga, Bruno Tanaka, Larissa Nascimento, Luiz Tenório, Denys Derlian, Ali Farzanehpour, Morteza Younesi, and Khahsyar Kianfar for their help, support, and encouragement. I will always cherish the memories we made together. I would also like to express my deepest condolences for the loss of our dear friend, Prof. Manuel Maleiro. His memory and friendship will always be with me.

¹Quote from "Into the Wild" (2007)

*"You think too much.
We don't always have to think to get going,
our fear will start to disappear as we do."*
— SAMAD BEHRANGI (1939-1968)

Resumo

Investigamos a massa e as funções de onda do estado ligado de três bósons dentro de uma estrutura relativística de três corpos no espaço de momento tridimensional. Utilizamos potenciais aumentados de Kamada e Glöcke com um potencial separável de curto alcance não relativístico, caracterizado por fatores de forma de Yamaguchi e Gaussianos. Ao conduzir esses fatores de forma para o limite de alcance zero, mantendo a energia de ligação de dois corpos fixa, demonstramos que as massas relativísticas de três bósons e as funções de onda tornam-se independentes do modelo, e o colapso de Thomas é evitado. Curiosamente, o limite não relativístico mantém o efeito Efimov. A estabilidade no limite de alcance zero é atribuída à redução do potencial aumentado com o aumento do momento do centro de massa do par virtual dentro do sistema de três bósons. Uma comparação é feita com os cálculos em coordenadas na frente de luz e Euclidianos, disponíveis na literatura, para validar nossas descobertas.

Em seguida, desenvolvemos um formalismo fundamental para estudar trions em materiais semicondutores em , disponíveis na literatura. As equações de Faddeev no espaço de momento descrevem a interação de três partículas diferentes que se encontram em duas dimensões. Resolvemos as equações integrais acopladas de Faddeev do trion usando tanto um potencial separável de curto alcance de um termo de Yamaguchi quanto a interação repulsiva Rytova-Keldysh (RK), que é aplicada à monocamadas de MoS₂. Devido ao desafio apresentado pelo potencial repulsivo elétron-elétron RK, dois métodos distintos de regularização são elaborados. O primeiro método regula a interação repulsiva na região do infravermelho, enquanto o segundo método a regula na região do ultravioleta. Através da extrapolação da energia do trion para a situação sem blindagem, resultados consistentes são obtidos para a camada de MoS₂, revelando uma energia de ligação do trion de $-49,5(1)$ meV para uma energia do éxciton de $-753,3$ meV. A estrutura do trion para ambos os potenciais RK e Yamaguchi é analisada em detalhes, enfatizando suas semelhanças gerais e a estrutura de cluster dominante, onde um éxciton fortemente ligado está fracamente ligado a um elétron. Isso é ainda manifestado na dominância de dois componentes de Faddeev sobre aquele em que o buraco é um espectador do par de elétrons em interação.

Na etapa seguinte, o trion foi estudado no espaço real. Para isso, transformamos as funções de onda do trion do momento para o espaço de configuração usando transfor-

madras de Fourier. Essa abordagem fornece a informações sobre o arranjo espacial e as correlações entre as partículas constituintes do trión. Investigamos a estrutura do trión no espaço de configuração usando ambos os potenciais de Yamaguchi e RK, demonstrando a importância dos efeitos de blindagem na distribuição espacial do trión. As funções de correlação e os valores esperados das coordenadas de Jacobi são calculados, revelando as configurações geométricas e a estrutura interna dos trions. O estudo confirma a precisão dos métodos numéricos e fornece uma compreensão abrangente das propriedades de ligação e estruturas dos trions em materiais semicondutores 2D.

Além dos estados ligados de três corpos em três dimensões e duas dimensões, estudamos os sistemas de quatro corpos (4B) no espaço de momento bidimensional usando o esquema de Faddeev-Yakubovsky (FY). O capítulo começa com uma base teórica da abordagem FY, seguida pela derivação das equações FY para um sistema 4B no espaço 2D. Apresentamos resultados numéricos para um sistema de partículas idênticas interagindo por meio de um potencial separável, demonstrando a eficácia do método iterativo na resolução das equações FY. Os resultados destacam as energias de ligação e as funções de onda do sistema 4B, fornecendo sobre as interações e a estabilidade dos biexcitons em materiais 2D. Este trabalho é uma etapa preparatória para estudos futuros mais detalhados, com o objetivo de explorar as propriedades físicas e potenciais aplicações de biexcitons em física da matéria condensada.

Ao combinar esses estudos de pesquisa, contribuimos para a compreensão dos estados ligados em sistemas de três bósons e fornecemos sobre as propriedades e estruturas de trions e biexcitons em materiais semicondutores em camadas.

Abstract

We investigate the three-boson bound-state mass and wave functions within a three-body relativistic framework in three-dimensional momentum space. We utilize Kamada, and Glöcke boosted potentials with a non-relativistic short-range separable potential characterized by Yamaguchi and Gaussian form factors. By driving these form factors towards the zero-range limit while keeping the two-body binding energy fixed, we demonstrate that the three-boson relativistic masses and wave functions become model-independent, and the Thomas collapse is avoided. Interestingly, the non-relativistic limit retains the Efimov effect. The stability in the zero-range limit is attributed to the reduction of the boosted potential with the increase of the virtual pair center of mass momentum within the three-boson system. A comparison is made with Light-Front and Euclidean calculations to validate our findings.

Next, we develop a fundamental formalism for studying trions in semiconductor layered materials. The Faddeev equations in momentum space describe the interaction of three different particles lying in two dimensions. We solve the trion Faddeev coupled integral equations using both a short-range one-term separable Yamaguchi potential and the repulsive Rytova-Keldysh (RK) interaction, which is applied to the MoS₂ layer. Due to the challenge posed by the repulsive electron-electron RK potential, two distinct regularization methods are devised. The first method regulates the repulsive interaction in the infrared region, while the second method regulates it in the ultraviolet region. Through extrapolation of the trion energy to the situation without screening, consistent results are obtained for the MoS₂ layer, revealing a trion binding energy of $-49.5(1)$ meV for an exciton energy of -753.3 meV. The trion structure for both RK and Yamaguchi potentials is analyzed in detail, emphasizing their overall similarities and the dominant cluster structure, where a firmly bound exciton is weakly bound to an electron. This is further manifested in the dominance of two Faddeev components over the one where the hole is a spectator of the interacting electron pair.

To investigate the trion further, we study it in real space by transforming the trion wave functions from momentum to configuration space using Fourier transforms. This approach provides insights into the spatial arrangement and correlations among trion constituent particles. We investigate the trion structure in configuration space using both Yamaguchi

and RK potentials, demonstrating the importance of screening effects on the trion's spatial distribution. The correlation functions and expectation values of Jacobi coordinates are calculated, revealing the geometrical configurations and internal structure of trions. The study confirms the accuracy of the numerical methods and provides a comprehensive understanding of trions' binding properties and structures in 2D semiconductor materials.

In addition to three-body bound states in three-dimensional and two-dimensional, we study the four-body (4B) systems in two-dimensional momentum space using the Faddeev-Yakubovsky (FY) scheme. The chapter begins with a theoretical foundation of the FY approach, followed by deriving the FY equations for a 4B system in 2D space. We present numerical results for a system of identical particles interacting through a separable potential, demonstrating the effectiveness of the iterative method in solving the FY equations. The results highlight the binding energies of the 4B system, providing insights into the interactions and stability of a 4B system in 2D materials. This work is a preparatory step for more detailed future studies, aiming to explore the physical properties and potential applications of biexcitons in condensed matter physics.

By combining these research studies, we contribute to understanding bound states in three-boson systems and provide insights into the properties and structures of trions and biexcitons in semiconductor monolayer materials.

List of Figures

FIGURE 2.1 – The geometry of vectors, \mathbf{p}, \mathbf{p}' & \mathbf{p}'' . The vector p is chosen to be parallel to the z -axis and vector \mathbf{p}' is in the $x - z$ plane, and \mathbf{p}'' is free in the 3D space. The angle variables defined in Eqs. (2.9) are indicated.	37
FIGURE 2.2 – The matrix elements of the nonrelativistic (left panel), the relativistic (middle panel) NN potentials and their differences (right panel) calculated by separable Yamaguchi potential with $\beta = 1$ as a function of 2B relative momenta p and p' . Results are obtained with λ_{nr} calculated with Eq. (2.7) with $E_d = -2.225$ MeV.	38
FIGURE 2.3 – The matrix elements of the nonrelativistic (a), and the boosted (b,d & f) 2B potentials and their differences (c,e & g) calculated by Yamaguchi separable potential as a function of 2B relative momenta p and p' with $k = 1, 5, 10 \text{ fm}^{-1}$. Results are obtained with λ_{nr} calculated with Eq. (2.7) with $E_d = -2.225$ MeV.	41
FIGURE 2.4 – The diagonal matrix elements of nonrelativistic and boosted potentials are computed for a diverse set of form factor parameters β for Yamaguchi-type potentials (upper panel) and Λ for Gaussian potentials (lower panel). The calculations are performed using various values of the boosted momentum k . These Figures are taken from (MOHSENI <i>et al.</i> , 2021).	43
FIGURE 2.5 – The diagonal matrix elements of the nonrelativistic potential obtained from a separable boosted potential, that reproduces the moving dimer binding energy, from the solution of Eq. (2.16). The plot is obtained for the potential parameter $\beta = 1 \text{ fm}^{-1}$ and different values of the boosted momentum k	47
FIGURE 2.6 – Set of Jacobi momenta for 3B system.	50

- FIGURE 2.7 – The geometry of vectors \mathbf{p}, \mathbf{k} & \mathbf{k}' . The vector k is chosen to be parallel to the z -axis and vector \mathbf{p} is in the $x - z$ plane, and \mathbf{k}' is free in the 3D space. The angle variables defined in Eqs. (2.59) are indicated. 52
- FIGURE 2.8 – The ground and first excited state binding energies as a function of the form factor parameters Λ (for Gaussian potential) and β (for Yamaguchi-type potential) obtained for a fixed 2B binding energy of -2.225 MeV. The first excited state energies are multiplied by a factor of 50. 60
- FIGURE 2.9 – The value of M_3/m as a function of M_2/m calculated from the 3B ground and first excited states obtained with form factor parameters $\beta = \Lambda = 2000 \text{ fm}^{-1}$ for Yamaguchi-type (solid lines) and Gaussian potentials (full circles). For comparison, our results with the Bethe-Salpeter (dashed line) and Light-Front (dash-dotted line) zero-range calculations of Ref. (YDREFORS *et al.*, 2017a) are added to the plot. This Figure is taken from (MOHSENI *et al.*, 2021). 62
- FIGURE 2.10 – Relativistic Faddeev components for 3B ground $\psi^{(0)}(p, k)$ and first excited $\psi^{(1)}(p, k)$ states calculated for Yamaguchi-type potential with form factor parameters $\beta = 200, 2000 \text{ fm}^{-1}$ and Gaussian potential with form factor parameters $\Lambda = 200, 2000 \text{ fm}^{-1}$. This Figure is taken from (MOHSENI *et al.*, 2021). 63
- FIGURE 3.1 – The geometry of vector \mathbf{p} & \mathbf{p}' . both vectors are chosen to be free in the 2D space. 67
- FIGURE 3.2 – Exciton ground and excited states wave functions in momentum $\psi^{(n)}(p)$ as a function of p 70
- FIGURE 3.3 – Jacobi momenta convention used through the paper. $\{i, j, k\}$ correspond to the indices associated with the three particles, and p_i and q_i are their Jacobi momenta given in Eqs. (2.47) and (2.48). 72
- FIGURE 3.4 – The geometry of vector , \mathbf{p}, \mathbf{p}' & \mathbf{q} . The vector p is chosen to be parallel to the x -axis and vector \mathbf{p}' , and \mathbf{p}'' are free in the 2D space. The angle variables defined in Eqs. (3.53) are indicated. . . . 76

- FIGURE 3.5 – The left panel displays a 3D plot of the 3B wave function, specifically for three attractive Yamaguchi-type potentials (3A). The right panel shows the relative percentage error. Both plots are generated for the angle $\phi_1 = 0$. The results are obtained using form factor parameters $\beta = m = 1$ and a potential strength λ chosen to reproduce a 2B binding energy of $E_{2B} = -0.1$. The calculations are performed with $\hbar c = \text{mass} = 1$ 85
- FIGURE 3.6 – The left panel displays a 3D plot of the 3B wave function, specifically for one repulsive potential (V_1) and two attractive Yamaguchi-type potentials (2A + R). The right panel shows the relative error. Both plots are generated for the angle $\phi_1 = 0$. The results are obtained using form factor parameters $\beta = m = 1$ and a potential strength λ chosen to reproduce a 2B binding energy of $E_{2B} = -0.1$. The calculations are performed with $\hbar c = \text{mass} = 1$ 86
- FIGURE 3.7 – The contour plot illustrates the 3B wave function calculated for three Yamaguchi-type potentials, where V_1 is repulsive while V_2 and V_3 are attractive. The plot represents the wave function's behavior as the magnitude of Jacobi momenta varies. The angles ϕ_1 and ϕ_2 are fixed at 0. The results are obtained using form factor parameters $\beta = m = 1$ and a potential strength λ chosen to reproduce a 2B binding energy of $E_{2B} = -0.1$. The calculations are conducted assuming $\hbar c = \text{mass} = 1$ 86
- FIGURE 3.8 – The screening function $V(q)/V_{ee}(q)$ as a function of the momentum transfer q for (blue curve) $V(q) \rightarrow e^{-l_0 q} V_{ee}(q)$ and (red curve) $V(q) \rightarrow (1 - e^{-l_0 q}) V_{ee}(q)$ with screening parameter $l_0 = 10 \text{ \AA}$. Figure is take from (MOHSENI *et al.*, 2023). 89
- FIGURE 3.9 – Extraction of trion binding energy E_t with a linear extrapolation on energies obtained from two screenings (see Table 3.9) at the physical points $l_0^{-1} = 0 \text{ \AA}^{-1}$ (left panel) and $l_0 = 0 \text{ \AA}$ (right panel). Figure is take from (MOHSENI *et al.*, 2023). 92
- FIGURE 3.10 – The evolution of the Faddeev components (top panels) $\psi_1(p_1, q_1, \phi_1 = 0)$ and (bottom panels) $\psi_2(p_1, q_1, \phi_1 = 0)$ obtained for the screening parameter $l_0 = 1, 30, 50, 70, 100 \text{ \AA}$ in the screening scheme $V_1(q) \rightarrow (1 - e^{-l_0 q}) V_{ee}(q)$. Figure is take from (MOHSENI *et al.*, 2023). 94

- FIGURE 3.11 –The evolution of the wave function $\Psi(p_1, q_1, \phi_1 = 0)$ (top panels) and $\Psi(p_2, q_2, \phi_2 = 0)$ (bottom panels) obtained for the screening parameter $l_0 = 1, 30, 50, 70, 100 \text{ \AA}$ in the screening scheme $V_1(q) \rightarrow (1 - e^{-l_0 q})V_{ee}(q)$. Figure is take from (MOHSENI *et al.*, 2023). 96
- FIGURE 3.12 –The evolution of the wave function $\Psi(p_1, q_1, \phi_1)$ with respect to the angle ϕ_1 for a fixed screening parameter $l_0 = 100 \text{ \AA}$ in the screening scheme $V_1(q) \rightarrow (1 - e^{-l_0 q})V_{ee}(q)$. Figure is take from (MOHSENI *et al.*, 2023). 97
- FIGURE 3.13 –Comparison between trion wave function calculated with RK potential (left panel) and re-scaled Yamaguchi potential model (right panel) for $\phi_1 = 0$. Figure is take from (MOHSENI *et al.*, 2023). 97
- FIGURE 4.1 – The geometry of vector \mathbf{p} & \mathbf{r} . The vector \mathbf{r} is chosen to be parallel to the x -axis, and vector \mathbf{p} is free in the 2D space. The angle variable is defined as $\hat{p} \cdot \hat{r} = \cos(\phi)$ 100
- FIGURE 4.2 – Ground state, first excited state, and second excited state 2B wave functions in configuration space $\psi^{(n)}(r)$ as a function of r . The calculations are performed with 61 mesh points for angle variables and 2000 mesh points for e-h relative distance N_r 102
- FIGURE 4.3 – Coordinate system for the solution of integral Eq. (4.6). 103
- FIGURE 4.4 – The correlation functions $c(r)$ and $c(R)$ calculated with three attractive Yamaguchi potentials. Our calculations are performed with 41 mesh points for angles (ϕ_R, ϕ_q) and 300 mesh points for Jacobi coordinates r, R , and p, q . The calculations are done with $\hbar c = mass = 1$. 105
- FIGURE 4.5 – The correlation functions $c(r)$ and $c(R)$ calculated with two attractive and one repulsive Yamaguchi potentials. Our calculations are performed with $N_{\phi_q} = 41, N_{\phi_R} = 61$, and 400 mesh points for Jacobi coordinates r and R , and 300 mesh points for Jacobi coordinates p and q . The calculations are done with $\hbar c = mass = 1$ 106
- FIGURE 4.6 – Linear extrapolation on $\sqrt{\langle r^2 \rangle}$ and $\sqrt{\langle R^2 \rangle}$ as a function of the inverse of the screening parameter l_0^{-1} for the screening potential $V_{ee}(q) \rightarrow (1 - e^{-l_0 q})V_{ee}(q)$ 111
- FIGURE 4.7 – The geometrical structure of the calculated trion in configuration space. 113
- FIGURE 5.1 – Eighteen different configurations of the 4B system. 117

FIGURE 5.2 – Definition of the four-body Jacobi momenta corresponding to the ψ_1 and ψ_2 type fragmentations.	120
FIGURE 5.3 – Coordinate system for the solution of integral equations (5.39) and (5.40).	124
FIGURE 5.4 – E_{4B}/E_{2B} as a function of E_{3B}/E_{2B} for ground (left panel) and first excited state (right panel) for separable potential with Yamaguchi and Gaussian form factor with $\beta = \Lambda = 1$ and different form factor power m	129
FIGURE C.1 – The dimer wave function was calculated using Model-1 and Model-2 of the MT potential, both as a function of relative momentum for a fixed angle (left panel), and as a function of relative momentum and the angle between them (right panel).	152
FIGURE C.2 – Dimer wave functions $\psi^{(n)}(p)$ as a function of relative momentum p for ground and excited states.	153
FIGURE F.1 – The coordinate system using for fourier transformation	157
FIGURE F.2 – Angular and momentum dependencies of the diagonal matrix element of the non-PW (top panel) and PW 2B potential obtained with MT model-1, with $p = p'$ for different PW number N_{pw}	160
FIGURE F.3 – Angular and momentum dependencies of the relative difference of 2B potentials obtained from non-PW and the summation of PWs up to N_{pw} calculated for MT model-1 potential.	160
FIGURE F.4 – Similar to Fig. F.2, but for fixed angle variable as a function of p and p'	161
FIGURE F.5 – Similar to Fig. F.3, but for fixed angle variable as a function of p and p'	161
FIGURE F.6 – Dimer wave functions $\psi^{(n)}(p)$ as a function of relative momentum p , for different PW channels corresponding to the numerical binding energies listed in Table F.2.	163

List of Tables

TABLE 2.1 –	Parameters for different models of the Yamaguchi (Y) potential. . .	36
TABLE 2.2 –	Relativistic 3B binding energy calculated for different models of Yamaguchi potential.	57
TABLE 2.3 –	The contributions of different relativistic corrections to the 3B binding energy.	58
TABLE 2.4 –	Nonrelativistic and relativistic 3B ground and first excited state binding energies for different values of the Yamaguchi form factor parameter β (upper panel), and Gaussian form factor Λ (lower panel).	59
TABLE 2.5 –	Relativistic trimer binding energy calculate with Eq. (2.78) for different dimer binding energies. In this table we fixed the potential parameter for Yamaguchi and Gaussian form factor $\beta = \Lambda = 2000 \text{ fm}^{-1}$	61
TABLE 2.6 –	3B ground and excited stated binding energies calculated with the Gaussian form factor with $\Lambda = 0.7 \text{ fm}^{-1}$ and $E_d = 0$	64
TABLE 3.1 –	The parameters of RK potentials defined in Eq. (3.7) for MoS_2 . The values for effective masses are taken from Ref. (KORMÁNYOS <i>et al.</i> , 2015)	69
TABLE 3.2 –	The parameters of electron-hole potentials defined in Eq. (3.8) for WS_2	70
TABLE 3.3 –	Exciton binding energies with RK potential defined in Eq. (3.8) for different dielectric constants ϵ_s	71

TABLE 3.4 –	Dimer and trimer binding energies E_{2B} and E_{3B} calculated for three attractive Yamaguchi-type potentials with form factor parameter $\beta = 1$ and different powers m . The potential strength λ is fitted to reproduce the desired 2B binding energy E_{2B} . The ratio of 3B and 2B binding energies E_{3B}/E_{2B} are compared with corresponding results from Ref. (ADHIKARI <i>et al.</i> , 1988). The calculations are done with $\hbar c = \text{mass} = 1$	83
TABLE 3.5 –	Expectation values (EV) of 3B free Hamiltonian $\langle H_0 \rangle$, pair interactions $\langle V_i \rangle$, total 2B interactions $\langle V \rangle$, 3B Hamiltonian $\langle H \rangle$, and eigenvalue E_{3B} calculated for Yamaguchi-type potentials (three attractive (3A) in the second column, two attractive plus one repulsive interaction (2A+R) in the third column), given in Eq. (3.85) with form factor parameters $\beta = m = 1$, and the potential strength λ that reproduces dimer binding energy $E_{2B} = -0.1$. The calculations are done with $\hbar c = \text{mass} = 1$	84
TABLE 3.6 –	The inner product of the Faddeev components $\langle \psi_i \psi_j \rangle$ and their contribution to the normalization of the 3B wave function $ \Psi\rangle$	88
TABLE 3.7 –	Expectation values (EV) in meV of the 3B free Hamiltonian $\langle H_0 \rangle$, pair interactions $\langle V_i \rangle$, total 2B interactions $\langle V \rangle$, 3B Hamiltonian $\langle H \rangle$, and binding energy E_{3B} in meV calculated for RK potentials (two attractive plus one repulsive interaction (2A+R)) given in Eq. (3.7) with screening parameter $l_0 = 100 \text{ \AA}$ in the scheme $V_1(q) \rightarrow (1 - e^{-l_0 q})V_{ee}(q)$	90
TABLE 3.8 –	The convergence of trion ground state binding energies (in meV) as a function of the number of mesh points for Jacobi momenta $N_p = N_q$ obtained for different values of screening parameter l_0 for screening electron-electron interactions $V(q) \rightarrow e^{-l_0 q}V_{ee}(q)$ (upper panel) and $V(q) \rightarrow (1 - e^{-l_0 q})V_{ee}(q)$ (lower panel). The last row of each panel shows the linear extrapolation of trion energy eigenvalues to an infinite number of mesh points.	91
TABLE 3.9 –	Trion ground state binding energies (E_{3B}) for different screening parameter l_0 obtained from two screening schemes shown in Fig. 3.8 and given in Eq. (3.88).	91
TABLE 3.10 –	The inner product of the Faddeev components $\langle \psi_i \psi_j \rangle$ and their contributions in the normalization of the 3B wave function $ \Psi\rangle$ obtained for the screening parameter $l_0 = 100 \text{ \AA}$ in the screening scheme $V_1(q) \rightarrow (1 - e^{-l_0 q})V_{ee}(q)$	93

TABLE 4.1 –	Convergence of exciton mean radius $\langle r \rangle$, and exciton binding energies for ground, first excited, and second excited state, presented as a function of mesh points for 2B relative momentum N_p . The calculations are performed with 61 mesh points for angle variables and 2000 mesh points for e-h relative distance N_r	101
TABLE 4.2 –	Two- and three-body binding energies and the Jacobi coordinates r and R expectation values calculated for Yamaguchi-type potentials with form factor parameter $\beta = 1$ and power $m = 1$. The potential strength λ is obtained from the pole property of 2B t -matrix at two-body binding energy E_2 . The potential strength λ is chosen to reproduce two-body binding energy E_2 of -0.1	106
TABLE 4.3 –	Two- and three-body binding energies and the Jacobi coordinates r and R expectation values calculated for Yamaguchi-type potentials (one repulsive and two attractive interaction) with form factor parameter $\beta = 1$ and power $m = 1$. The potential strength λ is obtained from the pole property of 2B t -matrix at two-body binding energy E_2 . The calculations are done with $\hbar c = mass = 1$	107
TABLE 4.4 –	RMS values of the Jacobi coordinate r and R calculated for RK potentials with screened ee interaction ($l_0 = 70$) as a function of the number of mesh points for Jacobi coordinates r , R , p , and q . The quantity $\Delta\%$ indicates the percentage accuracy for the satisfaction of the Pythagorean theorem.	109
TABLE 4.5 –	Same as Tabel 4.4, but with $l_0 = 80$	109
TABLE 4.6 –	Same as Tabel 4.4, but with $l_0 = 90$	110
TABLE 4.7 –	Same as Tabel 4.4, but with $l_0 = 100$	110
TABLE 4.8 –	The summary of the RMS values of the Jacobi coordinates r and R calculated for RK potentials with different values of the screening parameter l_0 for ee interaction. The quantity $\Delta\%$ indicates the percentage accuracy for the satisfaction of the Pythagorean theorem.	111
TABLE 4.9 –	Extrapolated RMS values of the Jacobi coordinates r and R for the RK potential in the limit of $1/l_0 \rightarrow 0$	111
TABLE 4.10 –	The RMS distance of the electrons and hole to the trion's center of mass and the associated angles calculated with the extrapolated data at $l_0^{-1} = 0$, listed in Table (4.9).	112

TABLE 5.1 –	three-body, $E_3^{(N)}$ and four-body $E_4^{(N)}$ ground ($N = 0$) and excited ($N = 1$) state binding energies, calculated for the Yamaguchi and Gaussian potentials with form factor parameter $\beta = \Lambda = 1$ and different form factor powers $m = 1, 2, 4$. The units are such that $\hbar = m = 1$ and the form factor parameter is taken as a unit.	128
TABLE A.1 –	The convergence of the matrix elements of the relativistic potential $V_r(p, p')$ (in units of MeV fm ³) as a function of iteration number calculated by Yamaguchi separable potential in the fixed points ($p = 0.05$ fm ⁻¹ , $p' = 0.10$ fm ⁻¹). The value of the nonrelativistic Yamaguchi separable potential $V_{nr}(p, p')$ is also given. Result are obtained with λ_{nr} calculated with Eq. (2.7) with $E_d = -2.225$ MeV.	145
TABLE A.2 –	The convergence of the matrix elements of the boosted potential $V_k(p, p')$ (in units of MeV fm ³) as a function of iteration number calculated by Yamaguchi separable potential in the fixed points ($p = 0.05$ fm ⁻¹ , $p' = 0.10$ fm ⁻¹) and for four different values of the Jacobi momentum $k = 1, 5, 10$ fm ⁻¹ . The value of the nonrelativistic Yamaguchi separable potential $V_{nr}(p, p')$ is also given. Result are obtained with λ_{nr} calculated with Eq. (2.7) with $E_d = -2.225$ MeV.	146
TABLE A.3 –	Convergence of the nonrelativistic (E_d^{nr}) and relativistic (E_d^{rel}) dimer binding energies as a function of the number of relative momentum mesh points N_p for the Yamaguchi-I potential.	146
TABLE A.4 –	Nonrelativistic and relativistic dimer binding energies for all Yamaguchi models	147
TABLE A.5 –	The boosted and nonrelativistic dimer binding energies in the unit of MeV. The nonrelativistic potentials obtained from a separable boosted potential by solving Eq. (2.16), and the boosted result are calculated directly from Eq. (2.29). The boosted potential strength λ_k is calculated by Eq. (2.30) when the dimer rest energy is $M_d = -2.225$ MeV.	147
TABLE A.6 –	The expectation value of Hamiltonian $\langle H \rangle = \langle H_0 \rangle + \langle V \rangle$ and nonrelativistic 3B binding Energy E_{nr}^{3B} , calculated for Yamaguchi-I potential, as a function of the number of mesh points for Jacobi momenta p and q ($N_p = N_q$).	148

TABLE A.7 – The expectation value of Hamiltonian $\langle H \rangle = \langle H_0 \rangle + \langle V \rangle$, nonrelativistic 3B binding Energy E_{nr}^{3B} , and relative percentage difference between them, calculated for four models of Yamaguchi potential.	148
TABLE C.1 – Parameters of two models of MT potential we use in 2D calculations.	150
TABLE C.2 – Convergence of 2B binding energy as a function of mesh points for angle variables N_ϕ . Upper panel is the result for angular-dependent dimer obtained by solving Eq. (3.3), bottom panel is the results for dimer without angular dependence using Eq. (3.4).	151
TABLE C.3 – The analytical and numerical dimer binding energies calculated for Coulomb potential Eq. (C.3). The calculations are performed with 500 mesh points for relative momenta and 40 mesh points for angle variables. Results are obtained with $\hbar c = \text{mass} = 1$	153
TABLE E.1 – The convergence of ground state exciton binding energies (meV) as a function of the number of mesh points N_p and N_ϕ . The calculations are performed for MoS ₂ substrate in s -wave. The last row shows the quadratic extrapolation of exciton energy eigenvalues to an infinite number of mesh points.	155
TABLE E.2 – Expectation values in meV of the 2B free Hamiltonian $\langle H_0 \rangle$, pair potentials $\langle V \rangle$, 2B Hamiltonian $\langle H \rangle$, and binding energy E_{2B} in meV calculated for RK potentials. The calculations are performed for MoS ₂ in s -wave channel ($m = 0$) with $N_\phi = 61$	156
TABLE F.1 – Dimer binding energies calculated with two models MT potential with parameters listed in Table C.1, with $m = 0$ and $m = 1$ PW channels.	159
TABLE F.2 – Dimer binding energy calculated for different partial waves channel with coulomb potential defined in Eq. (C.2).	162

Contents

1	INTRODUCTION	25
1.1	Motivation	25
1.2	The power of Faddeev-Yakubovsky equations in solving three- and four-body systems	26
1.3	Implications of relativistic effects in the zero range limit on three-Boson systems	27
1.4	Binding and structural properties of negatively charged trions in a suspended two-dimensional MoS ₂ layer	28
1.5	Outline	30
2	ZERO-RANGE LIMITS AND THREE-BOSON STABILITY IN BOOSTED POTENTIALS	32
2.1	Overview	32
2.2	Nonrelativistic, relativistic, and boosted potentials	35
2.2.1	Relativistic potentials	35
2.2.2	Boosted potentials	38
2.3	Two-body bound state	44
2.3.1	Nonrelativistic NN bound state	44
2.3.2	Relativistic NN bound state	45
2.3.3	Numerical results for dimer binding energy	45
2.4	Three-body bound state	47
2.4.1	Nonrelativistic Faddeev equations in momentum space	47
2.4.2	Relativistic Faddeev equation	53

2.4.3	Numerical results for nonrelativistic and relativistic trimer binding energies	56
2.5	Efimov physics	64
3	TRION IN TWO-DIMENSIONAL MOMENTUM SPACE	65
3.1	Overview	65
3.2	Two-dimensional exciton structure analysis through the application of the Lippmann-Schwinger equation	67
3.2.1	Non-partial wave representation	67
3.2.2	Partial wave representation	68
3.3	Faddeev equations for three different particles bound states in two dimensions	71
3.3.1	Expectation values and momentum distributions	79
3.3.2	Verification of the 3B Schrödinger equation in 2D	81
3.4	Short Range Yamaguchi potential	82
3.4.1	Yamaguchi trion clusterization	84
3.5	Rytova-Keldysh potential	88
3.5.1	Rytova-Keldysh trion clusterization	93
4	TRION IN TWO-DIMENSIONAL CONFIGURATION SPACE	99
4.1	Overview	99
4.2	Exciton structure in two-dimensions configuration space	100
4.3	Trion structure in two-dimensions configuration space	102
4.3.1	Correlation functions and expectation values	104
4.4	Trion calculation in configuration space: Yamaguchi potential	104
4.4.1	Three identical particles interacting with three attractive Yamaguchi potentials	105
4.4.2	Three identical particles interact with two attractive and one repulsive Yamaguchi potentials	106
4.4.3	Trion calculation in configuration space: RK potential	108
5	FOUR-BODY SYSTEM IN TWO-DIMENSIONAL SPACE	114
5.1	Overview	114

5.2 Faddeev-Yakubovsky equations for four identical particles bound states in two dimensions	115
5.2.1 Momentum space representation of Faddeev-Yakubovsky equations	119
5.2.2 Momentum space representation of Faddeev-Yakubovsky equations with separable potential	122
5.2.3 Numerical results	127
6 SUMMARY AND OUTLOOK	131
6.1 Calculating Efimov States in the Relativistic Regime	132
6.2 Calculating Trion Binding Energy Using Separable Potential	132
BIBLIOGRAPHY	133
APPENDIX A – CONVERGENCIES OF NUMERICAL SOLUTIONS INTRODUCED IN CHAPTER 2	145
APPENDIX B – ANALYTIC CALCULATION OF POTENTIAL STRENGTH	149
APPENDIX C – CALCULATING THE NON-PW DIMER BINDING ENERGY AND WAVE FUNCTION	150
APPENDIX D – FOURIER TRANSFORMATION OF MALFLIET-TJON POTENTIAL	154
APPENDIX E – EXCITON CONVERGENCE WITH RK POTENTIAL	155
APPENDIX F – PW AND NON PW RELATIONS AND CALCULATIONS	157
F.1 Derivation of the relation between the PW and non PW potential	157
F.2 PW wave and non PW dimer binding energy and wave function	159
APPENDIX G – t-MATRIX IN SEPARABLE FORM	164
APPENDIX H – RELATIONS BETWEEN DIFFERENT FRAGMENTATION IN THE FOUR-BODY SYSTEM	166

1 Introduction

1.1 Motivation

Quantum few-body physics has been a significant and influential aspect of atomic, molecular, and nuclear physics since the early stages of quantum mechanics. Since the mid-1950s, considerable advancements have been achieved within the scientific community regarding the development of theoretical physics methods to address few-body problems across various fields of physics.

In contrast to the two-body (2B) problem, which can be quickly and accurately solved, a quantum system with more than two nucleons is complicated. Many research groups worldwide have extensively studied and investigated bound three- and four-body systems, and specialized techniques for calculating binding energies, considering nucleon-nucleon (NN) and 3N interactions, have been developed.

In condensed matter physics, semiconductors facilitate the formation of bound states between electrons (e) and holes (h). An exciton represents an excitation within condensed matter, emerging when an electron from the conduction band and a hole from the valence band become bound due to the Coulomb attraction. This formation can be prompted by the absorption of a photon within a semiconductor, causing the electron to transition from the valence band to the conduction band, leaving a hole in the valence band behind. Notably, the exciton exists as an electrically neutral quasiparticle, enabling energy transport without simultaneous transfer of net electric charge. Although the exciton (electron and hole bound state) in traditional semiconductors is weakly bound as a result of intrinsic screening, the interaction between electrons and holes remains a crucial aspect for comprehending the optical properties of semiconductors and insulators (DRESSELHAUS, 1957; ELLIOTT, 1957).

In 1957, Skornyakov and Ter-Martirosyan (SKORNIKOV; TER-MARTIROSIAN, 1957) successfully tackled the quantum three-body problem and formulated equations to determine the wave function of a system consisting of three identical fermions in the scenario of zero-range forces. In 1958, Lampert introduced more intricate few-body systems comprising electrons and holes, namely, negatively charged trions (eeh) and positively charged

trions (ehh). These entities arise by binding an electron within a conduction band or a hole within a valence band to an exciton (LAMPERT, 1958).

Subsequently, Faddeev (FADDEEV, 1961) extended the integral equation approach (SKORNIAKOV; TER-MARTIROSIAN, 1957) to encompass interactions of both finite and long ranges. However, the study of trions was initially hindered due to their weak binding energy, which resulted from the strong screening of the Coulomb interaction in ordinary materials. The emergence of quantum wells, however, paved the way for the exploration of trion properties, as the reduced dimensionality in these structures effectively reduced the screening effects and allowed for more stable trion formation.

It is worth noting that trions in semiconductors are different from traditional 3B systems like the triton or the $^4\text{He}_3$ atomic trimer. The constituents of a trion experience two attractive interactions and one repulsive interaction.

In the following, the primary motivations of the author for undertaking this dissertation are succinctly addressed.

1.2 The power of Faddeev-Yakubovsky equations in solving three- and four-body systems

The Faddeev equations are a common and well-established method for studying systems composed of three-body (3B), including both bound and scattering states. These equations serve as a generalization of the three-particle Lippmann-Schwinger (LS) equation, which is commonly used to analyze two-particle systems in bound and scattering states. The key distinction is that for 2B systems, the Schrödinger equation can be directly utilized instead of the LS equation. However, when dealing with few-body systems consisting of three or more particles, employing the Schrödinger equation directly presents challenges regarding convergence and solution uniqueness (YAMASHITA *et al.*, 2018; GREENE *et al.*, 2017). To address these challenges, Faddeev proposed a solution by formulating a 3B system using the Schrödinger equation, which resulted in the development of an integral equation called the Faddeev equation (FADDEEV, 1961). This approach was later extended by Yakubovsky to encompass four-body (4B) systems, leading to the formulation of the Faddeev-Yakubovsky equations. The Faddeev-Yakubovsky (FY) equations provide a powerful non-perturbative method for solving the Schrödinger equation in three- and four-body systems, offering reliable and converged solutions. These equations have been extensively studied in the nonrelativistic regime across various branches of physics, including atomic, nuclear, and particle physics, for both bound and scattering states. The success of nonrelativistic three-body Faddeev calculations has been convincingly demonstrated in various studies, such as Refs. (CORNELIUS *et al.*, 1990; GLOECKLE *et al.*, 1996;

GLÖCKLE, 2012). We can also mention references concerning the bound-state four-body FY formalism, such as Refs. (GIBSON; LEHMAN, 1988; KAMADA *et al.*, 2001; FILIKHIN *et al.*, 2002; HADIZADEH *et al.*, 2012; LAZAUSKAS; CARBONELL, 2004; BAYEGAN *et al.*, 2008a) and references therein.

1.3 Implications of relativistic effects in the zero range limit on three-Boson systems

Understanding the interactions between nucleons is essential to understanding the structure and properties of few-body quantum system. It is also essential for accurately describing nuclear reactions.

Many experiments have been conducted at low energies (below the pion-production threshold), where nonrelativistic descriptions of nucleons are sufficient. The pion-production threshold is the energy at which pions are produced in NN scattering, which is approximately 300 MeV in the laboratory frame. The short-range part of the NN interaction, which occurs at distances less than 1.5 femtometers, can only be observed in scattering experiments with energies greater than 300 MeV. At the high energies, the kinetic energy of each nucleon is comparable to or even greater than the mass of a nucleon. This requires the development of relativistic nuclear theories and the use of Poincaré-invariant quantum mechanics to study these interactions. This research provides valuable insights into NN interactions and 3N forces.

The study of 3N systems offers an excellent avenue for microscopically examining inter-nucleon interactions. The Faddeev theory, which dates back to the 1960s (FADDEEV, 1960), serves as the foundation for investigating 3N problems. Nonrelativistic Faddeev calculations have been extensively conducted to analyze the 3N bound state and 3N scattering processes in the low-energy regime. However, the calculations have shown differences from experimental values. These discrepancies are attributed to two factors: the impact of 3B forces and relativistic effects.

While many studies have explored the impact of relativistic effects on bound states (KONDRATYUK *et al.*, 1981; GLÖCKLE *et al.*, 1986; KONDRATYUK *et al.*, 1989; SAMMARUCA *et al.*, 1992; STADLER; GROSS, 1997; CARBONELL; KARMANOV, 2003; KAMADA *et al.*, 2010; HADIZADEH *et al.*, 2014; POLYZOU; ELSTER, 2014) and scattering states (KAMADA, 2000; SEKIGUCHI *et al.*, 2005; KEISTER; POLYZOU, 2006; WITAŁA *et al.*, 2006; SKIBIŃSKI *et al.*, 2006; WITAŁA *et al.*, 2011) in quantum mechanical few-body system, there has been limited studies of the specific case of relativistic effects in the zero range limit using the FY equations, which in this limit, the short-range part of the interaction, where the wave function is most influenced, is neglected, and the focus is directed towards the long-range

part characterized by the scattering length (NAIDON; ENDO, 2017).

The distinction between relativistic and nonrelativistic dynamics arises from three factors (HADIZADEH *et al.*, 2020):

- (i) The momentum-dependent nature of the kinetic energy or free propagator,
- (ii) The relationship between potential operators and the 2B t -matrices,
- (iii) The structure of the momentum basis, which results in a non-identical Jacobian for the change of momentum variables and includes a permutation coefficient in the relativistic case.

In this work, we will utilize the aforementioned formulation to investigate the stability of three-boson systems under separable potentials, specifically Yamaguchi-type and Gaussian-type potentials, as they approach the zero-range limit. Our objective is to solve the relativistic Faddeev equations and extract the binding energies and corresponding wave functions. By studying these properties, we aim to gain insights into the behavior of the systems as the interaction range approaches zero.

1.4 Binding and structural properties of negatively charged trions in a suspended two-dimensional MoS₂ layer

The observation of a trion peak in quantum wells, which are two-dimensional (2D) systems, was first reported in 1993 (KHENG *et al.*, 1993). It was predicted that the trion energies in these systems would be approximately ten times higher than in the 3D case (STÉBÉ; AINANE, 1989). Hence, the experimental detection of trions should be considerably easier in 2D semiconductors compared to their 3D counterparts. The synthesis of 2D semiconductors (SONG *et al.*, 2013) has revealed that excitons and trions exhibit significantly larger binding energies (UGEDA *et al.*, 2014) compared to traditional materials. This enhancement arises from reduced screening effects, as the electric field lines extend beyond the boundaries of the 2D semiconductor (MAK *et al.*, 2013). In these systems, the strength of the interaction can be externally controlled by implementing appropriate dielectric engineering techniques (CHAVES *et al.*, 2020).

In terms of materials, the other highly researched 2D materials besides graphene are the semiconducting transition metal dichalcogenides (TMDs). These have the chemical formula MX_2 , where M stands for a transition metal like Mo or W, and X stands for a chalcogenide like S, Se, or Te (KORMÁNYOS *et al.*, 2015). In TMDs, the interaction between charge carriers primarily occurs through the screened Coulomb interaction, which, in the

classical regime, is described by the Rytova-Keldysh (RK) potential. This potential is obtained as the solution to the Poisson equation for an infinitesimally thin dielectric slab (CUDAZZO *et al.*, 2011).

Novel 2D materials offer exciting opportunities for exploring few-body systems. A wide range of materials, including TMDs, hexagonal boron nitride, and graphene, host excitons, trions, and biexcitons. Furthermore, in these systems, excitons and trions can exhibit strong coupling with light, giving rise to exciton-polaritons (LIU *et al.*, 2015; EPSTEIN *et al.*, 2020) and trion-polaritons (EMMANUELE *et al.*, 2020), respectively. These phenomena open up new avenues for studying the interactions and collective behavior of these excitations in the realm of 2D materials. Trion investigations in 2D materials have been the subject of several experiments. In the case of MoS₂, large trion binding energies have been observed. Experimental values ranging from 20-43 meV have been reported for samples deposited on SiO₂ substrates (MAK *et al.*, 2013; ROSS *et al.*, 2013; SOKLASKI *et al.*, 2014; ZHANG *et al.*, 2015b), while a value of 80 meV was measured for suspended samples (LIN *et al.*, 2019). Another study (LIN *et al.*, 2014) explored different substrates and provided an extrapolation curve indicating a trion binding energy of 44 meV for the suspended case. It is important to note that the trion binding energy is influenced by the dielectric environment (LIN *et al.*, 2014), doping levels (MAK *et al.*, 2013), and temperature (JADCZAK *et al.*, 2017). These factors contribute to the variations observed in the measured trion binding energies.

In the field of cold-atom physics, three-particle bound states also emerge. By employing trapping techniques, it becomes possible to gradually reduce the system's dimensionality from 3D to 2D (PETHICK; SMITH, 2008; BELLOTTI *et al.*, 2012; BELLOTTI *et al.*, 2013; BELLOTTI *et al.*, 2013; YAMASHITA *et al.*, 2014; BELLOTTI *et al.*, 2014). Consequently, the notable Efimov effect (EFIMOV, 1970) vanishes, and the previously observed log-periodic behavior of the wave function transforms into a power law dependence (ROSA *et al.*, 2022; ROSA *et al.*, 2018; YAMASHITA, 2019).

In the current work, we will focus on the study of trions in an undoped suspended MoS₂ layer at zero temperature. It is important to note that due to the idealized conditions of our investigation, we do not anticipate an exact match with experimental measurements conducted at finite temperatures and with residual doping. Nonetheless, our analysis aims to provide valuable insights and theoretical understanding of trion properties in this specific system. Numerous theoretical calculations have already been conducted to determine trion binding energies (BERKELBACH *et al.*, 2013a; KIDD *et al.*, 2016a; SZYNISZEWSKI *et al.*, 2017b; DONCK *et al.*, 2017; FILIKHIN *et al.*, 2018; KEZERASHVILI; TSIKLARI, 2017; CHANG; CHANG, 2021). Trions introduce a scenario where the system involves two identical particles, either eeh or ehh, thereby giving rise to a three-body system AAB when considering the two identical particles. To thoroughly explore such a three-body configuration, the Faddeev formalism emerges as the most rigorous method (KEZERASHVILI, 2019).

The objective of this work is to investigate negatively charged trions in a MoS_2 layer using the Faddeev equations approach in momentum and configuration space. Our focus will be on exploring the binding and structural properties of these trions within this specific material system.

1.5 Outline

In chapter 2, our focus is on investigating the structure of the relativistic and boosted potential in three dimensions (3D). To achieve this, we calculate the relativistic potential by deriving it from the corresponding nonrelativistic potential. Specifically, we employ various nonrelativistic Yamaguchi separable potential types. Subsequently, we proceed to calculate the relativistic binding energy of a three-body (3B) system in 3D. This is accomplished by utilizing the Faddeev equation and incorporating the boosted potential obtained in the previous step. Throughout this analysis, we maintain the fixed value of the binding energy for the two-body (2B) system. Moreover, we aim to investigate the behavior of the 3B system when the potential range approaching zero. This investigation is carried out while keeping the 2B binding energy constant by increasing the potential parameters for the Yamaguchi and Gaussian form factor. We also explore the behavior of the 3B system when the potential range is fixed, and the 2B binding energy is varied.

In chapter 3, we focus on the study of nonrelativistic trions in a two dimensions (2D) momentum space MoS_2 layer. We begin by studying the 2B properties in 2D. Subsequently, we proceed to calculate the trion binding energy in this system. This is accomplished by solving the three coupled Faddeev equations in momentum space. We also investigate the cluster structure of a system consisting of charged particles with attractive and repulsive interaction.

In chapter 4, we study the nonrelativistic trions in configuration space. By employing a Fourier transform, we convert the momentum space wave function into its configuration space representation, enabling us to analyze the spatial distribution and correlations of the trion's constituent particles. We investigate the trion structure using the Yamaguchi and Rytova-Keldysh (RK) potentials, employing regularization techniques to address the challenges posed by the long-range nature of the RK potential. Our calculations provide insights into the geometrical arrangement of the particles within the trion and highlight the accuracy of our numerical methods.

In chapter 5, we extend our investigation to four-body systems in two-dimensional momentum space using the Faddeev-Yakubovsky (FY) equations. We discuss the theoretical framework of the FY approach and its application to four interacting particles. The chapter outlines the derivation of the FY equations in 2D space, emphasizing per-

mutation symmetries and the decomposition of the wave function. Numerical results for a specific case involving identical particles interacting through a separable potential are presented, demonstrating the effectiveness of our iterative method. This chapter serves as a stepping stone for future studies on the physical problem of biexcitons in 2D systems.

In Chapter 6, we delve into the potential for uncovering new dimensions within few-body systems, extending the scope of this research.

It is noteworthy to mention that the outcomes presented in Chapter 2 have been built upon the work previously published in Ref. (MOHSENI *et al.*, 2021), while the results in Chapter 3 published in Ref. (MOHSENI *et al.*, 2023).

2 Zero-Range Limits and Three-Boson Stability in Boosted Potentials

2.1 Overview

In the study of the relativistic three-boson system, a key issue is its stability when considering a zero-range interaction (YDREFORS *et al.*, 2020). The zero-range 2B interaction represents a significant limiting scenario that captures essential characteristics observed in nuclear and atomic few-body systems (CARBONELL; KARMANOV, 2003; YAMASHITA *et al.*, 2003; BELLOTTI *et al.*, 2011). The concern arises from the known occurrence of the Thomas collapse (THOMAS, 1935; COUTINHO *et al.*, 1995) in the nonrelativistic three-boson system with contact potentials. In other words, the binding energy of a three-body system approaches $-\infty$ as the range of the interaction between the particles approaches zero. To address this issue, stability has been demonstrated by solving the Light-Front (LF) reduction of the Faddeev-Bethe-Salpeter (FBS) equation (CARBONELL; KARMANOV, 2003; KARMANOV; CARBONELL, 2004). Furthermore, stability in the three-boson system has been confirmed by solving the four-dimensional FBS equation for the contact interaction in Euclidean space (YDREFORS *et al.*, 2017b). These investigations have highlighted the significance of the implicit 3B interactions that arise from relativistic effects (KARMANOV; MARIS, 2009).

Given this background, it becomes relevant to explore the stability of the three-boson system with contact interactions using alternative frameworks for formulating the relativistic Faddeev equations. For instance, one approach is to employ boosted potentials (KAMADA; GLÖCKLE, 2007). This motivation arises from the need to understand the stability properties of the system under different theoretical formulations, which can shed light on the interplay between relativistic effects and contact interactions. The boost concept comes from the moving 2B subsystem in the rest frame of the three-particle system.

At the 2B level, the relativistic 2B potentials are specifically designed to ensure the preservation of dimer properties and 2B observables. These relativistic 2B potentials serve as inputs for calculating t -matrices. Several methods exist for computing the relativistic

2B t -matrices, including the following options:

- One approach involves solving the relativistic Lippmann-Schwinger equation using relativistic 2B potentials. These potentials can be derived from their nonrelativistic counterparts by solving a quadratic equation. Several computational methods have been developed to tackle this nonlinear equation, including the spectral expansion method (KAMADA *et al.*, 2002; GLÖCKLE *et al.*, 1986) and an iterative approach (KAMADA; GLÖCKLE, 2007). In the spectral expansion method, a completeness relation of the 2B bound and scattering states is inserted into the right side of the quadratic equation, followed by a projection into momentum space. alternatively, Kamada and Glöckle proposed a highly effective iterative scheme that has been successfully applied in two- and three-body calculations involving bound and scattering states, using a partial wave decomposition. In this study, we extend the implementation of the iterative scheme to 3B bound state calculations within a three-dimensional (3D) and partial wave (PW) framework. This extension involves directly computing the relativistic 2B t -matrices from the relativistic 2B potentials.
- Another option involves directly calculating the relativistic 2B t -matrices from their nonrelativistic counterparts. This approach employs a two-step process to achieve the desired results. In the first step, the relativistic right-half-shell 2B t -matrices are analytically computed based on the nonrelativistic right-half-shell 2B t -matrices. This calculation is followed by the determination of the fully off-shell 2B t -matrices in the second step. The second step involves solving the first resolvent equation using the Coester-Piper-Serduke transformation (COESTER *et al.*, 1975; KEISTER; POLYZOU, 2006). Notably, this method eliminates the need for the matrix elements of the relativistic 2B potentials. Its successful implementation has been demonstrated in 3B bound and scattering calculations employing a 3D approach (LIN *et al.*, 2007; LIN *et al.*, 2008; POLYZOU; ELSTER, 2014; ELSTER *et al.*, 2007; HADIZADEH *et al.*, 2014).

While these approaches have been effectively applied in the context of the NN problem and 3D framework (HADIZADEH; RADIN, 2017) with Malfliet Tjon (MT) potential, but its feature in the short and zero range limit has not been investigated. In order to investigate the stability of the three-boson system under contact potentials, we employ the framework of boosted potentials (KAMADA; GLÖCKLE, 2007), i.e., the moving 2B subsystem in the rest frame of the three-particle system (MOHSENI *et al.*, 2021). Once the boosted potential is determined, the 2B t -matrix within the rest frame of the 3B system can be computed, as required for the kernel of the relativistic Faddeev equations (HADIZADEH *et al.*, 2014; HADIZADEH *et al.*, 2020). The above formulation will be employed to investigate the stability of the three-boson system using separable potentials (specifically, Yamaguchi-type

and Gaussian-type potentials) as they approach the zero-range limit. Our objective is to solve the relativistic Faddeev equations, enabling us to determine the binding energies and corresponding wave functions and study their properties when the potential range is driven towards zero. It is important to emphasize that the relativistic Faddeev approach utilizing boosted potentials is not based on field theory; rather, it utilizes a relativistic version of the phenomenological 2B potential. This approach belongs to “instant” form, one of the three forms of relativistic dynamics proposed by Dirac in 1949 (DIRAC, 1949): the “instant” form, the “LF” form, and the “point” form. Each form of dynamics is characterized by the number of kinematical and dynamical boosts, which correspond to the generators of the Poincaré group. The kinematical boosts keep the initial state hypersurface invariant and do not contain the potential, while the dynamical ones depend on the potential. In the instant form, six out of the ten Poincaré group generators are kinematical, while the remaining four are dynamical and involve the potential. In the LF form, seven generators are kinematical, and three are dynamical. A comprehensive discussion on applying these dynamics forms to nuclear few-body systems can be found in Ref. (CARBONELL *et al.*, 1998).

The relativistic framework developed by Kamada and Glöckle falls within the class of “instant” form dynamics. Their approach, applied to few-nucleon systems, aims to preserve the relativistic 2B bound state (dimer) energy and nucleon-nucleon phase shifts as obtained in nonrelativistic calculations. Furthermore, it provides energy states with good angular momentum quantum numbers, as usual in the nonrelativistic frameworks. Consequently, the relativistic Faddeev approach with boosted potential can be viewed as one practical implementation of the instant form of dynamics. Furthermore, we will provide a quantitative comparison between the outcomes of the Kamada and Glöckle instant form framework and the results derived from LF and field theoretical models in the limit of zero-range potentials (CARBONELL *et al.*, 1998; CARBONELL; KARMANOV, 2003; KARMANOV; CARBONELL, 2004; YDREFORS *et al.*, 2017a; YDREFORS *et al.*, 2017b; ROSA *et al.*, 2022).

In Section 2.2.1 and Section 2.2.2, we present the formalism and numerical results for the relativistic and boosted potentials. Moving on, in Section 2.3, we explore the formalism and present our numerical results for the nonrelativistic and relativistic 2B binding energy. Finally, in Section 2.4, we examine the nonrelativistic and relativistic 3B bound states.

2.2 Nonrelativistic, relativistic, and boosted potentials

2.2.1 Relativistic potentials

As we discussed in Section 2.1 the first step toward the calculation of relativistic t -matrices and then 3B bound and scattering state is the calculation of the relativistic potentials from nonrelativistic ones (KAMADA; GLÖCKLE, 2007; HADIZADEH; RADIN, 2017; MOHSENI *et al.*, 2021; HADIZADEH *et al.*, 2021). The relationship between relativistic and nonrelativistic nucleon-nucleon (NN) potentials, denoted as V_r and V_{nr} respectively, emerges from a comparison of the nonrelativistic and relativistic Schrödinger equations. The well-known nonrelativistic Schrödinger equation is given by

$$\left(\frac{\hat{p}^2}{m} + V_{nr}\right) \psi_{nr} = \frac{p_0^2}{m} \psi_{nr}, \quad (2.1)$$

where we are assuming $\hbar c = 1$. In the relativistic framework, the Schrödinger equation takes the form

$$\left(2\sqrt{m^2 + \hat{p}^2} + V_r\right) \psi_r = 2\sqrt{m^2 + p_0^2} \psi_r. \quad (2.2)$$

By comparing Eqs (2.1) and (2.2), we arrive at a quadratic operator equation that relates the nonrelativistic and relativistic potentials (COESTER *et al.*, 1975; FRIAR, 1999; KAMADA; GLÖCKLE, 2007)

$$V_{nr} = \frac{1}{4m} \left(\omega(\hat{p}) V_r + V_r \omega(\hat{p}) + V_r^2 \right), \quad (2.3)$$

where $\omega(\mathbf{p}) = 2E(\mathbf{p}) = 2\sqrt{\mathbf{p}^2 + m^2}$, m is the mass of the nucleon, and \mathbf{p} is the relative momentum of the two-nucleon.

As is it shown in Ref. (HADIZADEH; RADIN, 2017), the matrix elements of relativistic potential, V_r , can be obtained from the nonrelativistic potential V_{nr} , by solving a quadratic integral equation

$$\langle \mathbf{p} | V_r | \mathbf{p}' \rangle + \frac{1}{\omega(p) + \omega(p')} \int_0^\infty d^3 p'' \langle \mathbf{p} | V_r | \mathbf{p}'' \rangle \langle \mathbf{p}'' | V_r | \mathbf{p}' \rangle = \frac{4m \langle \mathbf{p} | V_{nr} | \mathbf{p}' \rangle}{\omega(p) + \omega(p')}. \quad (2.4)$$

The nonrelativistic potential used in our study, as described by Eq. (2.4), is a spin-independent one-term separable potential (YAMAGUCHI, 1954a). The one-term separable potential can be represented in momentum space as

$$V(p, p') = \lambda g(p) g(p'), \quad (2.5)$$

here, λ represents the potential strength, and $g(p)$ is the form factor. For the Yamaguchi form factor (YAMAGUCHI, 1954b), $g(p)$ is defined as

$$g(p) = \frac{1}{p^2 + \beta^2}. \quad (2.6)$$

Table 2.1 provides the parameters for different models of the Yamaguchi potential used in our calculations. It is worth noting that we employ the value $\hbar^2/m = 41.470$ (MeV.fm²), where \hbar is the reduced Planck's constant and m represents the relevant mass.

TABLE 2.1 – Parameters for different models of the Yamaguchi (Y) potential.

Yamaguchi potential type	$-\lambda \times m$ [fm ⁻³]	β [fm ⁻¹]
Y-I	0.415	1.45
Y-II	0.353	1.45
Y-III	0.182	1.15
Y-IV	0.179	1.15

In general, to determine the potential strength λ , one can utilize the pole property of separable t -matrices and employ the following relation (SCHMID; ZIEGELMANN, 1974; PLATTER *et al.*, 2004a; HADIZADEH *et al.*, 2011; FREDERICO *et al.*, 2012)

$$\frac{1}{\lambda_{\text{nr}}} = 4\pi \int_0^\infty dp p^2 \frac{g^2(p)}{E_d - \frac{p^2}{m}}, \quad (2.7)$$

where λ_{nr} is the nonrelativistic potential strength and E_d is the binding energy of 2B bound state, also called *dimer*. Derivation of Eq. (2.7) is given in Appendix B. This equation allows us to determine the potential strength λ_{nr} by evaluating the integral involving the form factor $g(p)$ by fitting the dimer binding energy E_d .

For solving Eq. (2.4) in 3D, we define a coordinate system by choosing the relative momentum vector \mathbf{p} parallel to z -axis and vector \mathbf{p}' in the $x - z$ plane

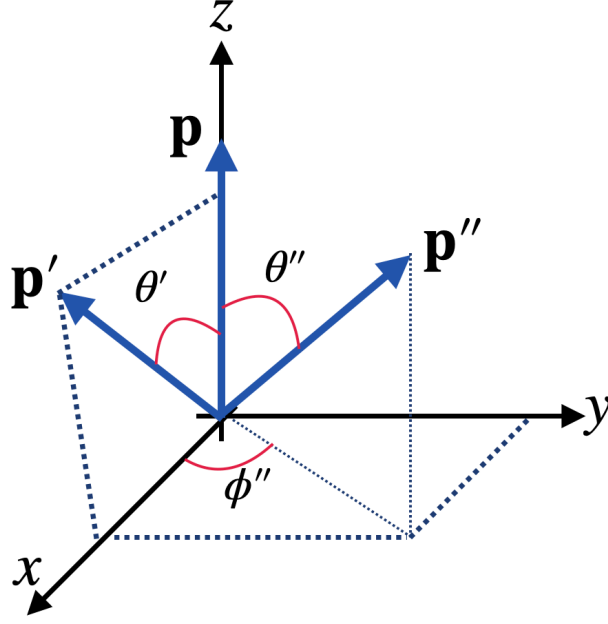


FIGURE 2.1 – The geometry of vectors, \mathbf{p} , \mathbf{p}' & \mathbf{p}'' . The vector p is chosen to be parallel to the z -axis and vector \mathbf{p}' is in the $x - z$ plane, and \mathbf{p}'' is free in the 3D space. The angle variables defined in Eqs. (2.9) are indicated.

Using this coordinate system, Eq. (2.4) can be written explicitly as

$$V_r(p, p', x') + \frac{1}{\omega(p) + \omega(p')} \int_0^\infty dp'' p''^2 \int_{-1}^1 dx'' \int_0^{2\pi} d\phi'' \times V_r(p, p'', x'') V_r(p'', p', y) = \frac{4m V_{nr}(p, p', x')}{\omega(p) + \omega(p')}, \quad (2.8)$$

where

$$\begin{aligned} y &= \hat{\mathbf{p}}'' \cdot \hat{\mathbf{p}}' = x' x'' + \sqrt{1 - x'^2} \sqrt{1 - x''^2} \cos \phi'', \\ x' &= \hat{\mathbf{p}}' \cdot \hat{\mathbf{p}}, \\ x'' &= \hat{\mathbf{p}}'' \cdot \hat{\mathbf{p}}. \end{aligned} \quad (2.9)$$

In s -wave, Eq. (2.8) can be expressed as

$$V_r(p, p') + \frac{4\pi}{\omega(p) + \omega(p')} \int_0^\infty dp'' p''^2 V_r(p, p'') V_r(p'', p') = \frac{4m V_{nr}(p, p')}{\omega(p) + \omega(p')}. \quad (2.10)$$

To solve Eq. (2.10), we employ an iteration technique. The iteration process begins with an initial guess for the relativistic potential $V_r^{(0)}(p, p')$, which is set to the right-hand side of Eq.(2.10)

$$V_r^{(0)}(p, p') = \frac{4m V_{nr}(p, p')}{\omega(p) + \omega(p')}. \quad (2.11)$$

The iteration continues until the calculated relativistic potential satisfies Eq. (2.10) at each set point (p, p') with a relative error of 10^{-6} . This convergence criterion ensures that the obtained relativistic potential sufficiently satisfies the equation.

Table A.1 presents an example of the convergence of the matrix elements of the relativistic potential $V_r(p, p')$ as a function of the iteration number.

In Fig. 2.2 we have shown our numerical results for the nonrelativistic, and relativistic potential calculated from the Yamaguchi potential when the potential strength is calculated by Eq. (2.7) with $E_d = -2.225$ MeV. The difference between the nonrelativistic and constructed relativistic potentials is also shown in the right panel.

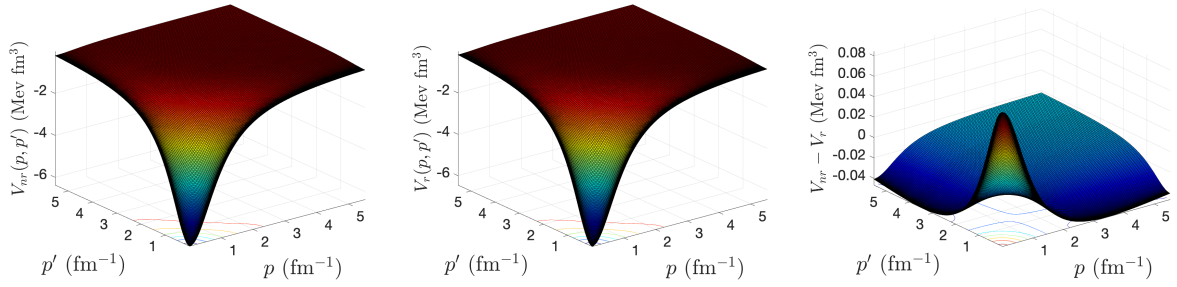


FIGURE 2.2 – The matrix elements of the nonrelativistic (left panel), the relativistic (middle panel) NN potentials and their differences (right panel) calculated by separable Yamaguchi potential with $\beta = 1$ as a function of 2B relative momenta p and p' . Results are obtained with λ_{nr} calculated with Eq. (2.7) with $E_d = -2.225$ MeV.

From the figures, it is evident that the constructed relativistic potential closely resembles the nonrelativistic potential. The main difference between nonrelativistic and constructed relativistic potential is observed at low momenta. In this region, the relativistic potential deviates slightly from the nonrelativistic one. Overall, the two potentials exhibit similar behavior and are in close agreement, indicating that the relativistic corrections have a limited impact on the potential shape, particularly at higher momenta.

2.2.2 Boosted potentials

The 2B boosted potentials, denoted as $V_{k_{ij}} \equiv V_k$, which are embedded in the 3B Hilbert space, can be derived from the relativistic 2B potential V_r through a nonlinear relationship (HADIZADEH *et al.*, 2020)

$$V_k = \left((\omega(\hat{p}) + V_r)^2 + \hat{k}^2 \right)^{\frac{1}{2}} - \left(\omega^2(\hat{p}) + \hat{k}^2 \right)^{\frac{1}{2}}, \quad (2.12)$$

where $\mathbf{k} = \mathbf{k}_i + \mathbf{k}_j$ is total momentum of the subsystem (ij) , $\omega(\hat{p}) = 2E(\hat{p}) = 2\sqrt{m^2 + \hat{p}^2}$, and \mathbf{p} is the relative momentum in the 2B subsystem (ij) . As mentioned in Section 2.1,

the dependence on k arises due to the fact that in a 3B system the 2B subsystems are not at rest. Obviously, for $\mathbf{k} = \mathbf{0}$ the boosted potential reduces to the relativistic potential, i.e. $V_k = V_r$.

Alternatively, according to the approach described in (KAMADA; GLÖCKLE, 2007), the boosted potential can be derived from the nonrelativistic potential using the quadratic equation

$$V_{nr} = \frac{1}{4m} \left(\omega_k(\hat{p}) V_k + V_k \omega_k(\hat{p}) + V_k^2 \right), \quad (2.13)$$

where $\omega_k(\hat{p}) = \left(\omega^2(\hat{p}) + \hat{k}^2 \right)^{\frac{1}{2}}$. By solving this quadratic equation, the boosted potential V_k can be obtained based on the given nonrelativistic potential V_{nr} . Indeed, when $\mathbf{k} = \mathbf{0}$, the Eq. (2.13) simplifies and confirms that for $k = 0$, the boosted potential can be reduced to the relativistic potential, as given by Eq. (2.3). This result is expected since in the case of $\mathbf{k} = \mathbf{0}$, there is no boost in momentum, and the relativistic effects are fully captured by the relativistic potential. Therefore, the boosted potential becomes equivalent to the relativistic potential in this limit.

The Eqs. (2.3) and (2.13) have same operator forms, where V_r and ω are replaced by V_k and ω_k , respectively. Hence, the boosted potential matrix elements can be obtained by utilizing the nonrelativistic potential elements and solving the following 3D integral equation

$$V_k(\mathbf{p}, \mathbf{p}') + \frac{1}{\omega_k(p) + \omega_k(p')} \int d^3 p'' V_k(\mathbf{p}, \mathbf{p}'') V_k(\mathbf{p}'', \mathbf{p}') = \frac{4m V_{nr}(\mathbf{p}, \mathbf{p}')}{\omega_k(p) + \omega_k(p')}. \quad (2.14)$$

An important feature of the boosted potential, as shown in Eq. (2.14), is its decreasing effect as the momentum of the spectator particle k increases. This behavior leads to a repulsive influence in the ultraviolet region (UV), counteracting the attractive forces at short range. We will explore these properties while studying the three-boson bound state in the limit of a zero range.

Similar to the calculation of the relativistic potential from the nonrelativistic one, the matrix elements of the boosted potential V_k can also be computed using the coordinate system defined in Fig. 2.1. Hence, Eq. (2.14) can be explicitly written as

$$\begin{aligned} V_k(p, p', x') + \frac{1}{\omega_k(p) + \omega_k(p')} \int_0^\infty dp'' p''^2 \int_{-1}^1 dx'' \int_0^{2\pi} d\phi'' &\times V_k(p, p'', x'') V_k(p'', p', y) \\ &= \frac{4m V_{nr}(p, p', x')}{\omega_k(p) + \omega_k(p')}. \end{aligned} \quad (2.15)$$

In this study, we adopt a similar methodology to the one employed in Section 2.2.1 for

calculating the boosted potential. This approach is based on the iterative technique proposed by Kamada and Glöckle (KAMADA; GLÖCKLE, 2007), which we previously utilized for deriving the relativistic potential from its nonrelativistic counterpart. The goal was to obtain the matrix elements of the boosted potential $V_k(p, p', x')$ based on the nonrelativistic potentials $V_{nr}(p, p', x')$. By iteratively evaluating the integral equation, we aimed to find a solution that satisfies the equation and provides the desired matrix elements of the boosted potential. The iteration process allows us to gradually improve the accuracy of the calculated values until convergence is achieved. To solve for the matrix elements of the boosted potential $V_k(p, p')$, we project Eq. (2.15) onto the s -wave channel, resulting in Eq. (2.16)

$$V_k(p, p') + \frac{4\pi}{\omega_k(p) + \omega_k(p')} \int_0^\infty dp'' p''^2 V_k(p, p'') V_k(p'', p') = \frac{4m V_{nr}(p, p')}{\omega_k(p) + \omega_k(p')}, \quad (2.16)$$

the iterative process begins with an initial guess for the matrix elements given by Eq. (2.17).

$$V_k^{(0)}(p, p') = \frac{4m V_{nr}(p, p')}{\omega_k(p) + \omega_k(p')}. \quad (2.17)$$

The iteration is then performed until convergence is achieved in the matrix elements of the boosted potential. Convergence is considered reached when the relative error falls below 10^{-6} for each grid point (p, p') . By iteratively improving the matrix elements using Eq. (2.16), we can obtain the desired solutions that satisfy the equation and provide accurate values for the boosted potential.

Table A.2 illustrates an example of the convergence of the matrix elements of the boosted potential $V_k(p, p')$ as a function of iteration number.

Fig. 2.3 presents the matrix elements of the nonrelativistic and boosted potentials, as well as the difference between them. Similar to the difference between the relativistic and nonrelativistic potentials (see Fig. 2.2), the difference between the boosted and nonrelativistic potentials is primarily noticeable in the low momentum region. The results show that the constructed boosted potential closely matches the nonrelativistic potential, but there are some differences, especially at low momenta. These differences become more pronounced as the boosted momenta increase.

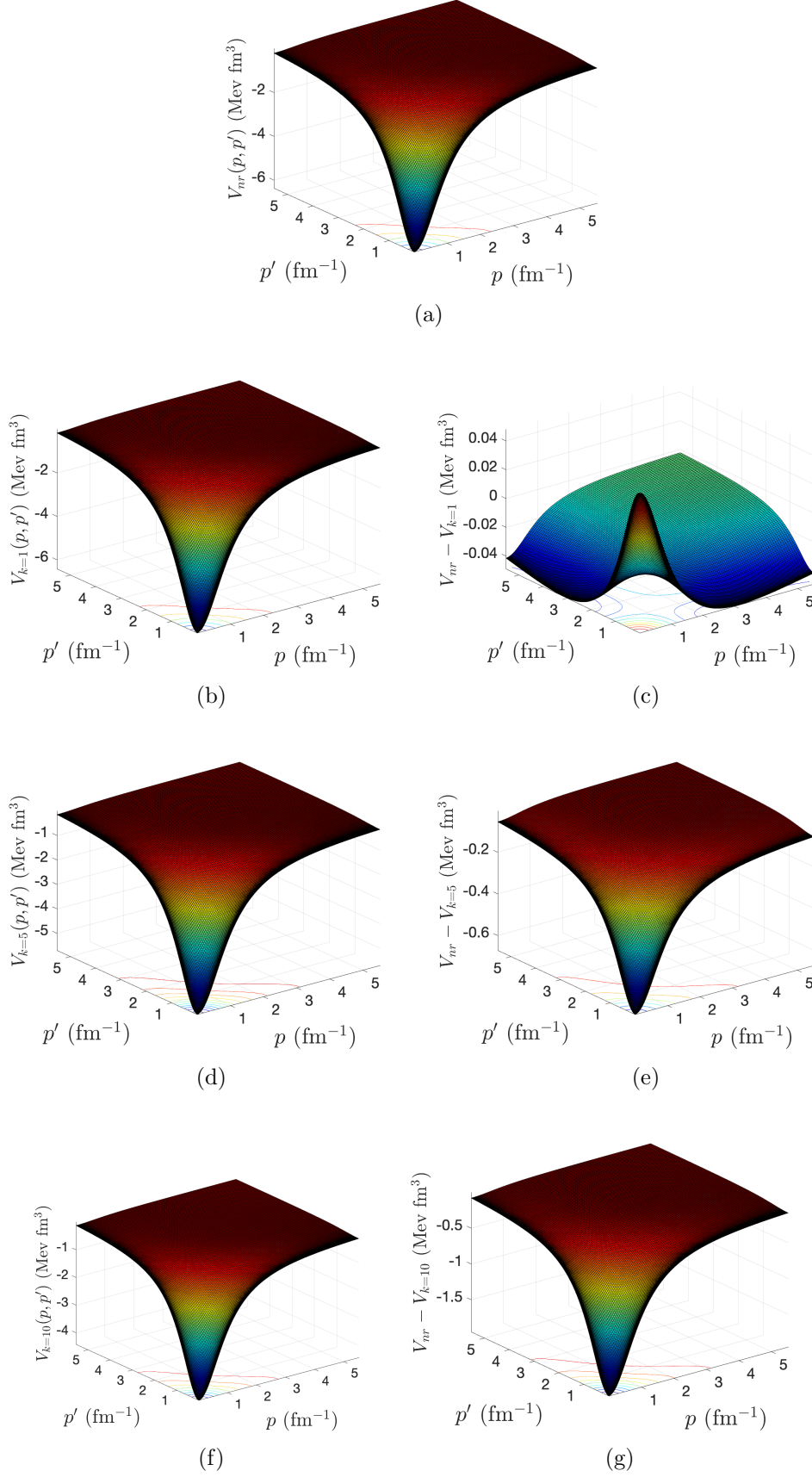


FIGURE 2.3 – The matrix elements of the nonrelativistic (a), and the boosted (b,d & f) 2B potentials and their differences (c,e & g) calculated by Yamaguchi separable potential as a function of 2B relative momenta p and p' with $k = 1, 5, 10 \text{ fm}^{-1}$. Results are obtained with λ_{nr} calculated with Eq. (2.7) with $E_d = -2.225 \text{ MeV}$.

For a comprehensive study of the properties of boosted potential we adopted Gaussian form factor which is given as (DELTUVA *et al.*, 2011)

$$g(p) = \exp\left(-\frac{p^2}{\Lambda^2}\right). \quad (2.18)$$

Fig. 2.4 shows the diagonal matrix elements of the nonrelativistic and boosted potentials for Yamaguchi-type potentials (upper panel) and Gaussian potentials (lower panel). The calculations are performed for various values of the boosted momentum k and a broad range of form factor parameters β for Yamaguchi potentials and Λ for Gaussian potentials. The potential strength λ_{nr} is determined using Eq. (2.7) with a fixed dimer binding energy of $E_d = -2.225$ MeV.

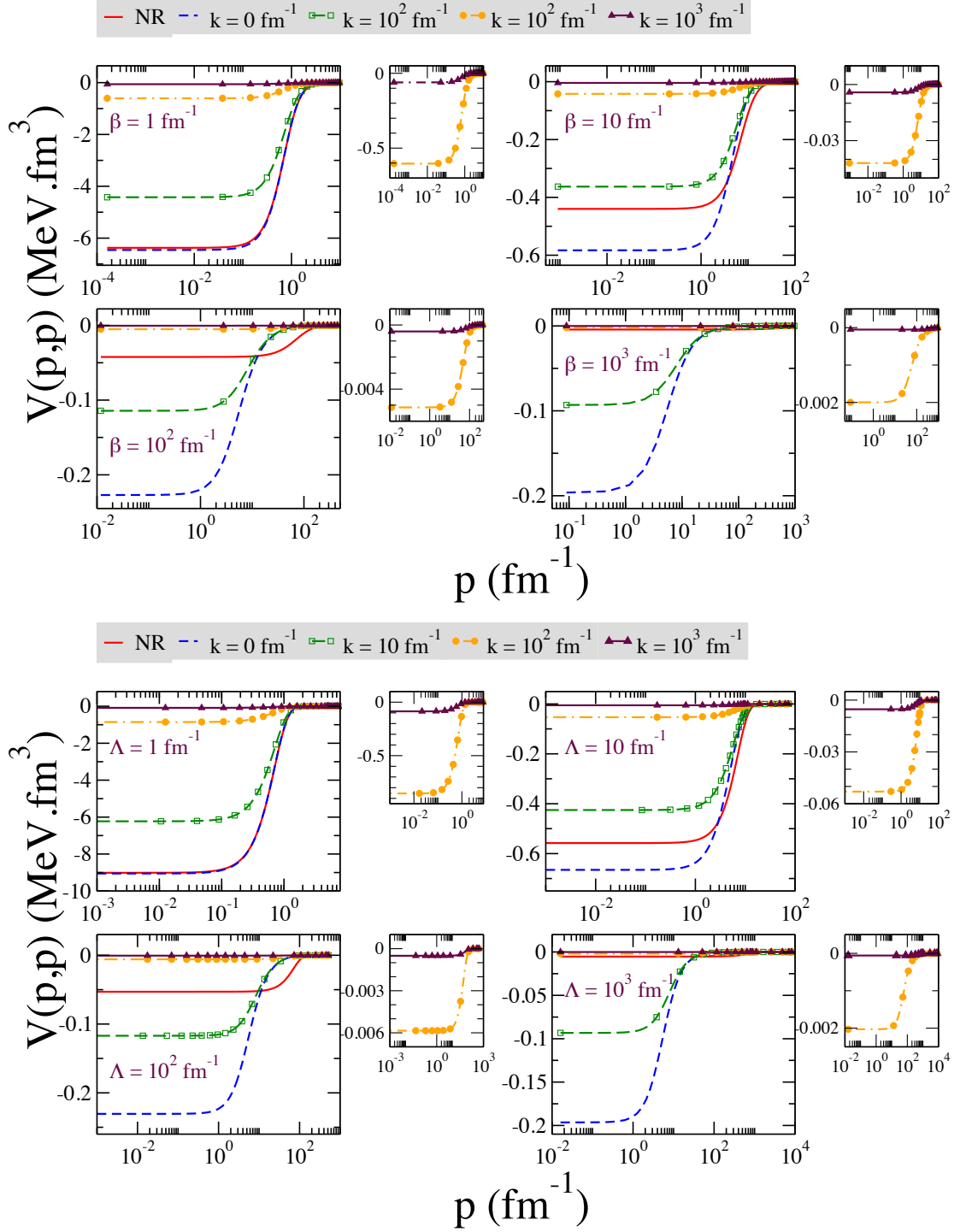


FIGURE 2.4 – The diagonal matrix elements of nonrelativistic and boosted potentials are computed for a diverse set of form factor parameters β for Yamaguchi-type potentials (upper panel) and Λ for Gaussian potentials (lower panel). The calculations are performed using various values of the boosted momentum k . These Figures are taken from (MOHSENI *et al.*, 2021).

From the Fig. 2.4, it is evident that the magnitude of the boosted potentials decreases as the boosted momentum k increases. This behavior is observed for both Yamaguchi-

type potentials and Gaussian potentials, indicating a general trend. The form factor parameters β and Λ control the range and smoothness of the potentials, and different values of these parameters lead to variations in the potentials' behavior.

2.3 Two-body bound state

2.3.1 Nonrelativistic NN bound state

The total Hamiltonian of two identical interacting particles in the center of mass (CM) of system in momentum space is given as

$$H^{nr} = H_0^{nr} + V_{nr}, \quad (2.19)$$

where $H_0^{nr} = \frac{p^2}{m}$ is nonrelativistic free Hamiltonian, p is the relative momentum between two particles and $V_{12} = V_{21} = V_{nr}$ is nonrelativistic 2B potential. The Schrödinger equation for 2B bound system is given as

$$(H_0^{nr} + V_{nr}) |\Psi_{nr}\rangle = E_d^{nr} |\Psi_{nr}\rangle, \quad (2.20)$$

where E_{nr} is 2B binding energy. One can rewrite the Schrödinger equation, Eq. (2.20) in integral form

$$|\Psi_{nr}\rangle = \frac{1}{E_d^{nr} - H_0^{nr}} V_{nr} |\Psi_{nr}\rangle, \quad (2.21)$$

the projection of nonrelativistic Schrödinger equation, Eq. (2.21) in momentum space can be written as

$$\psi_d^{nr}(\mathbf{p}) = \frac{1}{E_d^{nr} - \frac{\mathbf{p}^2}{m}} \int d^3p' V_{nr}(\mathbf{p}, \mathbf{p}') \psi_d^{nr}(\mathbf{p}'), \quad (2.22)$$

where the completeness relation of 2B basis states is given as

$$\int d^3p |\mathbf{p}\rangle \langle \mathbf{p}| \equiv \int_0^\infty dp p^2 \int_{-1}^{+1} dx \int_0^{2\pi} d\phi |\mathbf{p}\rangle \langle \mathbf{p}| = 1. \quad (2.23)$$

For a central potential and s -wave states, the integral form of the Schrödinger equation, Eq. (2.22), can be further simplified to

$$\psi_d^{nr}(p) = \frac{4\pi}{E_d^{nr} - \frac{p^2}{m}} \int_0^\infty dp' p'^2 V_{nr}(p, p') \psi_d^{nr}(p'). \quad (2.24)$$

By solving this integral equation, one can obtain the s -wave component of the dimer wave

function $\psi_d^{nr}(p)$, which describes the bound state of the two nucleons in the nonrelativistic framework.

2.3.2 Relativistic NN bound state

The form of the relativistic Schrödinger equation for the bound state of two identical interacting particles for mass operator h , is given by (BAKAMJIAN; THOMAS, 1953; FONG; SUCHER, 1964)

$$h|\psi_d^r\rangle = M_d|\psi_d^r\rangle, \quad (2.25)$$

where $M_d = E_d + 2m$ is the dimer mass, and E_d is dimer binding energy. The relativistic dimer wave function $|\psi_d^r\rangle$ satisfies the eigenvalue equation (HADIZADEH *et al.*, 2020)

$$\psi_d^r(\mathbf{p}) = \frac{1}{M_d - \omega(\mathbf{p})} \int d^3p' V_r(\mathbf{p}, \mathbf{p}') \psi_d(\mathbf{p}'). \quad (2.26)$$

where $\omega(\mathbf{p}) = 2E(\mathbf{p}) = 2\sqrt{m^2 + \mathbf{p}^2}$, m is the mass of the nucleons and \mathbf{p} is the relative momentum of two nucleons.

Similar to nonrelativistic case, Eq. (2.26) for an s -wave potential can be simplified as

$$\psi_d^r(p) = \frac{4\pi}{M_d - \omega(p)} \int_0^\infty dp' p'^2 V_r(p, p') \psi_d^r(p'). \quad (2.27)$$

2.3.3 Numerical results for dimer binding energy

To discretize the continuous momentum for solving Eqs. (2.24) and (2.27), we employed the Gauss-Legendre quadrature method. We used a hyperbolic plus linear mapping to divide the integration domain $[0, \infty)$ into subintervals $[0, p_1] \cup [p_1, p_2] \cup [p_2, p_{max}]$ (HADIZADEH; RADIN, 2017)

$$p = \frac{1+x}{\frac{1}{p_1} + (\frac{2}{p_2} - \frac{1}{p_1})x}, \quad p = \frac{p_{max} - p_2}{2}x + \frac{p_{max} + p_2}{2}. \quad (2.28)$$

Table A.3 presents the numerical result for the nonrelativistic (E_d^{nr}) and relativistic (E_d^{rel}) dimer binding energy as function of number of mesh points for relative momentum N_p .

An interesting and important characteristic of the boosted potential method is that the boosted potential $V_k(\mathbf{p}, \mathbf{p}')$ calculated for a specific momentum k satisfies the relativistic Schrödinger equation, as represented by Eq. (2.27). This means that the calculated boosted potentials accurately describe the behavior of a moving dimer with momentum

k . To show this we rewrite the Eq. (2.27) for a moving dimer with momentum k as

$$\psi_d^{boosted}(p) = \frac{4\pi}{\sqrt{M_d^2 + k^2} - \omega_k(p)} \int dp' p'^2 V_k(p, p') \psi_d^{boosted}(p'). \quad (2.29)$$

Here we suppose that when the nonrelativistic potential is separable, the boosted potential can be written in separable form. Consequently, we can express the boosted potential as $V_k(p, p') = \lambda_k g(p) g(p')$. Analogous to Eq. (2.7), we can determine the potential strength λ_k by solving the equation

$$\frac{1}{\lambda_k} = 4\pi \int_0^\infty dp'' p''^2 \frac{g^2(p'')}{\sqrt{M_d^2 + k^2} - \omega_k(p'')}. \quad (2.30)$$

We first consider the separable form for the boosted potential and calculate the potential strength λ_k using Eq. (2.30) with $M_d = -2.225$ MeV. Next, we calculate the boosted potential V_k by using the separable form of the boosted potential. Then, using the calculated V_k as input for the quadratic equation (2.16), we calculate the nonrelativistic potential V_{nr} for different boosted momenta k and potential parameters β . Finally, we solve Eq. (2.24) to calculate the nonrelativistic dimer binding energies for the obtained nonrelativistic potentials.

The numerical results for boosted and nonrelativistic dimer binding energies for different boosted momentum k and potential parameters β are given in Table A.5. As one can see, calculated boosted potentials $V_k(p, p')$ for a given momentum k satisfies Eq. (2.29) for moving dimer with momentum k with high accuracy. The consistency between the calculated potentials and the relativistic Schrödinger equation underscores the reliability and applicability of the boosted potential approach in studying the dynamics of interacting particles.

In Fig. 2.5 we show the diagonal matrix elements of the nonrelativistic potential obtained from a separable boosted potential, that reproduces the moving dimer binding energy, from the solution of Eq. (2.16). The plot is obtained for the potential parameter $\beta = 1 \text{ fm}^{-1}$ and different values of the boosted momentum k . As one can see, the diagonal matrix elements of the nonrelativistic potential are almost identical for different values of the boosted momentum k .

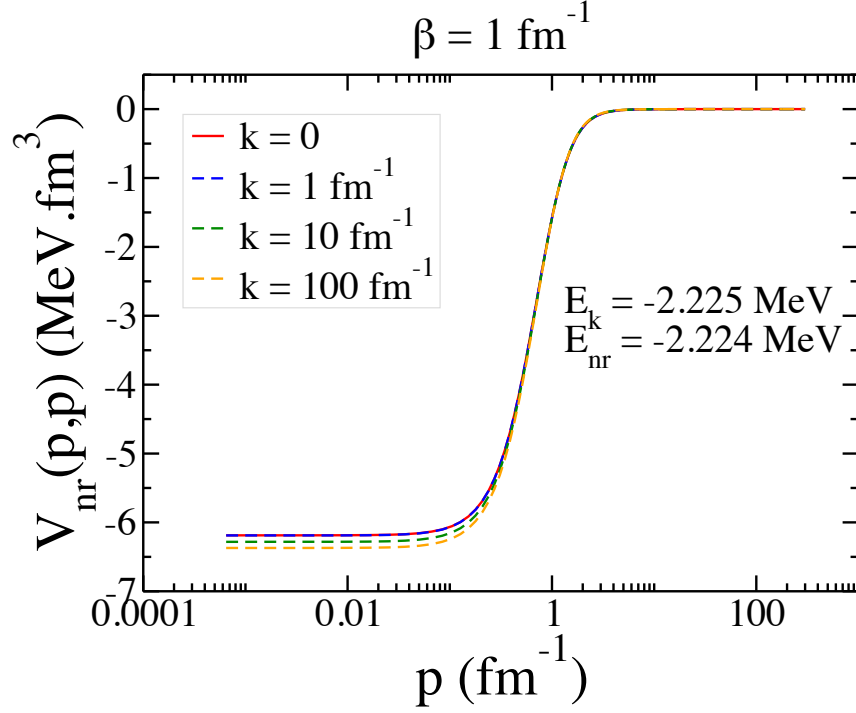


FIGURE 2.5 – The diagonal matrix elements of the nonrelativistic potential obtained from a separable boosted potential, that reproduces the moving dimer binding energy, from the solution of Eq. (2.16). The plot is obtained for the potential parameter $\beta = 1 \text{ fm}^{-1}$ and different values of the boosted momentum k .

2.4 Three-body bound state

2.4.1 Nonrelativistic Faddeev equations in momentum space

The nonrelativistic Schrödinger equation for the 3B bound system is given by

$$(H_0 + \sum_{i=1}^3 V_i)|\Psi\rangle = E|\Psi\rangle, \quad (2.31)$$

where we have introduced the notation

$$V_1 \equiv V_{23}, \quad V_2 \equiv V_{13}, \quad V_3 \equiv V_{12}. \quad (2.32)$$

To express Eq. (2.31) in integral form, we can rewrite it as

$$|\Psi\rangle = \frac{1}{E - H_0} \sum_{i=1}^3 V_i |\Psi\rangle = G_0 \sum_{i=1}^3 V_i |\Psi\rangle, \quad (2.33)$$

where $G_0 = \frac{1}{E - H_0}$ is free propagator. The wave function can be obtained by summing all Faddeev components, as

$$|\Psi\rangle = \sum_{i=1}^3 |\psi_i\rangle, \quad (2.34)$$

where

$$|\psi_i\rangle = G_0 V_i |\Psi\rangle = G_0 V_i \sum_{i=1}^3 |\psi_i\rangle. \quad (2.35)$$

By separating the Faddeev components ψ_i from the right-hand side of Eq. (2.35) we can write

$$\begin{aligned} (1 - G_0 V_i) |\psi_i\rangle &= G_0 V_i \sum_{j \neq i} |\psi_j\rangle \\ |\psi_i\rangle &= (1 - G_0 V_i)^{-1} G_0 V_i \sum_{j \neq i} |\psi_j\rangle. \end{aligned} \quad (2.36)$$

By expanding the term $(1 - G_0 V_i)^{-1}$, we have

$$\begin{aligned} (1 - G_0 V_i)^{-1} G_0 V_i &= (1 + G_0 V_i + G_0 V_i G_0 V_i + \dots) G_0 V_i \\ &= (G_0 V_i + G_0 V_i G_0 V_i + G_0 V_i G_0 V_i G_0 V_i + \dots) \\ &= G_0 (V_i + V_i G_0 V_i + V_i G_0 V_i G_0 V_i + \dots) \\ &\equiv G_0 t_i. \end{aligned} \quad (2.37)$$

Here, t_i is the two-body t -matrix defined as

$$t_i = V_i + V_i G_0 t_i, \quad (2.38)$$

Substituting this back into Eq. (2.36), we obtain

$$|\psi_i\rangle = G_0 t_i \sum_{j \neq i} |\psi_j\rangle. \quad (2.39)$$

In the general case of three different particle (GLÖCKLE, 2012) we can write these

three coupled equations as

$$\begin{aligned} |\psi_1\rangle &= G_0 t_1 (|\psi_2\rangle + |\psi_3\rangle), \\ |\psi_2\rangle &= G_0 t_2 (|\psi_3\rangle + |\psi_1\rangle), \\ |\psi_3\rangle &= G_0 t_3 (|\psi_1\rangle + |\psi_2\rangle). \end{aligned} \quad (2.40)$$

Considering the three identical particles, we can express $|\psi_2\rangle$ and $|\psi_3\rangle$ in terms of $|\psi_1\rangle$ as

$$\begin{aligned} |\psi_2\rangle &\equiv G_0 V_2 |\Psi\rangle = P_{12} P_{23} G_0 V_1 |\Psi\rangle \equiv P_{12} P_{23} |\psi_1\rangle, \\ |\psi_3\rangle &\equiv G_0 V_3 |\Psi\rangle = P_{13} P_{23} G_0 V_1 |\Psi\rangle \equiv P_{13} P_{23} |\psi_1\rangle. \end{aligned} \quad (2.41)$$

Thus, Eq. (2.40) reduces to a single equation:

$$|\psi_1\rangle = G_0 t_1 (P_{12} P_{23} + P_{13} P_{23}) |\psi_1\rangle, \quad (2.42)$$

$$|\psi\rangle = G_0 t P |\psi\rangle, \quad (2.43)$$

where $P = P_{12} P_{23} + P_{13} P_{23}$, and in the last equation for simplifying the notation we drop the indices. The 3B bound state wave function can be obtained from Eqs. (2.34) and (2.41) as

$$|\Psi\rangle = |\psi_1\rangle + |\psi_2\rangle + |\psi_3\rangle = |\psi_1\rangle + P_{12} P_{23} |\psi_1\rangle + P_{13} P_{23} |\psi_1\rangle = (1 + P) |\psi\rangle. \quad (2.44)$$

The free Hamiltonian H_0 in the laboratory frame can be expressed as a sum of the kinetic energies of each particle

$$H_0 = \sum_{i=1}^3 \frac{k_i^2}{2m_i}, \quad (2.45)$$

To address 3B problems effectively, a set of Jacobi momenta, shown in Fig. 2.6, are commonly employed. This choice of coordinates allows for the separation of the CM motion, thereby simplifying the problem. Consequently, the free Hamiltonian Eq. (2.45), takes the following form

$$H_0 = \frac{p_i^2}{2\mu_{jk}} + \frac{q_i^2}{2\mu_{i,jk}} + \frac{K^2}{2(m_i + m_j + m_k)}. \quad (2.46)$$

Here, \mathbf{p}_i represents the relative momentum in the 2B subsystem (jk) , \mathbf{q}_i is the momentum of the third particle (i) with respect to the 2B subsystem (jk) , μ_{jk} is the reduced mass of the (jk) pair, $\mu_{i,jk}$ is the reduced mass of the 3B system, and $K = \sum_{i=1}^3 k_i$ is the total CM momentum.

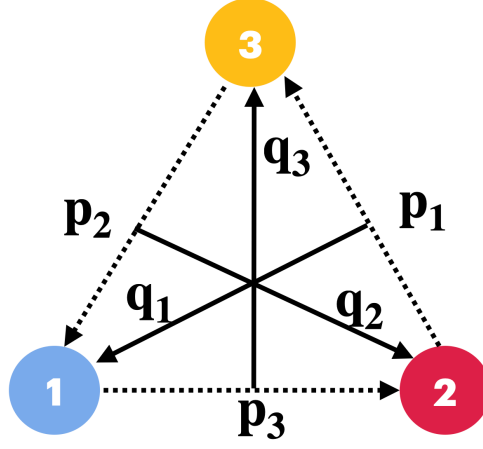


FIGURE 2.6 – Set of Jacobi momenta for 3B system.

In General case of three different particle the Jacobi momenta are defined as

$$\mathbf{p}_i = \frac{m_k \mathbf{k}_j - m_j \mathbf{k}_k}{m_j + m_k}, \quad (2.47)$$

$$\mathbf{q}_i = \frac{m_j + m_k}{m_i + m_j + m_k} \left[\mathbf{k}_i - \frac{m_i}{m_j + m_k} (\mathbf{k}_j + \mathbf{k}_k) \right], \quad (2.48)$$

where

$$\mu_{jk} = \frac{m_j m_k}{m_j + m_k}, \quad (2.49)$$

$$\mu_{i,jk} = \frac{m_i (m_j + m_k)}{m_i + m_j + m_k}. \quad (2.50)$$

In the case of three identical particles with masses $m_i = m_j = m_k = m$, we can simplify Eqs. (2.47) and (2.48) as

$$\mathbf{p} = \frac{\mathbf{k}_2 - \mathbf{k}_3}{2}, \quad (2.51)$$

$$\mathbf{q} = \frac{2}{3} \left(\mathbf{k}_1 - \frac{\mathbf{k}_2 + \mathbf{k}_3}{2} \right), \quad (2.52)$$

and in the 3B CM framework, where the total momentum K is zero, Eq. (2.46) simplifies as

$$H_0 = \frac{p^2}{m} + \frac{3q^2}{4m}. \quad (2.53)$$

For projecting the Faddeev equation onto momentum space, we introduce the 3B (3B) basis states denoted by $|\mathbf{p}\mathbf{q}\rangle$. These basis states are complete and normalized, satisfying

the completeness relation

$$\int d^3p \int d^3q |\mathbf{p}\mathbf{q}\rangle \langle \mathbf{p}\mathbf{q}| = 1. \quad (2.54)$$

Using these momentum basis, Eq. (2.43) can be written in momenta space as

$$\psi^{nr}(\mathbf{p}, \mathbf{q}) = \frac{1}{E - \frac{p^2}{m} + \frac{3q^2}{4m}} \int d^3q' t_s(\mathbf{p}, \frac{1}{2}\mathbf{q} + \mathbf{q}'; \epsilon) \psi(\mathbf{q} + \frac{1}{2}\mathbf{q}', \mathbf{q}'), \quad (2.55)$$

where $\epsilon = E - \frac{3q^2}{4m}$ is 2B subsystem energy and $t_s(\mathbf{p}, \mathbf{p}', \epsilon)$ is symmetric 2B t-matrix

$$t_s(\mathbf{p}, \mathbf{p}', \epsilon) = t(\mathbf{p}, \mathbf{p}', \epsilon) + t(\mathbf{p}, -\mathbf{p}', \epsilon). \quad (2.56)$$

The 2B t -matrix can be obtained by solving the Lippmann-Schwinger (LS) equation in momentum space. The LS equation for the 2B t -matrix is given by

$$t(\mathbf{p}, \mathbf{p}', \epsilon) = V(\mathbf{p}, \mathbf{p}') + \int d^3p'' V(\mathbf{p}, \mathbf{p}'') \frac{1}{\epsilon - \frac{p''^2}{m}} t(\mathbf{p}'', \mathbf{p}', \epsilon). \quad (2.57)$$

In the CM of the 3B system, where $q = k_1 = k$ as given by Eq. (2.52), we can rewrite Eq. (2.55) as

$$\psi^{nr}(\mathbf{p}, \mathbf{k}) = \frac{1}{E - \frac{p^2}{m} + \frac{3k^2}{4m}} \int d^3k' t_s(\mathbf{p}, \frac{1}{2}\mathbf{k} + \mathbf{k}'; \epsilon) \psi(\mathbf{k} + \frac{1}{2}\mathbf{k}', \mathbf{k}'). \quad (2.58)$$

To solve the 3D integral equation given by Eq. (2.58), we choose a coordinate system as shown in Fig. (2.7). In this coordinate system, the vectors \mathbf{p} , \mathbf{k} , and \mathbf{k}' are defined. The vector \mathbf{k} is chosen to be parallel to the z -axis, and the vector \mathbf{p} lies in the $x - z$ plane, and the vector \mathbf{k}' is free to move in the 3D space.

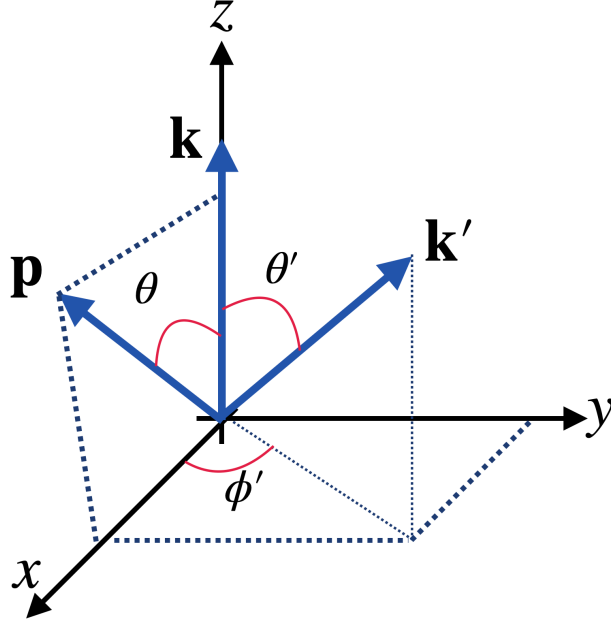


FIGURE 2.7 – The geometry of vectors \mathbf{p}, \mathbf{k} & \mathbf{k}' . The vector k is chosen to be parallel to the z -axis and vector \mathbf{p} is in the $x-z$ plane, and \mathbf{k}' is free in the 3D space. The angle variables defined in Eqs. (2.59) are indicated.

The angle variables are defined as

$$\begin{aligned} y &= \hat{\mathbf{p}} \cdot \hat{\mathbf{k}}' = xx' + \sqrt{1-x^2}\sqrt{1-x'^2} \cos \phi', \\ x &= \hat{\mathbf{p}} \cdot \hat{\mathbf{k}}, \\ x' &= \hat{\mathbf{p}} \cdot \hat{\mathbf{k}}'. \end{aligned} \quad (2.59)$$

By using the coordinate system in Fig. (2.7) we can write Eq. (2.58) as

$$\psi^{nr}(p, k, x) = \frac{1}{E - \frac{p^2}{m} + \frac{3k^2}{4m}} \int_0^\infty dk' k'^2 \int_{-1}^{+1} dx' \int_0^{2\pi} d\phi' t_s(p, |\frac{1}{2}\mathbf{k} + \mathbf{k}'|; \epsilon) \psi(|\mathbf{k} + \frac{1}{2}\mathbf{k}'|, k'). \quad (2.60)$$

The s -wave projection of Eq. (2.58) can be written as

$$\psi^{nr}(p, k) = 4\pi G_0^{nr}(p, k) \int_0^\infty dk' k'^2 \int_{-1}^1 dx' t_s(p, |\frac{1}{2}\mathbf{k} + \mathbf{k}'|; \epsilon) \psi(|\mathbf{k} + \frac{1}{2}\mathbf{k}'|, k'), \quad (2.61)$$

with

$$t(p, p', \epsilon) = V(p, p') + 4\pi \int_0^\infty dp'' p''^2 \frac{V(p, p'')}{\epsilon - \frac{p^2}{m}} t(p'', p', \epsilon). \quad (2.62)$$

For a one-term separable potential, the 2B t -matrix can be written in a separable form

as (PLATTER *et al.*, 2004a)

$$t(p, p', \epsilon) = \tau(\epsilon) g(p) g(p'), \quad (2.63)$$

here $\tau(\epsilon)$ can be obtained by

$$\tau(\epsilon) = \left[\frac{1}{\lambda_{nr}} - 4\pi \int_0^\infty dp'' p''^2 \frac{g^2(p'')}{\epsilon - \frac{p''^2}{m}} \right]^{-1}. \quad (2.64)$$

By utilizing the separable property of the t -matrix and the Faddeev component $\psi^{nr}(p, k)$, given in Eq. (2.63) and Eq. (2.66), respectively, the integral equation (2.65) can be further simplified.

By utilizing the separable property of t -matrix, Eq. (2.63), the Faddeev integral Eq. (2.61) can be simplify as

$$\psi^{nr}(p, k) = 4\pi G_0^{nr}(p, k) g(p) \tau(\epsilon) \int_0^\infty dk' k'^2 \int_{-1}^1 dx' g\left(\left|\frac{1}{2}\mathbf{k} + \mathbf{k}'\right|\right) \psi\left(\left|\mathbf{k} + \frac{1}{2}\mathbf{k}'\right|, k'\right) \quad (2.65)$$

This is an homogeneous integral equation in two variables. Let's define $F^{nr}(k)$ as the Faddeev component depending solely on the relative momentum k . Then, Eq. (2.65) can be further simplified as

$$\psi^{nr}(p, k) = G_0^{nr}(p, k) g(p) \tau(\epsilon) F^{nr}(k), \quad (2.66)$$

where

$$\begin{aligned} F^{nr}(k) &= 4\pi \int_0^\infty dk' k'^2 \int_{-1}^1 dx' g\left(\left|\frac{1}{2}\mathbf{k} + \mathbf{k}'\right|\right) G_0^{nr}\left(\left|\mathbf{k} + \frac{1}{2}\mathbf{k}'\right|, k'\right) g\left(\left|\mathbf{k} + \frac{1}{2}\mathbf{k}'\right|\right) \\ &\times \tau(\epsilon) F^{nr}(k'), \end{aligned} \quad (2.67)$$

which can be solved by direct diagonalization of the kernel, with no need for the iteration method.

2.4.2 Relativistic Faddeev equation

The 3B mass operator of three identical particles with mass m and momentum \mathbf{k}_i , interacting with pairwise potentials, in the relativistic quantum mechanics is defined as

$$M = M_0 + \sum_{i < j} V_{k_{ij}}. \quad (2.68)$$

The free-body mass operator M_0 in the 3B Hilbert space is given by

$$M_0 = \sum_{i=1}^3 (m^2 + k_i^2)^{\frac{1}{2}}. \quad (2.69)$$

Similar to nonrelativistic case, in the relativistic limit we work in the CM frame of 3B system, i.e. $K = 0$. In the relativistic framework, free propagator G_0 in Eq. (2.43) define as, $G_0 = (M_t - M_0)^{-1}$ where $M_t = E_t + 3m$ is the 3B mass eigenvalue.

The 3B relativistic Jacobi momentum p and q are obtained through a two-step process. Firstly, the momenta of individual particles, k , in the 3B system are boosted to the 3B CM, where the total momentum of the system is zero. Subsequently, the momenta of each 2B subsystem are boosted to their respective rest frames. The relativistic relative momenta p and q by assuming that all nucleons have the same mass, m , are defined as (FONG; SUCHER, 1964)

$$\begin{aligned} \mathbf{p}(\mathbf{k}_j, \mathbf{k}_k) &= \frac{1}{2} \left\{ (\mathbf{k}_j - \mathbf{k}_k) - \left(\mathbf{k}_{jk} \frac{E(\mathbf{k}_j) - E(\mathbf{k}_k)}{E(\mathbf{k}_j) + E(\mathbf{k}_k) + [(E(\mathbf{k}_j) + E(\mathbf{k}_k))^2 - \mathbf{k}_{jk}^2]^{\frac{1}{2}}} \right) \right\}, \\ \mathbf{q}(\mathbf{k}_i, \mathbf{k}_{jk}) &= \frac{1}{2} (\mathbf{k}_i - \mathbf{k}_{jk}) + \frac{\mathbf{K}}{2M_0} \left(\frac{(\mathbf{k}_i^2 - \mathbf{k}_{jk}^2)}{E_0 + \sqrt{E_0^2 - \mathbf{K}^2}} - (E(\mathbf{k}_i) - E(\mathbf{k}_{jk})) \right), \end{aligned} \quad (2.70)$$

where $\mathbf{k}_{jk} = \mathbf{k}_j + \mathbf{k}_k$. As mentioned earlier, in the 3B CM frame, denoted by $\mathbf{K} = 0$, the momentum vectors \mathbf{q} and \mathbf{k} are equivalent, i.e., $\mathbf{q} = \mathbf{k}$.

In order to solve the Faddeev equation, Eq. (2.43), in momentum space, one needs the 3B basis states which are composed of two relativistic Jacobi momentum vectors $|\mathbf{p} \mathbf{k}\rangle$. The free-body mass operator M_0 , given in Eq. (2.69), is diagonal in these basis states as

$$M_0 |\mathbf{p} \mathbf{k}\rangle = \left((\omega^2(p) + k^2)^{\frac{1}{2}} + \Omega(k) \right) |\mathbf{p} \mathbf{k}\rangle, \quad (2.71)$$

where $\Omega(k) = (m^2 + k^2)^{\frac{1}{2}}$. As shown in Ref. (HADIZADEH *et al.*, 2014) the representation of Faddeev equation (2.43) in the relativistic basis states $|\mathbf{p} \mathbf{k}\rangle$ leads to the following 3D integral equation

$$\psi^r(\mathbf{p}, \mathbf{k}) = \frac{1}{M_t - M_0(p, k)} \int d^3 k' N(\mathbf{k}, \mathbf{k}') t_k^{sym}(\mathbf{p}, \tilde{\pi}; \epsilon) \psi(\pi, \mathbf{k}'), \quad (2.72)$$

where $\epsilon = M_t - \Omega(k)$ is 2B subsystem energy, $t_k^{sym}(\mathbf{p}, \mathbf{p}'; \epsilon)$ is symmetrized boosted 2B t -matrix defined as $t_k^{sym}(\mathbf{p}, \mathbf{p}'; \epsilon) = t_k(\mathbf{p}, \mathbf{p}'; \epsilon) + t_k(\mathbf{p}, -\mathbf{p}'; \epsilon)$, and the Jacobian function $N(\mathbf{k}, \mathbf{k}')$ is defined as

$$N(\mathbf{k}, \mathbf{k}') = \mathcal{N}^{-1}(-\mathbf{k} - \mathbf{k}', \mathbf{k}') \mathcal{N}^{-1}(-\mathbf{k} - \mathbf{k}', \mathbf{k}), \quad (2.73)$$

here, \mathcal{N} represents the square root of the Jacobian associated with the conversion from the individual momenta \mathbf{k} and \mathbf{k}' of the subsystem to the relative momentum \mathbf{p} and the total 2B momentum $\mathbf{k} + \mathbf{k}'$ (LIN, 2008; HADIZADEH *et al.*, 2014),

$$\mathcal{N}(\mathbf{k}, \mathbf{k}') = \left(\frac{\partial(\mathbf{k}, \mathbf{k}')}{\partial(\mathbf{p}, \mathbf{k} + \mathbf{k}')} \right)^{\frac{1}{2}} = \left(\frac{\omega(p) + \omega(p)}{\Omega(k) + \Omega(k')} \frac{\Omega(k)\Omega(k')}{\omega(p)\omega(p)} \right)^{\frac{1}{2}}. \quad (2.74)$$

In the limit of nonrelativistic, when the momenta are significantly smaller than the masses, the Jacobian function N simplifies to one, resulting in the relativistic Jacobi momenta being equivalent to their nonrelativistic counterparts. The relativistic shifted momentum arguments in Eq. (2.72) are defined as

$$\begin{aligned} \tilde{\boldsymbol{\pi}} &= \mathbf{k}' + \frac{1}{2}C(\mathbf{k}, \mathbf{k}') \mathbf{k}, \\ \boldsymbol{\pi} &= \mathbf{k} + \frac{1}{2}C(\mathbf{k}', \mathbf{k}) \mathbf{k}', \end{aligned} \quad (2.75)$$

where the permutation coefficients $C(\mathbf{k}, \mathbf{k}')$ are defined as (LIN *et al.*, 2007)

$$C(\mathbf{k}, \mathbf{k}') \equiv 1 + \frac{\Omega(k') - \Omega(|\mathbf{k} + \mathbf{k}'|)}{\Omega(k') + \Omega(|\mathbf{k} + \mathbf{k}'|) + \sqrt{\left(\Omega(k') + \Omega(|\mathbf{k} + \mathbf{k}'|) \right)^2 - k^2}}. \quad (2.76)$$

In the nonrelativistic regime, when the momenta are much smaller than the masses, the permutation coefficient $C(\mathbf{k}, \mathbf{k}')$ equals one. This leads to the reduction of the relativistic shifted momenta $\tilde{\boldsymbol{\pi}}$ and $\boldsymbol{\pi}$ to their corresponding nonrelativistic counterparts. Same as Eq. (2.57) we can calculate the fully-off-shell boosted 2B t -matrices $t_k(\mathbf{p}, \mathbf{p}'; \epsilon)$ by solving the following relativistic LS equation

$$t_k(\mathbf{p}, \mathbf{p}'; \epsilon) = V_k(\mathbf{p}, \mathbf{p}') + \int d^3p'' \frac{V_k(\mathbf{p}, \mathbf{p}'')}{\epsilon - \left(\omega^2(p'') + k^2 \right)^{\frac{1}{2}}} t_k(\mathbf{p}'', \mathbf{p}'; \epsilon). \quad (2.77)$$

Using the coordinate system defined in Fig. 2.7, Eq. (2.72) in s -wave channel can be written as following integral equation

$$\psi^r(p, k) = 4\pi G_0^r(p, k) \int_0^\infty dk' k'^2 \int_{-1}^1 dx N(k, k', x) T_k(p, \tilde{\pi}; \epsilon) \psi(\pi, k'), \quad (2.78)$$

where

$$t_k(p, p'; \epsilon) = V_k(p, p') + 4\pi \int dp'' p''^2 \frac{V_k(p, p'')}{\epsilon - \left(\omega^2(p'') + k^2 \right)^{\frac{1}{2}}} t_k(p'', p'; \epsilon). \quad (2.79)$$

For a one-term separable boosted potential, the Faddeev integral equation (2.78) can be written as

$$\psi^r(p, k) = 4\pi G_0^r(p, k) g(p) \tau_k(\epsilon) \int_0^\infty dk' k'^2 \int_{-1}^1 dx g(\tilde{\pi}) N(k, k', x) \psi(\pi, k'), \quad (2.80)$$

where $\tau_k(\epsilon)$, similar to Eq. (2.64), can be obtained by

$$\tau_k(\epsilon) = \left[\frac{1}{\lambda_k} - 4\pi \int_0^\infty dp'' p''^2 \frac{g^2(p'')}{\epsilon - \omega_k(p'')} \right]^{-1}. \quad (2.81)$$

Similar to Eq. (2.66) the relativistic Faddeev component $\psi^r(\pi, k')$ can be written as

$$\psi^r(p, k) = G_0^r(p, k) g(p) \tau_k(\epsilon) F^r(k). \quad (2.82)$$

Therefore Eq. (2.80) can be simplified for Faddeev component $F^r(k)$ as

$$F^r(k) = 4\pi \int_0^\infty dk' k'^2 \int_{-1}^1 dx g(\tilde{\pi}) N(k, k', x) G_0^r(\pi, k') g(\pi) \tau_k(\epsilon) F^r(k'), \quad (2.83)$$

which can be solved by direct diagonalization of the kernel, with no need for the iteration method.

2.4.3 Numerical results for nonrelativistic and relativistic trimer binding energies

To calculate the binding energy of the nonrelativistic trimer, we employ the general 3D Faddeev integral equation, as given by Eq. (2.60). By obtaining the matrix elements of the nonrelativistic potentials $V_{nr}(p, p')$, we solve the LS integral Eq. (2.62) to determine the fully off-shell t -matrices $t(p, p'; \epsilon)$ for the 2B subsystem energies $\epsilon = E - \frac{3q^2}{4m}$.

The Faddeev integral equations, Eq. (2.60) can be schematically represented as an eigenvalue problem

$$\mathcal{K}(E) \cdot \psi = \lambda(E) \cdot \psi \quad (2.84)$$

The eigenvalue equation (2.84) is solved using the Lanczos iterative method, which has been successfully employed in calculations of two-, three-, and four-body bound states (BAYEGAN *et al.*, 2008b; HADIZADEH *et al.*, 2011; HADIZADEH *et al.*, 2014; HADIZADEH *et al.*, 2020; AHMADI *et al.*, 2020; MOHSENI *et al.*, 2023). The Lanczos method allows for the efficient determination of eigenvalues and eigenvectors of a matrix. In our case, the matrix is the kernel $\mathcal{K}(E)$ of the integral equation, with $\lambda(E)$ being its eigenvalue and ψ its corresponding eigenvector. The binding energy of 3B bound state can be obtained

when one of the eigenvalues obtained from the solution of Eq. (2.84) for an input energy becomes one ($\lambda(E) = 1$).

To initiate the iterative process, we start with an initial Gaussian guess for the Faddeev components and perform 6-10 iterations. Since the kernel $\mathcal{K}(E)$ is energy-dependent, we can start the solution of the eigenvalue equation with an initial guess for the 3B binding energy E_t^{nr} . The search for the binding energy is terminated when $|\lambda - 1| \leq 10^{-6}$, indicating convergence. By solving the integral equation (2.60) using the Lanczos method, we obtain the nonrelativistic 3B binding energies E_t^{nr} . The convergence of numerical solution for 3B nonrelativistic binding energy and expectation value for Hamiltonian is studied in Table A.6 for Yamaguchi-I.

To calculate the binding energy of the relativistic trimer, we utilize the general 3D Faddeev integral equation given by Eq. (2.72). By obtaining the matrix elements of the boosted potentials $V_k(p, p')$ from the nonrelativistic one, we solve the relativistic LS integral equation (2.79) to compute fully off-shell boosted t -matrices $t_k(p, p'; \epsilon)$ for 2B subsystem energies $\epsilon = M_t - \Omega(k)$ determined by the boosted momentum k . Subsequently, employing the Lanczos technique to solve the integral equation (2.72), we derive relativistic 3B binding energies E_r^{3B} and Faddeev components $\psi^r(p, k)$ for ground and excited states. We should mention that the matrix elements of boosted potentials are obtained from separable nonrelativistic potentials by solving the integral equation (2.14). The solution of Eq. (2.83) by direct diagonalization can serve as a benchmark to assess the accuracy of our numerical calculations for 3B binding energies. Table 2.2 shows the results for the relativistic binding energies E_t^r of the 3B system for different Yamaguchi type potentials by solving Eq. (2.72). Calculations are performed with $N_p = N_q = 60$ and $N_x = 40$.

TABLE 2.2 – Relativistic 3B binding energy calculated for different models of Yamaguchi potential.

Potential	E_r^{3B} (MeV)
Y-I	-24.529
Y-II	-11.993
Y-III	-9.0138
Y-IV	-8.3084

In Table 2.3, we present the contributions of different relativistic corrections to the binding energy of the 3B ground state. The calculations are performed using the Yamaguchi-IV potential and employing $N_x = 40$, $N_p = N_q = 60$ as the number of mesh points. The eigenvalue equation is solved with the Lanczos technique, iterated 6 times. To assess the accuracy of the Lanczos technique, we have cross-validated the results by solving Eq. (2.83) using the direct diagonalization method. This comparison demonstrates the high accuracy of the Lanczos results. Table 2.3 shows two of the relativistic corrections, N

and 2B t -matrices, decrease the 3B binding energies, and the other terms, i.e. C and G_0^{rel} , increase the 3B binding energy, but when we apply all the corrections together we see reduction in the trimer binding energy.

TABLE 2.3 – The contributions of different relativistic corrections to the 3B binding energy.

Relativistic Correction	E^{3B} (MeV)	$\frac{(E_{app}^{3B} - E_{nr}^{3B})}{E_{nr}^{3B}} \times 100$ %
	$E_{nr}^{3B} = -8.5121$	
N (the Jacobian function)	$E_{app}^{3B} = -8.4187$	-1.0972
C (the permutation coefficient)	$E_{app}^{3B} = -8.5990$	+1.0210
G_0^{rel} (the relativistic 3B free propagator)	$E_{app}^{3B} = -8.7496$	+2.7901
t_k (the boosted 2B t matrix)	$E_{app}^{3B} = -8.1094$	-4.7309
Full relativistic ($N + C + G_0^{rel} + t_k$)	$E_r^{3B} = -8.3084$	-2.3930

Now for studying the three-boson bound state mass and wave functions in the limit of a zero-range interaction, we use a nonrelativistic short-range separable potential, with Yamaguchi and Gaussian defined in Eqs. (2.6) and (2.18), and drive them towards the zero-range limit by letting the form factors' momentum scales go to large values while keeping the 2B binding fixed. Table 2.4 presents numerical results for the 3B binding energy, both for nonrelativistic and relativistic ground and excited states. The upper panel corresponds to the Yamaguchi potential, while the lower panel corresponds to the Gaussian form factor. These results are obtained by solving the integral equation (2.78) using boosted t -matrices obtained from boosted potentials, which are calculated by solving the integral equation (2.79). The boosted potentials are derived from separable nonrelativistic potentials, which are obtained by solving the integral equation (2.14). The nonrelativistic potential strength λ_{nr} is fitted to match the dimer binding energy of -2.225 MeV. The calculations are performed using 300 mesh points for Jacobi momenta p and k , and 40 mesh points for angle variables.

All the results reported in Table 2.4 have been double-checked by solving Eq. (2.67) for the nonrelativistic case and Eq. 2.83 for the relativistic case using the direct diagonalization method. This approach confirms the accuracy of the results obtained with the Lanczos method.

TABLE 2.4 – Nonrelativistic and relativistic 3B ground and first excited state binding energies for different values of the Yamaguchi form factor parameter β (upper panel), and Gaussian form factor Λ (lower panel).

Yamaguchi form factor				
$\beta(\text{fm}^{-1})$	$E_{PW}^{nr(0)}$	$E_{PW}^{r(0)}$	$E_{PW}^{nr(1)}$	$E_{PW}^{r(1)}$
20	-1, 218.54	-278.950	-8.62313	-4.49971
40	-4, 484.60	-381.098	-19.1179	-5.31494
100	-26, 607.6	-453.149	-73.7232	-5.95099
200	-104, 575	-453.962	-241.569	-6.07741
600	-929, 937	-408.406	$-1.87345 \cdot 10^3$	-5.56317
1,000	$-2.57612 \cdot 10^6$	-384.306	$-5.04258 \cdot 10^3$	-5.16628
2,000	$-1.02783 \cdot 10^7$	-356.855	$-1.97162 \cdot 10^4$	-4.88977
3,000	$-2.31177 \cdot 10^7$	-342.861	$-4.39916 \cdot 10^4$	-4.80777
Gaussian form factor				
$\Lambda(\text{fm}^{-1})$	$E_{PW}^{nr(0)}$	$E_{PW}^{r(0)}$	$E_{PW}^{nr(1)}$	$E_{PW}^{r(1)}$
20	-904.682	-267.227	-7.21647	-4.37757
40	-3304.11	-378.647	-15.2640	-5.28154
100	-19507.2	-461.251	-55.7591	-6.01010
200	-76528.3	-465.232	-177.968	-6.17579
400	$-3.03129 \cdot 10^5$	-437.114	-627.718	-5.95152
600	$-6.79811 \cdot 10^5$	-415.032	-1351.27	-5.70284
1000	$-1.88341 \cdot 10^6$	-387.864	-3619.81	-5.25234
2000	$-7.51885 \cdot 10^6$	-357.652	-14082.9	-4.91393
3000	$-16.9062 \cdot 10^6$	-344.329	-31391.2	-4.79630

Fig. 2.8 (taken from (MOHSENI *et al.*, 2021)) shows the binding energies of the three-boson system's ground and first excited states. These energies are plotted as a function of the potential range parameters β and Λ for the Yamaguchi and Gaussian form factors, respectively. In both cases, the calculations are performed with a nonrelativistic 2B binding energy fixed at -2.225 MeV, which corresponds to the dimer binding energy. As β and Λ increase, the three-boson system exhibits the phenomenon known as the Thomas collapse (THOMAS, 1935). In this collapse, the binding energy is proportional to $-\beta^2$ and $-\Lambda^2$. In our examples, this collapse occurs until reaching values around 200 fm^{-1} or an equivalent momentum of $0.4 \text{ GeV}/c$, which is comparable to the nucleon mass. However, the system experiences the influence of boosted effects, which stabilize it by introducing an induced repulsion. This repulsion acts to counterbalance the singular behavior of the collapse. As a result, the binding energy reaches a plateau, independent of the specific short-range potential model employed. This behavior suggests the existence of a well-defined zero-range limit for the Glöckle-Kamada boosted potentials within the framework of relativistic 3B framework (MOHSENI *et al.*, 2021).

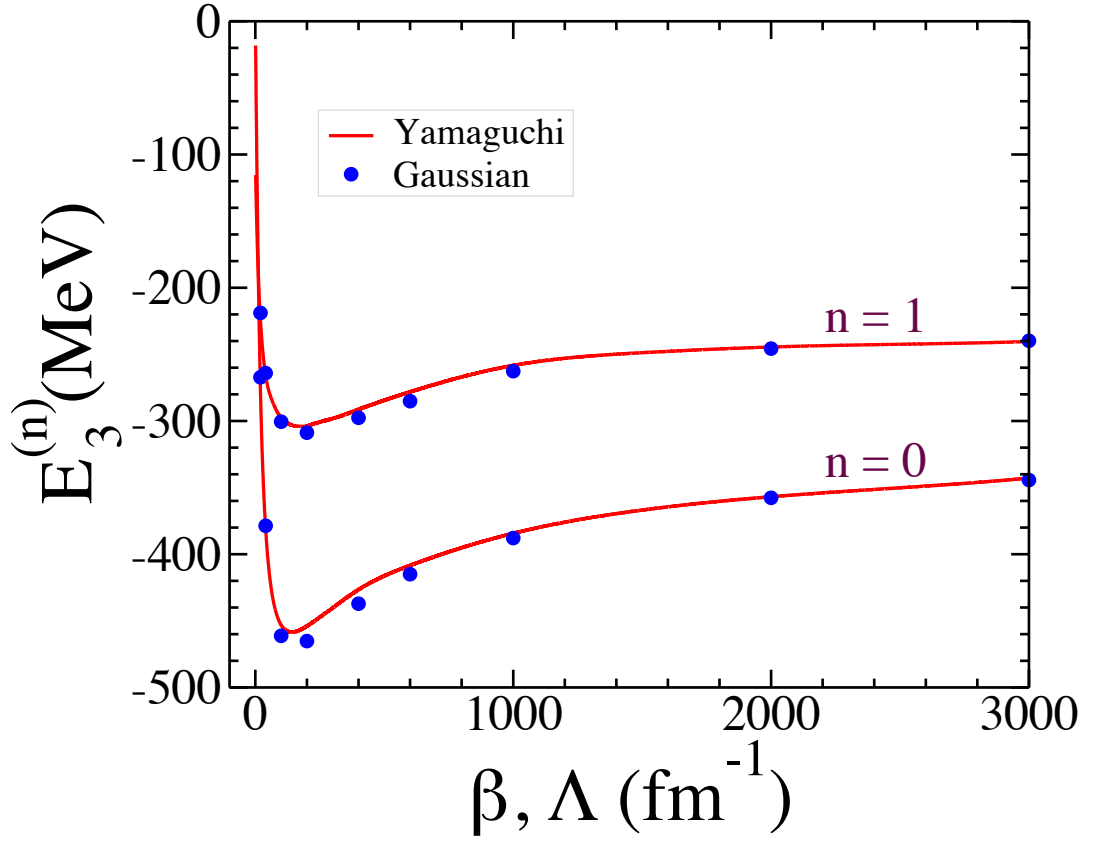


FIGURE 2.8 – The ground and first excited state binding energies as a function of the form factor parameters Λ (for Gaussian potential) and β (for Yamaguchi-type potential) obtained for a fixed 2B binding energy of -2.225 MeV. The first excited state energies are multiplied by a factor of 50.

Next, we proceed to modify the dimer binding energy and examine its impact on the trimer binding energy while keeping the potential parameters fixed. Table 2.5 presents the relativistic ground and excited state binding energies of the trimer for Yamaguchi and Gaussian form factors with $\beta = \Lambda = 2000 \text{ fm}^{-1}$.

TABLE 2.5 – Relativistic trimer binding energy calculate with Eq. (2.78) for different dimer binding energies. In this table we fixed the potential parameter for Yamaguchi and Gaussian form factor $\beta = \Lambda = 2000 \text{ fm}^{-1}$.

$E_d \text{ (MeV)}$	Yamaguchi		Gaussian	
	$E_{PW}^{r(0)} \text{ (MeV)}$	$E_{PW}^{r(1)} \text{ (MeV)}$	$E_{PW}^{r(0)} \text{ (MeV)}$	$E_{PW}^{r(1)} \text{ (MeV)}$
0	-295.655	-0.78180	-299.066	-0.79235
-2.225	-356.855	-4.88977	-357.684	-4.91434
-10	-424.703	-14.0795	-427.946	-14.1361
-20	-481.524	-24.4189	-486.443	-23.8862
-30	-528.124	-33.6088	-533.373	-33.6545
-40	-569.019	-43.3097	-574.329	-43.3554
-50	-606.141	-53.0641	-611.478	-53.1082
-100	-761.343	-100.568	-767.122	-103.661
-150	-891.408	-156.552	-897.716	-156.563

In Fig. 2.9, we present the ratio of the 3B mass to the particle mass (M_3/m) as a function of the ratio of the 2B mass to the particle mass (M_2/m). These results are obtained for the 3B ground and first excited states using large form factor parameters ($\beta = \Lambda = 2000 \text{ fm}^{-1}$). The plot represents the mass values in units relative to the particle mass, allowing for a direct comparison with previous calculations that utilized the Bethe-Salpeter (BS) and Light-Front (LF) equations (YDREFORS *et al.*, 2017a). Fig. 2.9 illustrates the universal behavior observed in our results when employing large form factor parameters for both Yamaguchi-type and Gaussian potentials. First, we observe that, in the 2B bound state region, both the LF and BS approaches have an unphysical 3B ground state with $M_3^2 < 0$, which are possible as the homogeneous integral equations, only depend on M_3^2 (YDREFORS *et al.*, 2017a). The physical “ground” state with $0 < M_3^2 < (m + M_2)^2$ from the solution of the LF and BS equations are indeed an excited state, and in this way, they are denoted in the Fig. 2.9. Our numerical analysis of the first excited bound state mass for a three-boson system, obtained using boosted potentials with large form factor parameters ($\beta = 2000 \text{ fm}^{-1}$ and $\Lambda = 2000 \text{ fm}^{-1}$), reveals a weaker attraction when compared to the results obtained with the LF and BS frameworks (YDREFORS *et al.*, 2017a).

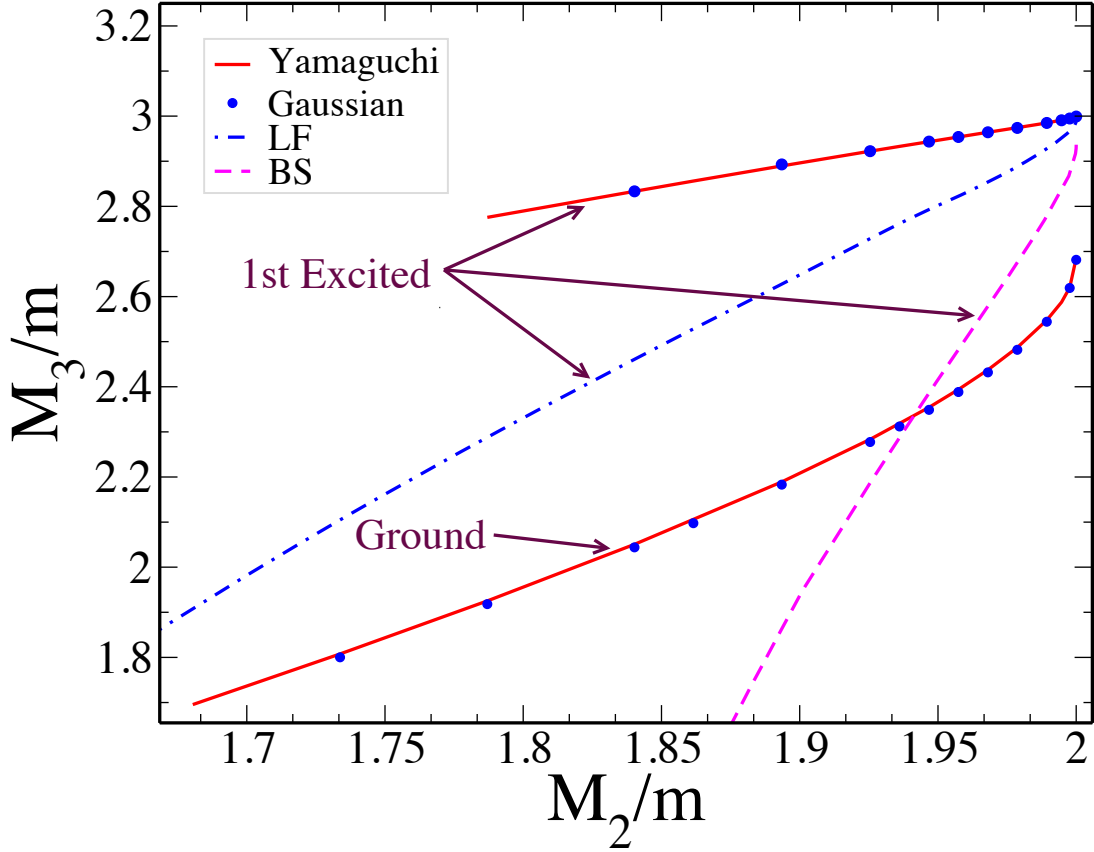


FIGURE 2.9 – The value of M_3/m as a function of M_2/m calculated from the 3B ground and first excited states obtained with form factor parameters $\beta = \Lambda = 2000 \text{ fm}^{-1}$ for Yamaguchi-type (solid lines) and Gaussian potentials (full circles). For comparison, our results with the Bethe-Salpeter (dashed line) and Light-Front (dash-dotted line) zero-range calculations of Ref. (YDREFORS *et al.*, 2017a) are added to the plot. This Figure is taken from (MOHSENI *et al.*, 2021).

The difference between the LF and BS approaches arises from the presence of attractive 3B effective potentials in the BS approach, which results from the implicit inclusion of an infinite set of LF Fock-components. This inclusion is absent in the LF equation, where the truncation is limited to the valence level (YDREFORS *et al.*, 2017a). From Fig. 2.9, it is evident that in the ultraviolet (UV) region, the boosted potential displays significantly weakened attractiveness due to the relativistic potential becoming softer, as a consequence of solving Eq. (2.14). This effect becomes apparent by observing the slower rate of decrease in M_3 by decreasing M_2 , in the calculation using the boosted potential, in comparison to the results obtained from the BS and LF approaches. The observed phenomenon of the 3B mass decreasing at a slower rate with an increase in the 2B binding, as depicted in Fig. 2.9, indicates a softening effect within the adopted relativistic framework. This softening effect suggests that as the 2B binding increases, the 3B bound state becomes more compact, which forces the system to explore the UV region where the effectiveness of the boosted potential diminishes. In contrast, the 2B amplitude considered in the LF and BS equations exhibits significantly less damping in the UV region, showing a behavior of

approximately $1/\log(k)$ (as described in Eq. (2) of Ref. (YDREFORS *et al.*, 2017a)). This behavior is considerably softer compared to the decrease observed in the matrix elements of the boosted potential, which follows a $1/k$ trend. This discussion highlights the weaker kernel provided by the boosted potential in the Faddeev equation when compared to the LF and BS counterparts.

In Fig. 2.10, we present the relativistic Faddeev components of the wave functions for both the ground state, $\psi^{(0)}(p, k)$, and the first excited state, $\psi^{(1)}(p, k)$. These wave functions are plotted as functions of the Jacobi momenta p and k , considering two sets of potential form factor parameters: one with small values and the other with large values of β and Λ . The corresponding binding energies are listed in Table 2.5.

The initial remarkable observation is the universality, or model independence, of $\psi^{(0)}(p, k)$ and $\psi^{(1)}(p, k)$ within momenta approximately up to the scale of β or Λ . However, for larger momenta, both potential models clearly show different decay behaviors. The Gaussian model exhibits the expected faster damping of the Faddeev component, while the Yamaguchi model continues to display a power-law behavior.

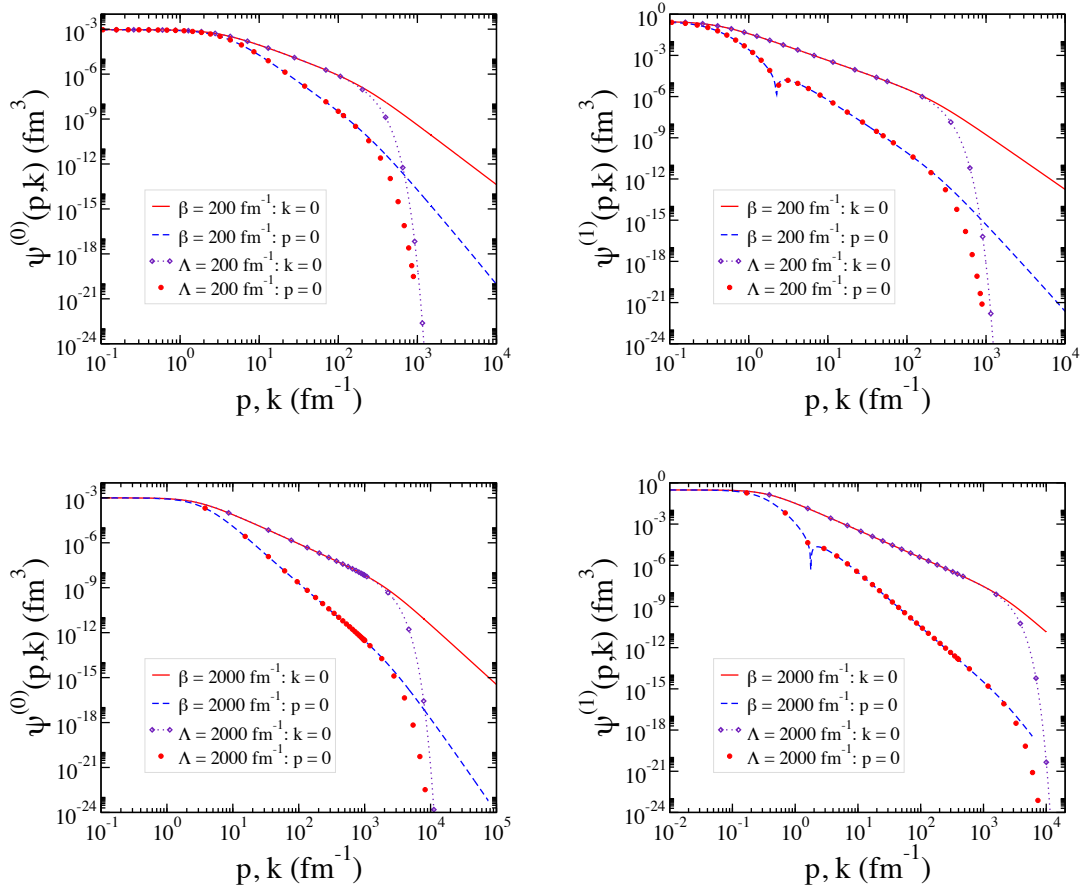


FIGURE 2.10 – Relativistic Faddeev components for 3B ground $\psi^{(0)}(p, k)$ and first excited $\psi^{(1)}(p, k)$ states calculated for Yamaguchi-type potential with form factor parameters $\beta = 200, 2000 \text{ fm}^{-1}$ and Gaussian potential with form factor parameters $\Lambda = 200, 2000 \text{ fm}^{-1}$. This Figure is taken from (MOHSENI *et al.*, 2021).

2.5 Efimov physics

One challenging test for our numerical calculation is the numerical calculation of Efimov states (EFIMOV, 1970). In Table 2.6, we present six states that have been obtained by solving the Eq. (2.61), utilizing a Gaussian form factor with a potential parameter of $\Lambda = 0.7 \text{ fm}^{-1}$. The calculations are performed with 900 mesh points for Jacobi momenta p and k , and 40 mesh points for angle variables. Potential strength λ is calculated by solving Eq. (2.7) with $E_d = 0$. Notably, the ratio of the two binding energies displayed in the table are perfectly match with the predicted results of the Efimov effect (DELTUVA, 2010). This agreement confirms the presence of the Efimov effect in our nonrelativistic calculations.

TABLE 2.6 – 3B ground and excited stated binding energies calculated with the Gaussian form factor with $\Lambda = 0.7 \text{ fm}^{-1}$ and $E_d = 0$.

n	E_{nr}^{3B} (MeV)	$E^{(n)}/E^{(n+1)}$	$E^{(n)}/E^{(n+1)}$ (DELTUVA, 2010)
0	-0.91924	548.114	548.114
1	$-1.67709 \cdot 10^{-3}$	515.213	515.214
2	$-3.25515 \cdot 10^{-6}$	515.035	515.036
3	$-6.32024 \cdot 10^{-9}$	515.035	515.035
4	$-1.22715 \cdot 10^{-11}$	515.035	515.035
5	$-2.38265 \cdot 10^{-14}$	515.035	—
6	$-4.62619 \cdot 10^{-17}$	—	—

The Efimov effect is mainly observed at low energies; therefore, relativity doesn't directly affect this phenomenon. However, when particle interactions occur within a range smaller than their Compton wavelength, relativistic corrections might influence the most tightly bound Efimov states (NAIDON; ENDO, 2017; YAMASHITA *et al.*, 2007).

3 Trion in Two-dimensional Momentum Space

3.1 Overview

Although graphene has spearheaded the advancement of two-dimensional (2D) materials due to its exceptional electronic properties, its lack of a band gap limits its potential and motivates the search for alternative semiconducting 2D materials, often referred to as "graphene with a band gap." Among the promising candidates are transition metal dichalcogenides (TMDs), which have undergone extensive investigation (KIDD *et al.*, 2016b). These 2D semiconductors are gaining significant attention as a promising advancement in semiconductor technology. Leveraging their unique properties, 2D semiconductors are finding applications in diverse fields. These include advanced flexible devices, where their flexibility plays a critical role; nanophotonic devices, which exploit their optical properties for enhanced functionality; and solar cells, which benefit from their high efficiency and lightweight nature (DAS *et al.*, 2019; IQBAL *et al.*, 2021; BELLANI *et al.*, 2021; BATI *et al.*, 2020; YU; SIVULA, 2017).

Such semiconducting materials exhibit a remarkably strong Coulomb interaction between charge carriers due to the reduced dimensionality. This enhanced interaction leads to the formation of tightly bound excitons and trions, which are of great interest in condensed matter physics.(CAVALCANTE *et al.*, 2018)

As proposed by Lampert (LAMPERT, 1958), when a single exciton interacts with an additional electron in a conduction band or a hole in a valence band, it forms charged exciton complexes known as negative (T^-) and positive (T^+) trions, respectively. Excitonic systems can also involve more than three particles, forming more complex many-body states (TUAN *et al.*, 2022; TUAN; DERY, 2022a; TUAN; DERY, 2022c; TUAN; DERY, 2022b). For instance, in monolayer WSe₂, a photoexcited electron-hole pair can interact with multiple reservoirs of distinguishable electrons due to the unique arrangement of spin-polarized conduction band valleys. This can give rise to the emergence of six-particle hexcitons or even eight-particle oxcitons. However, this thesis will focus primarily on three-particle

excitonic systems (trions) and their properties in two-dimensional materials.

Trions are intrinsically three-body systems, and the behavior of three-body systems undergoes significant changes when transitioning from two to three dimensions, as the dynamics and properties of quantum systems are profoundly affected by dimensional constraints. Two notable examples exemplifying the impact of spatial dimensions in the three-body sector are the Efimov effect (EFIMOV, 1970) and the Thomas collapse (THOMAS, 1935). Efimov states, observed and predicted for three identical bosons in 3D systems, are not present in 2D, even under the most favorable conditions of mass-imbalanced systems (ADHIKARI *et al.*, 1988). Similarly, in 1935, Thomas found that the energy of a three-identical-boson system subjected to short-range pairwise interactions in 3D grows without bounds when the interaction range approaches zero ($r_0 \rightarrow 0$). However, this effect was not observed in 2D systems. The absence of these phenomena in 2D highlights the dramatic influence of spatial dimensions on the behavior of three-body systems.

In this chapter, we establish the fundamental framework for investigating the negative trion, a three body bound state consists of two electrons and one hole, in semiconductor layered (2D) materials. To study the behavior of three particles in a 2D setting, we employ the Faddeev equations in momentum space. This approach is particularly insightful because the Faddeev equations are the most general equations for describing a non-relativistic three-body system within the potential approach, using only the masses of the particles and potential as inputs (FILIKHIN *et al.*, 2018). Specifically, we solve the coupled integral equations governing trion formation, considering both the short-range one-term separable Yamaguchi potential and the Rytova-Keldysh (RK) interaction, which are applied to the MoS₂ layer. By employing these approaches, we aim to gain insights into the properties and characteristics of trions. To tackle the difficulty posed by the repulsive electron-electron RK potential in numerically solving the Faddeev equations, we introduce two distinct regularization methods. The first method focuses on regulating the repulsive interaction in the infrared region, while the second method regulates it in the ultraviolet region. These regularization techniques effectively address the challenge posed by the repulsive component of the RK potential, allowing for accurate and reliable numerical solutions of the Faddeev equations.

3.2 Two-dimensional exciton structure analysis through the application of the Lippmann-Schwinger equation

3.2.1 Non-partial wave representation

One can write 3D nonrelativistic Schrödinger equation, Eq. (2.21), in 2D as

$$\psi(\mathbf{p}) = \frac{1}{E_d - \frac{p^2}{m}} \int_0^\infty dp' p' \int_0^{2\pi} d\phi' V(\mathbf{p}, \mathbf{p}') \psi(\mathbf{p}'), \quad (3.1)$$

where the completeness relation of 2B basis states is as

$$\int d^2p |\mathbf{p}\rangle \langle \mathbf{p}| \equiv \int_0^\infty dp p \int_0^{2\pi} d\phi |\mathbf{p}\rangle \langle \mathbf{p}| = 1. \quad (3.2)$$

For the numerical solution of the 2D integral equation (3.1), in the general case of angle-dependent, we adopt a coordinate system where all the vectors are free in the 2D, as depicted in Fig. (3.1).

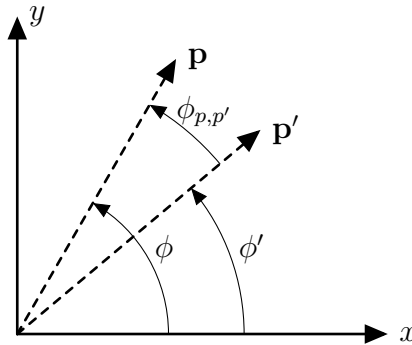


FIGURE 3.1 – The geometry of vector \mathbf{p} & \mathbf{p}' . both vectors are chosen to be free in the 2D space.

Using coordinate system defined in Fig. (3.1), Eq. (3.1) for angular-dependent dimer wave functions can be written as

$$\psi(p, \phi) = \frac{1}{E_d - \frac{p^2}{m}} \int_0^\infty dp' p' \int_0^{2\pi} d\phi' V(p, p', \phi_{p,p'}) \psi(p', \phi'). \quad (3.3)$$

We can simplify Eq. (3.3) by choosing a coordinate system where \mathbf{p} is parallel to the x -axis and just the integration vector \mathbf{p}' is free in the 2D space, therefore the dimer wave

function without angular dependency can be written as

$$\psi(p) = \frac{1}{E_d - \frac{p^2}{m}} \int_0^\infty dp' p' \int_0^{2\pi} d\phi' V(p, p', \phi') \psi(p'). \quad (3.4)$$

In Appendix C, we conduct a numerical examination where we calculate the dimer energy and wave function using Eqs. (3.3) and (3.4), employing the Malfliet Tjon and Coulomb potentials.

3.2.2 Partial wave representation

In the previous section, we focused on the non-PW representation of the LS Equation (3.1). In this chapter, we shift our attention to the PW representation of this equation, which is given as follows

$$\psi_m(p) = \frac{1}{E_d - \frac{p^2}{2\mu}} \int_0^\infty dp' p' V_m(p, p') \psi_m(p'), \quad (3.5)$$

with

$$V_m(p, p') = \int_0^{2\pi} d\phi V(p, p', \phi) \cos(m\phi), \quad (3.6)$$

where m indicates the PW channel. derivation of Eq. (3.6) is given in Appendix F.1. To thoroughly investigate PW Eq. (3.6), we utilize both the Malfliet Tjon and Coulomb potentials. We proceed by computing the binding energy and wave function of the PW dimer. The outcomes of this analysis are provided in Appendix F.2. In the following, we utilize a realistic potential to calculate exciton binding energy, which is the energy of bound states formed by an electron and a hole.

3.2.2.1 Electron-hole bound states

The Rytova–Keldysh potential describes the screened Coulomb interaction in momentum space is given by (RYTOVA, 1967; KELDYSH, 1979; RYTOVA, 2018; CUDAZZO *et al.*, 2011)

$$V_{eh}(q) = -\frac{1}{4\pi^2} \left(\frac{1}{4\pi\epsilon_0} \frac{2\pi e^2}{q(1+r_0q)} \right). \quad (3.7)$$

Here, the momentum transfer is defined as $|\mathbf{q}| = |\mathbf{p} - \mathbf{p}'|$, where r_0 represents the screening length in the absence of a substrate. In Ref. (KEZERASHVILI, 2019) it's shown that the RK

potential has lower strength compared to the Coulomb potential for small electron-hole distance, and as the distance increases, both potentials gradually approach convergence. Parameters for Eq. (3.7) are listed in Table 3.1 for MoS₂ material.

TABLE 3.1 – The parameters of RK potentials defined in Eq. (3.7) for MoS₂. The values for effective masses are taken from Ref. (KORMÁNYOS *et al.*, 2015)

$m_e(m_0)$	$m_h(m_0)$	r_0 (Å)
0.47	0.54	27.05
Constant Parameters		
$\epsilon_0/e^2 = \frac{1}{4\pi\alpha} \cdot \frac{1}{\hbar c} \text{ eV}^{-1} \cdot \text{Å}^{-1} \quad \hbar c = 1973.269804 \text{ eV} \cdot \text{Å};$		
$\alpha = 137.035999084 ; \quad m_0 = 0.510998950 \text{ MeV}$		

The value of the screening length r_0 is fitted to give an exciton binding energy of -753 meV in agreement with the value obtained from the measurement of the exciton position in the absorption spectrum of a suspended MoS₂ layer (KLOTS *et al.*, 2014) and the corresponding GW bandgap (ZHANG *et al.*, 2016).

In Table E.1, we present the results for the exciton binding energy obtained through the numerical solution of the partial wave LS equation Eq. (3.5), specifically in the s -wave ($m = 0$). In this table, the binding energy is listed as a function of the number of mesh points for the relative momentum (N_p) and the angle variable (N_ϕ). From Table E.1, it can be observed that even with a high number of mesh points, convergence is not achieved, indicating the complexity of the long-range RK potential. However, we can extrapolate the result to an infinite number of mesh points by fitting a quadratic function to the calculated binding energy. This extrapolated value is presented in the last row of Table E.1.

In Fig. 3.2, we show the exciton wave function in momentum space $\psi^{(n)}(p)$ as a function of relative momentum p , for the ground state ($n = 0$), first excited state ($n = 1$), and second excited state ($n = 2$) of the exciton. The calculations are performed with 61 mesh points for angle variables and 1000 mesh points for 2B relative momentum N_p .

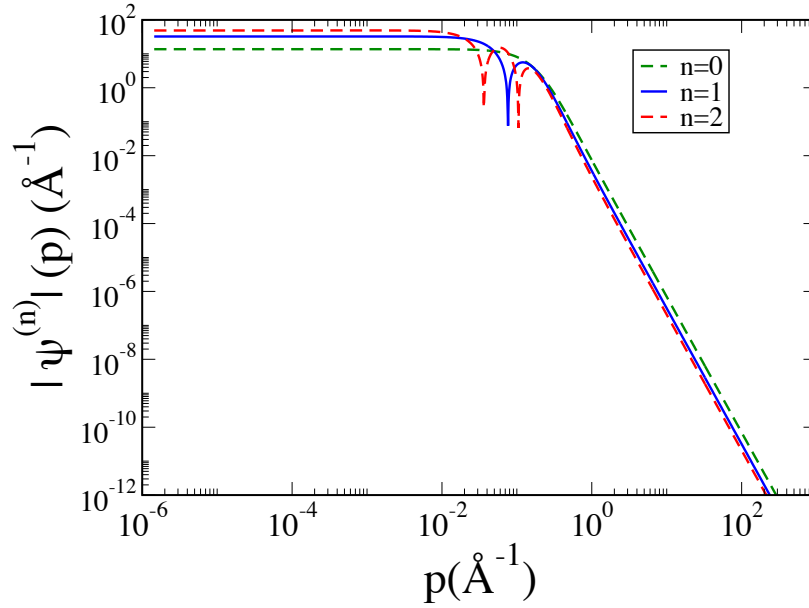


FIGURE 3.2 – Exciton ground and excited states wave functions in momentum $\psi^{(n)}(p)$ as a function of p .

To further investigate our numerical method and compare the results, we study substrate screening effects using the modified potential in Eq. (3.7), as proposed by Chernikov et al. (2014) (CHERNIKOV *et al.*, 2014)

$$V_{eh}(q) = -\frac{1}{4\pi^2} \left(\frac{1}{4\pi\epsilon_0} \frac{2\pi e^2}{q \left(\frac{1+\epsilon_s}{2} + r_0 q \right)} \right). \quad (3.8)$$

Here ϵ_s denotes the dielectric constant of the substrate. The specific values for these parameters in the case of WS₂ material can be found in Table 3.2.

TABLE 3.2 – The parameters of electron-hole potentials defined in Eq. (3.8) for WS₂.

$\mu(m_0)$	ϵ_s	r_0 (Å)
0.16	2.1 & 3.9	38
Constant Parameters		
$\epsilon_0/e^2 = \frac{1}{4\pi\alpha} \cdot \frac{1}{\hbar c} \text{ eV}^{-1} \cdot \text{Å}^{-1} \quad \hbar c = 1973.269804 \text{ eV} \cdot \text{Å};$		
$\alpha = 137.035999084 ; \quad m_0 = 0.510998950 \text{ MeV}$		

In Table 3.3, we present the exciton binding energies for different dielectric constants ϵ_s with the parameters listed in Table 3.2. The calculations are performed using 700 mesh points for relative momenta and 100 mesh points for angle variables.

TABLE 3.3 – Exciton binding energies with RK potential defined in Eq. (3.8) for different dielectric constants ϵ_s .

n	$E_{\epsilon_s=2.1}$ (eV)	$E_{\epsilon_s=3.9}$ (eV)
1	−0.402	−0.2831
2	−0.147	−0.0833
3	−0.080	−0.0405
4	−0.050	−0.0243
5	−0.035	−0.0165
6	−0.030	−0.0122

In our study, we were able to calculate five excited states for the given parameters in Table 3.2. In the study by Chernikov et al. (2014) (CHERNIKOV *et al.*, 2014), they reported four excited states, and our calculated results agree with their findings for these four states.

3.3 Faddeev equations for three different particles bound states in two dimensions

As it is given in Eq. (2.40), in the general case of three different particles, the three coupled Faddeev equations are given

$$\begin{aligned}
|\psi_1\rangle &= G_0 t_1 (|\psi_2\rangle + |\psi_3\rangle), \\
|\psi_2\rangle &= G_0 t_2 (|\psi_3\rangle + |\psi_1\rangle), \\
|\psi_3\rangle &= G_0 t_3 (|\psi_1\rangle + |\psi_2\rangle),
\end{aligned} \tag{3.9}$$

where 2B transition operators t_i are defined by the Lippmann–Schwinger equation

$$t_i = V_i + V_i G_0 t_i. \tag{3.10}$$

with $i = 1, 2, 3$.

To solve the coupled Faddeev Eq. (3.9) in momentum space, we consider the 3B basis states $|\mathbf{p}_i \mathbf{q}_i\rangle$, composed of two Jacobi momenta (see Fig. 3.3), which are defined in terms of the single particle momenta as

$$\begin{aligned}
\mathbf{p}_i &= \frac{m_k \mathbf{k}_j - m_j \mathbf{k}_k}{m_j + m_k}, \\
\mathbf{q}_i &= \frac{m_j + m_k}{m_i + m_j + m_k} \left(\mathbf{k}_i - \frac{m_i}{m_j + m_k} (\mathbf{k}_j + \mathbf{k}_k) \right),
\end{aligned} \tag{3.11}$$

where \mathbf{p}_i is the relative momentum of the pair jk , and \mathbf{q}_i is the relative momentum of the third particle i with respect to the pair jk . The completeness relation of 3B basis states in 2D is defined as

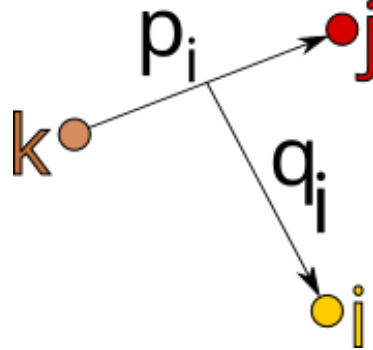


FIGURE 3.3 – Jacobi momenta convention used through the paper. $\{i, j, k\}$ correspond to the indices associated with the three particles, and p_i and q_i are their Jacobi momenta given in Eqs. (2.47) and (2.48).

$$\int d^2 p_i \int d^2 q_i |\mathbf{p}_i \mathbf{q}_i\rangle \langle \mathbf{p}_i \mathbf{q}_i| \equiv 2\pi \int_0^\infty dp_i p_i \int_0^\infty dq_i q_i \int_0^{2\pi} d\phi_{p_i, q_i} = 1. \quad (3.12)$$

The Jacobi momenta in the different two-body subsystems related to each other via

i. Corresponding Jacobi momenta in $(1, 23)$ cluster

$$\begin{aligned} \mathbf{p}_1(\mathbf{p}_2, \mathbf{q}_2) &= -\frac{m_2}{m_2 + m_3} \mathbf{p}_2 + \frac{m_3(m_1 + m_2 + m_3)}{(m_1 + m_3)(m_2 + m_3)} \mathbf{q}_2, \\ \mathbf{q}_1(\mathbf{p}_2, \mathbf{q}_2) &= -\mathbf{p}_2 - \frac{m_1}{m_1 + m_3} \mathbf{q}_2, \\ \mathbf{p}_1(\mathbf{p}_3, \mathbf{q}_3) &= -\frac{m_3}{m_2 + m_3} \mathbf{p}_3 - \frac{m_2(m_1 + m_2 + m_3)}{(m_1 + m_2)(m_2 + m_3)} \mathbf{q}_3, \\ \mathbf{q}_1(\mathbf{p}_3, \mathbf{q}_3) &= \mathbf{p}_3 - \frac{m_1}{m_1 + m_2} \mathbf{q}_3. \end{aligned} \quad (3.13)$$

ii. Corresponding Jacobi momenta in $(2, 13)$ cluster

$$\begin{aligned} \mathbf{p}_2(\mathbf{p}_1, \mathbf{q}_1) &= -\frac{m_1}{m_1 + m_3} \mathbf{p}_1 - \frac{m_3(m_1 + m_2 + m_3)}{(m_2 + m_3)(m_1 + m_3)} \mathbf{q}_1, \\ \mathbf{q}_2(\mathbf{p}_1, \mathbf{q}_1) &= \mathbf{p}_1 - \frac{m_2}{m_2 + m_3} \mathbf{q}_1, \\ \mathbf{p}_2(\mathbf{p}_3, \mathbf{q}_3) &= -\frac{m_3}{m_1 + m_3} \mathbf{p}_3 + \frac{m_1(m_1 + m_2 + m_3)}{(m_1 + m_2)(m_1 + m_3)} \mathbf{q}_3, \\ \mathbf{q}_2(\mathbf{p}_3, \mathbf{q}_3) &= -\mathbf{p}_3 - \frac{m_2}{m_1 + m_2} \mathbf{q}_3. \end{aligned} \quad (3.14)$$

iii. Corresponding Jacobi momenta in $(3, 12)$ cluster

$$\begin{aligned}
\mathbf{p}_3(\mathbf{p}_1, \mathbf{q}_1) &= -\frac{m_1}{m_1 + m_2} \mathbf{p}_1 + \frac{m_2(m_1 + m_2 + m_3)}{(m_2 + m_3)(m_1 + m_2)} \mathbf{q}_1, \\
\mathbf{q}_3(\mathbf{p}_1, \mathbf{q}_1) &= -\mathbf{p}_1 - \frac{m_3}{m_2 + m_3} \mathbf{q}_1, \\
\mathbf{p}_3(\mathbf{p}_2, \mathbf{q}_2) &= -\frac{m_2}{m_1 + m_2} \mathbf{p}_2 - \frac{m_1(m_1 + m_2 + m_3)}{(m_1 + m_3)(m_1 + m_2)} \mathbf{q}_2, \\
\mathbf{q}_3(\mathbf{p}_2, \mathbf{q}_2) &= \mathbf{p}_2 - \frac{m_3}{m_1 + m_3} \mathbf{q}_2.
\end{aligned} \tag{3.15}$$

The relation between different Jacobi momenta can be summarized as

$$\mathbf{p}_i(\mathbf{p}_j, \mathbf{q}_j) \equiv \mathcal{P}_{ij}(\mathbf{p}_j, \mathbf{q}_j) = \alpha_{ij} \mathbf{p}_j + \beta_{ij} \mathbf{q}_j, \tag{3.16}$$

$$\mathbf{q}_i(\mathbf{p}_j, \mathbf{q}_j) \equiv \mathcal{Q}_{ij}(\mathbf{p}_j, \mathbf{q}_j) = \gamma_{ij} \mathbf{p}_j + \eta_{ij} \mathbf{q}_j, \tag{3.17}$$

where

$$\alpha_{ij} = -\frac{m_j}{m_{jk}}, \tag{3.18}$$

$$\beta_{ij} = \mathcal{E}_{ij} \frac{m_k m_{ijk}}{m_{ik} m_{jk}}, \tag{3.19}$$

$$\gamma_{ij} = -\mathcal{E}_{ij}, \tag{3.20}$$

$$\eta_{ij} = -\frac{m_i}{m_{ik}}, \tag{3.21}$$

$$m_{ij} = m_i + m_j, \tag{3.22}$$

$$m_{ijk} = m_i + m_j + m_k, \tag{3.23}$$

and

$$\mathcal{E}_{ij} = \begin{cases} 1 & \text{if } (i, j) = (1, 2), (2, 3), (3, 1) \\ -1 & \text{if } (i, j) = (2, 1), (3, 2), (1, 3). \end{cases} \tag{3.24}$$

In order to solve the three coupled equations (3.9) in momentum space, we can project the Faddeev components onto their own basis by using the momenta basis defined in Eq. (3.17), therefore we have

$$\langle \mathbf{p}_1 \mathbf{q}_1 | \psi_1 \rangle = G_0^{(1,23)}(E, p_1, q_1) \left[\langle \mathbf{p}_1 \mathbf{q}_1 | t_1 | \psi_2 \rangle + \langle \mathbf{p}_1 \mathbf{q}_1 | t_1 | \psi_3 \rangle \right], \tag{3.25}$$

$$\langle \mathbf{p}_2 \mathbf{q}_2 | \psi_2 \rangle = G_0^{(2,13)}(E, p_2, q_2) \left[\langle \mathbf{p}_2 \mathbf{q}_2 | t_2 | \psi_1 \rangle + \langle \mathbf{p}_2 \mathbf{q}_2 | t_2 | \psi_3 \rangle \right], \tag{3.26}$$

$$\langle \mathbf{p}_3 \mathbf{q}_3 | \psi_3 \rangle = G_0^{(3,12)}(E, p_3, q_3) \left[\langle \mathbf{p}_3 \mathbf{q}_3 | t_3 | \psi_1 \rangle + \langle \mathbf{p}_3 \mathbf{q}_3 | t_3 | \psi_2 \rangle \right], \tag{3.27}$$

where free propagator is defined as

$$G_0^{(i,jk)}(E, p_i, q_i) = \frac{1}{E - \frac{p_i^2}{2\mu_{jk}} - \frac{q_i^2}{2\mu_{i,jk}}}. \quad (3.28)$$

Using completeness relations, Eq. (3.12) we can write the three coupled equations in the momentum space as

$$\begin{aligned} \langle \mathbf{p}_1 \mathbf{q}_1 | \psi_1 \rangle &= G_0^{(1,23)}(E, p_1, q_1) \int d^2 p'_1 \int d^2 q'_1 \\ &\times \left[\langle \mathbf{p}_1 \mathbf{q}_1 | t_1 | \mathbf{p}'_1 \mathbf{q}'_1 \rangle \langle \mathbf{p}'_1 \mathbf{q}'_1 | \psi_2 \rangle + \langle \mathbf{p}_1 \mathbf{q}_1 | t_1 | \mathbf{p}'_1 \mathbf{q}'_1 \rangle \langle \mathbf{p}'_1 \mathbf{q}'_1 | \psi_3 \rangle \right] \\ &= G_0^{(1,23)}(E, p_1, q_1) \int d^2 p'_1 \int d^2 q'_1 \langle \mathbf{p}_1 \mathbf{q}_1 | t_1 | \mathbf{p}'_1 \mathbf{q}'_1 \rangle \\ &\times \left[\langle \mathbf{p}'_1 \mathbf{q}'_1 | \psi_2 \rangle + \langle \mathbf{p}'_1 \mathbf{q}'_1 | \psi_3 \rangle \right], \end{aligned} \quad (3.29)$$

$$\begin{aligned} \langle \mathbf{p}_2 \mathbf{q}_2 | \psi_2 \rangle &= G_0^{(2,13)}(E, p_2, q_2) \int d^2 p'_2 \int d^2 q'_2 \\ &\times \left[\langle \mathbf{p}_2 \mathbf{q}_2 | t_2 | \mathbf{p}'_2 \mathbf{q}'_2 \rangle \langle \mathbf{p}'_2 \mathbf{q}'_2 | \psi_1 \rangle + \langle \mathbf{p}_2 \mathbf{q}_2 | t_2 | \mathbf{p}'_2 \mathbf{q}'_2 \rangle \langle \mathbf{p}'_2 \mathbf{q}'_2 | \psi_3 \rangle \right] \\ &= G_0^{(2,13)}(E, p_2, q_2) \int d^2 p'_2 \int d^2 q'_2 \langle \mathbf{p}_2 \mathbf{q}_2 | t_2 | \mathbf{p}'_2 \mathbf{q}'_2 \rangle \\ &\times \left[\langle \mathbf{p}'_2 \mathbf{q}'_2 | \psi_1 \rangle + \langle \mathbf{p}'_2 \mathbf{q}'_2 | \psi_3 \rangle \right], \end{aligned} \quad (3.30)$$

$$\begin{aligned} \langle \mathbf{p}_3 \mathbf{q}_3 | \psi_3 \rangle &= G_0^{(3,12)}(E, p_3, q_3) \int d^2 p'_3 \int d^2 q'_3 \\ &\times \left[\langle \mathbf{p}_3 \mathbf{q}_3 | t_3 | \mathbf{p}'_3 \mathbf{q}'_3 \rangle \langle \mathbf{p}'_3 \mathbf{q}'_3 | \psi_1 \rangle + \langle \mathbf{p}_3 \mathbf{q}_3 | t_3 | \mathbf{p}'_3 \mathbf{q}'_3 \rangle \langle \mathbf{p}'_3 \mathbf{q}'_3 | \psi_2 \rangle \right] \\ &= G_0^{(3,12)}(E, p_3, q_3) \int d^2 p'_3 \int d^2 q'_3 \langle \mathbf{p}_3 \mathbf{q}_3 | t_3 | \mathbf{p}'_3 \mathbf{q}'_3 \rangle \\ &\times \left[\langle \mathbf{p}'_3 \mathbf{q}'_3 | \psi_1 \rangle + \langle \mathbf{p}'_3 \mathbf{q}'_3 | \psi_2 \rangle \right], \end{aligned} \quad (3.31)$$

where

$$\langle \mathbf{p}_1 \mathbf{q}_1 | t_1 | \mathbf{p}'_1 \mathbf{q}'_1 \rangle = \delta(\mathbf{q}_1 - \mathbf{q}'_1) \langle \mathbf{p}_1 | t_1 | \mathbf{p}'_1 \rangle, \quad (3.32)$$

$$\langle \mathbf{p}_2 \mathbf{q}_2 | t_2 | \mathbf{p}'_2 \mathbf{q}'_2 \rangle = \delta(\mathbf{q}_2 - \mathbf{q}'_2) \langle \mathbf{p}_2 | t_2 | \mathbf{p}'_2 \rangle, \quad (3.33)$$

$$\langle \mathbf{p}_3 \mathbf{q}_3 | t_3 | \mathbf{p}'_3 \mathbf{q}'_3 \rangle = \delta(\mathbf{q}_3 - \mathbf{q}'_3) \langle \mathbf{p}_3 | t_3 | \mathbf{p}'_3 \rangle. \quad (3.34)$$

In order to evaluate Eqs. (3.29), (3.30), and (3.31) we need to calculate the following

terms

$$\langle \mathbf{p}'_1 \mathbf{q}'_1 | \psi_2 \rangle, \quad (3.35)$$

$$\langle \mathbf{p}'_1 \mathbf{q}'_1 | \psi_3 \rangle, \quad (3.36)$$

$$\langle \mathbf{p}'_2 \mathbf{q}'_2 | \psi_1 \rangle, \quad (3.37)$$

$$\langle \mathbf{p}'_2 \mathbf{q}'_2 | \psi_3 \rangle, \quad (3.38)$$

$$\langle \mathbf{p}'_3 \mathbf{q}'_3 | \psi_1 \rangle, \quad (3.39)$$

$$\langle \mathbf{p}'_3 \mathbf{q}'_3 | \psi_2 \rangle. \quad (3.40)$$

For example, to evaluate Eq. (3.35), we can insert the completeness relation Eq. (3.12) into Eq. (3.35), yielding

$$\langle \mathbf{p}'_1 \mathbf{q}'_1 | \psi_2 \rangle = \int d^2 p''_2 \int d^2 q''_2 \langle \mathbf{p}'_1 \mathbf{q}'_1 | \mathbf{p}''_2 \mathbf{q}''_2 \rangle \langle \mathbf{p}''_2 \mathbf{q}''_2 | \psi_2 \rangle. \quad (3.41)$$

Eq. (3.14) allows to evaluate $\langle \mathbf{p}'_1 \mathbf{q}'_1 | \mathbf{p}''_2 \mathbf{q}''_2 \rangle$

$$\langle \mathbf{p}'_1 \mathbf{q}'_1 | \mathbf{p}''_2 \mathbf{q}''_2 \rangle = \delta(\mathbf{p}''_2 - \mathbf{p}_2(\mathbf{p}'_1, \mathbf{q}'_1)) \delta(\mathbf{q}''_2 - \mathbf{q}_2(\mathbf{p}'_1, \mathbf{q}'_1)). \quad (3.42)$$

By utilizing the delta function property, we can eliminate the integrals over p''_2 and q''_2 , leading to the following expression

$$\langle \mathbf{p}'_1 \mathbf{q}'_1 | \psi_2 \rangle = \langle \mathbf{p}_2(\mathbf{p}'_1, \mathbf{q}'_1), \mathbf{q}_2(\mathbf{p}'_1, \mathbf{q}'_1) | \psi_2 \rangle. \quad (3.43)$$

Similarly we can write the other terms in Eqs. (3.36)-(3.40) as

$$\langle \mathbf{p}'_1 \mathbf{q}'_1 | \psi_3 \rangle = \langle \mathbf{p}_3(\mathbf{p}'_1, \mathbf{q}'_1), \mathbf{q}_3(\mathbf{p}'_1, \mathbf{q}'_1) | \psi_3 \rangle, \quad (3.44)$$

$$\langle \mathbf{p}'_2 \mathbf{q}'_2 | \psi_1 \rangle = \langle \mathbf{p}_1(\mathbf{p}'_2, \mathbf{q}'_2), \mathbf{q}_1(\mathbf{p}'_2, \mathbf{q}'_2) | \psi_1 \rangle, \quad (3.45)$$

$$\langle \mathbf{p}'_2 \mathbf{q}'_2 | \psi_3 \rangle = \langle \mathbf{p}_3(\mathbf{p}'_2, \mathbf{q}'_2), \mathbf{q}_3(\mathbf{p}'_2, \mathbf{q}'_2) | \psi_3 \rangle, \quad (3.46)$$

$$\langle \mathbf{p}'_3 \mathbf{q}'_3 | \psi_1 \rangle = \langle \mathbf{p}_1(\mathbf{p}'_3, \mathbf{q}'_3), \mathbf{q}_1(\mathbf{p}'_3, \mathbf{q}'_3) | \psi_1 \rangle, \quad (3.47)$$

$$\langle \mathbf{p}'_3 \mathbf{q}'_3 | \psi_2 \rangle = \langle \mathbf{p}_2(\mathbf{p}'_3, \mathbf{q}'_3), \mathbf{q}_2(\mathbf{p}'_3, \mathbf{q}'_3) | \psi_2 \rangle. \quad (3.48)$$

By substituting Eqs. (3.44), (3.45), and (3.32) into Eq. (3.29), we can rewrite it as

$$\begin{aligned} \langle \mathbf{p}_1 \mathbf{q}_1 | \psi_1 \rangle &= G_0^{(1,23)}(E, p_1, q_1) \int d^2 p'_1 \int d^2 q'_1 \\ &\times \delta(\mathbf{q}_1 - \mathbf{q}'_1) \langle \mathbf{p}_1 | t_1 | \mathbf{p}'_1 \rangle \\ &\times \left[\langle \mathbf{p}_2(\mathbf{p}'_1, \mathbf{q}'_1), \mathbf{q}_2(\mathbf{p}'_1, \mathbf{q}'_1) | \psi_2 \rangle + \langle \mathbf{p}_3(\mathbf{p}'_1, \mathbf{q}'_1), \mathbf{q}_3(\mathbf{p}'_1, \mathbf{q}'_1) | \psi_3 \rangle \right], \end{aligned} \quad (3.49)$$

By utilizing the delta function $\delta(\mathbf{q}_1 - \mathbf{q}'_1)$, we can eliminate the integral over q'_1 in Eq. (3.49). The equation can be rewritten as

$$\begin{aligned} \langle \mathbf{p}_1 \mathbf{q}_1 | \psi_1 \rangle &= G_0^{(1,23)}(E, p_1, q_1) \int d^2 p'_1 \langle \mathbf{p}_1 | t_1 | \mathbf{p}'_1 \rangle \\ &\times \left[\langle \mathbf{p}_2(\mathbf{p}'_1, \mathbf{q}_1), \mathbf{q}_2(\mathbf{p}'_1, \mathbf{q}_1) | \psi_2 \rangle + \langle \mathbf{p}_3(\mathbf{p}'_1, \mathbf{q}_1), \mathbf{q}_3(\mathbf{p}'_1, \mathbf{q}_1) | \psi_3 \rangle \right]. \end{aligned} \quad (3.50)$$

Similarly, for the other Faddeev components, Eqs. (3.30) and (3.31), we have

$$\begin{aligned} \langle \mathbf{p}_2 \mathbf{q}_2 | \psi_2 \rangle &= G_0^{(2,13)}(E, p_2, q_2) \int d^2 p'_2 \langle \mathbf{p}_2 | t_2 | \mathbf{p}'_2 \rangle \\ &\times \left[\langle \mathbf{p}_1(\mathbf{p}'_2, \mathbf{q}_2), \mathbf{q}_1(\mathbf{p}'_2, \mathbf{q}_2) | \psi_1 \rangle + \langle \mathbf{p}_3(\mathbf{p}'_2, \mathbf{q}_2), \mathbf{q}_3(\mathbf{p}'_2, \mathbf{q}_2) | \psi_3 \rangle \right], \end{aligned} \quad (3.51)$$

$$\begin{aligned} \langle \mathbf{p}_3 \mathbf{q}_3 | \psi_3 \rangle &= G_0^{(3,12)}(E, p_3, q_3) \int d^2 p'_3 \langle \mathbf{p}_3 | t_3 | \mathbf{p}'_3 \rangle \\ &\times \left[\langle \mathbf{p}_1(\mathbf{p}'_3, \mathbf{q}_3), \mathbf{q}_1(\mathbf{p}'_3, \mathbf{q}_3) | \psi_1 \rangle + \langle \mathbf{p}_2(\mathbf{p}'_3, \mathbf{q}_3), \mathbf{q}_2(\mathbf{p}'_3, \mathbf{q}_3) | \psi_2 \rangle \right]. \end{aligned} \quad (3.52)$$

To solve the 2D integral equations (3.50), (3.51), and (3.52), as illustrated in the figure below, we adopt a coordinate system where \mathbf{p}_i is parallel to the x -axis, while \mathbf{q} and \mathbf{p}' are free in the 2D space.

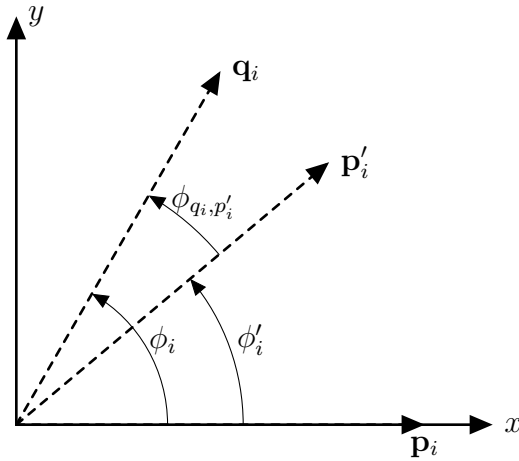


FIGURE 3.4 – The geometry of vector \mathbf{p} , \mathbf{p}' & \mathbf{q} . The vector p is chosen to be parallel to the x -axis and vector \mathbf{p}' , and \mathbf{p}'' are free in the 2D space. The angle variables defined in Eqs. (3.53) are indicated.

The angle variables will be defined as

$$\begin{aligned} (\hat{\mathbf{q}}_i, \hat{\mathbf{p}}'_i) &= \phi_{q_i, p'_i} = \phi_i - \phi'_i, \\ (\hat{\mathbf{q}}_i, \hat{\mathbf{p}}_i) &= \phi_i, \\ (\hat{\mathbf{p}}'_i, \hat{\mathbf{p}}_i) &= \phi'_i. \end{aligned} \quad (3.53)$$

Using the coordinate system in Fig. 3.4, Eqs. (3.50)-(3.52) can be written explicitly as

$$\begin{aligned} \psi_1(p_1, q_1, \phi_1) &= \frac{1}{E - \frac{p_1^2}{2\mu_{23}} - \frac{q_1^2}{2\mu_{1,23}}} \int_0^\infty dp'_1 p'_1 \int_0^{2\pi} d\phi'_1 t_1(p_1, p'_1, \phi'_1; \epsilon_1) \\ &\times \left[\psi_2(\mathcal{P}_{21}, \mathcal{Q}_{21}, \phi_{21}) + \psi_3(\mathcal{P}_{31}, \mathcal{Q}_{31}, \phi_{31}) \right], \end{aligned} \quad (3.54)$$

$$\begin{aligned} \psi_2(p_2, q_2, \phi_2) &= \frac{1}{E - \frac{p_2^2}{2\mu_{13}} - \frac{q_2^2}{2\mu_{2,13}}} \int_0^\infty dp'_2 p'_2 \int_0^{2\pi} d\phi'_2 t_2(p_2, p'_2, \phi'_2; \epsilon_2) \\ &\times \left[\psi_1(\mathcal{P}_{12}, \mathcal{Q}_{12}, \phi_{12}) + \psi_3(\mathcal{P}_{32}, \mathcal{Q}_{32}, \phi_{32}) \right], \end{aligned} \quad (3.55)$$

$$\begin{aligned} \psi_3(p_3, q_3, \phi_3) &= \frac{1}{E - \frac{p_3^2}{2\mu_{12}} - \frac{q_3^2}{2\mu_{3,12}}} \int_0^\infty dp'_3 p'_3 \int_0^{2\pi} d\phi'_3 t_3(p_3, p'_3, \phi'_3; \epsilon_3) \\ &\times \left[\psi_1(\mathcal{P}_{13}, \mathcal{Q}_{13}, \phi_{13}) + \psi_2(\mathcal{P}_{23}, \mathcal{Q}_{23}, \phi_{23}) \right]. \end{aligned} \quad (3.56)$$

Three Faddeev coupled equations (3.54)-(3.56) can be written in a compact form as

$$\begin{aligned} \psi_i(p_i, q_i, \phi_i) &= \frac{1}{E - \frac{p_i^2}{2\mu_{jk}} - \frac{q_i^2}{2\mu_{i,jk}}} \int_0^\infty dp'_i p'_i \int_0^{2\pi} d\phi'_i \\ &\times t_i(p_i, p'_i, \phi'_i; \epsilon_i) \left[\psi_j(\mathcal{P}_{ji}, \mathcal{Q}_{ji}, \phi_{ji}) + \psi_k(\mathcal{P}_{ki}, \mathcal{Q}_{ki}, \phi_{ki}) \right], \end{aligned} \quad (3.57)$$

where shifted momentum and angle variables are defined as

$$\mathcal{P}_{ij} \equiv \mathcal{P}_{ij}(\mathbf{p}'_j, \mathbf{q}_j) = |\alpha_{ij}\mathbf{p}'_j + \beta_{ij}\mathbf{q}_j| = \sqrt{(\mathcal{P}_{ij}^X)^2 + (\mathcal{P}_{ij}^Y)^2}, \quad (3.58)$$

$$\mathcal{Q}_{ij} \equiv \mathcal{Q}_{ij}(\mathbf{p}'_j, \mathbf{q}_j) = |\gamma_{ij}\mathbf{p}'_j + \eta_{ij}\mathbf{q}_j| = \sqrt{(\mathcal{Q}_{ij}^X)^2 + (\mathcal{Q}_{ij}^Y)^2}, \quad (3.59)$$

$$\phi_{ij} = (\hat{\mathcal{P}}_{ij}, \hat{\mathcal{Q}}_{ij}) = \text{atan2}(\text{det}, \text{dot}), \quad 0 < \phi_{ij} < 2\pi \quad (3.60)$$

with

$$\mathcal{P}_{ij}^X = \alpha_{ij}p'_j \cos(\phi'_j) + \beta_{ij}q_j \cos(\phi_j), \quad \mathcal{P}_{ij}^Y = \alpha_{ij}p'_j \sin(\phi'_j) + \beta_{ij}q_j \sin(\phi_j), \quad (3.61)$$

$$\mathcal{Q}_{ij}^X = \gamma_{ij}p'_j \cos(\phi'_j) + \eta_{ij}q_j \cos(\phi_j), \quad \mathcal{Q}_{ij}^Y = \gamma_{ij}p'_j \sin(\phi'_j) + \eta_{ij}q_j \sin(\phi_j), \quad (3.62)$$

and

$$\begin{cases} \text{det} = \mathcal{P}_{ij}^X \cdot \mathcal{Q}_{ij}^Y - \mathcal{P}_{ij}^Y \cdot \mathcal{Q}_{ij}^X, \\ \text{dot} = \mathcal{P}_{ij}^X \cdot \mathcal{Q}_{ij}^X + \mathcal{P}_{ij}^Y \cdot \mathcal{Q}_{ij}^Y. \end{cases} \quad (3.63)$$

By choosing the coordinate system where \mathbf{p}' is parallel to the x -axis, \mathbf{p} and \mathbf{p}'' are

free in the 2D space, and $\phi_{p_i, p'_i} = \phi_i - \phi'_i$, 2B t -matrices $t_i(p_i, p'_i, \phi'_i; \epsilon_i)$ can be obtained from the solution of 2D Lippmann-Schwinger integral equation as

$$t_i(p_i, p'_i, \phi_i; \epsilon_i) = v_i(p_i, p'_i, \phi_i) + \int_0^\infty dp''_i p''_i \int_0^{2\pi} d\phi''_i v_i(p_i, p''_i, \phi_{p_i, p''_i}) \frac{1}{\epsilon_i - \frac{p''_i{}^2}{2\mu_{jk}}} t_i(p''_i, p'_i, \phi''_i; \epsilon_i), \quad (3.64)$$

where 2B subsystem energy is defined by $\epsilon_i = E - \frac{q_i^2}{2\mu_{i,jk}}$.

We should mention, since RK potential, Eq. (3.7) is not well behaved when two momentum vectors p and p' have the same magnitude, and they are aligned, $q = 0$. To address this issue, instead of solving the non-PW equation (3.64), we first compute the PW potential from the non-PW potential using Eq. (3.6), then, we determine the PW t -matrices using the following relation, which establishes the connection between the PW and non-PW 2B t -matrices

$$t_m(p, p'; E) = V_m(p, p') + \int_0^\infty dp'' p'' V_m(p, p'') \frac{1}{E - \frac{p''^2}{2\mu}} t_m(p'', p'; E), \quad (3.65)$$

then we sum over the PW components to obtain the non-PW t -matrix using the following equation (ADHIKARI, 1986)

$$t(\mathbf{p}, \mathbf{p}'; E) = \frac{1}{2\pi} \sum_{m=0}^{\infty} \epsilon_m \cos(m\phi) t_m(p, p'; E), \quad \epsilon_m = \begin{cases} 1 & m = 0 \\ 2 & m \neq 0. \end{cases} \quad (3.66)$$

The three-body wave function can be obtained by adding Faddeev components in different subsystems as given in Eq. (3.57)

$$\Psi = \sum_{i=1}^3 \psi_i, \quad (3.67)$$

where

$$\langle \mathbf{p}_1 \mathbf{q}_1 | \Psi \rangle = \langle \mathbf{p}_1 \mathbf{q}_1 | \psi_1 \rangle + \langle \mathbf{p}_1 \mathbf{q}_1 | \psi_2 \rangle + \langle \mathbf{p}_1 \mathbf{q}_1 | \psi_3 \rangle. \quad (3.68)$$

Using the completeness relation Eq. (3.12), one has that

$$\langle \mathbf{p}_1 \mathbf{q}_1 | \psi_2 \rangle = \int d^2 p'_2 \int d^2 q'_2 \langle \mathbf{p}_1 \mathbf{q}_1 | \mathbf{p}'_2 \mathbf{q}'_2 \rangle \langle \mathbf{p}'_2 \mathbf{q}'_2 | \psi_2 \rangle, \quad (3.69)$$

$$\langle \mathbf{p}_1 \mathbf{q}_1 | \psi_3 \rangle = \int d^2 p'_3 \int d^2 q'_3 \langle \mathbf{p}_1 \mathbf{q}_1 | \mathbf{p}'_3 \mathbf{q}'_3 \rangle \langle \mathbf{p}'_3 \mathbf{q}'_3 | \psi_3 \rangle, \quad (3.70)$$

where

$$\langle \mathbf{p}_1 \mathbf{q}_1 | \mathbf{p}'_2 \mathbf{q}'_2 \rangle = \delta(\mathbf{p}'_2 - \mathbf{p}_2(\mathbf{p}_1, \mathbf{q}_1)) \delta(\mathbf{q}'_2 - \mathbf{q}_2(\mathbf{p}_1, \mathbf{q}_1)), \quad (3.71)$$

$$\langle \mathbf{p}_1 \mathbf{q}_1 | \mathbf{p}'_3 \mathbf{q}'_3 \rangle = \delta(\mathbf{p}'_3 - \mathbf{p}_3(\mathbf{p}_1, \mathbf{q}_1)) \delta(\mathbf{q}'_3 - \mathbf{q}_3(\mathbf{p}_1, \mathbf{q}_1)). \quad (3.72)$$

Hence Eq. (3.68) can be written as

$$\begin{aligned} \Psi(p_1, q_1, \phi_1) &= \psi_1(p_1, q_1, \phi_1) \\ &+ \psi_2(\mathcal{P}_{21}(\mathbf{p}_1, \mathbf{q}_1), \mathcal{Q}_{21}(\mathbf{p}_1, \mathbf{q}_1), \phi_{21}) \\ &+ \psi_3(\mathcal{P}_{31}(\mathbf{p}_1, \mathbf{q}_1), \mathcal{Q}_{31}(\mathbf{p}_1, \mathbf{q}_1), \phi_{31}). \end{aligned} \quad (3.73)$$

In the general case of three not identical particle, 3B wave function in momentum space is given By

$$\begin{aligned} \Psi(p_i, q_i, \phi_i) &= \psi_i(p_i, q_i, \phi_i) + \psi_j(\mathcal{P}_{ji}(p_i, q_i, \phi_i), \mathcal{Q}_{ji}(p_i, q_i, \phi_i), \phi_{ji}(p_i, q_i, \phi_i)) \\ &+ \psi_k(\mathcal{P}_{ki}(p_i, q_i, \phi_i), \mathcal{Q}_{ki}(p_i, q_i, \phi_i), \phi_{ki}(p_i, q_i, \phi_i)). \end{aligned} \quad (3.74)$$

This indicates that we need three-dimensional interpolation to evaluate the 3B wave function in two dimensions, which, in our study, carries on with cubic hermitian splines as given in ref. (HÜBER, 1997).

The wave function is normalized as

$$\begin{aligned} \langle \Psi | \Psi \rangle &= \sum_{i=1}^3 \langle \Psi | \psi_i \rangle = \\ &= 2\pi \int_0^\infty dp_i p_i \int_0^\infty dq_i q_i \int_0^{2\pi} d\phi_i \Psi^2(p_i, q_i, \phi_i) \\ &= 2\pi \int_0^\infty dp_i p_i \int_0^\infty dq_i q_i \int_0^{2\pi} d\phi_i \Psi(p_i, q_i, \phi_i) \\ &\times \left[\psi_i(p_i, q_i, \phi_i) \right. \\ &\quad + \psi_j(\mathcal{P}_{ji}(\mathbf{p}_i, \mathbf{q}_i), \mathcal{Q}_{ji}(\mathbf{p}_i, \mathbf{q}_i), \phi_{ji}) \\ &\quad \left. + \psi_k(\mathcal{P}_{ki}(\mathbf{p}_i, \mathbf{q}_i), \mathcal{Q}_{ki}(\mathbf{p}_i, \mathbf{q}_i), \phi_{ki}) \right] = 1. \end{aligned} \quad (3.75)$$

3.3.1 Expectation values and momentum distributions

By having the 3B wave function and Faddeev components, the expectation value of 3B Hamiltonian $\langle \Psi | H | \Psi \rangle$ can be obtained as

$$\langle \Psi | H | \Psi \rangle = \langle \Psi | H_0 | \Psi \rangle + \langle \Psi | V | \Psi \rangle = \sum_{m,n=1}^3 \langle \psi_m | H_0 | \psi_n \rangle + \sum_{m,n,i=1}^3 \langle \psi_m | V_i | \psi_n \rangle. \quad (3.76)$$

where

$$\begin{aligned}
\langle \Psi | H_0 | \Psi \rangle &\equiv \sum_{m,n=1}^3 \langle \psi_m | H_0 | \psi_n \rangle \\
&= 2\pi \int_0^\infty dp_m p_m \int_0^\infty dq_m q_m \left(\frac{p_m^2}{2\mu_{2B}} + \frac{q_m^2}{2\mu_{3B}} \right) \int_0^{2\pi} d\phi_m \Psi^2(p_m, q_m, \phi_m) \\
&= 2\pi \sum_{m,n=1}^3 \int_0^\infty dp_m p_m \int_0^\infty dq_m q_m \left(\frac{p_m^2}{2\mu_{2B}} + \frac{q_m^2}{2\mu_{3B}} \right) \\
&\quad \times \int_0^{2\pi} d\phi_m \psi_m(p_m, q_m, \phi_m) \\
&\quad \times \psi_n(\mathcal{P}_{nm}(p_m, q_m, \phi_m), \mathcal{Q}_{nm}(p_m, q_m, \phi_m), \phi_{nm}),
\end{aligned} \tag{3.77}$$

and

$$\begin{aligned}
\langle \Psi | V | \Psi \rangle &= \sum_{i=1}^3 \langle \Psi | V_i | \Psi \rangle \equiv \sum_{m,n,i=1}^3 \langle \psi_m | V_i | \psi_n \rangle \\
&= \sum_{i=1}^3 \int d^2 p_i \int d^2 q_i \int d^2 p'_i \int d^2 q'_i \langle \Psi | \mathbf{p}_i \mathbf{q}_i \rangle \langle \mathbf{p}_i \mathbf{q}_i | V_i | \mathbf{p}'_i \mathbf{q}'_i \rangle \langle \mathbf{p}'_i \mathbf{q}'_i | \Psi \rangle \\
&= \sum_{m,n,i=1}^3 \int d^2 p_i \int d^2 q_i \int d^2 p'_i \int d^2 q'_i \langle \psi_m | \mathbf{p}_i \mathbf{q}_i \rangle \langle \mathbf{p}_i \mathbf{q}_i | V_i | \mathbf{p}'_i \mathbf{q}'_i \rangle \langle \mathbf{p}'_i \mathbf{q}'_i | \psi_n \rangle \\
&= \sum_{i=1}^3 \int d^2 p_i \int d^2 q_i \int d^2 p'_i \Psi(\mathbf{p}_i, \mathbf{q}_i) V_i(\mathbf{p}_i, \mathbf{p}'_i) \Psi(\mathbf{p}'_i, \mathbf{q}_i) \\
&= \sum_{m,n,i=1}^3 \int d^2 p_i \int d^2 q_i \int d^2 p'_i \psi_m(\mathcal{P}_{mi}(\mathbf{p}_i, \mathbf{q}_i), \mathcal{Q}_{mi}(\mathbf{p}_i, \mathbf{q}_i)) V_i(\mathbf{p}_i, \mathbf{p}'_i) \\
&\quad \times \psi_n(\mathcal{P}_{ni}(\mathbf{p}'_i, \mathbf{q}_i), \mathcal{Q}_{ni}(\mathbf{p}'_i, \mathbf{q}_i)).
\end{aligned} \tag{3.78}$$

Using the coordinate system defined in Fig. 3.4 and the angle variables defined in Eq. (3.53), we can express Eq. (3.78) as follows

$$\begin{aligned}
\langle \Psi | V | \Psi \rangle &\equiv \sum_{m,n,i=1}^3 \langle \psi_m | V_i | \psi_n \rangle \\
&= 2\pi \sum_{i=1}^3 \int_0^\infty dp_i p_i \int_0^\infty dq_i q_i \int_0^{2\pi} d\phi_i \int_0^\infty dp'_i p'_i \int_0^{2\pi} d\phi'_i \\
&\quad \times \Psi(p_i, q_i, \phi_i) V_i(p_i, p'_i, \phi'_i) \Psi(p'_i, q_i, \phi_i - \phi'_i) \\
&= 2\pi \sum_{m,n,i=1}^3 \int_0^\infty dp_i p_i \int_0^\infty dq_i q_i \int_0^{2\pi} d\phi_i \int_0^\infty dp'_i p'_i \int_0^{2\pi} d\phi'_i \\
&\quad \times \psi_m(\mathcal{P}_{mi}(p_i, q_i, \phi_i), \mathcal{Q}_{mi}(p_i, q_i, \phi_i), \phi_{mi}(p_i, q_i, \phi_i)) \\
&\quad \times V_i(p_i, p'_i, \phi'_i) \\
&\quad \times \psi_n(\mathcal{P}_{ni}(p'_i, q_i, \phi'_i, \phi_i), \mathcal{Q}_{ni}(p'_i, q_i, \phi'_i, \phi_i), \phi_{ni}(p'_i, q_i, \phi'_i, \phi_i)).
\end{aligned} \tag{3.79}$$

To validate our numerical methods and formalism, we will later compare the expectation value of the Hamiltonian, calculated using Eq. (3.76), with the eigenvalue obtained from the Faddeev equation.

In practical applications, direct access to the wave function is often unavailable, and only specific matrix elements are accessible (ELSTER *et al.*, 1999). One such example, which can be approximated through electron scattering, is the momentum distribution. In our study, this momentum distribution is expressed as

$$N(p_i) = 2\pi p_i \int_0^\infty dq_i q_i \int_0^{2\pi} d\phi_i \Psi^2(p_i, q_i, \phi_i), \quad (3.80)$$

$$N(q_i) = 2\pi q_i \int_0^\infty dp_i p_i \int_0^{2\pi} d\phi_i \Psi^2(p_i, q_i, \phi_i). \quad (3.81)$$

3.3.2 Verification of the 3B Schrödinger equation in 2D

A rigorous test of the accuracy of our numerical methods and the quality of the wave function is to check whether the Schrödinger equation is satisfied at each mesh point, as highlighted in Ref. (ELSTER *et al.*, 1999). The Schrödinger equation for the bound state of three particles is given by

$$E_t |\Psi\rangle = H |\Psi\rangle = (H_0 + V_i + V_j + V_k) |\Psi\rangle. \quad (3.82)$$

Using the three different sets of Jacobi momenta in momentum space, we obtain

$$\begin{aligned} E_t \Psi(\mathbf{p}_i, \mathbf{q}_i) &= \left[\frac{p_i^2}{2\mu_{jk}} + \frac{q_i^2}{2\mu_{i,jk}} \right] \Psi(\mathbf{p}_i, \mathbf{q}_i) \\ &+ \int d^2 p'_i V_i(\mathbf{p}_i, \mathbf{p}'_i) \Psi(\mathbf{p}'_i, \mathbf{q}_i) \\ &+ \int d^2 p'_j V_j(\mathcal{P}_{ji}(\mathbf{p}_i, \mathbf{q}_i), \mathbf{p}'_j) \Psi(\mathbf{p}'_j, \mathcal{Q}_{ji}(\mathbf{p}_i, \mathbf{q}_i)) \\ &+ \int d^2 p'_k V_k(\mathcal{P}_{ki}(\mathbf{p}_i, \mathbf{q}_i), \mathbf{p}'_k) \Psi(\mathbf{p}'_k, \mathcal{Q}_{ki}(\mathbf{p}_i, \mathbf{q}_i)). \end{aligned} \quad (3.83)$$

By considering the coordinate system illustrated in Fig. 3.4, where \mathbf{p}_1 is parallel to the x -axis, Eq. (3.83) can be written as

$$\begin{aligned} E_t \Psi(p_i, q_i, \phi_i) &= \left[\frac{p_i^2}{2\mu_{jk}} + \frac{q_i^2}{2\mu_{i,jk}} \right] \Psi(p_i, q_i, \phi_i) \\ &+ \int_0^\infty dp'_i p'_i \int_0^{2\pi} d\phi'_i V_i(p_i, p'_i, \phi'_i) \Psi(p'_i, q_i, \phi_i - \phi'_i) \\ &+ \int_0^\infty dp'_j p'_j \int_0^{2\pi} d\phi'_j V_j(\mathcal{P}_{ji}(p_i, q_i, \phi_i), p'_j, \phi_{\mathcal{P}_{ji}, p'_j}) \Psi(p'_j, \mathcal{Q}_{ji}(p_i, q_i, \phi_i), \phi_{\mathcal{Q}_{ji}, p'_j}) \\ &+ \int_0^\infty dp'_k p'_k \int_0^{2\pi} d\phi'_k V_k(\mathcal{P}_{ki}(p_i, q_i, \phi_i), p'_k, \phi_{\mathcal{P}_{ki}, p'_k}) \end{aligned}$$

$$\times \Psi(p'_k, \mathcal{Q}_{ki}(p_i, q_i, \phi_i), \phi_{\mathcal{Q}_{ki}, p'_k}). \quad (3.84)$$

3.4 Short Range Yamaguchi potential

To test the formulation of the coupled Faddeev integral equations (3.57) and to validate our numerical solution, we first utilize the one-term separable potential with Yamaguchi-type form factors given as

$$\langle \mathbf{p} | V | \mathbf{p}' \rangle = -\lambda g(p)g(p'); \quad g(p) = \frac{1}{(\beta^2 + p^2)^m}. \quad (3.85)$$

We are providing the numerical results for the binding energies and wave functions of 3B systems using two different combinations of interactions. The first combination involves three attractive potentials, while the second combination consists of two attractive and one repulsive Yamaguchi-type potentials. These calculations are conducted considering three particles with identical masses. To avoid any confusion, let us clarify the notation used. The 3B binding energy is represented as E_{3B} , which refers to the eigenvalue of the 3B Hamiltonian. On the other hand, the trion binding energy is denoted as E_t , representing the difference between the binding energies of the 2B and 3B systems. In Table 3.4, we present the binding energies of a 3B system obtained by solving the three coupled Faddeev integral equations (3.57). The system consists of three identical particles with a mass of 1, interacting through attractive Yamaguchi potentials. The input 2B t -matrices are derived from the s -wave interactions. We have calculated the ratios of the 3B and 2B binding energies for various potential strengths, λ , and form factor powers (m), and our results exhibit excellent agreement with the corresponding findings from Ref. (ADHIKARI *et al.*, 1988), where they solved a single equation.

TABLE 3.4 – Dimer and trimer binding energies E_{2B} and E_{3B} calculated for three attractive Yamaguchi-type potentials with form factor parameter $\beta = 1$ and different powers m . The potential strength λ is fitted to reproduce the desired 2B binding energy E_{2B} . The ratio of 3B and 2B binding energies E_{3B}/E_{2B} are compared with corresponding results from Ref. (ADHIKARI *et al.*, 1988). The calculations are done with $\hbar c = \text{mass} = 1$.

λ	E_2	E_3/E_2	E_3/E_2 (ADHIKARI <i>et al.</i> , 1988)
$m = 1$			
0.0602	-0.0019	9.21	9.21
0.0863	-0.0100	6.83	6.83
0.1838	-0.1000	4.58	4.58
$m = 2$			
0.0801	-0.0032	7.30	7.30
0.1400	-0.0211	5.14	5.14
$m = 4$			
0.0481	-0.0001	11.54	11.53
0.0731	-0.0010	7.91	7.91
0.1861	-0.0200	4.55	4.55
$m = 10$			
0.0561	0.0001	10.05	10.05
0.0923	0.0010	6.61	6.61
0.1562	0.0050	4.89	4.99

Table 3.4 confirms the validity and accuracy of the numerical method used to solve the three coupled Faddeev equations.

Now, we can proceed to make one attractive interaction repulsive, bringing us one step closer to a realistic system. In Table 3.5, we present the expectation values, denoted as EV, and energy (E_{3B}) obtained from three attractive Yamaguchi potentials (3A) in the first column. In the second column, we present the results obtained when two interactions are attractive and one is repulsive (2A+R), obtained by solving the coupled Faddeev integral equations.

TABLE 3.5 – Expectation values (EV) of 3B free Hamiltonian $\langle H_0 \rangle$, pair interactions $\langle V_i \rangle$, total 2B interactions $\langle V \rangle$, 3B Hamiltonian $\langle H \rangle$, and eigenvalue E_{3B} calculated for Yamaguchi-type potentials (three attractive (3A) in the second column, two attractive plus one repulsive interaction (2A+R) in the third column), given in Eq. (3.85) with form factor parameters $\beta = m = 1$, and the potential strength λ that reproduces dimer binding energy $E_{2B} = -0.1$. The calculations are done with $\hbar c = \text{mass} = 1$.

EV	3A	2A + R
$\langle H_0 \rangle$	+0.46887	+0.15756
$\langle V_1 \rangle$	-0.30904	+0.03260
$\langle V_2 \rangle$	-0.30904	-0.15526
$\langle V_3 \rangle$	-0.30904	-0.15523
$\langle V \rangle$	-0.92712	-0.27789
$\langle H \rangle$	-0.45825	-0.12033
E_{3B}	-0.45824	-0.12034
$\left \frac{(\langle H \rangle - E_{3B})}{E_{3B}} \right \times 100\%$	+0.00218	+0.00831

Table 3.5 reveals some interesting qualitative observations. Notably, when the sign of the potential V_1 is reversed and becomes repulsive, the state expands due to a significant reduction in the energy splitting between the 2B and 3B states. This can be observed through the decrease in the quantity $|E_{3B} - E_{2B}| = 0.3582$ to 0.0203, indicating a diminished energy difference between the 3B and 2B systems. As a result, the kinetic energy is significantly decreased to approximately one-third of its value when only attractive potentials are present. The repulsive interaction depletes the wave function when particles 2 and 3 are within the range of the potential, leading to a negative expectation value $\langle V_1 \rangle$. In comparison to the attractive case, this value is reduced to one-tenth of its magnitude. Additionally, the expectation values $\langle V_2 \rangle$ and $\langle V_3 \rangle$ are reduced by half. As a result of our mesh point selection, the equality $\langle V_2 \rangle = \langle V_3 \rangle$ holds with a precision of 0.02%, leading to an error of approximately 0.008% in the computation of $\langle H \rangle$. This error is four times larger than the error observed in the attractive case.

3.4.1 Yamaguchi trion clusterization

Figs. 3.5 and 3.6, taken from (MOHSENI *et al.*, 2023), depict the magnitude of the 3B wave function in two scenarios involving Yamaguchi interactions. The left panel displays the wave function's dependence on the magnitudes of Jacobi momenta p_1 and q_1 , with the angle between them fixed at $\phi_1 = 0$. To assess the numerical accuracy of our calculations, we utilize the ratio $|(E\Psi - H\Psi)/(E\Psi)|$ calculated with Eq. (3.84), which is depicted in the right panels of Figs. 3.5 and 3.6 for the 3A and 2A+R cases, respectively.

In the first case, illustrated in Fig. 3.5, we observe the eigenstate of the 3B system characterized by three attractive potentials (3A). The plot reveals a somewhat symmetric

momentum distribution, which can be attributed to the identical masses and bosonic symmetry of the system.

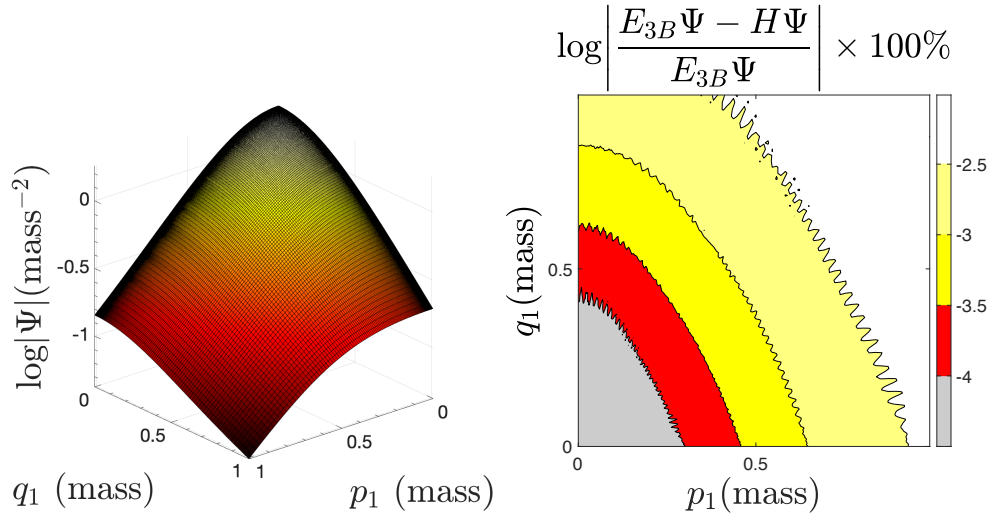


FIGURE 3.5 – The left panel displays a 3D plot of the 3B wave function, specifically for three attractive Yamaguchi-type potentials (3A). The right panel shows the relative percentage error. Both plots are generated for the angle $\phi_1 = 0$. The results are obtained using form factor parameters $\beta = m = 1$ and a potential strength λ chosen to reproduce a 2B binding energy of $E_{2B} = -0.1$. The calculations are performed with $\hbar c = \text{mass} = 1$.

On the other hand, the second case displayed in Fig. 3.6 presents the wave function for a weakly bound state, which emerges from one repulsive potential V_1 and two attractive potentials (2A+R). It is clear the introduction of the repulsive potential leads to the formation of a node line in the wave function. Additionally, the wave function becomes more sharply peaked around the origin, primarily due to the small binding energy (see Table 3.5).

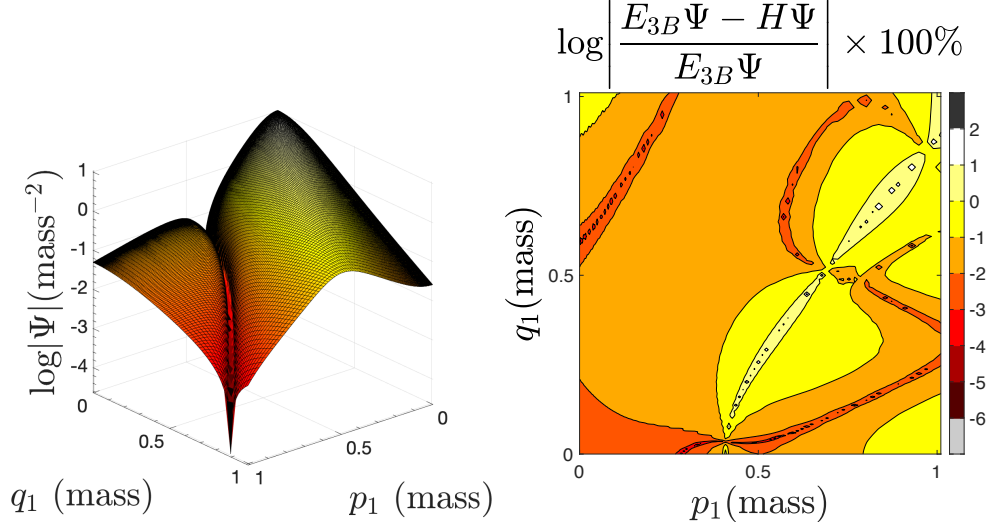


FIGURE 3.6 – The left panel displays a 3D plot of the 3B wave function, specifically for one repulsive potential (V_1) and two attractive Yamaguchi-type potentials ($2A + R$). The right panel shows the relative error. Both plots are generated for the angle $\phi_1 = 0$. The results are obtained using form factor parameters $\beta = m = 1$ and a potential strength λ chosen to reproduce a 2B binding energy of $E_{2B} = -0.1$. The calculations are performed with $\hbar c = \text{mass} = 1$.

As anticipated, the 3A case exhibits satisfactory numerical accuracy, while the $2A+R$ case demonstrates accurate results, particularly outside the node region. As expected, the largest errors for the $2A+R$ case in the right panel of Fig. 3.6 coincide with the node of the 3B wave function. Furthermore, in Fig. 3.7 which is taken from (MOHSENI *et al.*, 2023), we present contour plots of the $2A+R$ model in the $(p_1 \times q_1)$ -plane for $\phi_1 = 0$ (left panel) and in the $(p_2 \times q_2)$ -plane for $\phi_2 = 0$ (right panel).

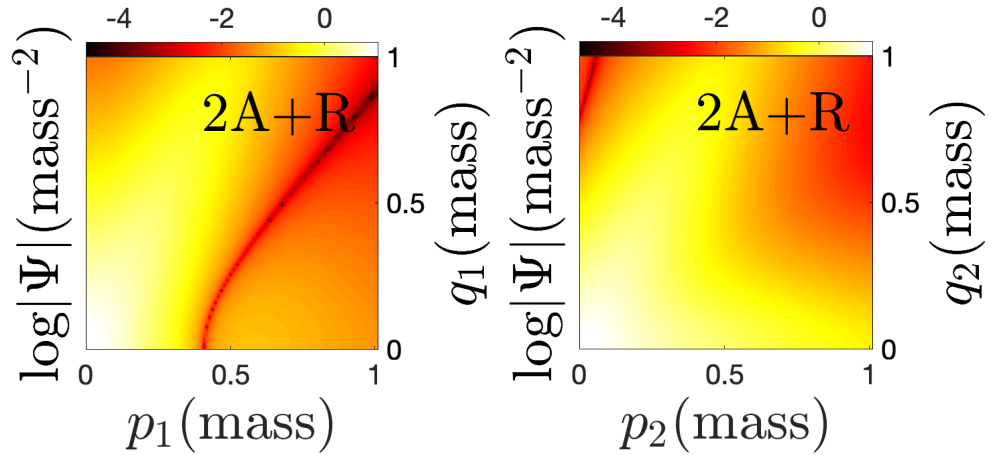


FIGURE 3.7 – The contour plot illustrates the 3B wave function calculated for three Yamaguchi-type potentials, where V_1 is repulsive while V_2 and V_3 are attractive. The plot represents the wave function's behavior as the magnitude of Jacobi momenta varies. The angles ϕ_1 and ϕ_2 are fixed at 0. The results are obtained using form factor parameters $\beta = m = 1$ and a potential strength λ chosen to reproduce a 2B binding energy of $E_{2B} = -0.1$. The calculations are conducted assuming $\hbar c = \text{mass} = 1$.

The node line, which is visible in the left panel of Fig. 3.7, is similar to the left panel

in Fig. 3.6. This node line arises from the cancellation between ψ_1 and $\psi_2 + \psi_3$ as a result of the reversed sign of ψ_1 compared to ψ_2 and ψ_3 originating from the repulsive potential V_1 . Consequently,

$$\psi_1(p_1, q_1, 0) = -\psi_2(p_2, q_2, \phi_2) - \psi_3(p_3, q_3, \phi_3), \quad (3.86)$$

where $\phi_{2,3} = 0$, and these relations implicitly define the node line. The node line can be understood by rewriting the momenta labeled by 2 and 3 according to

$$\mathbf{p}_2 = -\frac{1}{2}\mathbf{p}_1 - \frac{3}{4}\mathbf{q}_1, \quad \mathbf{q}_2 = \mathbf{p}_1 - \frac{1}{2}\mathbf{q}_1, \quad (3.87a)$$

$$\mathbf{p}_3 = -\frac{1}{2}\mathbf{p}_1 + \frac{3}{4}\mathbf{q}_1, \quad \mathbf{q}_3 = -\mathbf{p}_1 - \frac{1}{2}\mathbf{q}_1. \quad (3.87b)$$

The node line is barely seen in the right panel of Fig. 3.7, with the momenta expressed in terms of p_2 and q_2 with $\phi_2 = 0$.

Another property of the wave function is the well-defined maximum seen in both Figs. 3.6 and 3.7, which can be qualitatively understood by a semiclassical picture. In this dominant configuration, the electron, and hole (referred to as particle 1) are very close and they are “moving together”. This relationship between the momenta p_1 and q_1 provides an interpretation for the observed pattern of the maximum in the left panel of Fig. 3.6 and the whitish-yellow color region in Fig. 3.7, specifically along the line $p_1 \propto q_1$ for the 2A+R model. In other words, the relative velocity between the two electrons is the same as the velocity between the widely separated electron and the hole, which forms the strongly bound exciton. This correspondence becomes particularly evident when $\phi_1 = 0$. Moreover, this interpretation also explains the pattern of the maximum in the wave function, featuring two branches observed in the right panel of Fig. 3.6 in the $(p_2 \times q_2)$ -plane. It is important to highlight the practical significance of such plots, as they provide valuable insights into the regions where the wave function exhibits significant amplitude. This information is crucial for accurately distributing mesh points and obtaining precise solutions to the Faddeev equations.

It is important to highlight that each Faddeev component of the wave function in our system carries the asymptotic behavior of the wave function in each pairwise interaction channel (FADDEEV, 1960). The clustering of the wave function can be illustrated by the following scheme: $\psi_2 \sim [3(e)1(h)]-2(e)$ and $\psi_3 \sim [1(h)2(e)]-3(e)$. These two configurations are expected to be the dominant ones, with the electrons in a spin singlet state or an antisymmetric combination of different valley states. This is supported by the observations in Table 3.6, where the Faddeev component ψ_1 is significantly suppressed compared to ψ_2 and ψ_3 , as indicated by the one order of magnitude difference in their inner products.

TABLE 3.6 – The inner product of the Faddeev components $\langle \psi_i | \psi_j \rangle$ and their contribution to the normalization of the 3B wave function $|\Psi\rangle$.

	$j = 1$	$j = 2$	$j = 3$
$i = 1$	0.0560	-0.1047	-0.1047
$i = 2$	-0.1047	0.4400	0.2413
$i = 3$	-0.1047	0.2413	0.4403

Let us now turn our attention to Fig. 3.7 (right panel) and examine the modulus of the wave function, $|\Psi|$, in the $(p_2 \times q_2)$ -plane. We can identify two branches where $|\Psi|$ is larger: one for small q_2 and a diagonal one. The lower branch corresponds to the contribution of ψ_2 for $q_2 \approx 0$, which represents the relative momentum of the weakly bound spectator particle 2(e) with respect to the strongly correlated pair of particles 1 and 3.

The range of values observed for p_2 can be attributed to the small size of the strongly bound exciton in the $[3(e)1(h)]$ —2(e) configuration. On the other hand, the diagonal branch characterized by $p_2 \propto q_2$, where the probability density of momentum is enhanced, corresponds to the dominance of ψ_3 associated with the $[1(h)2(e)]$ —3(e) configuration. In this configuration, electron 2 moves together with hole 1, reflecting the strong binding of the exciton, while electron 3 acts as a spectator.

3.5 Rytova-Keldysh potential

Expanding on the insights gained from the 2D calculations with 2A+R Yamaguchi potential model, we explore the binding energy and structure of trions in the MoS₂ layer using the RK potential described by Eq. (3.7) with parameters listed in Table 3.1.

The previous example discussed in Section 3.4 has already provided insights into the accuracy of our numerical solutions for the Faddeev equations. We observed that the accuracy decreases in the case of the 2A+R Yamaguchi potential compared to the attractive 3A case (see Table 3.5). This behavior was expected due to the small binding energy of trions and the presence of a node in the wave function. Furthermore, the numerical solution becomes more challenging when considering the RK potential, which has a longer range compared to the Yamaguchi model. This is due to the competition between attraction and repulsion of equal strength. To address this numerical challenge, we introduce two different regulators (DELTUVA *et al.*, 2005) to screen the repulsive RK potential between the two electrons, namely

$$V(q) \rightarrow (1 - e^{-l_0 q})V_{ee}(q) \quad \text{or} \quad e^{-l_0 q}V_{ee}(q). \quad (3.88)$$

In the first case, $V(q) \rightarrow (1 - e^{-l_0 q})$, the RK potential is damped at small momentum or large distance, while in the second case, $V(q) \rightarrow e^{-l_0 q} V_{ee}(q)$, it is damped at large momentum or small distance. Fig. 3.8 illustrates quantitatively both screenings, Eq. (3.88), with $l_0 = 10 \text{ \AA}$.

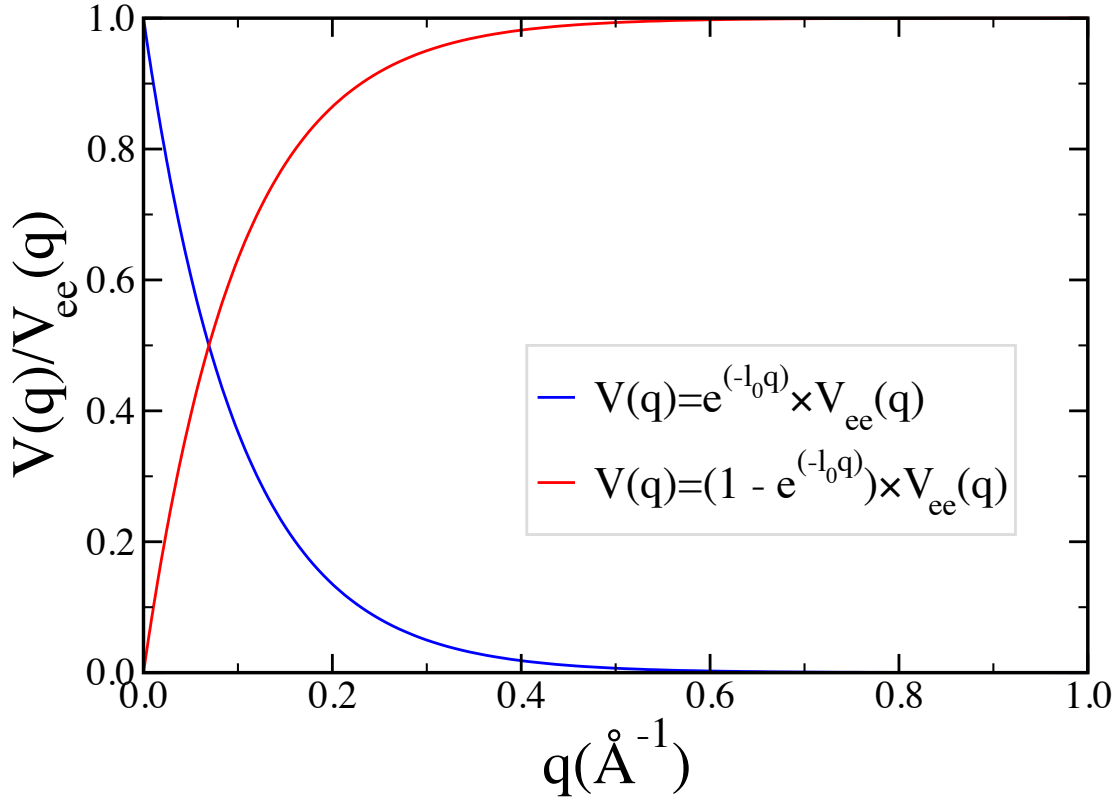


FIGURE 3.8 – The screening function $V(q)/V_{ee}(q)$ as a function of the momentum transfer q for (blue curve) $V(q) \rightarrow e^{-l_0 q} V_{ee}(q)$ and (red curve) $V(q) \rightarrow (1 - e^{-l_0 q}) V_{ee}(q)$ with screening parameter $l_0 = 10 \text{ \AA}$. Figure is taken from (MOHSENI *et al.*, 2023).

In our calculations, the results for the trion binding energy will be obtained by extrapolating to $l_0^{-1} = 0$ and $l_0 = 0$ for the first and second screening scheme, respectively. Prior to that, we present the expectation values of the RK potential screened at low momenta for $l_0 = 100 \text{ \AA}$ in Table 3.7 in the scheme $V_1(q) \rightarrow (1 - e^{-l_0 q}) V_{ee}(q)$.

TABLE 3.7 – Expectation values (EV) in meV of the 3B free Hamiltonian $\langle H_0 \rangle$, pair interactions $\langle V_i \rangle$, total 2B interactions $\langle V \rangle$, 3B Hamiltonian $\langle H \rangle$, and binding energy E_{3B} in meV calculated for RK potentials (two attractive plus one repulsive interaction (2A+R)) given in Eq. (3.7) with screening parameter $l_0 = 100 \text{ \AA}$ in the scheme $V_1(q) \rightarrow (1 - e^{-l_0 q})V_{ee}(q)$.

EV	2A + R
$\langle H_0 \rangle$	+247.66
$\langle V_1 \rangle$	+443.39
$\langle V_2 \rangle$	-825.90
$\langle V_3 \rangle$	-825.76
$\langle V \rangle$	-1208.27
$\langle H \rangle$	-960.61
E_{3B}	-960.58
$\left \frac{(\langle H \rangle - E_{3B})}{E_{3B}} \right \times 100\%$	+0.00312

The contribution of the spectator electron external to the exciton, leads to a slightly larger expectation value of the kinetic energy compared to the exciton case. In Table E.2, the kinetic energy for the exciton is found to be 214.64 meV, whereas for the trion, it is 247.66 meV. Furthermore, the expectation values of the attractive potentials V_2 and V_3 for the trion are slightly smaller in magnitude compared to the exciton, which has an expectation value of -967.96 meV. In the trion, the magnitude of the potential energy for the repulsive potential is approximately half that of the attractive potentials. This can be understood as the electrons should be more separated than the relative distance within the strongly bound electron-hole pair. It is worth noting that the trion and exciton have a splitting of 207.29 meV, indicating that the trion is weakly bound compared to the exciton. Table 3.7 demonstrates the high accuracy of our solution by comparing the expectation value of the Hamiltonian $\langle H \rangle$ and the energy E_{3B} obtained from solving the coupled Faddeev integral equations. The deviation between these two values is remarkably small, with only a 0.003% difference.

Table 3.8 presents the numerical results for the 3B energy eigenvalues obtained by solving the coupled Faddeev integral Eqs. (3.57). The calculations are performed for the RK potential given in Eq. (3.7), considering two different screening schemes for electron-electron interactions, as illustrated in Fig. 3.8 and described in Eq. (3.88). The results are shown for various values of the screening parameter l_0 , as a function of the number of mesh points for Jacobi momenta $N_p = N_q$. As one can see, even with a high number of mesh points, convergence is not achieved. However, the results exhibit an accurate linear behavior, allowing us to fit a linear function with high accuracy. last row of the Table 3.8, shows the linear extrapolated result to $N_p, N_q \rightarrow \infty$.

TABLE 3.8 – The convergence of trion ground state binding energies (in meV) as a function of the number of mesh points for Jacobi momenta $N_p = N_q$ obtained for different values of screening parameter l_0 for screening electron-electron interactions $V(q) \rightarrow e^{-l_0 q} V_{ee}(q)$ (upper panel) and $V(q) \rightarrow (1 - e^{-l_0 q}) V_{ee}(q)$ (lower panel). The last row of each panel shows the linear extrapolation of trion energy eigenvalues to an infinite number of mesh points.

$N_p = N_q$	$l_0(\text{\AA})$									
	25	20	17	15	13	11	10	9	8	7
200	-1275.6	-1231.1	-1197.7	-1171.8	-1142.5	-1109.0	-1090.5	-1070.8	-1049.8	-1027.6
250	-1258.7	-1214.2	-1180.8	-1155.0	-1125.6	-1092.2	-1073.7	-1054.1	-1033.0	-1011.5
300	-1248.3	-1203.8	-1170.4	-1144.6	-1115.3	-1081.8	-1063.4	-1043.7	-1022.8	-1000.7
350	-1241.3	-1196.8	-1163.5	-1137.7	-1108.3	-1074.9	-1056.5	-1036.8	-1016.0	-993.7
$N_p, N_q \rightarrow \infty$	-1195.1	-1150.6	-1117.3	-1091.5	-1062.2	-1028.9	-1010.6	-991.0	-970.3	-948.0

$N_p = N_q$	$l_0(\text{\AA})$									
	1	5	10	15	20	30	50	70	90	100
200	-1588.7	-1447.8	-1346.2	-1279.4	-1231.0	-1165.0	-1090.8	-1049.3	-1023.3	-1014.8
250	-1558.6	-1418.8	-1318.1	-1251.8	-1203.8	-1138.2	-1064.7	-1023.6	-998.3	-988.8
300	-1540.0	-1400.9	-1300.7	-1234.8	-1187.0	-1121.7	-1048.4	-1007.1	-981.1	-972.3
350	-1527.5	-1388.9	-1289.1	-1223.3	-1175.7	-1110.6	-1037.5	-996.3	-970.0	-960.6
$N_p, N_q \rightarrow \infty$	-1444.8	-1309.6	-1212.0	-1147.7	-1101.2	-1037.3	-965.6	-924.8	-898.2	-888.0

The extrapolated results obtained from Table 3.8 are summarized in Table 3.9 for the two implemented forms of screening in the RK electron-electron repulsive potential.

TABLE 3.9 – Trion ground state binding energies (E_{3B}) for different screening parameter l_0 obtained from two screening schemes shown in Fig. 3.8 and given in Eq. (3.88).

$V(q) \rightarrow e^{-l_0 q} V_{ee}(q)$		$V(q) \rightarrow (1 - e^{-l_0 q}) V_{ee}(q)$	
$l_0(\text{\AA})$	$E_{3B}(\text{meV})$	$l_0(\text{\AA})$	$E_{3B}(\text{meV})$
25	-1195.1	1	-1444.8
20	-1150.6	5	-1309.6
17	-1117.3	10	-1212.0
15	-1091.5	15	-1147.7
13	-1062.2	20	-1101.2
11	-1028.9	30	-1037.3
10	-1010.6	50	-965.6
9	-991.0	70	-924.8
8	-970.3	90	-898.2
7	-948.0	100	-888.0

The extrapolation of trion energies, as shown in Fig. 3.9, is presented in two forms: (1) as a function of l_0^{-1} in the left panel, representing short-distance screening, and (2) as a function of l_0 in the right panel, representing long-distance screening. The results demonstrate a clear linear trend, enabling an accurate extrapolation of the trion binding energy. Extrapolating the binding energies using the linear fits obtained from the first

screening (left panel) in the range of 70 to 100 \AA^{-1} yields a trion binding energy of -49.6 meV. Similarly, extrapolating the second screening (right panel) in the range of 7 to 10 \AA results in a trion binding energy of -49.4 meV. These extrapolated values are consistent with previous experimental findings reported in Refs. (LIN *et al.*, 2014; LIN *et al.*, 2019).

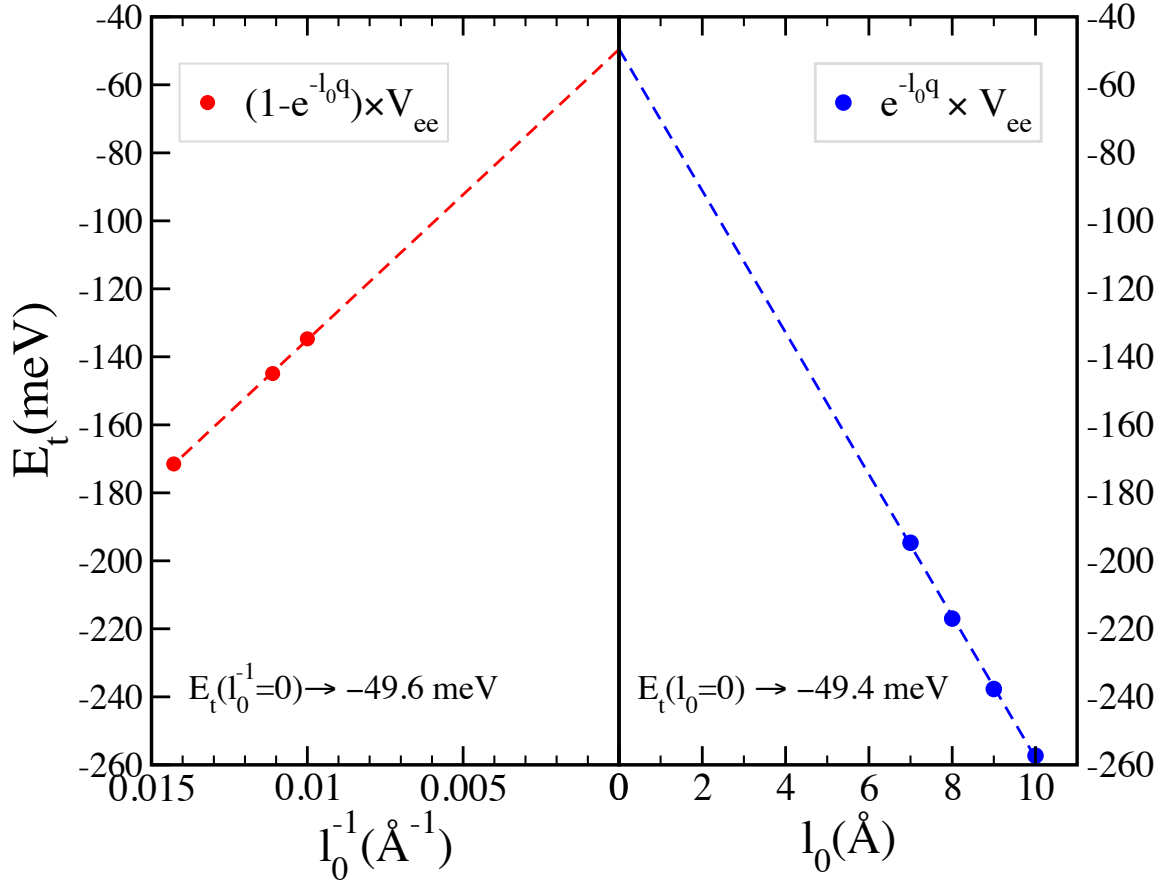


FIGURE 3.9 – Extraction of trion binding energy E_t with a linear extrapolation on energies obtained from two screenings (see Table 3.9) at the physical points $l_0^{-1} = 0 \text{ \AA}^{-1}$ (left panel) and $l_0 = 0 \text{ \AA}$ (right panel). Figure is taken from (MOHSENI *et al.*, 2023).

It is important to note that in excitonic physics, the interaction between electrons and holes consists of both an attractive screened interaction and a repulsive exchange interaction. However, for strongly bound excitons, the exchange interaction typically makes a small contribution, as demonstrated in Ref. (WANG *et al.*, 2018). In the case of the trion, in addition to the electron-hole interaction, there is also an exchange term for the electron-electron interaction. However, due to the weak binding of the electron in the trion to the exciton and the small momenta involved compared to the reciprocal vector, the exchange terms are expected to have a lesser impact on determining the trion binding energy compared to their contribution to the exciton energy, which is already small in this scenario. Nevertheless, the Faddeev approach employed for solving the Hamiltonian eigenvalue problem in momentum space can handle non-local exchange terms in a similar

manner as done for the exciton Hamiltonian (SCHMIDT *et al.*, 2003), although this aspect remains for future investigation.

3.5.1 Rytova-Keldysh trion clusterization

The trion structure is examined using the screened electron-electron potential $V_1(q) \rightarrow (1 - e^{-l_0 q})V_{ee}(q)$ with $l_0 = 100 \text{ \AA}$. We specifically chose this model because the electron-electron potential is screened at large distances, which combines with the natural screening of the exciton interaction with the spectator electron. These two effects act in a coherent manner, resulting in the trion being strongly bound with an energy of -207.3 meV compared to the extrapolated value of -49.6 meV . It is important to note that the small trion binding energy, relative to the exciton, will be further emphasized as we approach the converged trion calculation with the RK potential. Our analysis is based on the screened electron-electron potential, which is currently a limitation of our numerical method when applied to the repulsive RK potential. However, despite this limitation, we examine the structure of the trion within the screened model to gain insights and compare it with the 2A+R Yamaguchi model. It is important to highlight that we are specifically studying a negatively charged trion consisting of one hole and two electrons, where the two electrons have the same effective mass. In TMDs, electrons typically have the same mass if they belong to the same band or minimum point. This holds true for two scenarios: 1) intravalley electrons with the same spin or 2) intervalley electrons with opposite spins. However, in our work, we neglect the spin-orbit coupling in the conduction band, which allows us to consider the electrons to have the same mass. The overlaps between the Faddeev components of the wave function are given in Table 3.10.

TABLE 3.10 – The inner product of the Faddeev components $\langle \psi_i | \psi_j \rangle$ and their contributions in the normalization of the 3B wave function $|\Psi\rangle$ obtained for the screening parameter $l_0 = 100 \text{ \AA}$ in the screening scheme $V_1(q) \rightarrow (1 - e^{-l_0 q})V_{ee}(q)$.

	$j = 1$	$j = 2$	$j = 3$
$i = 1$	0.1772	-0.2808	-0.2806
$i = 2$	-0.2808	0.5197	0.4534
$i = 3$	-0.2806	0.4534	0.5190

Consistently, the relative normalization of the component $\langle \psi_1 | \psi_1 \rangle$, where the hole serves as the spectator particle in the interacting electron-electron pair, is nearly three times smaller than $\langle \psi_2 | \psi_2 \rangle = \langle \psi_3 | \psi_3 \rangle$. This observation aligns with our findings in the 2A+R Yamaguchi model (see Table 3.6), where we also observe a significantly reduced overlap $\langle \psi_1 | \psi_1 \rangle$ compared to the overall normalization of the wave function. The configuration in which the hole acts as a spectator in the interacting electron-electron pair

is suppressed, indicating a preference for clusterization of the wave function where the electron and hole are in close proximity, primarily forming the exciton, with an additional distant spectator electron. Furthermore, we observe that $\langle \psi_1 | \psi_{2,3} \rangle$ has an opposite sign compared to $\langle \psi_2 | \psi_3 \rangle$, which reflects the repulsive interaction between the electrons. When comparing these findings with the overlaps of the 2A+R Yamaguchi potentials presented in Table 3.6, we can see that the suppression of ψ_1 is much more dramatic for the former model. The reason for this difference can be attributed to two factors: (i) the relatively smaller gap between the binding energies of the 3B and 2B states in the Yamaguchi model, which is $(E_{3B} - E_{2B})/E_{3B} = 0.169$, compared to 0.216 in the RK screened model, and (ii) the short-range nature of the Yamaguchi potential, whereas the RK potential exhibits a long-range tail. However, it should be noted that the RK trion possesses a significantly smaller 3B binding energy compared to the corresponding binding energy obtained for the screened RK electron-electron potential. Namely, the extrapolated value of -802.9 meV in Fig. 3.9 yields $(E_{3B} - E_{2B})/E_{3B} = 0.061$. Consequently, we expect a more evident clusterization of the exciton within the trion. Fig. 3.10 displays the results for the Faddeev components $\psi_1(p_1, q_1, \phi_1 = 0)$ (top panel) and $\psi_2(p_2, q_2, \phi_2 = 0) = \psi_3(p_3, q_3, \phi_3 = 0)$ (bottom panel), where the momenta are defined in terms of p_1 and q_1 . The calculations were performed for different values of l_0 , specifically $l_0 = 1, 30, 50, 70, 100 \text{ \AA}$ (from left to right panels), with the electron-electron screened potential given by $V_1(q) \rightarrow (1 - e^{-l_0 q})V_{ee}(q)$.

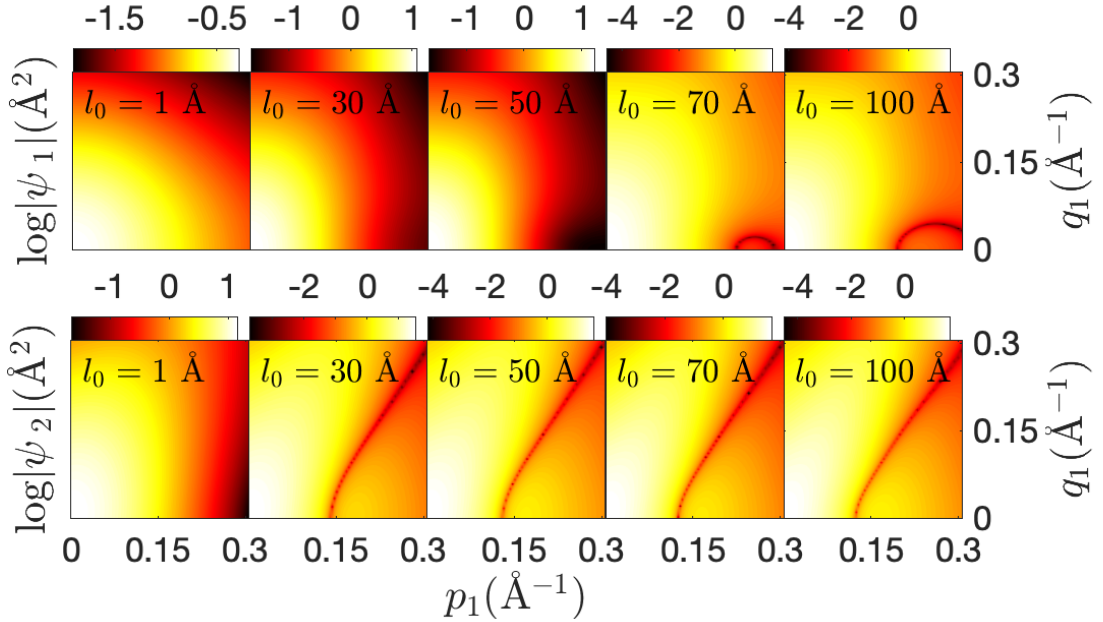


FIGURE 3.10 – The evolution of the Faddeev components (top panels) $\psi_1(p_1, q_1, \phi_1 = 0)$ and (bottom panels) $\psi_2(p_1, q_1, \phi_1 = 0)$ obtained for the screening parameter $l_0 = 1, 30, 50, 70, 100 \text{ \AA}$ in the screening scheme $V_1(q) \rightarrow (1 - e^{-l_0 q})V_{ee}(q)$. Figure is taken from (MOHSENI *et al.*, 2023).

From Fig. 3.10, it is evident that as the screening parameter l_0 increases, the trion binding weakens, and the electrons experience a repulsive force, causing them to move away from each other. Simultaneously, one of the electrons remains in close proximity to

the hole, resulting in the dominant configurations $\psi_2 \sim [3(e)1(h)]-2(e)$ and $\psi_3 \sim [1(h)2(e)]-3(e)$ (the square brackets represent the exciton).

On the other hand, $\psi_1(p_1, q_1, 0)$ primarily reflects the short-range repulsion, causing the spreading of q_1 and p_1 towards larger values, as depicted in the top panels of Fig. 3.10. For small values of l_0 , where the long-range tail of the repulsive potential is effectively suppressed, we observe that the momentum distribution of $\psi_1(p_1, q_1, 0)$ exhibits larger trion bindings with a tendency towards symmetry in p_1 and q_1 . This implies a geometric configuration where the hole is equally separated from the two electrons, disfavoring the cluster structure against a more symmetrical configuration, schematically like e-h-e. As the value of l_0 increases, signifying increased repulsion and a more pronounced short-range interaction, the node in ψ_1 appears at larger values of p_1 . The bottom panel of Fig. 3.10 illustrates the evolution of $\psi_2(p_2(\mathbf{p}_1, \mathbf{q}_1), q_2(\mathbf{p}_1, \mathbf{q}_1), \phi_2 = 0)$ for $\phi_1 = 0$ as a function of l_0 in the $(p_1 \times q_1)$ -plane. Similar to the observations made in the top panel of Fig. 3.10 for ψ_1 , we see that as l_0 increases, the configuration transitions from a symmetrical arrangement (e-h-e) to a cluster structure ($[3(e)1(h)]-2(e)$).

The presence of a node line along with the cluster structure becomes more pronounced when the long-range screening is reduced, causing the electron to be weakly bound compared to the exciton. In regions where the cluster structure dominates, characterized by $p_1 \propto q_1$, higher amplitude values of the wave function are observed, consistent with the findings discussed earlier for the 2A+R Yamaguchi 3B model. The top panel of Fig. 3.11 displays the wave function in the $p_1 \times q_1$ plane, while the bottom panel shows it in the $p_2 \times q_2$ plane for various l_0 values ranging from 1 to 100\AA , with $\phi_1 = \phi_2 = 0$. When the screening is reduced at large distances, the pattern observed for ψ_2 in the $(p_1 \times q_1)$ plane (as seen in the bottom panels of Fig. 3.10) becomes more evident due to its dominance over ψ_1 . It is important to note that ψ_2 is equivalent to ψ_3 in the symmetric configuration of the two electrons, where they must be in a singlet spin state or an antisymmetric combination of different valley states.

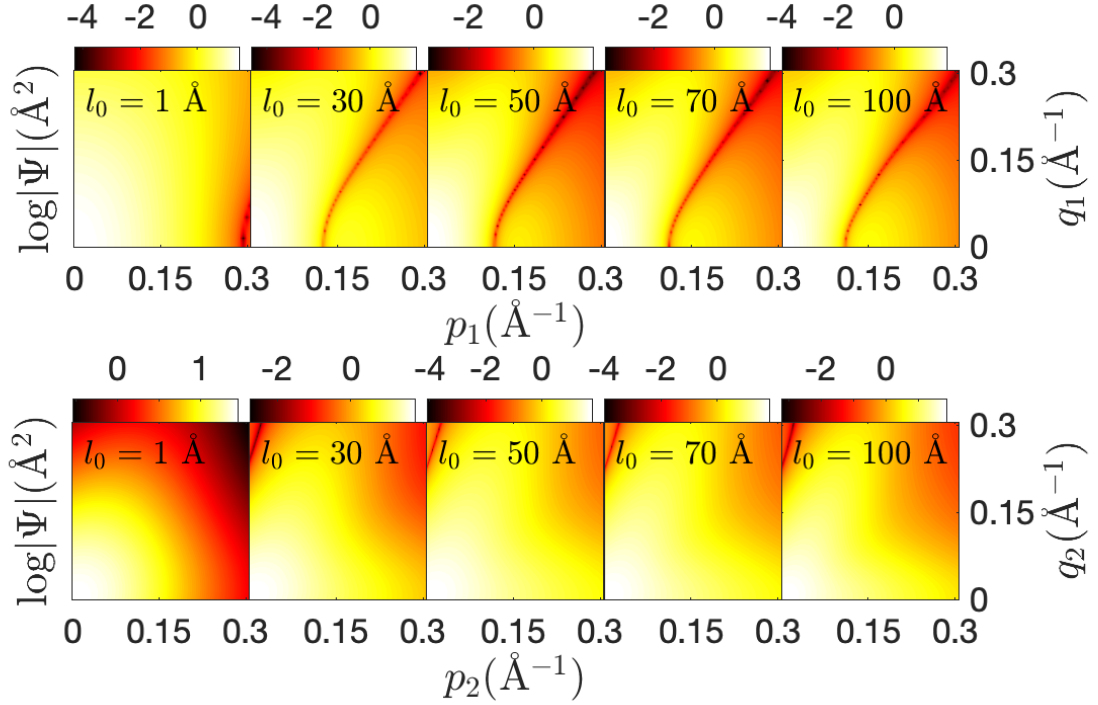


FIGURE 3.11 – The evolution of the wave function $\Psi(p_1, q_1, \phi_1 = 0)$ (top panels) and $\Psi(p_2, q_2, \phi_2 = 0)$ (bottom panels) obtained for the screening parameter $l_0 = 1, 30, 50, 70, 100$ \AA in the screening scheme $V_1(q) \rightarrow (1 - e^{-l_0 q})V_{ee}(q)$. Figure is taken from (MOHSENI *et al.*, 2023).

In the bottom panels of Fig. 3.11, the results for the wave function are presented in the $(p_2 \times q_2)$ plane, where again, the more symmetric e–h–e configuration dominates at the strong trion binding and weaker repulsion between the electrons. By reducing the screening of the repulsive potential, the electron turns to be weakly bound to the exciton, and the system presents an evident cluster structure with the coherent superposition of the two configurations $[3(e)1(h)]-2(e)$ and $[1(h)2(e)]-3(e)$. The top panels of Fig. 3.11 demonstrate the behavior of the wave function in terms of p_2 and q_2 , revealing two branches of higher probability density: one for $p_2 \propto q_2$ and another for small q_2 with p_2 spreading within the displayed region. This behavior, which was also observed in the 2A+R Yamaguchi model, is associated with the cluster structure discussed in detail in Section 3.4.1.

In Fig. 3.12, the angular dependence in ϕ_1 is explored for $l_0 = 100$ \AA .

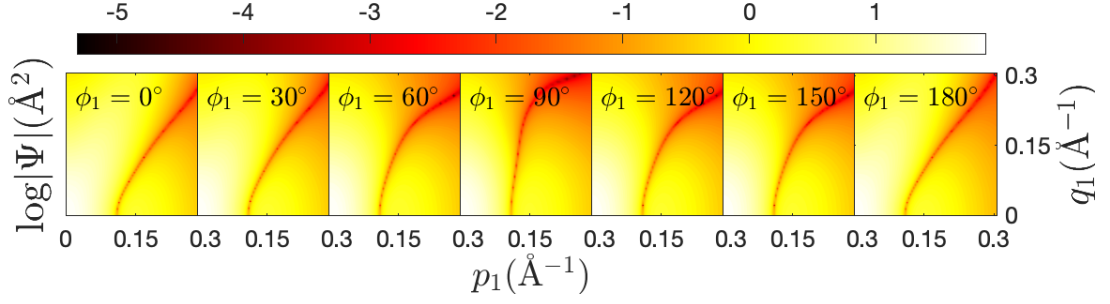


FIGURE 3.12 – The evolution of the wave function $\Psi(p_1, q_1, \phi_1)$ with respect to the angle ϕ_1 for a fixed screening parameter $l_0 = 100 \text{ \AA}$ in the screening scheme $V_1(q) \rightarrow (1 - e^{-l_0 q})V_{ee}(q)$. Figure is taken from (MOHSENI *et al.*, 2023).

It is worth noting that the results remain the same at $\phi_1 = \theta$ or $\phi_1 = 180^\circ - \theta$ due to the wave function's symmetry when exchanging the momentum of the electrons. The configuration space wave function exhibits symmetry upon electron exchange, as the antisymmetry is guaranteed by the spin state. The slope of the node line is distorted as ϕ_1 transitions between \mathbf{p}_1 and \mathbf{q}_1 , appearing more elongated at 90° . The general format of the node line is preserved regardless of the ϕ_1 parameters, indicating that the e-h-e system features a hole with a small momentum with respect to the center of mass of the electron pair. It is evident that the wave function's zero in the $(p_1 \times q_1)$ plane originates at $q_1 = 0$.

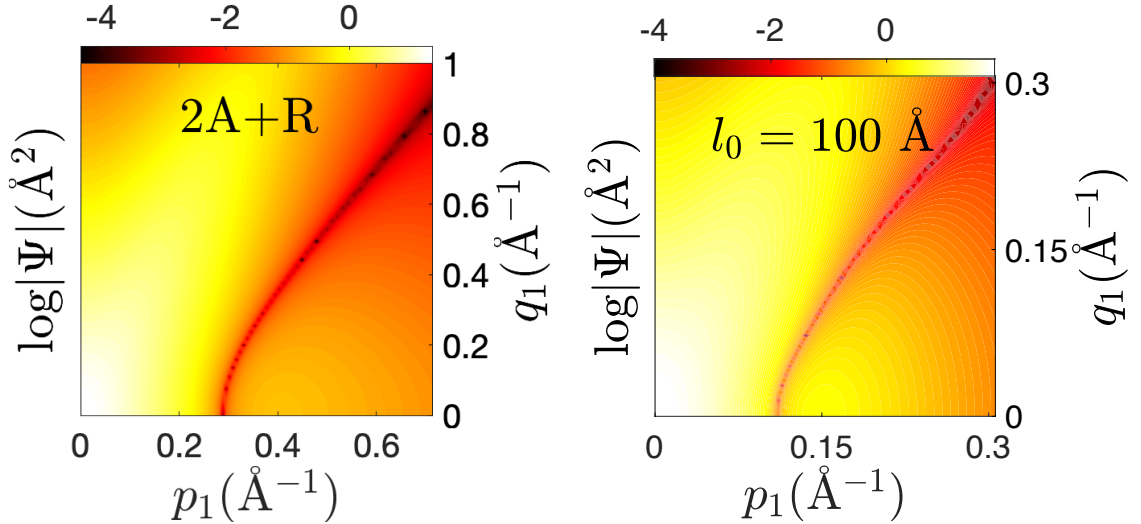


FIGURE 3.13 – Comparison between trion wave function calculated with RK potential (left panel) and re-scaled Yamaguchi potential model (right panel) for $\phi_1 = 0$. Figure is taken from (MOHSENI *et al.*, 2023).

Finally, in Fig. 3.13, we directly compare the wave functions of the trion computed using the RK model (left panel) and the 2A+R Yamaguchi model (right panel). To achieve this comparison, we rescaled the Yamaguchi separable potential model to physical units corresponding to the exciton and trion. In the Yamaguchi model, the exciton and trion

results were obtained in units of $\hbar = m = 1$. To convert to physical units, we have that

$$E_{2B} = -\frac{\hbar^2}{m_e} \lambda^2 0.1 \quad \text{and} \quad E_{3B} = -\frac{\hbar^2}{m_e} \lambda^2 0.12034.$$

To obtain the dimensional constant λ , we use the exciton binding energy $E_{2B} = -753$ meV and the average mass $m = (m_e + m_h)/2 = 0.505, m_0$, yielding $\lambda = 0.706576 \text{ \AA}^{-1}$. In the 2A+R Yamaguchi model, the trion binding energy is given in meV units as $E_t = 153.225$ meV, which is comparable to the value of 207.26 meV obtained from the regulated repulsive RK potential with $l_0 = 100 \text{ \AA}$, as shown in Table 3.7. After rescaling the wave functions to physical units, the comparison reveals that the trion wave functions obtained from calculations using the RK and 2A+R Yamaguchi potentials exhibit a remarkably similar structure. Particularly, the node line, representing the region of zero amplitude, has the same shape in both cases. Additionally, the region where the wave function reaches its highest values is located to the left of the node line, where $p_1 \propto q_1$. However, it should be noted that the node line is shifted to larger values of p_1 in the 2A+R Yamaguchi model compared to the RK potential. This shift can be attributed to the contrasting characteristics of the short-range nature of the Yamaguchi potential and the long-range behavior of the RK potential.

4 Trion in Two-dimensional Configuration Space

4.1 Overview

The previous chapter focused on understanding the trion's wave function in momentum space. Now, we will shift our focus to configuration space, which allows us to visualize the trion's structure in real space. This shift will help us understand how the trion's particles are arranged and give us better insight into how they interact.

Previous studies have employed various methods to investigate trions in configuration space. Density functional theory, leveraging approximations to the exchange-correlation functional, (SZYNISZEWSKI *et al.*, 2017a; COURTADE *et al.*, 2017), Variational approaches, leveraging trial wave functions and optimization techniques, (BERKELBACH *et al.*, 2013b; KIDD *et al.*, 2016b; SERGEEV; SURIS, 2001), and Path integral Monte Carlo simulations, offering a powerful stochastic approach, (SZYNISZEWSKI *et al.*, 2017a; KYLÄNPÄÄ; KOMSA, 2015). These diverse methodologies have collectively contributed to our understanding of trions in configuration space, albeit with varying degrees of computational complexity and accuracy. However, we will use the Faddeev formalism, a powerful tool for studying three-body systems. By solving the Faddeev equations and transforming the solutions into configuration space, we can get a very accurate picture of the trion's structure. In this chapter, we will use the Faddeev formalism to study the trion's configuration-space wave function with two different potentials: the Yamaguchi potential and the Rytova-Keldysh (RK) potential. The Yamaguchi potential is more straightforward and will help us test our methods. The RK potential is more realistic and describes the long-range interactions in 2D materials.

This chapter aims to provide a complete picture of the trion's structure, connecting the abstract momentum space, discussed in chapter 3, with the real-world configuration space. This understanding will be valuable for theoretical and experimental research on trions in 2D materials.

4.2 Exciton structure in two-dimensions configuration space

The Fourier transformation of the exciton wave function from momentum space, as calculated in Sec. 3.2.2, to configuration space is given by

$$\psi(\mathbf{r}) = \int d^2p \psi(\mathbf{p}) e^{i\mathbf{p} \cdot \mathbf{r}}. \quad (4.1)$$

This Fourier transformation allows us to obtain the exciton wave function in configuration space $\psi(r)$ from the corresponding wave function in momentum space $\psi(p)$. The function $\psi(r)$ represents the probability amplitude of finding the electron and hole separated by a distance r in the 2D plane. By choosing the coordinate system showing in Fig. 4.1, the angle variable ϕ is defined as $\hat{p} \cdot \hat{r} = \cos(\phi)$.

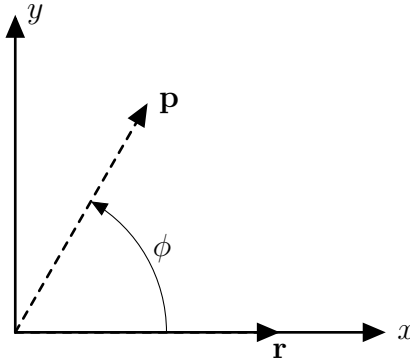


FIGURE 4.1 – The geometry of vector \mathbf{p} & \mathbf{r} . The vector \mathbf{r} is chosen to be parallel to the x -axis, and vector \mathbf{p} is free in the 2D space. The angle variable is defined as $\hat{p} \cdot \hat{r} = \cos(\phi)$.

Therefore Eq. (4.1) can be written as

$$\psi(r) = \int_0^\infty dp p \int_0^{2\pi} d\phi \psi(p) e^{ipr \cos(\phi)}. \quad (4.2)$$

Using the Jacobi-Anger expansion, we can write the Eq. (4.2) as

$$\begin{aligned} \psi(r) &= \int_0^\infty dp p \psi(p) \int_0^{2\pi} d\phi \sum_{m=0}^\infty \epsilon_m i^m J_m(pr) \cos(m\phi) \\ &= \int_0^\infty dp p \psi(p) \sum_{m=0}^\infty \epsilon_m i^m J_m(pr) \int_0^{2\pi} d\phi \cos(m\phi), \end{aligned} \quad (4.3)$$

where $J_m(pr)$ is m -th order Bessel function of the first kind, and considering the orthogonality over the interval 0 to 2π , we have

$$\int_0^{2\pi} d\phi \cos(m\phi) = \begin{cases} 2\pi & m = 0, \\ 0 & m \neq 0. \end{cases} \quad (4.4)$$

For the s -wave ($m = 0$), Eq. (4.3) simplifies to

$$\psi(r) = 2\pi \int_0^\infty dp p \psi(p) J_0(pr). \quad (4.5)$$

Similar to Table E.2, we present the convergence of the exciton mean radius $\langle r \rangle$ and the exciton binding energies for the ground, first excited, and second excited states as a function of the number of mesh points for the 2B relative momentum N_p . The calculations are performed with 61 mesh points for the angle variables and 2000 mesh points for the 2B relative distance N_r . The last row corresponds to quadratic extrapolation on $1/N_p \rightarrow 0$.

TABLE 4.1 – Convergence of exciton mean radius $\langle r \rangle$, and exciton binding energies for ground, first excited, and second excited state, presented as a function of mesh points for 2B relative momentum N_p . The calculations are performed with 61 mesh points for angle variables and 2000 mesh points for e-h relative distance N_r .

N_p	ground state		1st excited state		2nd excited state	
	$\langle r \rangle^{(0)}$	$E_{2B}^{(0)}$	$\langle r \rangle^{(1)}$	$E_{2B}^{(1)}$	$\langle r \rangle^{(2)}$	$E_{2B}^{(2)}$
300	7.434	−785.7	25.45	−352.6	48.46	−215.2
400	7.484	−775.2	25.71	−343.8	49.14	−207.0
500	7.511	−769.5	25.85	−339.0	49.50	−202.5
600	7.527	−766.1	25.93	−336.1	49.73	−199.8
700	7.537	−763.8	25.98	−334.2	49.87	−198.0
800	7.543	−762.3	26.02	−332.9	49.97	−196.7
900	7.548	−761.1	26.05	−331.9	50.04	−195.8
1000	7.551	−760.3	26.06	−331.2	50.09	−195.1
Quad. extrap.@ $1/N_p \rightarrow 0$	7.577	−753.3	26.21	−325.1	50.52	−189.4

Figure 4.2 illustrates the exciton wave functions in configuration space, $\psi^{(n)}(r)$, as a function of r . The ground state, first excited state, and second excited state wave functions are shown, highlighting the differences in their spatial extents and nodal structures.

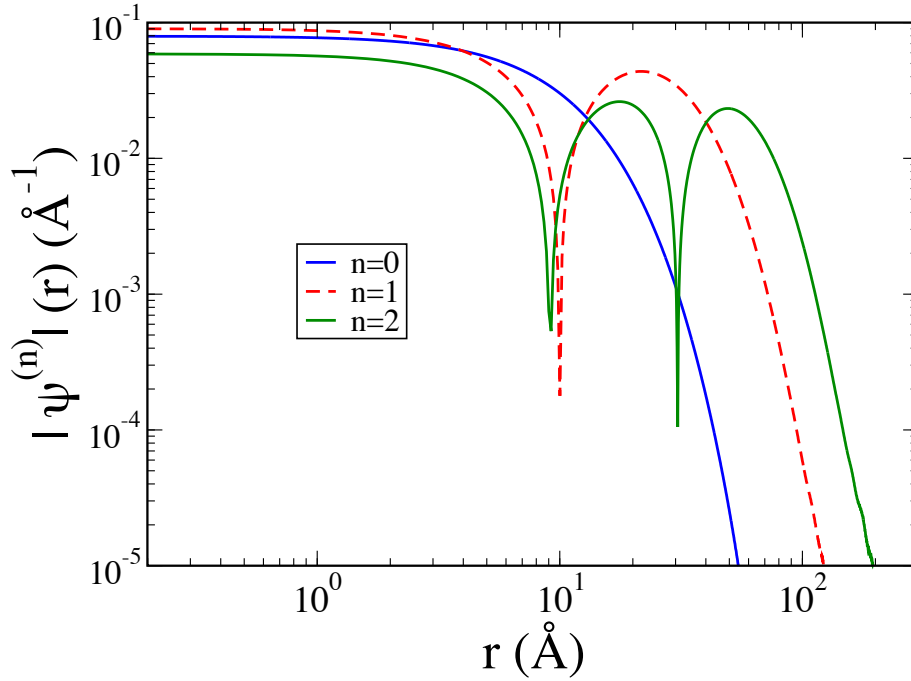


FIGURE 4.2 – Ground state, first excited state, and second excited state 2B wave functions in configuration space $\psi^{(n)}(r)$ as a function of r . The calculations are performed with 61 mesh points for angle variables and 2000 mesh points for e-h relative distance N_r .

4.3 Trion structure in two-dimensions configuration space

The Fourier transform of trion wave function from momentum space $\Psi(\mathbf{p}, \mathbf{q})$, calculate in Eq. (3.74), to the configuration space $\Psi(\mathbf{r}, \mathbf{R})$, is given by

$$\Psi(\mathbf{r}, \mathbf{R}) = \int d^2p \int d^2q \Psi(\mathbf{p}, \mathbf{q}) e^{i\mathbf{p} \cdot \mathbf{r}} e^{i\mathbf{q} \cdot \mathbf{R}}. \quad (4.6)$$

Here the variables \mathbf{r} and \mathbf{R} are conjugate to the Jacobi momenta \mathbf{p}, \mathbf{q} of a 3B system and given as (GREENE *et al.*, 2017)

$$\begin{aligned} \mathbf{r}_i &= \mathbf{r}_j - \mathbf{r}_k, \\ \mathbf{R}_i &= \mathbf{r}_i - \frac{m_j \mathbf{r}_j + m_k \mathbf{r}_k}{m_j + m_k}. \end{aligned} \quad (4.7)$$

Where r_1, r_2 , and r_3 are the coordinates of three particles in configuration space. By choosing the coordinate system of Fig. 4.3

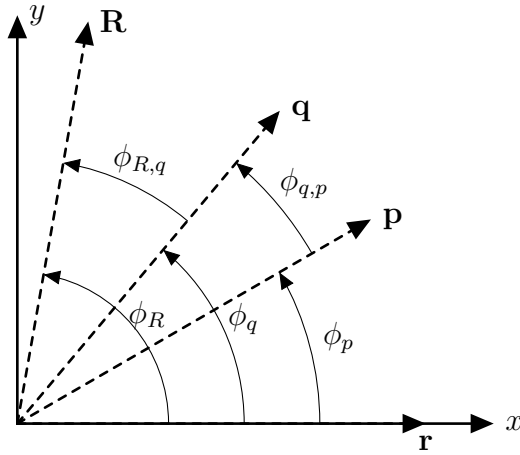


FIGURE 4.3 – Coordinate system for the solution of integral Eq. (4.6).

the angle variables will be defined as

$$(\hat{\mathbf{p}}, \hat{\mathbf{r}}) = \phi_p, \quad (4.8)$$

$$(\hat{\mathbf{q}}, \hat{\mathbf{r}}) = \phi_q, \quad (4.9)$$

$$(\hat{\mathbf{R}}, \hat{\mathbf{r}}) = \phi_R, \quad (4.10)$$

$$(\hat{\mathbf{R}}, \hat{\mathbf{q}}) = \phi_{R,q} = \phi_R - \phi_q, \quad (4.11)$$

$$(\hat{\mathbf{q}}, \hat{\mathbf{p}}) = \phi_{q,p} = \phi_q - \phi_p. \quad (4.12)$$

For the explicit calculation of the double Fourier transformation Eq. (4.6) we first consider the \mathbf{q} -integration

$$\int d^2 q e^{i\mathbf{q} \cdot \mathbf{R}} \Psi(\mathbf{p}, \mathbf{q}) = \int_0^\infty dq q \int_0^{2\pi} d\phi_q \Psi(p, q, \phi_{q,p}) e^{iqR \cos(\phi_{R,q})} \equiv \Psi_p(p, R, \phi_p, \phi_R), \quad (4.13)$$

then, we consider the integration over \mathbf{p}

$$\int d^2 p \Psi_p(p, R, \phi_p, \phi_R) e^{i\mathbf{p} \cdot \mathbf{r}} = \int_0^\infty dp p \int_0^{2\pi} d\phi_p \Psi_p(p, R, \phi_p, \phi_R) e^{ipr \cos(\phi_p)}. \quad (4.14)$$

Finally, the Fourier transform of $\Psi(p, q, \hat{\mathbf{p}} \cdot \hat{\mathbf{q}})$ can be calculated as

$$\Psi(r, R, \phi_R) = \int_0^\infty dp p \int_0^{2\pi} d\phi_p \Psi_p(p, R, \phi_p, \phi_R) e^{ipr \cos(\phi_p)}, \quad (4.15)$$

where

$$\Psi_p(p, R, \phi_p, \phi_R) \equiv \int_0^\infty dq q \int_0^{2\pi} d\phi_q \Psi(p, q, \phi_{q,p}) e^{iqR \cos(\phi_{R,q})}. \quad (4.16)$$

4.3.1 Correlation functions and expectation values

To investigate the structure of the 3B system in configuration space, we studied the pair correlation function. The correlation functions are given by

$$c(r) = 2\pi r \int_0^\infty dR R \int_0^{2\pi} d\phi_R \Psi^2(r, R, \phi_R), \quad (4.17)$$

$$c(R) = 2\pi R \int_0^\infty dr r \int_0^{2\pi} d\phi_R \Psi^2(r, R, \phi_R). \quad (4.18)$$

The correlation function $c(r)$ describes the probability to find two particles within a relative distance r and $c(R)$ describes the probability to find a particle at a distance R with the respect to the center of mass of 2B system.

The expectation values of the Jacobi coordinates r and R can be calculated as

$$\langle r_i \rangle = 2\pi \int_0^\infty dr_i r_i \int_0^\infty dR_i R_i \int_0^{2\pi} d\phi_{R_i} r_i \Psi^2(r_i, R_i, \phi_{R_i}), \quad (4.19)$$

$$\langle R_i \rangle = 2\pi \int_0^\infty dr_i r_i \int_0^\infty dR_i R_i \int_0^{2\pi} d\phi_{R_i} R_i \Psi^2(r_i, R_i, \phi_{R_i}), \quad (4.20)$$

the subscripts i indicated the spectator particle in the 3B system. The wave function in configuration space is normalized as

$$2\pi \int_0^\infty dr_i r_i \int_0^\infty dR_i R_i \int_0^{2\pi} d\phi_{R_i} \Psi^2(r_i, R_i, \phi_{R_i}) = 1. \quad (4.21)$$

4.4 Trion calculation in configuration space: Yamaguchi potential

The Yamaguchi potential, as discussed in section 3.3.2, characterized by its short-range nature, simplifies calculations and provides a foundational understanding of the trion system's fundamental properties in two-dimensional materials. This interaction model allows us to validate our numerical methods and formalism.

We start our study by considering a system of three identical particles with three attractive interactions. Next, we focus on a more realistic scenario by considering a system with two attractive and one repulsive Yamaguchi potential. This setup simulates the behavior of a trion where two particles experience attraction while the third particle experiences repulsion. The correlation functions for this 2A+R configuration provide insights into the spatial distribution and clustering behavior of the trion's constituent particles.

4.4.1 Three identical particles interacting with three attractive Yamaguchi potentials

Separable potential with Yamaguchi form factor, as defined in Eq. (3.85), is given as

$$\langle \mathbf{p} | V | \mathbf{p}' \rangle = -\lambda g(p)g(p'); \quad g(p) = \frac{1}{(\beta^2 + p^2)^m}. \quad (4.22)$$

In Fig. 4.4, the correlation functions $c(r)$ and $c(R)$, calculated by Eqs. (4.17) and (4.18), are displayed for this case.

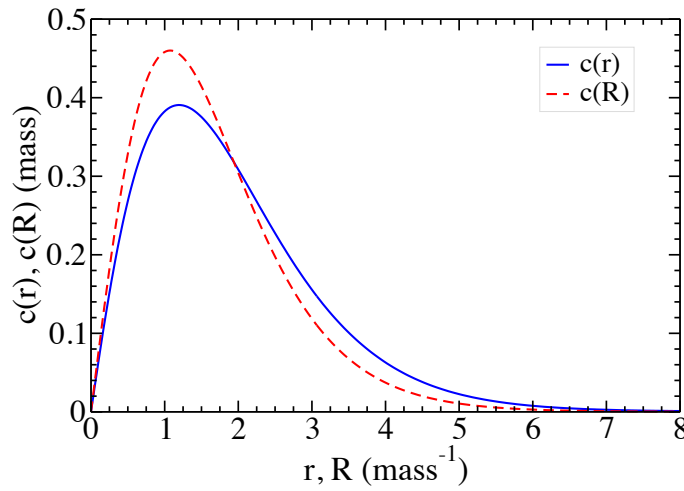


FIGURE 4.4 – The correlation functions $c(r)$ and $c(R)$ calculated with three attractive Yamaguchi potentials. Our calculations are performed with 41 mesh points for angles (ϕ_R, ϕ_q) and 300 mesh points for Jacobi coordinates r , R , and p , q . The calculations are done with $\hbar c = \text{mass} = 1$.

Since, in this section, we are studying a system consisting of three identical particles and three attractive interactions, the ground state configuration that maximizes the probability of finding the particles is an equilateral triangle. In this context, the expectation values $\langle r \rangle$ and $\langle R \rangle$ represent the length of the triangle's sides and its height, respectively. The relationship between these two quantities in an equilateral triangle is given by

$$\langle R \rangle / \langle r \rangle = \sqrt{3}/2 = 0.866. \quad (4.23)$$

In Table 4.2, we present the results for the two- and three-body binding energies, along with the expectation values of the Jacobi coordinates r , and R , calculated for Yamaguchi-type potentials with a form factor parameter ($\beta = 1$) and power ($m = 1$). The potential strength λ is chosen to reproduce two-body binding energy E_2 of -0.1 . To assess the accuracy of our numerical calculations, we introduce a quantity δ , which quantifies the deviation of the calculated ratio $\langle R \rangle / \langle r \rangle$ from the expected value for an equilateral triangle

configuration, which is defined as

$$\delta = \left(\frac{\langle R \rangle / \langle r \rangle - \sqrt{3}/2}{\sqrt{3}/2} \right) \times 100\%. \quad (4.24)$$

TABLE 4.2 – Two- and three-body binding energies and the Jacobi coordinates r and R expectation values calculated for Yamaguchi-type potentials with form factor parameter $\beta = 1$ and power $m = 1$. The potential strength λ is obtained from the pole property of 2B t -matrix at two-body binding energy E_2 . The potential strength λ is chosen to reproduce two-body binding energy E_2 of -0.1 .

λ	E_2	$\langle r_{2B} \rangle$	E_3/E_2	$\langle r \rangle$	$\langle R \rangle$	$\langle R \rangle / \langle r \rangle$	$\delta\%$
0.1838	-0.1000	2.596	4.58	1.902	1.649	0.867	0.028

The accuracy of 0.028% in our calculations, as presented in Table 4.2, demonstrates the high reliability of our numerical results.

4.4.2 Three identical particles interact with two attractive and one repulsive Yamaguchi potentials

To simulate a more realistic scenario than Sec. 4.4.1, we modify the system of three identical particles by making one of the attractive interactions repulsive. In Fig. 4.5, we present the correlation functions $c(r)$ and $c(R)$ for this 2A+R configuration.

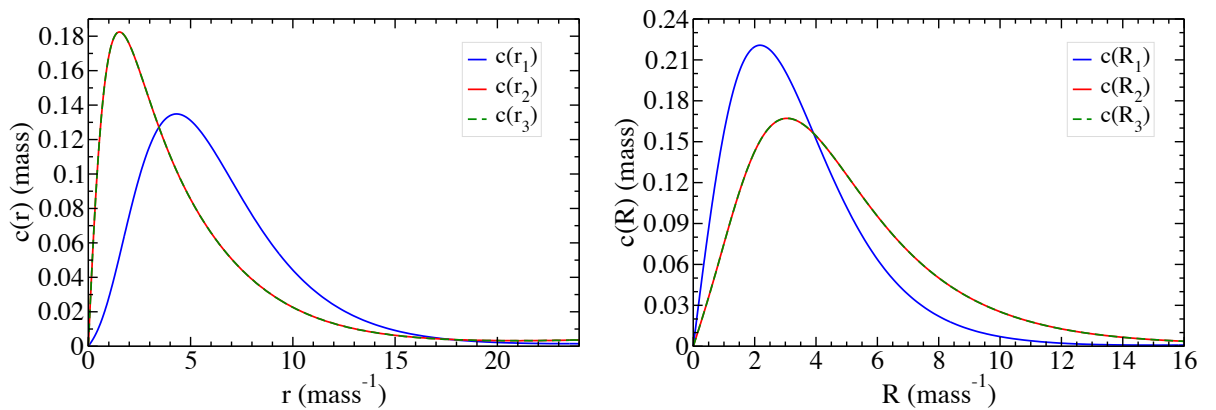


FIGURE 4.5 – The correlation functions $c(r)$ and $c(R)$ calculated with two attractive and one repulsive Yamaguchi potentials. Our calculations are performed with $N_{\phi_q} = 41$, $N_{\phi_R} = 61$, and 400 mesh points for Jacobi coordinates r and R , and 300 mesh points for Jacobi coordinates p and q . The calculations are done with $\hbar c = \text{mass} = 1$.

Since the studied 3B systems consist of two electrons and one hole, the most probable configuration for the ground state is an isosceles triangle, where the two electrons occupy

the base vertices and the hole occupies the apex vertex. In this case, we expect our calculations to satisfy the Pythagorean theorem, as given by

$$\begin{aligned}\Delta &= \langle R_1^2 \rangle + \frac{1}{4} \langle r_1^2 \rangle - \langle r_2^2 \rangle \\ &= \langle R_1^2 \rangle + \frac{1}{4} \langle r_1^2 \rangle - \langle r_3^2 \rangle = 0.\end{aligned}\tag{4.25}$$

Table 4.3 presents the two- and three-body binding energies, along with the expectation values of the Jacobi coordinates r and R , for a system with two attractive and one repulsive Yamaguchi-type potential. The potential strength λ is chosen to reproduce two-body binding energy E_2 of -0.1 . The results are categorized based on the different 3B chains: (ee, h) represents the configuration where the two electrons (e) are considered as a pair, and the hole (h) is the third particle. Conversely, (eh, e) denotes the configuration where an electron and hole form a pair, with the remaining electron as the third particle.

The expectation values $\langle r \rangle$ and $\langle R \rangle$ provide insights into the spatial arrangement of the particles within each 3B chain. In the (ee, h) chain, the larger value of $\langle r \rangle$ compared to $\langle R \rangle$ suggests that the two electrons are likely to be further apart than from the center of mass of the electron pair. This can be attributed to the repulsive interaction between the electrons. In contrast, for the (eh, e) chains, the values of $\langle r \rangle$ and $\langle R \rangle$ are comparable, indicating a more isosceles triangular configuration. This suggests that the attractive interaction between the electron and hole in the (eh) pair dominates, leading to a closer proximity.

To assess the accuracy of our calculations, we examine the quantity Δ , defined in Eq. (4.25), which measures the satisfaction of the Pythagorean theorem. The results in Table 4.3 demonstrate that our calculations satisfy the Pythagorean theorem with an accuracy of 0.104% for the (eh, e) chain and 0.190% for the (eh, e) chain. This high level of accuracy indicates the reliability of our numerical results even when repulsive interactions are present in the system.

TABLE 4.3 – Two- and three-body binding energies and the Jacobi coordinates r and R expectation values calculated for Yamaguchi-type potentials (one repulsive and two attractive interaction) with form factor parameter $\beta = 1$ and power $m = 1$. The potential strength λ is obtained from the pole property of 2B t -matrix at two-body binding energy E_2 . The calculations are done with $\hbar c = mass = 1$.

λ	E_2	$\langle r_{2B} \rangle$	E_3/E_2	
0.184	-0.100	2.596	1.203	
3B chain	$\langle r \rangle$	$\langle R \rangle$	$\langle R \rangle / \langle r \rangle$	$\Delta\%$
(ee, h)	6.338	3.445	0.543	—
(eh, e)	4.676	4.805	1.028	0.104
(eh, e)	4.672	4.805	1.028	0.190

4.4.3 Trion calculation in configuration space: RK potential

This section extends our analysis to investigate the trion within the MoS₂ single layer using the RK potential, as defined in Eq. (3.7), and given by

$$V_{eh}(q) = -\frac{1}{4\pi^2} \left(\frac{1}{4\pi\epsilon_0} \frac{2\pi e^2}{q(1+r_0q)} \right). \quad (4.26)$$

We employ the same methodology, utilizing the Fourier transform, Eq. (4.15), to transition the wave function from momentum to configuration space.

Following Sec. 3.5, where we encountered challenges in numerical calculations due to the long-range nature of the RK potential, we anticipate similar difficulties in configuration space. This is because we are utilizing the Fourier transform of the momentum space representation, which inherits the complexities associated with the long-range behavior of the RK potential. To address this numerical challenge, we will employ the same regularization techniques introduced in Sec. 3.5. These techniques involve screening the repulsive electron-electron RK potential to facilitate accurate and reliable numerical solutions in configuration space.

To systematically investigate the impact of screening on the trion binding energy and wave function, we employ the screening model $V(q) \rightarrow (1 - e^{-l_0q})V_{ee}(q)$ with varying screening lengths l_0 . This approach allows us to gradually increase the screening effect and observe its influence on the trion properties.

Tables 4.4 - 4.7 present the root-mean-square (RMS) values of the Jacobi coordinates r and R for the RK potential with screened electron-electron interaction, calculated for different screening parameters $l_0 = 70, 80, 90$ and 100 \AA . The last row of these tables shows the linear extrapolation to infinite mesh points. The calculations are performed as a function of the number of mesh points used for the Jacobi coordinates in configuration space (N_r and N_R) and momentum space (N_p and N_q). The quantity $\Delta\%$ in the tables represents the percentage accuracy with which the calculated values satisfy the Pythagorean theorem defined in Eq. (4.25).

TABLE 4.4 – RMS values of the Jacobi coordinate r and R calculated for RK potentials with screened ee interaction ($\mathbf{l}_0 = \mathbf{70}$) as a function of the number of mesh points for Jacobi coordinates r , R , p , and q . The quantity $\Delta\%$ indicates the percentage accuracy for the satisfaction of the Pythagorean theorem.

$N_r = N_R = N_p = N_q = N$	3B chain	$\sqrt{\langle r^2 \rangle}$	$\sqrt{\langle R^2 \rangle}$	$\sqrt{\langle R^2 \rangle / \langle r^2 \rangle}$	$\Delta\%$
200	(ee, h)	19.764	10.108	0.5115	—
	(eh, e)	14.113	15.462	1.0956	0.3298
	(eh, e)	14.113	15.461	1.0955	0.3275
250	(ee, h)	20.158	10.346	0.5132	—
	(eh, e)	14.422	15.778	1.0940	0.3123
	(eh, e)	14.422	15.777	1.0939	0.3061
300	(ee, h)	20.439	10.514	0.5144	—
	(eh, e)	14.640	16.002	1.0931	0.3089
	(eh, e)	14.640	16.001	1.0929	0.2980
350	(ee, h)	20.619	10.621	0.5151	—
	(eh, e)	14.779	16.146	1.0925	0.3094
	(eh, e)	14.780	16.1442	1.0923	0.2928
Linear extrapolation @ $1/N \rightarrow 0$	(ee, h)	21.769	11.310	0.5195	—
Linear extrapolation @ $1/N \rightarrow 0$	(eh, e)	15.675	17.066	1.0887	0.2779

TABLE 4.5 – Same as Tabel 4.4, but with $\mathbf{l}_0 = \mathbf{80}$.

$N_r = N_R = N_p = N_q = N$	3B chain	$\sqrt{\langle r^2 \rangle}$	$\sqrt{\langle R^2 \rangle}$	$\sqrt{\langle R^2 \rangle / \langle r^2 \rangle}$	$\Delta\%$
200	(ee, h)	20.039	10.276	0.5128	—
	(eh, e)	14.330	15.684	1.0945	0.3298
	(eh, e)	14.329	15.684	1.0945	0.3275
250	(ee, h)	20.389	10.512	0.5156	—
	(eh, e)	14.621	15.966	1.0920	0.3123
	(eh, e)	14.621	15.965	1.0919	0.3061
300	(ee, h)	20.696	10.702	0.5171	—
	(eh, e)	14.863	16.213	1.0908	0.3089
	(eh, e)	14.864	16.212	1.0906	0.2980
350	(ee, h)	20.892	10.820	0.5179	—
	(eh, e)	15.016	16.370	1.0902	0.3094
	(eh, e)	15.017	16.368	1.090	0.2928
Linear extrapolation @ $1/N \rightarrow 0$	(ee, h)	22.025	11.548	0.5239	—
Linear extrapolation @ $1/N \rightarrow 0$	(eh, e)	15.931	17.283	1.0849	0.3289

TABLE 4.6 – Same as Tabel 4.4, but with $\mathbf{l}_0 = \mathbf{90}$.

$N_r = N_R = N_p = N_q = N$	3B chain	$\sqrt{\langle r^2 \rangle}$	$\sqrt{\langle R^2 \rangle}$	$\sqrt{\langle R^2 \rangle / \langle r^2 \rangle}$	$\Delta\%$
200	(ee, h)	20.353	10.463	0.5141	–
	(eh, e)	14.573	15.935	1.0935	0.3146
	(eh, e)	14.572	15.934	1.0935	0.3252
250	(ee, h)	20.773	10.734	0.5167	–
	(eh, e)	14.914	16.273	1.0911	0.2961
	(eh, e)	14.621	15.965	1.0919	0.3108
300	(ee, h)	20.888	10.867	0.5202	–
	(eh, e)	15.047	16.375	1.0883	0.3248
	(eh, e)	15.049	16.373	1.0880	0.3085
350	(ee, h)	21.094	10.989	0.5210	–
	(eh, e)	15.206	16.540	1.0877	0.3301
	(eh, e)	15.208	16.538	1.0874	0.3075
Linear extrapolation @ $1/N \rightarrow 0$	(ee, h)	22.040	11.685	0.5302	–
Linear extrapolation @ $1/N \rightarrow 0$	(eh, e)	16.032	17.317	1.0801	0.3714

TABLE 4.7 – Same as Tabel 4.4, but with $\mathbf{l}_0 = \mathbf{100}$.

$N_r = N_R = N_p = N_q = N$	3B chain	$\sqrt{\langle r^2 \rangle}$	$\sqrt{\langle R^2 \rangle}$	$\sqrt{\langle R^2 \rangle / \langle r^2 \rangle}$	$\Delta\%$
200	(ee, h)	20.492	10.575	0.5160	–
	(eh, e)	14.701	16.052	1.0918	0.3136
	(eh, e)	14.700	16.051	1.0919	0.3295
250	(ee, h)	21.017	10.895	0.5184	–
	(eh, e)	15.114	16.471	1.0898	0.2960
	(eh, e)	15.113	16.471	1.0898	0.3113
300	(ee, h)	20.976	10.966	0.5228	–
	(eh, e)	15.149	16.454	1.0861	0.3312
	(eh, e)	15.15	16.452	1.0859	0.3134
350	(ee, h)	21.214	11.115	0.5239	–
	(eh, e)	15.338	16.646	1.0853	0.3426
	(eh, e)	15.339	16.643	1.0850	0.3170
Linear extrapolation @ $1/N \rightarrow 0$	(ee, h)	22.105	11.808	0.5342	–
Linear extrapolation @ $1/N \rightarrow 0$	(eh, e)	16.142	17.383	1.0769	0.3924

The extrapolated results obtained from Tables 4.4 - 4.7 are summarized in Table 4.8.

TABLE 4.8 – The summary of the RMS values of the Jacobi coordinates r and R calculated for RK potentials with different values of the screening parameter l_0 for ee interaction. The quantity $\Delta\%$ indicates the percentage accuracy for the satisfaction of the Pythagorean theorem.

l_0	$\sqrt{\langle r^2 \rangle}$		$\sqrt{\langle R^2 \rangle}$		$\Delta \%$
	(ee,h)	(eh,e)	(ee,h)	(eh,e)	
70	21.769	15.675	11.310	17.066	0.27790
80	22.025	15.931	11.548	17.283	0.32890
90	22.040	16.032	11.685	17.317	0.37140
100	22.105	16.142	11.808	17.376	0.39240

The next step is to extrapolate the data reported in Table 4.8 to the system with no screening parameter. The linear extrapolation of the trion RMS values, at the physical point $l_0^{-1} \rightarrow 0 \text{ \AA}^{-1}$, for the Jacobi coordinates r and R is shown in Fig. 4.6.

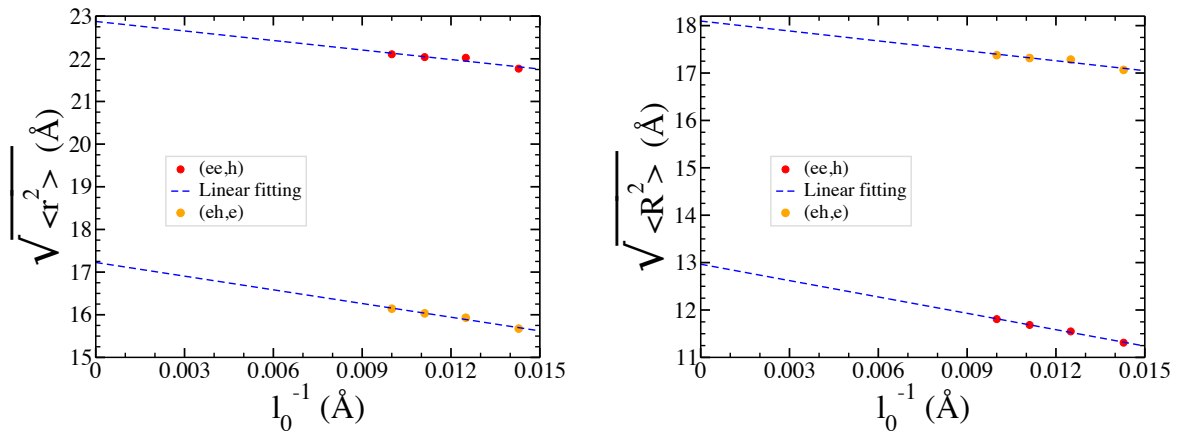


FIGURE 4.6 – Linear extrapolation on $\sqrt{\langle r^2 \rangle}$ and $\sqrt{\langle R^2 \rangle}$ as a function of the inverse of the screening parameter l_0^{-1} for the screening potential $V_{ee}(q) \rightarrow (1 - e^{-l_0 q})V_{ee}(q)$.

Upon linear extrapolation to the physical limit of $l_0^{-1} = 0 \text{ \AA}^{-1}$, the RMS values for the Jacobi coordinates are found to be $\sqrt{\langle r^2 \rangle} = 22.876 \text{ \AA}$ and $\sqrt{\langle R^2 \rangle} = 12.966 \text{ \AA}$ for the (ee, h) chain, and $\sqrt{\langle r^2 \rangle} = 17.226 \text{ \AA}$ and $\sqrt{\langle R^2 \rangle} = 18.096 \text{ \AA}$ for the (eh, e) chain. These results are shown in Table 4.9.

TABLE 4.9 – Extrapolated RMS values of the Jacobi coordinates r and R for the RK potential in the limit of $1/l_0 \rightarrow 0$.

$\sqrt{\langle r^2 \rangle}$		$\sqrt{\langle R^2 \rangle}$		$\Delta \%$
(ee,h)	(eh,e)	(ee,h)	(eh,e)	
22.876	17.226	12.966	18.096	0.74470

The calculated inter-particle separations of ground-state trions are consistent with

the result calculated by variational methods (CHANG; CHANG, 2021; BERKELBACH *et al.*, 2013b) and path-integral Monte Carlo method (KYLÄNPÄÄ; KOMSA, 2015).

Furthermore, by using the results presented in Table 4.9 the electron and hole RMS distances to the center of mass of trion can be evaluated from $\langle r_{ee}^2 \rangle$, $\langle r_{eh}^2 \rangle$ and $\langle R_{ee,h}^2 \rangle$, respectively by (HIYAMA *et al.*, 2022)

$$\langle r_e^2 \rangle^{\frac{1}{2}} = \sqrt{\frac{2\langle r_{eh}^2 \rangle + \langle r_{ee}^2 \rangle}{6} - \frac{2\langle R_{ee,h}^2 \rangle}{9}}, \quad (4.27)$$

$$\langle r_h^2 \rangle^{\frac{1}{2}} = 2 \frac{\langle R_{ee,h}^2 \rangle^{\frac{1}{2}}}{3}. \quad (4.28)$$

Also, the average relative angles are given by

$$\theta_{eh} = \cos^{-1} \left(\frac{\langle r_h^2 \rangle + \langle r_e^2 \rangle - \langle r_{eh}^2 \rangle}{2\sqrt{\langle r_h^2 \rangle \langle r_e^2 \rangle}} \right), \quad (4.29)$$

$$\theta_{ee} = \cos^{-1} \left(1 - \frac{1}{2} \frac{\langle r_{ee}^2 \rangle}{\langle r_e^2 \rangle} \right), \quad (4.30)$$

quantify the geometry of trion and satisfy the following relation

$$\delta = \theta_{ee} + 2\theta_{eh} = 360^\circ. \quad (4.31)$$

Using Eqs. (4.28) - (4.31), the electron and hole RMS distances to the center of mass of the trion, the associated angles, and the deviation from the Pythagorean theorem are calculated and presented in Table 4.10.

TABLE 4.10 – The RMS distance of the electrons and hole to the trion’s center of mass and the associated angles calculated with the extrapolated data at $l_0^{-1} = 0$, listed in Table (4.9).

$\langle r_e^2 \rangle^{\frac{1}{2}}$	$\langle r_h^2 \rangle^{\frac{1}{2}}$	θ_{eh}	θ_{ee}	$\left(\frac{\delta - 360^\circ}{360^\circ} \right) \times 100 \%$
12.197	8.6440	110.33°	139.36°	0.0024

Figure 4.7 illustrates the geometrical structure of the trion calculated in configuration space. It is worth mentioning that Fig 4.7 shows trion in the real scale in our calculation.

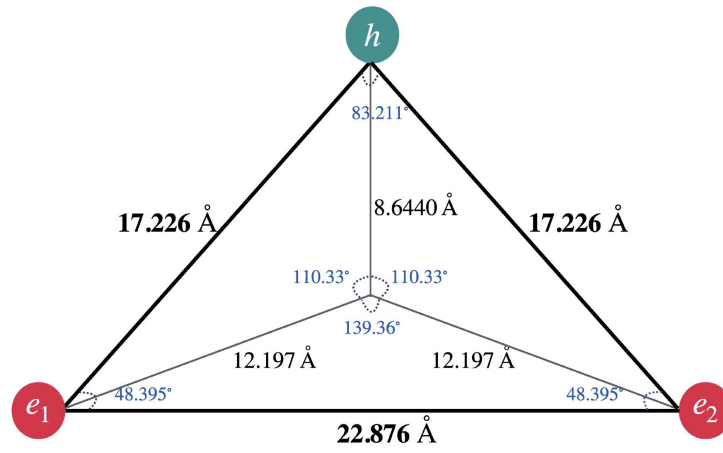


FIGURE 4.7 – The geometrical structure of the calculated trion in configuration space.

5 Four-body System in Two-dimensional Space

5.1 Overview

In this chapter, we explore the application of the Faddeev-Yakubovsky (FY) scheme to the study of four-body (4B) systems in two-dimensional (2D) momentum space. The FY is a robust mathematical framework used to solve the Schrödinger equation for few-body systems, providing a detailed understanding of the interactions and bound states within 4B systems (GIBSON; LEHMAN, 1979; FONSECA, 1984; KAMADA; GLÖCKLE, 1992; GLÖCKLE; KAMADA, 1993; NOGGA *et al.*, 2002; CIESIELSKI; CARBONELL, 1998).

Four-body systems in 2D are particularly relevant in condensed matter physics, where they can be realized as biexcitons in semiconductors. A biexciton is a bound state of two excitons, which are bound states of an electron and a hole. Biexcitons have been observed in various 2D materials, such as transition metal dichalcogenides (TMDs) and layered semiconductors. The formation of biexcitons is influenced by factors such as the strength of the Coulomb interaction, the effective masses of the charge carriers, and the dielectric screening of the environment (KIDD *et al.*, 2016b; SZYNISZEWSKI *et al.*, 2017a; ZHANG *et al.*, 2014; ZHANG *et al.*, 2015b; ZHANG *et al.*, 2015a; KYLÄNPÄÄ; KOMSA, 2015; VELIZHANIN; SAXENA, 2015). The calculations presented in this work have implications for understanding biexcitons' behavior in 2D materials and predicting the properties of novel quantum phases in cold atom systems. The developed theoretical framework can be extended to investigate more complex few-body configurations and to explore the effects of external fields and interactions with other quasiparticles.

The chapter begins with an introduction to the theoretical foundations of the FY approach. We discuss how the FY equations extend the Faddeev equations, initially formulated for three-body systems, to accommodate the complexities of four interacting particles.

We then examine the specific formulation of the FY equations for a 4B system in 2D space. The chapter outlines the derivation of these equations, emphasizing the role

of permutation symmetries and the decomposition of the wave function into components corresponding to different partitions of the 4B system. This decomposition allows for a systematic treatment of the inter-particle interactions and the identification of bound states.

To illustrate the practical application of these techniques, we present numerical results for a specific case involving identical particles interacting through a separable potential. This example serves as a proof of concept, demonstrating the effectiveness of the iterative method in solving the FY equations and providing insights into the binding energies and 4B wave function.

While this chapter focuses on the theoretical and numerical aspects of the FY scheme with separable potential, it is essential to note that these efforts are preparatory steps for more detailed future studies. Specifically, the methodologies and results discussed here are intended to facilitate comprehensive investigations into the physical problem of real 4B systems in 2D like biexcitons. Future research will build upon the foundational work presented in this chapter to explore the interactions, stability, and potential applications of biexcitons in condensed matter physics.

5.2 Faddeev-Yakubovsky equations for four identical particles bound states in two dimensions

The Schrödinger equation for the bound state of four identical particles interacting with pairwise forces is given as

$$(H_o + V_{ij})|\Psi\rangle = E|\Psi\rangle, \quad (5.1)$$

where V_{ij} is the two-body potential, which is given as

$$V_{ij} = v_{12} + v_{13} + v_{14} + v_{23} + v_{24} + v_{34} = \sum_{i < j} v_{ij}. \quad (5.2)$$

Equation (5.1) can be written in the integral form

$$|\Psi\rangle = \frac{1}{E - H_o} V_{ij} |\Psi\rangle \equiv G_o V_{ij} |\Psi\rangle, \quad (5.3)$$

where $G_0 = \frac{1}{E - H_0}$ is the free propagator, and E is 4B binding energy. Then, we introduce the so-called Faddeev component, $|\psi_{ij}\rangle$, and write the wave function as

$$\begin{aligned} |\Psi\rangle &= \sum_{i < j} |\psi_{ij}\rangle \\ &= G_0 t_{ij} (|\psi_{ik}\rangle + |\psi_{il}\rangle + |\psi_{jk}\rangle + |\psi_{jl}\rangle + |\psi_{kl}\rangle), \end{aligned} \quad (5.4)$$

where

$$\begin{aligned} |\psi_{ij}\rangle &= G_0 V_{ij} |\Psi\rangle, \\ &= G_0 V_{ij} \sum_{k < l} |\psi_{kl}\rangle, \\ &= G_0 V_{ij} |\psi_{ij}\rangle + G_0 V_{ij} \sum_{kl \neq ij} |\psi_{kl}\rangle. \end{aligned} \quad (5.5)$$

It is a straightforward way to use the Lippmann-Schwinger equation for the two-body t -matrix

$$t_{ij} = V_{ij} + V_{ij} G_0 t_{ij}, \quad (5.6)$$

and write

$$|\psi_{ij}\rangle = G_0 t_{ij} \sum_{kl \neq ij} |\psi_{kl}\rangle. \quad (5.7)$$

Among various possibilities to decompose $|\psi_{ij}\rangle$ into FY components, we choose the following one

$$\begin{aligned} |\psi_{ijk,l;ij}\rangle &\equiv G_0 t_{ij} (|\psi_{ik}\rangle + |\psi_{jk}\rangle), \\ |\psi_{ijl,k;ij}\rangle &\equiv G_0 t_{ij} (|\psi_{il}\rangle + |\psi_{jl}\rangle), \\ |\psi_{ij,kl;ij}\rangle &\equiv G_0 t_{ij} |\psi_{kl}\rangle. \end{aligned} \quad (5.8)$$

The FY component $|\psi_{ijk,l;ij}\rangle$ belongs to a $3+1$ partition, where a single particle is bound to a three-body subsystem. This notation indicates that the 2B subsystem ij interacts with the third particle k and forms a three-body subsystem. This three-body subsystem, ijk , then interacts with the fourth particle l and constructs the 4B system. On the other hand, the FY component $|\psi_{ij,kl;ij}\rangle$ is associated with a $2+2$ partition, where two dimers are bound. This notation illustrates a scenario where particles i and j form a two-body subsystem while particles k and l form another. These two subsystems, ij and kl , then interact.

Following the notation defined in Eq. (5.8) we can write Eq. (5.7) as

$$|\psi_{ij}\rangle = |\psi_{ijk,l;ij}\rangle + |\psi_{ijl,k;ij}\rangle + |\psi_{ij,kl;ij}\rangle, \quad (5.9)$$

this shows the FY components are indeed a decomposition of the Faddeev equation, and every $|\psi_{ij}\rangle$ component contains two $3+1$ type chains and one $2+2$ type chain. Therefore, wave function $|\Psi\rangle$ contains twelve different $3+1$ type chains and six $2+2$ type chains. As shown in Fig. 5.1, the 4B system, in the general case of not identical particles, has eighteen FY components (HADIZADEH; BAYEGAN, 2007; NOGGA, 2003).

$$1234 \Rightarrow \left\{ \begin{array}{l} 3+1 \rightarrow \left\{ \begin{array}{l} 123, 4 \rightarrow \left\{ \begin{array}{l} 12, 3, 4 \equiv \psi_{123,4;12} \\ 13, 2, 4 \equiv \psi_{123,4;13} \\ 23, 1, 4 \equiv \psi_{123,4;23} \end{array} \right. \\ 124, 3 \rightarrow \left\{ \begin{array}{l} 12, 4, 3 \equiv \psi_{124,3;12} \\ 14, 2, 3 \equiv \psi_{124,3;14} \\ 24, 1, 3 \equiv \psi_{124,3;24} \end{array} \right. \\ 134, 2 \rightarrow \left\{ \begin{array}{l} 13, 4, 2 \equiv \psi_{134,2;13} \\ 14, 3, 2 \equiv \psi_{134,2;14} \\ 34, 1, 2 \equiv \psi_{134,2;34} \end{array} \right. \\ 234, 1 \rightarrow \left\{ \begin{array}{l} 23, 4, 1 \equiv \psi_{234,1;23} \\ 24, 3, 1 \equiv \psi_{234,1;24} \\ 34, 2, 1 \equiv \psi_{234,1;34} \end{array} \right. \end{array} \right. \\ 2+2 \rightarrow \left\{ \begin{array}{l} 12, 34 \rightarrow \left\{ \begin{array}{l} 12, 3, 4 \equiv \psi_{12,34;12} \\ 34, 1, 2 \equiv \psi_{12,34;34} \end{array} \right. \\ 13, 24 \rightarrow \left\{ \begin{array}{l} 13, 2, 4 \equiv \psi_{13,24;13} \\ 24, 1, 3 \equiv \psi_{13,24;24} \end{array} \right. \\ 14, 23 \rightarrow \left\{ \begin{array}{l} 14, 2, 3 \equiv \psi_{14,23;14} \\ 23, 1, 4 \equiv \psi_{14,23;23} \end{array} \right. \end{array} \right. \end{array} \right.$$

FIGURE 5.1 – Eighteen different configurations of the 4B system.

If we consider identical particles (here bosons since we are omitting spin), the four-body wave function $|\Psi\rangle$ has to be fully symmetric. Consequently, all twelve components of the $3+1$ type are identical in their functional form, and only the particles are permuted. The same is true for the six components of $2+2$ type. Therefore, we consider a system where particle 1 and 2 are constructing the two-body subsystem and rewriting Eq. (5.9)

for this system as

$$\begin{aligned}
|\psi_{12}\rangle &= G_0 t_{12}(|\psi_{13}\rangle + |\psi_{23}\rangle + |\psi_{14}\rangle + |\psi_{24}\rangle + |\psi_{34}\rangle) \\
&= G_0 t_{12}(|\psi_{13}\rangle + |\psi_{23}\rangle) \\
&+ G_0 t_{12}(|\psi_{14}\rangle + |\psi_{24}\rangle) \\
&+ G_0 t_{12}|\psi_{34}\rangle \\
&= |\psi_{123,4;12}\rangle + |\psi_{124,3;12}\rangle + |\psi_{12,34;12}\rangle,
\end{aligned} \tag{5.10}$$

in the last line, we use Eq. (5.9). To simplify the notation, let's use $|\psi_1\rangle = |\psi_{123,4;12}\rangle$ and $|\psi_2\rangle = |\psi_{12,34;12}\rangle$. We can write the second term of the Eq. (5.10) with permuting between the particles 3 and 4, therefore

$$|\psi_{12}\rangle = |\psi_1\rangle + P_{34}|\psi_1\rangle + |\psi_2\rangle, \tag{5.11}$$

where P_{34} is the permutation operator between particles 3 and 4. In Ref. (HADIZADEH; BAYEGAN, 2007), it is shown that from Eq. (5.8), we can obtain the following equations

$$\begin{aligned}
|\psi_1\rangle &= G_0 t_{12} P[(1 + P_{34})|\psi_1\rangle + |\psi_2\rangle], \\
|\psi_2\rangle &= G_0 t_{12} \tilde{P}[(1 + P_{34})|\psi_1\rangle + |\psi_2\rangle],
\end{aligned} \tag{5.12}$$

where P and \tilde{P} are the permutation operators and define as

$$\begin{aligned}
P &= P_{12}P_{23} + P_{13}P_{23}, \\
\tilde{P} &= P_{13}P_{24}.
\end{aligned} \tag{5.13}$$

The four-body wave function is the sum of all 18 Yakubovsky components

$$\begin{aligned}
|\Psi\rangle &= |\psi_{12}\rangle + |\psi_{13}\rangle + |\psi_{14}\rangle + |\psi_{23}\rangle + |\psi_{24}\rangle + |\psi_{34}\rangle \\
&= |\psi_{12}\rangle + P_{12}P_{23}|\psi_{12}\rangle + P_{13}P_{23}|\psi_{12}\rangle + P_{34}|\psi_{13}\rangle + P_{34}|\psi_{23}\rangle + P_{13}P_{24}|\psi_{12}\rangle \\
&= |\psi_{12}\rangle + (P_{12}P_{23} + P_{13}P_{23} + P_{14})|\psi_1\rangle + P_{34}(P_{12}P_{23} + P_{13}P_{23})|\psi_1\rangle + P_{13}P_{24}|\psi_1\rangle \\
&= |\psi_{12}\rangle + P|\psi_{12}\rangle + P_{34}P|\psi_{12}\rangle + \tilde{P}|\psi_{12}\rangle \\
&= (1 + P + P_{34}P + \tilde{P})|\psi_{12}\rangle \\
&= (1 + P + P_{34}P + \tilde{P})[(1 + P_{34})|\psi_1\rangle + |\psi_2\rangle],
\end{aligned} \tag{5.14}$$

in the last line, we used Eq. (5.11). The 3 + 1 and 2 + 2 components can be written separately in Eq. (5.14) and

$$|\Psi\rangle = |\Psi_1\rangle + |\Psi_2\rangle, \tag{5.15}$$

where

$$\begin{aligned} |\Psi_1\rangle &= (1 + P + P_{34}P + \tilde{P})(1 + P_{34})|\psi_1\rangle \\ |\Psi_2\rangle &= (1 + P + P_{34}P + \tilde{P})|\psi_2\rangle. \end{aligned} \quad (5.16)$$

The symmetry property of $|\psi_1\rangle$ under exchange of particles 1 and 2, and $|\psi_2\rangle$ under separate exchanges of particles 1, 2 and 3, 4 guarantee that $|\Psi\rangle$ is totally symmetric.

5.2.1 Momentum space representation of Faddeev-Yakubovsky equations

To solve the coupled Eqs. (5.12), in 2D momentum space, we introduce standard Jacobi momenta sets corresponding to both 3 + 1 (123, 4; 12) and 2 + 2 (12, 34; 12) chains. We denote the Jacobi momenta for the 3 + 1 partition with \mathbf{u}_i and the 2 + 2 partition with \mathbf{v}_i . These Jacobi momenta are defined as

$$\begin{aligned} \mathbf{u}_1 &= \frac{\mathbf{k}_1 - \mathbf{k}_2}{2}, & \mathbf{v}_1 &= \frac{\mathbf{k}_1 - \mathbf{k}_2}{2}, \\ \mathbf{u}_2 &= \frac{2}{3}(\mathbf{k}_3 - \frac{\mathbf{k}_1 + \mathbf{k}_2}{2}), & \mathbf{v}_2 &= \frac{\mathbf{k}_1 + \mathbf{k}_2}{2} - \frac{\mathbf{k}_3 + \mathbf{k}_4}{2}, \\ \mathbf{u}_3 &= \frac{3}{4}(\mathbf{k}_4 - \frac{\mathbf{k}_1 + \mathbf{k}_2 + \mathbf{k}_3}{3}), & \mathbf{v}_3 &= \frac{\mathbf{k}_3 - \mathbf{k}_4}{2}. \end{aligned} \quad (5.17)$$

As shown in Fig. 5.2, the momentum vector \mathbf{u}_1 represents the momentum of particles 1 and 2 in the center of the mass frame of the binary system (12). The momentum vector \mathbf{u}_2 represents the momentum of particle 3 in the center of mass frame of the three-body system (123), and the momentum vector \mathbf{u}_3 represents the momentum of particle 4 in the center of mass frame of the four-body system (1234). The momentum vectors \mathbf{v}_1 and \mathbf{v}_3 represent the momentum of particles 1, 2, and 3, 4, respectively, in the center of mass frame of the binary systems (12) and (34). The momentum vector \mathbf{v}_2 represents the momentum of these two binary subsystems in their center of mass frame.

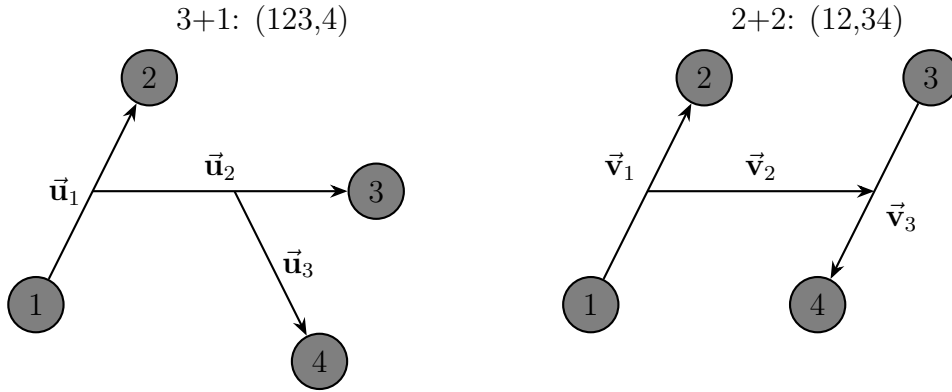


FIGURE 5.2 – Definition of the four-body Jacobi momenta corresponding to the ψ_1 and ψ_2 type fragmentations.

The 4B basis states corresponding to each Jacobi momenta set are defined by

$$\begin{aligned} &|\mathbf{u}_1 \mathbf{u}_2 \mathbf{u}_3\rangle, \\ &|\mathbf{v}_1 \mathbf{v}_2 \mathbf{v}_3\rangle, \end{aligned} \quad (5.18)$$

These two basis states are complete in the 4B Hilbert space

$$\int D^2 A \quad |\mathbf{A}_1 \mathbf{A}_2 \mathbf{A}_3\rangle \langle \mathbf{A}_1 \mathbf{A}_2 \mathbf{A}_3| = 1, \quad (5.19)$$

where \mathbf{A}_i indicates each one of \mathbf{u}_i and \mathbf{v}_i vectors and $D^2 A \equiv d^2 A_1 d^2 A_2 d^2 A_3$. Also, they are normalized according to

$$\langle \mathbf{A}_1 \mathbf{A}_2 \mathbf{A}_3 | \mathbf{A}'_1 \mathbf{A}'_2 \mathbf{A}'_3 \rangle = \delta^2(\mathbf{A}_1 - \mathbf{A}'_1) \delta^2(\mathbf{A}_2 - \mathbf{A}'_2) \delta^2(\mathbf{A}_3 - \mathbf{A}'_3). \quad (5.20)$$

Now, we project Eqs. (5.12), into basis states introduced in Eq. (5.18)

$$\begin{aligned} \langle \mathbf{u}_1 \mathbf{u}_2 \mathbf{u}_3 | \psi_1 \rangle &= \int D^2 u'' \langle \mathbf{u}_1 \mathbf{u}_2 \mathbf{u}_3 | G_0 t P (1 + P_{34}) | \mathbf{u}''_1 \mathbf{u}''_2 \mathbf{u}''_3 \rangle \langle \mathbf{u}''_1 \mathbf{u}''_2 \mathbf{u}''_3 | \psi_1 \rangle \\ &+ \int D^2 v' \langle \mathbf{u}_1 \mathbf{u}_2 \mathbf{u}_3 | G_0 t P | \mathbf{v}'_1 \mathbf{v}'_2 \mathbf{v}'_3 \rangle \langle \mathbf{v}'_1 \mathbf{v}'_2 \mathbf{v}'_3 | \psi_2 \rangle, \\ \langle \mathbf{v}_1 \mathbf{v}_2 \mathbf{v}_3 | \psi_2 \rangle &= \int D^2 u' \langle \mathbf{v}_1 \mathbf{v}_2 \mathbf{v}_3 | G_0 t \tilde{P} (1 + P_{34}) | \mathbf{u}'_1 \mathbf{u}'_2 \mathbf{u}'_3 \rangle \langle \mathbf{u}'_1 \mathbf{u}'_2 \mathbf{u}'_3 | \psi_1 \rangle \\ &+ \int D^2 v' \langle \mathbf{v}_1 \mathbf{v}_2 \mathbf{v}_3 | G_0 t \tilde{P} | \mathbf{v}'_1 \mathbf{v}'_2 \mathbf{v}'_3 \rangle \langle \mathbf{v}'_1 \mathbf{v}'_2 \mathbf{v}'_3 | \psi_2 \rangle. \end{aligned}$$

It is convenient to insert again the completeness relations between permutation operators, it results

$$\begin{aligned} \langle \mathbf{u}_1 \mathbf{u}_2 \mathbf{u}_3 | \psi_1 \rangle &= \int D^2 u' \int D^2 u'' \langle \mathbf{u}_1 \mathbf{u}_2 \mathbf{u}_3 | G_0 t P | \mathbf{u}'_1 \mathbf{u}'_2 \mathbf{u}'_3 \rangle \\ &\times \langle \mathbf{u}'_1 \mathbf{u}'_2 \mathbf{u}'_3 | (1 + P_{34}) | \mathbf{u}''_1 \mathbf{u}''_2 \mathbf{u}''_3 \rangle \langle \mathbf{u}''_1 \mathbf{u}''_2 \mathbf{u}''_3 | \psi_1 \rangle \end{aligned}$$

$$\begin{aligned}
& + \int D^2 u' \int D^2 v' \langle \mathbf{u}_1 \mathbf{u}_2 \mathbf{u}_3 | G_0 t P | \mathbf{u}'_1 \mathbf{u}'_2 \mathbf{u}'_3 \rangle \\
& \quad \times \langle \mathbf{u}'_1 \mathbf{u}'_2 \mathbf{u}'_3 | \mathbf{v}'_1 \mathbf{v}'_2 \mathbf{v}'_3 \rangle \langle \mathbf{v}'_1 \mathbf{v}'_2 \mathbf{v}'_3 | \psi_2 \rangle, \\
\langle \mathbf{v}_1 \mathbf{v}_2 \mathbf{v}_3 | \psi_2 \rangle & = \int D^2 v' \int D^2 u' \langle \mathbf{v}_1 \mathbf{v}_2 \mathbf{v}_3 | G_0 t \tilde{P} | \mathbf{v}'_1 \mathbf{v}'_2 \mathbf{v}'_3 \rangle \\
& \quad \times \langle \mathbf{v}'_1 \mathbf{v}'_2 \mathbf{v}'_3 | (1 + P_{34}) | \mathbf{u}'_1 \mathbf{u}'_2 \mathbf{u}'_3 \rangle \langle \mathbf{u}'_1 \mathbf{u}'_2 \mathbf{u}'_3 | \psi_1 \rangle \\
& + \int D^2 v' \langle \mathbf{v}_1 \mathbf{v}_2 \mathbf{v}_3 | G_0 t \tilde{P} | \mathbf{v}'_1 \mathbf{v}'_2 \mathbf{v}'_3 \rangle \langle \mathbf{v}'_1 \mathbf{v}'_2 \mathbf{v}'_3 | \psi_2 \rangle. \tag{5.21}
\end{aligned}$$

For evaluating the coupled equations, Eq. (5.21), we need to evaluate the following matrix elements

$$\begin{aligned}
& \langle \mathbf{u}_1 \mathbf{u}_2 \mathbf{u}_3 | G_0 t P | \mathbf{u}'_1 \mathbf{u}'_2 \mathbf{u}'_3 \rangle, \\
& \langle \mathbf{v}_1 \mathbf{v}_2 \mathbf{v}_3 | G_0 t \tilde{P} | \mathbf{v}'_1 \mathbf{v}'_2 \mathbf{v}'_3 \rangle, \\
& \langle \mathbf{u}'_1 \mathbf{u}'_2 \mathbf{u}'_3 | (1 + P_{34}) | \mathbf{u}''_1 \mathbf{u}''_2 \mathbf{u}''_3 \rangle, \\
& \langle \mathbf{v}'_1 \mathbf{v}'_2 \mathbf{v}'_3 | (1 + P_{34}) | \mathbf{u}'_1 \mathbf{u}'_2 \mathbf{u}'_3 \rangle. \tag{5.22}
\end{aligned}$$

Details of evaluating the matrix elements of Eqs. (5.22) are presented in appendix H, and the results are

$$\begin{aligned}
\langle \mathbf{u}_1 \mathbf{u}_2 \mathbf{u}_3 | G_0 t P | \mathbf{u}'_1 \mathbf{u}'_2 \mathbf{u}'_3 \rangle & = \frac{\delta^2(\mathbf{u}_3 - \mathbf{u}'_3)}{E - \frac{u_1^2}{m} - \frac{3u_2^2}{4m} - \frac{2u_3^2}{3m}} \\
& \quad \left\{ \delta^2(\mathbf{u}_2 + \mathbf{u}'_1 + \frac{1}{2}\mathbf{u}'_2) \langle \mathbf{u}_1 | t(\epsilon) | \frac{1}{2}\mathbf{u}_2 + \mathbf{u}'_2 \rangle \right. \\
& \quad \left. + \delta^2(\mathbf{u}_2 - \mathbf{u}'_1 + \frac{1}{2}\mathbf{u}'_2) \langle \mathbf{u}_1 | t(\epsilon) | \frac{-1}{2}\mathbf{u}_2 - \mathbf{u}'_2 \rangle \right\}, \tag{5.23}
\end{aligned}$$

$$\langle \mathbf{v}_1 \mathbf{v}_2 \mathbf{v}_3 | G_0 t \tilde{P} | \mathbf{v}'_1 \mathbf{v}'_2 \mathbf{v}'_3 \rangle = \frac{\delta^2(\mathbf{v}_2 + \mathbf{v}'_2) \delta^2(\mathbf{v}_3 - \mathbf{v}'_1)}{E - \frac{v_1^2}{m} - \frac{v_2^2}{2m} - \frac{v_3^2}{m}} \langle \mathbf{v}_1 | t(\epsilon^*) | \mathbf{v}'_3 \rangle, \tag{5.24}$$

$$\begin{aligned}
\langle \mathbf{u}'_1 \mathbf{u}'_2 \mathbf{u}'_3 | (1 + P_{34}) | \mathbf{u}''_1 \mathbf{u}''_2 \mathbf{u}''_3 \rangle & = \delta^2(\mathbf{u}'_1 - \mathbf{u}''_1) \\
& \times \left\{ \delta^2(\mathbf{u}'_2 - \mathbf{u}''_2) \delta^2(\mathbf{u}'_3 - \mathbf{u}''_3) \right. \\
& \quad \left. + \delta^2(\mathbf{u}'_2 - \frac{1}{3}\mathbf{u}''_2 - \frac{8}{9}\mathbf{u}''_3) \delta^2(\mathbf{u}'_3 - \mathbf{u}''_2 + \frac{1}{3}\mathbf{u}''_3) \right\}, \tag{5.25}
\end{aligned}$$

$$\begin{aligned}
\langle \mathbf{v}'_1 \mathbf{v}'_2 \mathbf{v}'_3 | (1 + P_{34}) | \mathbf{u}'_1 \mathbf{u}'_2 \mathbf{u}'_3 \rangle & = \langle \mathbf{v}'_1 \mathbf{v}'_2 \mathbf{v}'_3 | \mathbf{u}'_1 \mathbf{u}'_2 \mathbf{u}'_3 \rangle + {}_{123,4;12} \langle \mathbf{v}'_1 \mathbf{v}'_2 \mathbf{v}'_3 | \mathbf{u}'_1 \mathbf{u}'_2 \mathbf{u}'_3 \rangle {}_{124,3;12} \\
& = \delta^2(\mathbf{u}'_1 - \mathbf{v}'_1) \\
& \times \left\{ \delta^2(\mathbf{u}'_2 + \frac{2}{3}\mathbf{v}'_2 - \frac{2}{3}\mathbf{v}'_3) \delta^2(\mathbf{u}'_3 + \frac{1}{2}\mathbf{v}'_2 + \mathbf{v}'_3) \right. \\
& \quad \left. + \delta^2(\mathbf{u}'_2 + \frac{2}{3}\mathbf{v}'_2 + \frac{2}{3}\mathbf{v}'_3) \delta^2(\mathbf{u}'_3 + \frac{1}{2}\mathbf{v}'_2 - \mathbf{v}'_3) \right\}. \tag{5.26}
\end{aligned}$$

Inserting Eqs. (5.23), (5.24), (5.25) and (5.26) in Eq. (5.21), and eliminating the two-dimensional integrals by the delta functions yields the following coupled integral equations for the FY components

$$\begin{aligned} \langle \mathbf{u}_1 \mathbf{u}_2 \mathbf{u}_3 | \psi_1 \rangle &= \frac{1}{E - \frac{u_1^2}{m} - \frac{3u_2^2}{4m} - \frac{2u_3^2}{3m}} \int d^2 u'_2 \langle \mathbf{u}_1 | t_s(\epsilon) | \frac{1}{2} \mathbf{u}_2 + \mathbf{u}'_2 \rangle \\ &\times \left\{ \langle \mathbf{u}_2 + \frac{1}{2} \mathbf{u}'_2, \mathbf{u}'_2, \mathbf{u}_3 | \psi_1 \rangle \right. \\ &+ \langle \mathbf{u}_2 + \frac{1}{2} \mathbf{u}'_2, \frac{1}{3} \mathbf{u}'_2 + \frac{8}{9} \mathbf{u}_3, \mathbf{u}'_2 - \frac{1}{3} \mathbf{u}_3 | \psi_1 \rangle \\ &+ \left. \langle \mathbf{u}_2 + \frac{1}{2} \mathbf{u}'_2, -\mathbf{u}'_2 - \frac{2}{3} \mathbf{u}_3, \frac{1}{2} \mathbf{u}'_2 - \frac{2}{3} \mathbf{u}_3 | \psi_2 \rangle \right\}, \end{aligned} \quad (5.27)$$

$$\begin{aligned} \langle \mathbf{v}_1 \mathbf{v}_2 \mathbf{v}_3 | \psi_2 \rangle &= \frac{\frac{1}{2}}{E - \frac{v_1^2}{m} - \frac{v_2^2}{2m} - \frac{v_3^2}{m}} \int d^2 v'_3 \langle \mathbf{v}_1 | t_s(\epsilon^*) | \mathbf{v}'_3 \rangle \\ &\times \left\{ 2 \langle \mathbf{v}_3, \frac{2}{3} \mathbf{v}_2 + \frac{2}{3} \mathbf{v}'_3, \frac{1}{2} \mathbf{v}_2 - \mathbf{v}'_3 | \psi_1 \rangle + \langle \mathbf{v}_3, -\mathbf{v}_2, \mathbf{v}'_3 | \psi_2 \rangle \right\} \end{aligned} \quad (5.28)$$

Here $\langle \mathbf{a} | t_s(\epsilon) | \mathbf{b} \rangle$ generally represents the symmetrized two-body t -matrix, which is defined as

$$\langle \mathbf{a} | t_s(\epsilon) | \mathbf{b} \rangle = \langle \mathbf{a} | t(\epsilon) | \mathbf{b} \rangle + \langle \mathbf{a} | t(\epsilon) | -\mathbf{b} \rangle. \quad (5.29)$$

5.2.2 Momentum space representation of Faddeev-Yakubovsky equations with separable potential

As mentioned in chapter 2, the two body t -matrix for the separable potential has a separable form and it is given by

$$t(\mathbf{p}, \mathbf{p}', \epsilon) = \frac{1}{2\pi} t(p, p', \epsilon) = \frac{1}{2\pi} \tau(\epsilon) g(p) g(p'), \quad (5.30)$$

where the reduced scattering amplitude $\tau(\epsilon)$, given by

$$\tau(\epsilon) = \left[\lambda^{-1} - \int d^2 p \frac{g^2(p)}{\epsilon - p^2/m} \right]^{-1}, \quad (5.31)$$

and the potential strength λ can be obtained by the pole property of the 2B t -matrix at $\epsilon = B_2$

$$\lambda^{-1} = \int d^2 p \frac{g^2(p)}{B_2 - p^2/m}. \quad (5.32)$$

By using Eq. (5.30), we can simplify Eqs. (5.27) and (5.28) as

$$\langle \mathbf{u}_1 \mathbf{u}_2 \mathbf{u}_3 | \psi_1 \rangle = G_0(u_1, u_2, u_3) \int d^2 u'_2 \frac{2}{2\pi} \tau(\epsilon) g(\mathbf{u}_1) g\left(\frac{1}{2} \mathbf{u}_2 + \mathbf{u}'_2\right)$$

$$\begin{aligned} & \times \left\{ \langle \mathbf{u}_2 + \frac{1}{2}\mathbf{u}'_2, \mathbf{u}'_2, \mathbf{u}_3 | \psi_1 \rangle \right. \\ & + \langle \mathbf{u}_2 + \frac{1}{2}\mathbf{u}'_2, \frac{1}{3}\mathbf{u}'_2 + \frac{8}{9}\mathbf{u}_3, \mathbf{u}'_2 - \frac{1}{3}\mathbf{u}_3 | \psi_1 \rangle \\ & \left. + \langle \mathbf{u}_2 + \frac{1}{2}\mathbf{u}'_2, -\mathbf{u}'_2 - \frac{2}{3}\mathbf{u}_3, \frac{1}{2}\mathbf{u}'_2 - \frac{2}{3}\mathbf{u}_3 | \psi_2 \rangle \right\}, \end{aligned} \quad (5.33)$$

$$\begin{aligned} \langle \mathbf{v}_1 \mathbf{v}_2 \mathbf{v}_3 | \psi_2 \rangle &= \frac{1}{2} G_0(v_1, v_2, v_3) \times \int d^2 v'_3 \frac{2}{2\pi} \tau(\epsilon^*) g(\mathbf{v}_1) g(\mathbf{v}'_3) \\ &\times \left\{ 2 \langle \mathbf{v}_3, \frac{2}{3}\mathbf{v}_2 + \frac{2}{3}\mathbf{v}'_3, \frac{1}{2}\mathbf{v}_2 - \mathbf{v}'_3 | \psi_1 \rangle + \langle \mathbf{v}_3, -\mathbf{v}_2, \mathbf{v}'_3 | \psi_2 \rangle \right\} \end{aligned} \quad (5.34)$$

By taking the independent argument outside of the integrals, we can rewrite Eqs. (5.33) and (5.34) as

$$\begin{aligned} \langle \mathbf{u}_1 \mathbf{u}_2 \mathbf{u}_3 | \psi_1 \rangle &= \frac{1}{\pi} G_0(u_1, u_2, u_3) \tau(\epsilon) g(\mathbf{u}_1) \int d^2 u'_2 g(\frac{1}{2}\mathbf{u}_2 + \mathbf{u}'_2) \\ &\times \left\{ \langle \mathbf{u}_2 + \frac{1}{2}\mathbf{u}'_2, \mathbf{u}'_2, \mathbf{u}_3 | \psi_1 \rangle \right. \\ &+ \langle \mathbf{u}_2 + \frac{1}{2}\mathbf{u}'_2, \frac{1}{3}\mathbf{u}'_2 + \frac{8}{9}\mathbf{u}_3, \mathbf{u}'_2 - \frac{1}{3}\mathbf{u}_3 | \psi_1 \rangle \\ &+ \langle \mathbf{u}_2 + \frac{1}{2}\mathbf{u}'_2, -\mathbf{u}'_2 - \frac{2}{3}\mathbf{u}_3, \frac{1}{2}\mathbf{u}'_2 - \frac{2}{3}\mathbf{u}_3 | \psi_2 \rangle \left. \right\}, \end{aligned} \quad (5.35)$$

$$\begin{aligned} \langle \mathbf{v}_1 \mathbf{v}_2 \mathbf{v}_3 | \psi_2 \rangle &= \frac{1}{\pi} G_0(v_1, v_2, v_3) \tau(\epsilon^*) g(\mathbf{v}_1) \int d^2 v'_3 g(\mathbf{v}'_3) \\ &\times \left\{ \langle \mathbf{v}_3, \frac{2}{3}\mathbf{v}_2 + \frac{2}{3}\mathbf{v}'_3, \frac{1}{2}\mathbf{v}_2 - \mathbf{v}'_3 | \psi_1 \rangle + \frac{1}{2} \langle \mathbf{v}_3, -\mathbf{v}_2, \mathbf{v}'_3 | \psi_2 \rangle \right\} \end{aligned} \quad (5.36)$$

where the free propagator for $3 + 1$ and $2 + 2$ clusters is given as

$$G_0(u_1, u_2, u_3) = \frac{1}{E - \frac{u_1^2}{m} - \frac{3u_2^2}{4m} - \frac{2u_3^2}{3m}}; \quad G_0(v_1, v_2, v_3) = \frac{1}{E - \frac{v_1^2}{m} - \frac{v_2^2}{2m} - \frac{v_3^2}{m}}. \quad (5.37)$$

As is shown in Ref. (HADIZADEH *et al.*, 2012), Eqs. (5.35) and (5.36) for a separable potential can be written as within new definition of FY components as

$$\begin{aligned} \psi_1(\mathbf{u}_1, \mathbf{u}_2, \mathbf{u}_3) &= G_0(u_1, u_2, u_3) g(\mathbf{u}_1) \mathcal{K}(\mathbf{u}_2, \mathbf{u}_3), \\ \psi_2(\mathbf{v}_1, \mathbf{v}_2, \mathbf{v}_3) &= G_0(v_1, v_2, v_3) g(\mathbf{v}_1) \mathcal{H}(\mathbf{v}_2, \mathbf{v}_3). \end{aligned} \quad (5.38)$$

By using the new definition given in Eq. (5.38), we can rewrite Eqs. (5.35) and (5.36) as

$$\begin{aligned} \mathcal{K}(\mathbf{u}_2, \mathbf{u}_3) &= \frac{1}{\pi} \tau(\epsilon) \int d^2 u'_2 g(\frac{1}{2}\mathbf{u}_2 + \mathbf{u}'_2) g(\mathbf{u}_2 + \frac{1}{2}\mathbf{u}'_2) \\ &\times \left\{ G_0(|\mathbf{u}_2 + \frac{1}{2}\mathbf{u}'_2|, u'_2, u_3) \mathcal{K}(\mathbf{u}'_2, \mathbf{u}_3) \right. \\ &+ G_0(|\mathbf{u}_2 + \frac{1}{2}\mathbf{u}'_2|, |\frac{1}{3}\mathbf{u}'_2 + \frac{8}{9}\mathbf{u}_3|, |\mathbf{u}'_2 - \frac{1}{3}\mathbf{u}_3|) \mathcal{K}(\frac{1}{3}\mathbf{u}'_2 + \frac{8}{9}\mathbf{u}_3, \mathbf{u}'_2 - \frac{1}{3}\mathbf{u}_3) \\ &+ G_0(|\mathbf{u}_2 + \frac{1}{2}\mathbf{u}'_2|, |-\mathbf{u}'_2 - \frac{2}{3}\mathbf{u}_3|, |\frac{1}{2}\mathbf{u}'_2 - \frac{2}{3}\mathbf{u}_3|) \end{aligned}$$

$$\times \mathcal{H}(-\mathbf{u}'_2 - \frac{2}{3}\mathbf{u}_3, \frac{1}{2}\mathbf{u}'_2 - \frac{2}{3}\mathbf{u}_3) \Big\}, \quad (5.39)$$

$$\begin{aligned} \mathcal{H}(\mathbf{v}_2, \mathbf{v}_3) &= \frac{1}{\pi} \tau(\epsilon^*) \int d^2 v'_3 g(\mathbf{v}'_3) g(\mathbf{v}_3) \\ &\times \left\{ G_0(v_3, |\frac{2}{3}\mathbf{v}_2 + \frac{2}{3}\mathbf{v}'_3|, |\frac{1}{2}\mathbf{v}_2 - \mathbf{v}'_3|) \mathcal{K}(\frac{2}{3}\mathbf{v}_2 + \frac{2}{3}\mathbf{v}'_3, \frac{1}{2}\mathbf{v}_2 - \mathbf{v}'_3) \right. \\ &\quad \left. + \frac{1}{2} G_0(v_3, -v_2, v'_3) \mathcal{H}(-\mathbf{v}_2, \mathbf{v}'_3) \right\}. \end{aligned} \quad (5.40)$$

To solve the two-dimensional integral Eqs. (5.39) and (5.40), as shown in Fig. 5.3, we choose a coordinate system where \mathbf{u}_3 and \mathbf{v}_2 are parallel to the x -axis, and other vectors are free in 2D space.

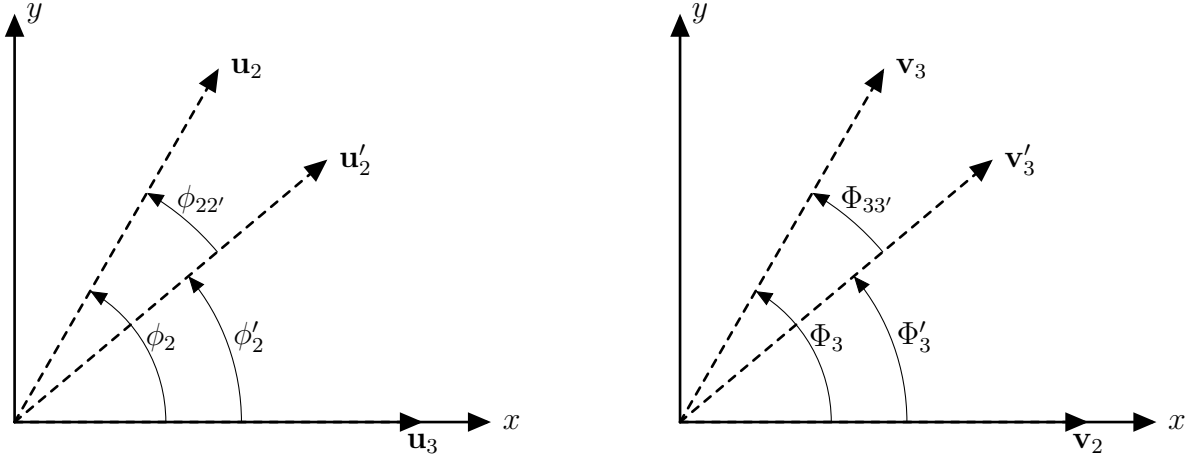


FIGURE 5.3 – Coordinate system for the solution of integral equations (5.39) and (5.40).

And the angle variables are defined as

$$\begin{aligned} (\hat{\mathbf{u}}_3, \hat{\mathbf{u}}_2) &= \phi_2, \\ (\hat{\mathbf{u}}_3, \hat{\mathbf{u}}'_2) &= \phi'_2, \\ (\hat{\mathbf{u}}_2, \hat{\mathbf{u}}'_2) &\equiv \phi_{22'} = \phi_2 - \phi'_2, \\ (\hat{\mathbf{v}}_2, \hat{\mathbf{v}}_3) &= \Phi_3, \\ (\hat{\mathbf{v}}_2, \hat{\mathbf{v}}'_3) &= \Phi'_3, \\ (\hat{\mathbf{v}}_3, \hat{\mathbf{v}}'_3) &\equiv \Phi_{33'} = \Phi'_3 - \Phi_3. \end{aligned} \quad (5.41)$$

By considering the coordinate system defined in Fig. 5.3 and the angle variable in Eq. (5.41), we can write Eqs. (5.39) and (5.40) as

$$\begin{aligned} \mathcal{K}(u_2, u_3, \phi_2) &= \frac{1}{\pi} \tau(\epsilon) \int_0^\infty du'_2 u'_2 \int_0^{2\pi} d\phi'_2 g(\tilde{\pi}) g(\pi_1) \\ &\times \left\{ G_0(\pi_1, u'_2, u_3) \mathcal{K}(u'_2, u_3, \phi'_2) \right. \\ &\quad \left. + G_0(\pi_1, \pi_2, \pi_3) \mathcal{K}(\pi_2, \pi_3, \phi_{\pi_2\pi_3}) \right\} \end{aligned}$$

$$+G_0(\pi_1, \pi_4, \pi_5)\mathcal{H}(\pi_4, \pi_5, \phi_{\pi_4\pi_5})\Big\}, \quad (5.42)$$

$$\begin{aligned} \mathcal{H}(v_2, v_3, \Phi_3) &= \frac{1}{\pi}\tau(\epsilon^*) \int_0^\infty dv'_3 v'_3 \int_0^{2\pi} d\Phi'_3 g(v'_3)g(v_3) \\ &\times \left\{ G_0(v_3, \Sigma_1, \Sigma_2)\mathcal{K}(\Sigma_1, \Sigma_2, \Phi_{\Sigma_1\Sigma_2}) \right. \\ &\quad \left. + \frac{1}{2}G_0(v_3, |-v_2|, v'_3)\mathcal{H}(|-v_2|, v'_3, \pi - \Phi'_3) \right\}, \end{aligned} \quad (5.43)$$

where the shifted momentum arguments are defined as

$$\begin{aligned} \tilde{\pi} &\equiv \tilde{\pi}(u_2, u'_2, \phi_2, \phi'_2) = \left| \frac{1}{2}\mathbf{u}_2 + \mathbf{u}'_2 \right| = \sqrt{(\tilde{\pi}^X)^2 + (\tilde{\pi}^Y)^2}, \\ \pi_1 &\equiv \pi_1(u_2, u'_2, \phi_2, \phi'_2) = \left| \mathbf{u}_2 + \frac{1}{2}\mathbf{u}'_2 \right| = \sqrt{(\pi_1^X)^2 + (\pi_1^Y)^2}, \\ \pi_2 &\equiv \pi_2(u'_2, u_3, \phi'_2) = \left| \frac{1}{3}\mathbf{u}'_2 + \frac{8}{9}\mathbf{u}_3 \right| = \sqrt{(\pi_2^X)^2 + (\pi_2^Y)^2}, \\ \pi_3 &\equiv \pi_3(u'_2, u_3, \phi'_2) = \left| \mathbf{u}'_2 - \frac{1}{3}\mathbf{u}_3 \right| = \sqrt{(\pi_3^X)^2 + (\pi_3^Y)^2}, \\ \pi_4 &\equiv \pi_4(u'_2, u_3, \phi'_2) = \left| -\mathbf{u}'_2 - \frac{2}{3}\mathbf{u}_3 \right| = \sqrt{(\pi_4^X)^2 + (\pi_4^Y)^2}, \\ \pi_5 &\equiv \pi_5(u'_2, u_3, \phi'_2) = \left| \frac{1}{2}\mathbf{u}'_2 - \frac{2}{3}\mathbf{u}_3 \right| = \sqrt{(\pi_5^X)^2 + (\pi_5^Y)^2}. \end{aligned} \quad (5.44)$$

$$\begin{aligned} \Sigma_1 &\equiv \Sigma_1(v_2, v'_3, \Phi'_3) = \left| \frac{2}{3}\mathbf{v}_2 + \frac{2}{3}\mathbf{v}'_3 \right| = \frac{2}{3}\sqrt{(\Sigma_1^X)^2 + (\Sigma_1^Y)^2}, \\ \Sigma_2 &\equiv \Sigma_2(v_2, v'_3, \Phi'_3) = \left| \frac{1}{2}\mathbf{v}_2 - \mathbf{v}'_3 \right| = \sqrt{(\Sigma_2^X)^2 + (\Sigma_2^Y)^2}, \end{aligned} \quad (5.45)$$

where

$$\begin{aligned} \tilde{\pi}^X &= \frac{1}{2}u_2 \cos(\phi_2) + u'_2 \cos(\phi'_2), \\ \tilde{\pi}^Y &= \frac{1}{2}u_2 \sin(\phi_2) + u'_2 \sin(\phi'_2), \\ \pi_1^X &= u_2 \cos(\phi_2) + \frac{1}{2}u'_2 \cos(\phi'_2), \\ \pi_1^Y &= u_2 \sin(\phi_2) + \frac{1}{2}u'_2 \sin(\phi'_2), \\ \pi_2^X &= \frac{1}{3}u'_2 \cos(\phi'_2) + \frac{8}{9}u_3, \\ \pi_2^Y &= \frac{1}{3}u'_2 \sin(\phi'_2), \\ \pi_3^X &= u'_2 \cos(\phi'_2) - \frac{1}{3}u_3, \\ \pi_3^Y &= u'_2 \sin(\phi'_2), \\ \pi_4^X &= -u'_2 \cos(\phi'_2) - \frac{2}{3}u_3, \\ \pi_4^Y &= -u'_2 \sin(\phi'_2), \end{aligned}$$

$$\begin{aligned}
\pi_5^X &= \frac{1}{2}u'_2 \cos(\phi'_2) - \frac{2}{3}u_3, \\
\pi_5^Y &= \frac{1}{2}u'_2 \sin(\phi'_2), \\
\Sigma_1^X &= v_2 + v'_3 \cos(\Phi'_3), \\
\Sigma_1^Y &= v'_3 \sin(\Phi'_3), \\
\Sigma_2^X &= \frac{1}{2}v_2 - v'_3 \cos(\Phi'_3), \\
\Sigma_2^Y &= -v'_3 \sin(\Phi'_3),
\end{aligned} \tag{5.46}$$

$$\begin{aligned}
\Phi_{AB} &= (\hat{A}, \hat{B}) = \text{atan2}(\text{det}, \text{dot}) \quad 0 < \Phi_{AB} < 2\pi \\
\phi_{AB} &= (\hat{A}, \hat{B}) = \text{atan2}(\text{det}, \text{dot}) \quad 0 < \phi_{AB} < 2\pi
\end{aligned} \tag{5.47}$$

with

$$\begin{cases} \text{det} = A^X \cdot B^Y - A^Y \cdot B^X \\ \text{dot} = A^X \cdot B^X + A^Y \cdot B^Y. \end{cases} \tag{5.48}$$

It is worth mentioning that the first term in the right-hand side of the equation Eq. (5.42) is the three-boson bound-state equation.

Faddeev-Yakubovsky equations, Eqs. (5.42) and (5.43), in s -wave projection can be written as

$$\begin{aligned}
\int_0^{2\pi} d\phi_2 \mathcal{K}(u_2, u_3, \phi_2) &= \frac{1}{\pi} \tau(\epsilon) \int du'_2 u'_2 \int_0^{2\pi} d\phi_2 \int_0^{2\pi} d\phi'_2 g(\tilde{\pi}) g(\pi_1) \\
&\times \left\{ G_0(\pi_1, u'_2, u_3) \mathcal{K}(u'_2, u_3, \phi'_2) \right. \\
&\quad + G_0(\pi_1, \pi_2, \pi_3) \mathcal{K}(\pi_2, \pi_3, \phi_{\pi_2 \pi_3}) \\
&\quad \left. + G_0(\pi_1, \pi_4, \pi_5) \mathcal{H}(\pi_4, \pi_5, \phi_{\pi_4 \pi_5}) \right\}
\end{aligned} \tag{5.49}$$

$$\begin{aligned}
\int_0^{2\pi} d\Phi_3 \mathcal{H}(v_2, v_3, \Phi_3) &= \frac{1}{\pi} \tau(\epsilon^*) \int dv'_3 v'_3 \int_0^{2\pi} d\Phi_3 \int_0^{2\pi} d\Phi'_3 g(v'_3) g(v_3) \\
&\times \left\{ G_0(v_3, \Sigma_1, \Sigma_2) \mathcal{K}(\Sigma_1, \Sigma_2, \Phi_{\Sigma_1 \Sigma_2}) \right. \\
&\quad \left. + \frac{1}{2} G_0(v_3, |-v_2|, v'_3) \mathcal{H}(|-v_2|, v'_3, \pi - \Phi'_3) \right\}.
\end{aligned} \tag{5.50}$$

Since in s -wave, FY components have no angular dependency, we can simplify Eqs. (5.53) and (5.54) as

$$\begin{aligned}
\mathcal{K}(u_2, u_3) &= 2\tau(\epsilon) \int du'_2 u'_2 \frac{1}{2\pi} \int_0^{2\pi} d\phi_2 \frac{1}{2\pi} \int_0^{2\pi} d\phi'_2 g(\tilde{\pi}) g(\pi_1) \\
&\times \left\{ G_0(\pi_1, u'_2, u_3) \mathcal{K}(u'_2, u_3) + G_0(\pi_1, \pi_2, \pi_3) \mathcal{K}(\pi_2, \pi_3) \right.
\end{aligned}$$

$$+G_0(\pi_1, \pi_4, \pi_5)\mathcal{H}(\pi_4, \pi_5)\Big\}, \quad (5.51)$$

$$\begin{aligned} \mathcal{H}(v_2, v_3) &= 2\tau(\epsilon^*)g(v_3) \int dv'_3 v'_3 g(v'_3) \\ &\times \left\{ \frac{1}{2\pi} \int_0^{2\pi} d\Phi'_3 G_0(v_3, \Sigma_1, \Sigma_2) \mathcal{K}(\Sigma_1, \Sigma_2) + \frac{1}{2} G_0(v_3, v_2, v'_3) \mathcal{H}(v_2, v'_3) \right\}. \end{aligned} \quad (5.52)$$

Equations (5.51) and (5.52) can be more simplified for zero-range interactions, i.e., $g(p) = 1$, as

$$\begin{aligned} \mathcal{K}(u_2, u_3) &= 2\tau(\epsilon) \int_0^\infty du'_2 u'_2 \frac{1}{2\pi} \int_0^{2\pi} d\phi_2 \frac{1}{2\pi} \int_0^{2\pi} d\phi'_2 \\ &\times \left\{ G_0(\pi_1, u'_2, u_3) \mathcal{K}(u'_2, u_3) + G_0(\pi_1, \pi_2, \pi_3) \mathcal{K}(\pi_2, \pi_3) \right. \\ &\left. + G_0(\pi_1, \pi_4, \pi_5) \mathcal{H}(\pi_4, \pi_5) \right\}, - \end{aligned} \quad (5.53)$$

$$\begin{aligned} \mathcal{H}(v_2, v_3) &= 2\tau(\epsilon^*) \int_0^\infty dv'_3 v'_3 \\ &\times \left\{ \frac{1}{2\pi} \int_0^{2\pi} d\Phi'_3 G_0(v_3, \Sigma_1, \Sigma_2) \mathcal{K}(\Sigma_1, \Sigma_2) + \frac{1}{2} G_0(v_3, v_2, v'_3) \mathcal{H}(v_2, v'_3) \right\}. \end{aligned} \quad (5.54)$$

5.2.3 Numerical results

In this section, we show the numerical results of the 4B bound state in 2D by solving Eqs. (5.51) and (5.52) for the separable potential with Yamaguchi form factor, $g(p) = (p^2 + \beta^2)^{-m}$, and Gaussian form factor, $g(p) = \exp(-\frac{p^2}{\Lambda^2})^m$.

In Table 5.1, we present 3B and 4B binding energy ratios for both ground ($N = 0$) and excited ($N = 1$) states for different dimer binding energies. The results are with form factor parameter $\beta = \Lambda = 1$, and different form factor powers $m = 1, 2, 4$. It should be mentioned that in all calculations, $\hbar c = 1$.

Yamaguchi			Gaussian		Yamaguchi		Gaussian	
E_2	$E_3^{(0)}/E_2$	$E_3^{(1)}/E_2$	$E_3^{(0)}/E_2$	$E_3^{(1)}/E_2$	$E_4^{(0)}/E_2$	$E_4^{(1)}/E_2$	$E_4^{(0)}/E_2$	$E_4^{(1)}/E_2$
$m = 1$								
10^{-7}	16.47	1.269	16.47	1.269	193.2	24.98	193.1	24.96
10^{-6}	16.27	1.265	16.27	1.265	179.7	24.15	179.1	24.10
10^{-5}	15.53	1.250	15.50	1.250	144.1	21.42	142.7	21.30
10^{-4}	13.55	1.208	13.45	1.205	91.51	16.49	89.31	16.27
10^{-3}	10.22	1.130	10.03	1.126	47.16	11.07	44.98	10.77
10^{-2}	6.830	1.050	6.582	1.044	22.42	6.958	20.76	6.633
$m = 2$								
10^{-7}	16.45	1.269	16.44	1.269	190.6	24.54	190.6	24.80
10^{-6}	16.13	1.262	16.12	1.262	171.3	23.35	170.9	23.50
10^{-5}	15.07	1.241	16.12	1.240	128.2	19.99	127.3	19.97
10^{-4}	12.59	1.186	12.53	1.185	75.16	14.68	74.00	14.55
10^{-3}	9.020	1.101	8.917	1.099	36.72	9.492	35.69	9.332
10^{-2}	5.890	1.031	5.757	1.027	17.35	5.924	16.61	5.759
$m = 4$								
10^{-7}	16.38	1.265	16.38	1.265	186.8	24.30	186.8	24.56
10^{-6}	15.92	1.258	15.91	1.258	160.5	22.55	160.3	22.69
10^{-5}	14.47	1.228	14.46	1.228	111.4	18.46	110.9	18.46
10^{-4}	11.53	1.162	11.49	1.161	60.84	12.93	60.26	12.86
10^{-3}	7.910	1.075	7.852	1.073	28.69	8.136	28.22	8.055
10^{-2}	5.124	1.018	5.059	1.016	13.80	5.137	13.48	5.074

TABLE 5.1 – three-body, $E_3^{(N)}$ and four-body $E_4^{(N)}$ ground ($N = 0$) and excited ($N = 1$) state binding energies, calculated for the Yamaguchi and Gaussian potentials with form factor parameter $\beta = \Lambda = 1$ and different form factor powers $m = 1, 2, 4$. The units are such that $\hbar = m = 1$ and the form factor parameter is taken as a unit.

In Fig. 5.4, we show the calculated 4B binding energy as a function of 3B binding energies ratios for both ground and first excited states for different form factor power $m = 1, 2, 4$.

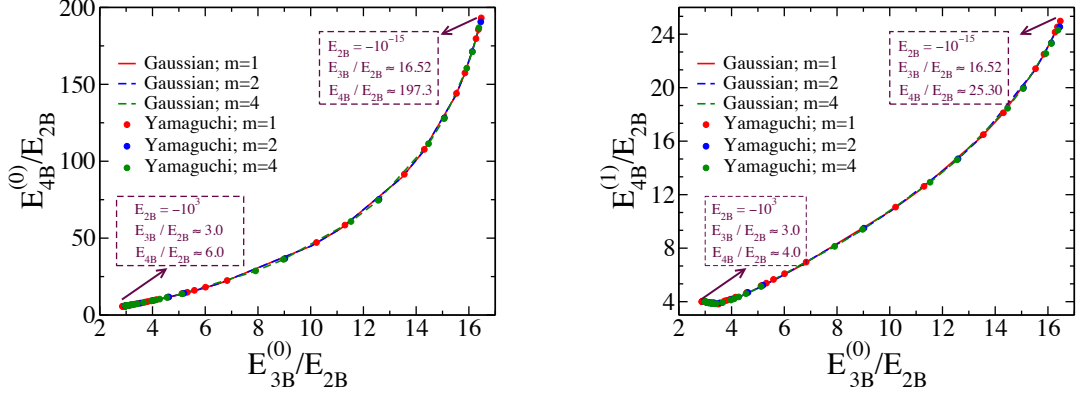


FIGURE 5.4 – E_{4B}/E_{2B} as a function of E_{3B}/E_{2B} for ground (left panel) and first excited state (right panel) for separable potential with Yamaguchi and Gaussian form factor with $\beta = \Lambda = 1$ and different form factor power m .

It is worth mentioning that our numerical results for three and four-body ground and excited state binding by solving Eq. (5.53) and Eq. (5.54), by considering a small dimer binding energy of $E_2 = 10^{-15}$ are

$$\begin{aligned} E_3^{(0)}/E_2 &= 16.52, & E_3^{(1)}/E_2 &= 1.270, \\ E_4^{(0)}/E_2 &= 197.3, & E_4^{(1)}/E_2 &= 25.30, \end{aligned} \quad (5.55)$$

which are in excellent agreement with results of Ref. (PLATTER *et al.*, 2004b) and the ground state energy ratios of Ref. (BAZAK; PETROV, 2018).

In the left panel of Fig. 5.4, we observe that for strongly bound dimer, in our case $E_{2B} = -10^3$, and therefore very compact concerning the interaction range $\Lambda^{-1} = 1$, the ground state of the trimer and tetramer tends to be a collection of bosonic pair, namely three and six, respectively, which explains the results found numerically. For the tetramer excited state, right panel of Fig. 5.4, which is below the ground state trimer, one could interpret that this excited state is the trimer added to a boson, which interacts with one of the bosons of the trimer, which will add one unit of the pair energy, giving the value of four for the ratio of the excited tetramer energy to the dimer one.

The plots in Fig. 5.4 show an independence on the separable form factor and smoothly interpolates between the strongly bound dimer and the weakly bound one. It is worth mentioning that for these separable potential models, the trimer energy encapsulates all the relevant physical information. It suggests that the knowledge of the zero angular momentum trimer and dimer energies is sufficient to fix the ground and excited tetramer

energies, independent of the specific pairwise short-range interaction model. In the case of the strongly bound dimer, the dimers are frozen in the trimer and tetramer bound states. This is evident in the ratios of the energies of the tetramer and trimer to the dimer energy. Furthermore, the dimer is in the classically allowed region. This observation supports a simple interpretation of the values of the tetramer and trimer energies. On the other hand, in the case of weakly bound dimers, the states extend mainly into the classically forbidden region.

6 Summary and outlook

In this thesis, we have advanced the application of the Faddeev technique to investigate three-body nuclear systems and two-dimensional (2D) semiconductor materials. We have established a comprehensive understanding of the mass and wave functions of three-boson bound states within a relativistic three-body framework in three-dimensional momentum space. Our study has successfully demonstrated that the relativistic masses and wave functions of three bosons become model-independent and avoid the Thomas collapse as the range of interaction approaches zero.

Furthermore, we developed a fundamental approach to study trions in layered 2D semiconductor materials. We solved the Faddeev equations in momentum space for trions using both a short-range separable Yamaguchi potential and the Rytova-Keldysh (RK) potential applied to the MoS₂ layer. We employed two distinct regularization methods to address the challenge posed by the repulsive electron-electron RK potential. This approach led to consistent results between the two methods for the MoS₂ layer and revealed a trion binding energy of $-49.5(1)$ meV for an exciton energy of -753.3 meV. To investigate the trion in real space, we transformed the trion wave functions from momentum to configuration space using Fourier transforms, which provided insights into the spatial arrangement and correlations among the trion's constituent particles. The accuracy of the numerical methods was confirmed through geometrical properties, offering a comprehensive understanding of trions' binding properties and structures in 2D semiconductor materials.

Additionally, the current study examined four-body (4B) systems in 2D momentum space using the Faddeev-Yakubovsky (FY) scheme. We began with a theoretical foundation of the FY approach and then derived the FY equations for a 4B system in 2D space. Numerical results for a system of identical particles interacting through a separable potential were presented, demonstrating the effectiveness of the iterative method in solving the FY equations.

In the following, we outline the ongoing research and future directions that extend from the findings and methodologies presented in this thesis. These areas of exploration build upon the foundation laid here and open doors to delve deeper into the intricate

nature of few-body systems.

6.1 Calculating Efimov States in the Relativistic Regime

Continuing our investigation into the fascinating realm of few-body physics, our immediate focus is directed towards the calculation of Efimov states in the relativistic regime. While the Efimov effect is primarily observed in low-energy scenarios, where relativistic effects are often negligible, probing its behavior under relativistic conditions holds the promise of uncovering new facets. By integrating the principles of relativistic quantum mechanics into our calculations, we aim to unravel how these deeply bound states respond to relativistic corrections. This endeavor not only contributes to the theoretical understanding of Efimov states but also offers a unique perspective on the interplay between relativity and few-body systems.

6.2 Calculating Trion Binding Energy Using Separable Potential

Another avenue of ongoing research involves the computation of trion binding energies using a separable potential approach. By employing this technique, we anticipate gaining deeper insights into the trion's binding behavior within semiconducting layered materials. This study not only enriches our understanding of trion properties but also offers the potential to refine the existing methodologies in the field of semiconductor physics. The application of separable potentials provides a powerful tool to dissect the intricacies of trion binding and to explore how different potential components contribute to the overall trion stability.

In conclusion, the chapters of this thesis represent significant steps in our journey through the intricate landscape of few-body systems. The ongoing and forthcoming work described here not only extends the boundaries of our understanding but also underscores the continuous nature of scientific exploration. As we delve further into these promising areas of research, we remain committed to unraveling the mysteries of few-body systems and their diverse manifestations in the realms of both theoretical and applied physics.

Bibliography

ADHIKARI, S. K. Quantum scattering in two dimensions. **American Journal of Physics**, American Association of Physics Teachers, v. 54, n. 4, p. 362–367, 1986.

ADHIKARI, S. K.; DELFINO, A.; FREDERICO, T.; GOLDMAN, I. D.; TOMIO, L. Efimov and thomas effects and the model dependence of three-particle observables in two and three dimensions. **Phys. Rev. A**, American Physical Society, v. 37, p. 3666–3673, May 1988. Available at: <https://link.aps.org/doi/10.1103/PhysRevA.37.3666>.

AHMADI, M.; HADIZADEH, M. R.; RADIN, M.; BAYEGAN, S. Novel regularization scheme for nucleon-nucleon lattice simulations with effective field theory. **Phys. Rev. C**, American Physical Society, v. 102, p. 044001, Oct 2020. Available at: <https://link.aps.org/doi/10.1103/PhysRevC.102.044001>.

BAKAMJIAN, B.; THOMAS, L. Relativistic particle dynamics. ii. **Physical Review**, APS, v. 92, n. 5, p. 1300, 1953.

BATI, A. S.; BATMUNKH, M.; SHAPTER, J. G. Emerging 2d layered materials for perovskite solar cells. **Advanced Energy Materials**, Wiley Online Library, v. 10, n. 13, p. 1902253, 2020.

BAYEGAN, S.; HADIZADEH, M. R.; GLÖCKLE, W. A realistic formalism for 4 n bound state in a three-dimensional yakubovsky scheme. **Progress of Theoretical Physics**, Oxford University Press, v. 120, n. 5, p. 887–916, 2008.

BAYEGAN, S.; HADIZADEH, M. R.; HARZCHI, M. Three-nucleon bound state in a spin-isospin dependent three dimensional approach. **Phys. Rev. C**, American Physical Society, v. 77, p. 064005, Jun 2008. Available at: <https://link.aps.org/doi/10.1103/PhysRevC.77.064005>.

BAZAK, B.; PETROV, D. S. Energy of n two-dimensional bosons with zero-range interactions. **New Journal of Physics**, IOP Publishing, v. 20, n. 2, p. 023045, 2018.

BELLANI, S.; BARTOLOTTA, A.; AGRESTI, A.; CALOGERO, G.; GRANCINI, G.; CARLO, A. D.; KYMAKIS, E.; BONACCORSO, F. Solution-processed two-dimensional materials for next-generation photovoltaics. **Chemical Society Reviews**, Royal Society of Chemistry, v. 50, n. 21, p. 11870–11965, 2021.

BELLOTTI, F.; FREDERICO, T.; YAMASHITA, M. T.; FEDOROV, D.; JENSEN, A.; ZINNER, N. T. Dimensional effects on the momentum distribution of bosonic trimer

- states. **Physical Review A—Atomic, Molecular, and Optical Physics**, APS, v. 87, n. 1, p. 013610, 2013.
- BELLOTTI, F. F.; FREDERICO, T.; YAMASHITA, M.; FEDOROV, D.; JENSEN, A.; ZINNER, N. T. Mass-imbalanced three-body systems in 2d: bound states and the analytical approach to the adiabatic potential. **Few-Body Systems**, Springer, v. 55, p. 847–850, 2014.
- BELLOTTI, F. F.; FREDERICO, T.; YAMASHITA, M. T.; FEDOROV, D. V.; JENSEN, A. S.; ZINNER, N. T. Scaling and universality in two dimensions: three-body bound states with short-ranged interactions. **Journal of Physics B: Atomic, Molecular and Optical Physics**, IOP Publishing, v. 44, n. 20, p. 205302, 2011.
- BELLOTTI, F. F.; FREDERICO, T.; YAMASHITA, M. T.; FEDOROV, D. V.; JENSEN, A. S.; ZINNER, N. T. Supercircle description of universal three-body states in two dimensions. **Physical Review A—Atomic, Molecular, and Optical Physics**, APS, v. 85, n. 2, p. 025601, 2012.
- BELLOTTI, F. F.; FREDERICO, T.; YAMASHITA, M. T.; FEDOROV, D. V.; JENSEN, A. S.; ZINNER, N. T. Mass-imbalanced three-body systems in two dimensions. **Journal of Physics B: Atomic, Molecular and Optical Physics**, IOP Publishing, v. 46, n. 5, p. 055301, 2013.
- BERKELBACH, T. C.; HYBERTSEN, M. S.; REICHMAN, D. R. Theory of neutral and charged excitons in monolayer transition metal dichalcogenides. **Phys. Rev. B**, American Physical Society, v. 88, p. 045318, Jul 2013. Available at: <https://link.aps.org/doi/10.1103/PhysRevB.88.045318>.
- BERKELBACH, T. C.; HYBERTSEN, M. S.; REICHMAN, D. R. Theory of neutral and charged excitons in monolayer transition metal dichalcogenides. **Physical Review B—Condensed Matter and Materials Physics**, APS, v. 88, n. 4, p. 045318, 2013.
- CARBONELL, J.; DESPLANQUES, B.; KARMANOV, V.; MATHIOT, J.-F. Explicitly covariant light-front dynamics and relativistic few-body systems. **Physics Reports**, v. 300, n. 5, p. 215–347, 1998. ISSN 0370-1573. Available at: <https://www.sciencedirect.com/science/article/pii/S0370157397000902>.
- CARBONELL, J.; KARMANOV, V. A. Three-boson relativistic bound states with zero-range two-body interaction. **Phys. Rev. C**, American Physical Society, v. 67, p. 037001, Mar 2003. Available at: <https://link.aps.org/doi/10.1103/PhysRevC.67.037001>.
- CAVALCANTE, L.; COSTA, D. R. da; FARIAS, G.; REICHMAN, D.; CHAVES, A. Stark shift of excitons and trions in two-dimensional materials. **Physical Review B**, APS, v. 98, n. 24, p. 245309, 2018.
- CHANG, Y.-W.; CHANG, Y.-C. Variationally optimized orbital approach to trions in two-dimensional materials. **The Journal of Chemical Physics**, AIP Publishing, v. 155, n. 2, 2021.
- CHAVES, A.; AZADANI, J. G.; ALSALMAN, H.; COSTA, D. D.; FRISENDA, R.; CHAVES, A.; SONG, S. H.; KIM, Y. D.; HE, D.; ZHOU, J. *et al.* Bandgap engineering of two-dimensional semiconductor materials. **npj 2D Materials and Applications**, Nature Publishing Group UK London, v. 4, n. 1, p. 29, 2020.

- CHERNIKOV, A.; BERKELBACH, T. C.; HILL, H. M.; RIGOSI, A.; LI, Y.; ASLAN, B.; REICHMAN, D. R.; HYBERTSEN, M. S.; HEINZ, T. F. Exciton binding energy and nonhydrogenic rydberg series in monolayer ws_2 . **Phys. Rev. Lett.**, American Physical Society, v. 113, p. 076802, Aug 2014. Available at: <https://link.aps.org/doi/10.1103/PhysRevLett.113.076802>.
- CIESIELSKI, F.; CARBONELL, J. Solutions of the faddeev-yakubovsky equations for the four nucleon scattering states. **Physical Review C**, APS, v. 58, n. 1, p. 58, 1998.
- COESTER, F.; PIEPER, S. C.; SERDUKE, F. Relativistic effects in phenomenological nucleon-nucleon potentials and nuclear matter. **Physical Review C**, APS, v. 11, n. 1, p. 1, 1975.
- CORNELIUS, T.; GLÖCKLE, W.; HAIDENBAUER, J.; KOIKE, Y.; PLESSAS, W.; WITALA, H. Predictions of the paris n-n potential for three-nucleon continuum observables: Comparison of two approaches. **Physical Review C**, APS, v. 41, n. 6, p. 2538, 1990.
- COURTADE, E.; SEMINA, M.; MANCA, M.; GLAZOV, M.; ROBERT, C.; CADIZ, F.; WANG, G.; TANIGUCHI, T.; WATANABE, K.; PIERRE, M. *et al.* Charged excitons in monolayer ws_2 : Experiment and theory. **Physical Review B**, APS, v. 96, n. 8, p. 085302, 2017.
- COUTINHO, F. A. B.; PEREZ, J. F.; WRESZINSKI, W. F. A variational proof of the thomas effect. **Journal of Mathematical Physics**, American Institute of Physics, v. 36, n. 4, p. 1625–1635, 1995.
- CUDAZZO, P.; TOKATLY, I. V.; RUBIO, A. Dielectric screening in two-dimensional insulators: Implications for excitonic and impurity states in graphane. **Phys. Rev. B**, American Physical Society, v. 84, p. 085406, Aug 2011. Available at: <https://link.aps.org/doi/10.1103/PhysRevB.84.085406>.
- DAS, S.; PANDEY, D.; THOMAS, J.; ROY, T. The role of graphene and other 2d materials in solar photovoltaics. **Advanced Materials**, Wiley Online Library, v. 31, n. 1, p. 1802722, 2019.
- DELTUVA, A. Efimov physics in bosonic atom-trimer scattering. **Physical Review A**, APS, v. 82, n. 4, p. 040701, 2010.
- DELTUVA, A.; FONSECA, A. C.; SAUER, P. U. Momentum-space treatment of the coulomb interaction in three-nucleon reactions with two protons. **Phys. Rev. C**, American Physical Society, v. 71, p. 054005, May 2005. Available at: <https://link.aps.org/doi/10.1103/PhysRevC.71.054005>.
- DELTUVA, A.; LAZAUSKAS, R.; PLATTER, L. Universality in four-body scattering. **Few-Body Systems**, Springer, v. 51, n. 2-4, p. 235–247, 2011.
- DIRAC, P. A. M. Forms of relativistic dynamics. **Rev. Mod. Phys.**, American Physical Society, v. 21, p. 392–399, Jul 1949. Available at: <https://link.aps.org/doi/10.1103/RevModPhys.21.392>.

DONCK, M. Van der; ZARENIA, M.; PEETERS, F. M. Excitons and trions in monolayer transition metal dichalcogenides: A comparative study between the multiband model and the quadratic single-band model. **Phys. Rev. B**, American Physical Society, v. 96, p. 035131, Jul 2017. Available at: <https://link.aps.org/doi/10.1103/PhysRevB.96.035131>.

DRESSELHAUS, G. Absorption coefficients for exciton absorption lines. **Phys. Rev.**, American Physical Society, v. 106, p. 76–78, Apr 1957. Available at: <https://link.aps.org/doi/10.1103/PhysRev.106.76>.

EFIMOV, V. Energy levels arising from resonant two-body forces in a three-body system. **Physics Letters B**, v. 33, n. 8, p. 563–564, 1970. ISSN 0370-2693. Available at: <https://www.sciencedirect.com/science/article/pii/0370269370903497>.

ELLIOTT, R. J. Intensity of optical absorption by excitons. **Phys. Rev.**, American Physical Society, v. 108, p. 1384–1389, Dec 1957. Available at: <https://link.aps.org/doi/10.1103/PhysRev.108.1384>.

ELSTER, C.; LIN, T.; POLYZOU, W.; GLÖCKLE, W. Relativistic three-body scattering in a first order faddeev formulation. **arXiv preprint arXiv:0708.3868**, 2007.

ELSTER, C.; SCHADOW, W.; NOGGA, A.; GLÖCKLE, W. Three-body bound-state calculations without angular-momentum decomposition. **Few-Body Systems**, Springer, v. 27, p. 83–105, 1999.

EMMANUELE, R.; SICH, M.; KYRIIENKO, O.; SHAHNAZARYAN, V.; WITHERS, F.; CATANZARO, A.; WALKER, P.; BENIMETSKIY, F.; SKOLNICK, M.; TARTAKOVSKII, A. *et al.* Highly nonlinear trion-polaritons in a monolayer semiconductor. **Nature communications**, Nature Publishing Group UK London, v. 11, n. 1, p. 3589, 2020.

EPSTEIN, I.; CHAVES, A. J.; RHODES, D. A.; FRANK, B.; WATANABE, K.; TANIGUCHI, T.; GIESSEN, H.; HONE, J. C.; PERES, N. M.; KOPPENS, F. H. Highly confined in-plane propagating exciton-polaritons on monolayer semiconductors. **2D Materials**, IOP Publishing, v. 7, n. 3, p. 035031, 2020.

FADDEEV, L. Scattering theory for a three-particle system. *In: Fifty Years of Mathematical Physics: Selected Works of Ludwig Faddeev*. [S.l.]: World Scientific, 1960. p. 37–42.

FADDEEV, L. Zhetf (ussr) 39 (1960) 1459. **JETP (Sov. Phys.)**, v. 12, n. 1014, p. 216, 1961.

FILIKHIN, I.; KEZERASHVILI, R. Y.; VLAHOVIC, B. On binding energy of trions in bulk materials. **Physics Letters A**, Elsevier, v. 382, n. 11, p. 787–791, 2018.

FILIKHIN, I.; YAKOVLEV, S.; ROUDNEV, V.; VLAHOVIC, B. The 4he tetramer ground state in the faddeev-yakubovsky differential equations formalism. **Journal of Physics B: Atomic, Molecular and Optical Physics**, IOP Publishing, v. 35, n. 3, p. 501, 2002.

FONG, R.; SUCHER, J. Relativistic particle dynamics and the s matrix. **Journal of Mathematical Physics**, American Institute of Physics, v. 5, n. 4, p. 456–470, 1964.

- FONSECA, A. C. Four-body calculation of the four-nucleon system: Binding energies and scattering results. **Physical Review C**, APS, v. 30, n. 1, p. 35, 1984.
- FREDERICO, T.; DELFINO, A.; TOMIO, L.; YAMASHITA, M. T. Universal aspects of light halo nuclei. **Progress in Particle and Nuclear Physics**, Elsevier, v. 67, n. 4, p. 939–994, 2012.
- FRIAR, J. Equivalence of nonstatic two-pion-exchange nucleon-nucleon potentials. **Physical Review C**, APS, v. 60, n. 3, p. 034002, 1999.
- GIBSON, B. F.; LEHMAN, D. Exact four-body calculation of the $4\lambda\text{he}-4\lambda\text{h}$ binding energy difference. **Nuclear Physics A**, Elsevier, v. 329, n. 3, p. 308–330, 1979.
- GIBSON, B. F.; LEHMAN, D. Four-body calculation of the $0+-1+$ binding energy difference in the $a=4\lambda$ hypernuclei. **Physical Review C**, APS, v. 37, n. 2, p. 679, 1988.
- GLÖCKLE, W. **The quantum mechanical few-body problem**. [S.l.]: Springer Science & Business Media, 2012.
- GLÖCKLE, W.; KAMADA, H. On the inclusion of 3n-forces into the 4n-yakubovsky equations. **Nuclear Physics A**, Elsevier, v. 560, n. 1, p. 541–547, 1993.
- GLÖCKLE, W.; LEE, T.-S.; COESTER, F. Relativistic effects in three-body bound states. **Physical Review C**, APS, v. 33, n. 2, p. 709, 1986.
- GLOECKLE, W.; WITAŁA, H.; HÜBER, D.; KAMADA, H.; GOLAK, J. The three-nucleon continuum: achievements, challenges and applications. **Physics Reports**, Elsevier, v. 274, n. 3-4, p. 107–285, 1996.
- GREENE, C. H.; GIANNAKEAS, P.; PÉREZ-RÍOS, J. Universal few-body physics and cluster formation. **Reviews of Modern Physics**, APS, v. 89, n. 3, p. 035006, 2017.
- HADIZADEH, M.; BAYEGAN, S. Four-body bound-state calculations in three-dimensional approach. **Few-Body Systems**, Springer, v. 40, n. 3, p. 171–191, 2007.
- HADIZADEH, M.; ELSTER, C.; POLYZOU, W. Relativistic three-body bound state in a 3d formulation. **Physical Review C**, APS, v. 90, n. 5, p. 054002, 2014.
- HADIZADEH, M.; RADIN, M. Calculation of relativistic nucleon-nucleon potentials in three dimensions. **The European Physical Journal A**, Springer, v. 53, n. 2, p. 18, 2017.
- HADIZADEH, M.; RADIN, M.; MOHSENI, K. A three-dimensional momentum-space calculation of three-body bound state in a relativistic faddeev scheme. **Scientific Reports**, Nature Publishing Group UK London, v. 10, n. 1, p. 1949, 2020.
- HADIZADEH, M.; RADIN, M.; NAZARI, F. Relativistic nucleon–nucleon potentials in a spin-dependent three-dimensional approach. **Scientific Reports**, Nature Publishing Group UK London, v. 11, n. 1, p. 17550, 2021.
- HADIZADEH, M.; YAMASHITA, M. T.; TOMIO, L.; DELFINO, A.; FREDERICO, T. Binding and structure of tetramers in the scaling limit. **Physical Review A—Atomic, Molecular, and Optical Physics**, APS, v. 85, n. 2, p. 023610, 2012.

- HADIZADEH, M. R.; YAMASHITA, M. T.; TOMIO, L.; DELFINO, A.; FREDERICO, T. Scaling properties of universal tetramers. **Phys. Rev. Lett.**, American Physical Society, v. 107, p. 135304, Sep 2011. Available at: <https://link.aps.org/doi/10.1103/PhysRevLett.107.135304>.
- HIYAMA, E.; LAZAUSKAS, R.; CARBONELL, J.; FREDERICO, T. Scaling of the b 19 two-neutron halo properties close to unitarity. **Physical Review C**, APS, v. 106, n. 6, p. 064001, 2022.
- HÜBER, D. H. wita la, a. nogga, w. glöckle, h. kamada. **Few-Body Systems**, v. 22, p. 107, 1997.
- IQBAL, T.; FATIMA, S.; BIBI, T.; ZAFAR, M. Graphene and other two-dimensional materials in advance solar cells. **Optical and Quantum Electronics**, Springer, v. 53, n. 5, p. 228, 2021.
- JADCZAK, J.; DELGADO, A.; BRYJA, L.; HUANG, Y.; HAWRYLAK, P. Robust high-temperature trion emission in monolayers of mo (s y se 1- y) 2 alloys. **Physical Review B**, APS, v. 95, n. 19, p. 195427, 2017.
- KAMADA, H. A practical method for relativistic 3n-scattering calculations with realistic potentials. In: **Few-Body Problems in Physics' 99**. [S.l.]: Springer, 2000. p. 433–438.
- KAMADA, H.; GLÖCKLE, W. Solutions of the yakubovsky equations for four-body model systems. **Nuclear Physics A**, Elsevier, v. 548, n. 2, p. 205–226, 1992.
- KAMADA, H.; GLÖCKLE, W. Realistic two-nucleon potentials for the relativistic two-nucleon schrödinger equation. **Physics Letters B**, Elsevier, v. 655, n. 3-4, p. 119–125, 2007.
- KAMADA, H.; GLÖCKLE, W.; GOLAK, J.; ELSTER, C. Lorentz boosted nn potential for few-body systems: Application to the three-nucleon bound state. **Physical Review C**, APS, v. 66, n. 4, p. 044010, 2002.
- KAMADA, H.; GLÖCKLE, W.; WITAŁA, H.; GOLAK, J.; SKIBIŃSKI, R.; POLYZOU, W.; ELSTER, C. Calculations of the triton binding energy with a lorentz boosted nucleon-nucleon potential. In: EDP SCIENCES. **EPJ Web of Conferences. Proceedings** [...]. [S.l.: s.n.], 2010. v. 3, p. 05025.
- KAMADA, H.; NOGGA, A.; GLOECKLE, W.; HIYAMA, E.; KAMIMURA, M.; VARGA, K.; SUZUKI, Y.; VIVIANI, M.; KIEVSKY, A.; ROSATI, S. *et al.* Benchmark test calculation of a four-nucleon bound state. **Physical Review C**, APS, v. 64, n. 4, p. 044001, 2001.
- KARMANOV, V.; CARBONELL, J. Critical stability of three-body relativistic bound states with zero-range interaction. **Few-Body Systems**, Springer, v. 34, p. 85–90, 2004.
- KARMANOV, V.; MARIS, P. Manifestation of three-body forces in three-body bethe–salpeter and light-front equations. **Few-Body Systems**, Springer, v. 46, n. 2, p. 95–113, 2009.
- KEISTER, B.; POLYZOU, W. Quantitative relativistic effects in the three-nucleon problem. **Physical Review C**, APS, v. 73, n. 1, p. 014005, 2006.

KELDysh, L. Pis'ma zh. eksp. teor. fiz. 29 (1979) 716[59] j. cibert, pm petroff, gj dolan, dj. werder, si. **JETP Lett**, v. 29, p. 658, 1979.

KEZERASHVILI, R. Y. Few-body systems in condensed matter physics. **Few-Body Systems**, Springer, v. 60, n. 3, p. 52, 2019.

KEZERASHVILI, R. Y.; TSIKLARI, S. M. Trion and biexciton in monolayer transition metal dichalcogenides. **Few-Body Systems**, Springer, v. 58, p. 1–5, 2017.

KHENG, K.; COX, R. T.; AUBIGNÉ, M. Y. d'; BASSANI, F.; SAMINADAYAR, K.; TATARENKO, S. Observation of negatively charged excitons x^- in semiconductor quantum wells. **Phys. Rev. Lett.**, American Physical Society, v. 71, p. 1752–1755, Sep 1993. Available at: <https://link.aps.org/doi/10.1103/PhysRevLett.71.1752>.

KIDD, D. W.; ZHANG, D. K.; VARGA, K. Binding energies and structures of two-dimensional excitonic complexes in transition metal dichalcogenides. **Phys. Rev. B**, American Physical Society, v. 93, p. 125423, Mar 2016. Available at: <https://link.aps.org/doi/10.1103/PhysRevB.93.125423>.

KIDD, D. W.; ZHANG, D. K.; VARGA, K. Binding energies and structures of two-dimensional excitonic complexes in transition metal dichalcogenides. **Physical Review B**, APS, v. 93, n. 12, p. 125423, 2016.

KLOTS, A.; NEWAZ, A.; WANG, B.; PRASAI, D.; KRZYŻANOWSKA, H.; LIN, J.; CAUDEL, D.; GHIMIRE, N.; YAN, J.; IVANOV, B. *et al.* Probing excitonic states in suspended two-dimensional semiconductors by photocurrent spectroscopy. **Scientific reports**, Nature Publishing Group UK London, v. 4, n. 1, p. 6608, 2014.

KONDRATYUK, L.; LEV, F.; SOLOVIEV, V. Relativistic correction to the triton binding energy in the framework of relativistic hamiltonian dynamics. **Few-Body Systems**, Springer, v. 7, n. 2, p. 55–77, 1989.

KONDRATYUK, L.; VOGELZANG, J.; FANCHENKO, M. Relativistic correction to the binding energy of three nucleons in the poincaré invariant theory. **Physics Letters B**, Elsevier, v. 98, n. 6, p. 405–408, 1981.

KORMÁNYOS, A.; BURKARD, G.; GMITRA, M.; FABIAN, J.; ZÓLYOMI, V.; DRUMMOND, N. D.; FAL'KO, V. $k \cdot p$ theory for two-dimensional transition metal dichalcogenide semiconductors. **2D Materials**, IOP Publishing, v. 2, n. 2, p. 022001, 2015.

KORMÁNYOS, A.; BURKARD, G.; GMITRA, M.; FABIAN, J.; ZÓLYOMI, V.; DRUMMOND, N. D.; FAL'KO, V. $k \cdot p$ theory for two-dimensional transition metal dichalcogenide semiconductors. **2D Materials**, v. 2, n. 2, p. 022001, apr 2015.

KYLÄNPÄÄ, I.; KOMSA, H.-P. Binding energies of exciton complexes in transition metal dichalcogenide monolayers and effect of dielectric environment. **Physical Review B**, APS, v. 92, n. 20, p. 205418, 2015.

LAMPERT, M. A. Mobile and immobile effective-mass-particle complexes in nonmetallic solids. **Phys. Rev. Lett.**, American Physical Society, v. 1, p. 450–453, Dec 1958. Available at: <https://link.aps.org/doi/10.1103/PhysRevLett.1.450>.

LAZAUSKAS, R.; CARBONELL, J. Ab-initio calculations of four-nucleon elastic scattering. **Few-Body Systems**, Springer, v. 34, p. 105–111, 2004.

LIN, T. **Poincaré-Invariant Three-Nucleon Scattering**. Thesis (Doutorado) — Ohio University, 2008.

LIN, T.; ELSTER, C.; POLYZOU, W.; GLÖCKLE, W. First order relativistic three-body scattering. **Physical Review C**, APS, v. 76, n. 1, p. 014010, 2007.

LIN, T.; ELSTER, C.; POLYZOU, W.; GLÖCKLE, W. Relativistic effects in exclusive pd breakup scattering at intermediate energies. **Physics Letters B**, Elsevier, v. 660, n. 4, p. 345–349, 2008.

LIN, T.-Y.; LEE, Y.-C.; LEE, Y.-W.; CHANG, S.-W.; MA, D.-L.; LIN, B.-C.; CHEN, H.-L. Air gap-based cavities dramatically enhance the true intrinsic spectral signals of suspended and pristine two-dimensional materials. **The Journal of Physical Chemistry C**, ACS Publications, v. 123, n. 9, p. 5667–5679, 2019.

LIN, Y.; LING, X.; YU, L.; HUANG, S.; HSU, A. L.; LEE, Y.-H.; KONG, J.; DRESSELHAUS, M. S.; PALACIOS, T. Dielectric screening of excitons and trions in single-layer mos2. **Nano letters**, ACS Publications, v. 14, n. 10, p. 5569–5576, 2014.

LIU, X.; GALFSKY, T.; SUN, Z.; XIA, F.; LIN, E.-c.; LEE, Y.-H.; KÉNA-COHEN, S.; MENON, V. M. Strong light–matter coupling in two-dimensional atomic crystals. **Nature Photonics**, Nature Publishing Group UK London, v. 9, n. 1, p. 30–34, 2015.

MAK, K. F.; HE, K.; LEE, C.; LEE, G. H.; HONE, J.; HEINZ, T. F.; SHAN, J. Tightly bound trions in monolayer mos2. **Nature materials**, Nature Publishing Group UK London, v. 12, n. 3, p. 207–211, 2013.

MALFLIET, R.; TJON, J. Solution of the faddeev equations for the triton problem using local two-particle interactions. **Nuclear Physics A**, Elsevier, v. 127, n. 1, p. 161–168, 1969.

MOHSENI, K.; CHAVES, A.; COSTA, D. da; FREDERICO, T.; HADIZADEH, M. Three-boson stability for boosted interactions towards the zero-range limit. **Physics Letters B**, Elsevier, v. 823, p. 136773, 2021.

MOHSENI, K.; HADIZADEH, M. R.; FREDERICO, T.; COSTA, D. R. da; CHAVES, A. J. Trion clustering structure and binding energy in two-dimensional semiconductor materials: Faddeev equations approach. **Phys. Rev. B**, American Physical Society, v. 107, p. 165427, Apr 2023. Available at: <https://link.aps.org/doi/10.1103/PhysRevB.107.165427>.

NAIDON, P.; ENDO, S. Efimov physics: a review. **Reports on Progress in Physics**, IOP Publishing, v. 80, n. 5, p. 056001, 2017.

NOGGA, A. **Nuclear and hypernuclear three- and four-body bound states**. Thesis (doctoralthesis) — Ruhr-Universität Bochum, Universitätsbibliothek, 2003.

NOGGA, A.; KAMADA, H.; GLOECKLE, W.; BARRETT, B. The α particle based on modern nuclear forces. **Physical Review C**, APS, v. 65, n. 5, p. 054003, 2002.

- OLSEN, T.; LATINI, S.; RASMUSSEN, F.; THYGESEN, K. S. Simple screened hydrogen model of excitons in two-dimensional materials. **Physical review letters**, APS, v. 116, n. 5, p. 056401, 2016.
- PARFITT, D.; PORTNOI, M. The two-dimensional hydrogen atom revisited. **Journal of Mathematical Physics**, American Institute of Physics, v. 43, n. 10, p. 4681–4691, 2002.
- PETHICK, C. J.; SMITH, H. **Bose–Einstein condensation in dilute gases**. [S.l.]: Cambridge university press, 2008.
- PLATTER, L.; HAMMER, H.-W.; MEISSNER, U.-G. Four-boson system with short-range interactions. **Physical Review A**, APS, v. 70, n. 5, p. 052101, 2004.
- PLATTER, L.; HAMMER, H.-W.; MEISSNER, U.-G. Universal properties of the four-boson system in two dimensions. **Few-Body Systems**, Springer, v. 35, p. 169–174, 2004.
- POLYZOU, W.; ELSTER, C. Relativistic formulation of reaction theory. **Journal of Physics G: Nuclear and Particle Physics**, IOP Publishing, v. 41, n. 9, p. 094006, 2014.
- ROSA, D.; FREDERICO, T.; KREIN, G.; YAMASHITA, M. Efimov effect in a d -dimensional born–oppenheimer approach. **Journal of Physics B: Atomic, Molecular and Optical Physics**, IOP Publishing, v. 52, n. 2, p. 025101, 2018.
- ROSA, D. S.; FREDERICO, T.; KREIN, G.; YAMASHITA, M. T. d -dimensional three-body bound-state problem with zero-range interactions. **Phys. Rev. A**, American Physical Society, v. 106, p. 023311, Aug 2022. Available at: <https://link.aps.org/doi/10.1103/PhysRevA.106.023311>.
- ROSS, J. S.; WU, S.; YU, H.; GHIMIRE, N. J.; JONES, A. M.; AIVAZIAN, G.; YAN, J.; MANDRUS, D. G.; XIAO, D.; YAO, W. *et al.* Electrical control of neutral and charged excitons in a monolayer semiconductor. **Nature communications**, Nature Publishing Group UK London, v. 4, n. 1, p. 1474, 2013.
- RYTOVA, N. Vestn. mosk. univ. **Ser. Fiz. Astron.**, v. 3, p. 30, 1967.
- RYTOVA, N. S. Screened potential of a point charge in a thin film. **arXiv preprint arXiv:1806.00976**, 2018.
- SAMMARRUCA, F.; XU, D.; MACHLEIDT, R. Relativistic corrections to the triton binding energy. **Physical Review C**, APS, v. 46, n. 5, p. 1636, 1992.
- SCHMID, E.; ZIEGELMANN, H. **The Quantum Mechanical Three-body Problem**. Elsevier Science & Technology, 1974. (Vieweg tracts in pure and applied physics). ISBN 9780080182407. Available at: <https://books.google.com.br/books?id=CDO3AAAAIAAJ>.
- SCHMIDT, W. G.; GLUTSCH, S.; HAHN, P. H.; BECHSTEDT, F. Efficient $\mathcal{O}(N^2)$ method to solve the bethe-salpeter equation. **Phys. Rev. B**, American Physical Society, v. 67, p. 085307, Feb 2003. Available at: <https://link.aps.org/doi/10.1103/PhysRevB.67.085307>.

- SEKIGUCHI, K.; SAKAI, H.; WITAŁA, H.; GLÖCKLE, W.; GOLAK, J.; HATANAKA, K.; HATANO, M.; ITOH, K.; KAMADA, H.; KUBOKI, H. *et al.* Resolving the discrepancy of 135 meV p-d elastic scattering cross sections and relativistic effects. **Physical review letters**, APS, v. 95, n. 16, p. 162301, 2005.
- SERGEEV, R.; SURIS, R. Singlet and triplet states of x^+ and x -trions in two-dimensional quantum wells. **Nanotechnology**, IOP Publishing, v. 12, n. 4, p. 597, 2001.
- SKIBIŃSKI, R.; WITAŁA, H.; GOLAK, J. Relativistic effects in exclusive neutron-deuteron breakup. **The European Physical Journal A-Hadrons and Nuclei**, Springer, v. 30, n. 2, p. 369–380, 2006.
- SKORNIAKOV, G. V.; TER-MARTIROSIAN, K. A. Equivalence of nonstatic two-pion-exchange nucleon-nucleon potentials. **Sov. Phys. JETP**, Sov. Phys. JETP, v. 4, n. 3, p. 648, 1957.
- SOKLASKI, R.; LIANG, Y.; YANG, L. Temperature effect on optical spectra of monolayer molybdenum disulfide. **Applied Physics Letters**, AIP Publishing, v. 104, n. 19, 2014.
- SONG, X.; HU, J.; ZENG, H. Two-dimensional semiconductors: recent progress and future perspectives. **Journal of Materials Chemistry C**, Royal Society of Chemistry, v. 1, n. 17, p. 2952–2969, 2013.
- STADLER, A.; GROSS, F. Relativistic calculation of the triton binding energy and its implications. **Physical Review Letters**, APS, v. 78, n. 1, p. 26, 1997.
- STÉBÉ, B.; AINANE, A. Ground state energy and optical absorption of excitonic trions in two dimensional semiconductors. **Superlattices and microstructures**, Elsevier, v. 5, n. 4, p. 545–548, 1989.
- SZYNISZEWSKI, M.; MOSTAANI, E.; DRUMMOND, N.; FAL'KO, V. I. Binding energies of trions and biexcitons in two-dimensional semiconductors from diffusion quantum monte carlo calculations. **Physical Review B**, APS, v. 95, n. 8, p. 081301, 2017.
- SZYNISZEWSKI, M.; MOSTAANI, E.; DRUMMOND, N. D.; FAL'KO, V. I. Binding energies of trions and biexcitons in two-dimensional semiconductors from diffusion quantum monte carlo calculations. **Phys. Rev. B**, American Physical Society, v. 95, p. 081301, Feb 2017. Available at: <https://link.aps.org/doi/10.1103/PhysRevB.95.081301>.
- THOMAS, L. H. The interaction between a neutron and a proton and the structure of h^3 . **Phys. Rev.**, American Physical Society, v. 47, p. 903–909, Jun 1935. Available at: <https://link.aps.org/doi/10.1103/PhysRev.47.903>.
- TUAN, D. V.; DERY, H. Composite excitonic states in doped semiconductors. **Phys. Rev. B**, American Physical Society, v. 106, p. L081301, Aug 2022. Available at: <https://link.aps.org/doi/10.1103/PhysRevB.106.L081301>.
- TUAN, D. V.; DERY, H. Tetrons, pexcitons, and hexcitons in monolayer transition-metal dichalcogenides. **arXiv preprint arXiv:2202.08379**, 2022.

TUAN, D. V.; DERY, H. Turning many-body problems to few-body ones in photoexcited semiconductors using the stochastic variational method in momentum space, svm-k. **arXiv preprint arXiv:2202.08378**, 2022.

TUAN, D. V.; SHI, S.-F.; XU, X.; CROOKER, S. A.; DERY, H. Six-body and eight-body exciton states in monolayer wse 2. **Physical Review Letters**, APS, v. 129, n. 7, p. 076801, 2022.

UGEDA, M. M.; BRADLEY, A. J.; SHI, S.-F.; JORNADA, F. H. D.; ZHANG, Y.; QIU, D. Y.; RUAN, W.; MO, S.-K.; HUSSAIN, Z.; SHEN, Z.-X. *et al.* Giant bandgap renormalization and excitonic effects in a monolayer transition metal dichalcogenide semiconductor. **Nature materials**, Nature Publishing Group UK London, v. 13, n. 12, p. 1091–1095, 2014.

VELIZHANIN, K. A.; SAXENA, A. Excitonic effects in two-dimensional semiconductors: Path integral monte carlo approach. **Physical Review B**, APS, v. 92, n. 19, p. 195305, 2015.

WANG, G.; CHERNIKOV, A.; GLAZOV, M. M.; HEINZ, T. F.; MARIE, X.; AMAND, T.; URBASZEK, B. Colloquium: Excitons in atomically thin transition metal dichalcogenides. **Rev. Mod. Phys.**, American Physical Society, v. 90, p. 021001, Apr 2018. Available at: <https://link.aps.org/doi/10.1103/RevModPhys.90.021001>.

WITAŁA, H.; GOLAK, J.; SKIBIŃSKI, R.; GLÖCKLE, W.; POLYZOU, W.; KAMADA, H. Relativistic effects in neutron–deuteron elastic scattering and breakup. **Few-Body Systems**, Springer, v. 49, n. 1-4, p. 61–64, 2011.

WITAŁA, H.; SKIBIŃSKI, R.; GOLAK, J.; GLÖCKLE, W.; NOGGA, A.; KAMADA, H. The elastic pd scattering analyzing powers and spin correlation coefficients at e lab $p = 135$ and 200 mev: Three-nucleon force and relativistic effects. **The European Physical Journal A-Hadrons and Nuclei**, Springer, v. 29, n. 2, p. 141–146, 2006.

YAMAGUCHI, Y. Two-nucleon problem when the potential is nonlocal but separable. i. **Phys. Rev.**, American Physical Society, v. 95, p. 1628–1634, Sep 1954. Available at: <https://link.aps.org/doi/10.1103/PhysRev.95.1628>.

YAMAGUCHI, Y. Two-nucleon problem when the potential is nonlocal but separable. i. **Phys. Rev.**, American Physical Society, v. 95, p. 1628–1634, Sep 1954. Available at: <https://link.aps.org/doi/10.1103/PhysRev.95.1628>.

YAMASHITA, M. Dimensional effects in efimov physics. **Few-Body Systems**, Springer, v. 60, p. 1–10, 2019.

YAMASHITA, M.; BELLOTTI, F. F.; FREDERICO, T.; FEDOROV, D. V.; JENSEN, A. S.; ZINNER, N. T. Weakly bound states of two-and three-boson systems in the crossover from two to three dimensions. **Journal of Physics B: Atomic, Molecular and Optical Physics**, IOP Publishing, v. 48, n. 2, p. 025302, 2014.

YAMASHITA, M. T.; FREDERICO, T.; TOMIO, L. Comment on “efimov states and their fano resonances in a neutron-rich nucleus”. **Physical review letters**, APS, v. 99, n. 26, p. 269201, 2007.

- YAMASHITA, M. T.; FREDERICO, T.; TOMIO, L.; DELFINO, A. Weakly bound atomic trimers in ultracold traps. **Physical Review A**, APS, v. 68, n. 3, p. 033406, 2003.
- YAMASHITA, M. T.; ROSA, D.; SANDOVAL, J. Few-body techniques using momentum space for bound and continuum states. **Few-Body Systems**, Springer, v. 59, p. 1–11, 2018.
- YANG, X.; GUO, S.; CHAN, F.; WONG, K.; CHING, W. Analytic solution of a two-dimensional hydrogen atom. i. nonrelativistic theory. **Physical Review A**, APS, v. 43, n. 3, p. 1186, 1991.
- YDREFORS, E.; Alvarenga Nogueira, J.; GIGANTE, V.; FREDERICO, T.; KARMANOV, V. Three-body bound states with zero-range interaction in the bethe–salpeter approach. **Physics Letters B**, v. 770, p. 131–137, 2017. ISSN 0370-2693. Available at: <https://www.sciencedirect.com/science/article/pii/S037026931730309X>.
- YDREFORS, E.; NOGUEIRA, J.; GIGANTE, V.; FREDERICO, T.; KARMANOV, V. Three-body bound states with zero-range interaction in the bethe-salpeter approach. **Physics Letters B**, v. 770, 03 2017.
- YDREFORS, E.; NOGUEIRA, J. A.; KARMANOV, V.; FREDERICO, T. Three-boson bound states in minkowski space with contact interactions. **Physical Review D**, APS, v. 101, n. 9, p. 096018, 2020.
- YU, X.; SIVULA, K. Layered 2d semiconducting transition metal dichalcogenides for solar energy conversion. **Current Opinion in Electrochemistry**, Elsevier, v. 2, n. 1, p. 97–103, 2017.
- ZHANG, C.; GONG, C.; NIE, Y.; MIN, K.-A.; LIANG, C.; OH, Y. J.; ZHANG, H.; WANG, W.; HONG, S.; COLOMBO, L. *et al.* Systematic study of electronic structure and band alignment of monolayer transition metal dichalcogenides in van der waals heterostructures. **2D Materials**, IOP Publishing, v. 4, n. 1, p. 015026, 2016.
- ZHANG, C.; WANG, H.; CHAN, W.; MANOLATOU, C.; RANA, F. Absorption of light by excitons and trions in monolayers of metal dichalcogenide mo s 2: Experiments and theory. **Physical Review B**, APS, v. 89, n. 20, p. 205436, 2014.
- ZHANG, D. K.; KIDD, D. W.; VARGA, K. Excited biexcitons in transition metal dichalcogenides. **Nano letters**, ACS Publications, v. 15, n. 10, p. 7002–7005, 2015.
- ZHANG, Y.; LI, H.; WANG, H.; LIU, R.; ZHANG, S.-L.; QIU, Z.-J. On valence-band splitting in layered mos2. **ACS nano**, ACS Publications, v. 9, n. 8, p. 8514–8519, 2015.

Appendix A - Convergencies of numerical solutions introduced in chapter 2

Constructing the relativistic potential from the nonrelativistic one

Table A.1 shows the convergence of the numerical solution of Eq. (2.10) concerning the iteration number. The calculations are performed using the separable Yamaguchi potential with fixed points $p = 0.05 \text{ fm}^{-1}$ and $p' = 0.10 \text{ fm}^{-1}$. The potential strength λ_{nr} is calculated using Eq. (2.7) with $E_d = -2.225 \text{ MeV}$.

TABLE A.1 – The convergence of the matrix elements of the relativistic potential $V_r(p, p')$ (in units of MeV fm^3) as a function of iteration number calculated by Yamaguchi separable potential in the fixed points ($p = 0.05 \text{ fm}^{-1}$, $p' = 0.10 \text{ fm}^{-1}$). The value of the nonrelativistic Yamaguchi separable potential $V_{nr}(p, p')$ is also given. Result are obtained with λ_{nr} calculated with Eq. (2.7) with $E_d = -2.225 \text{ MeV}$.

		$V_{nr}(p, p')$
		-6.29691170
Iteration #		$V_r(p, p')$
0		-6.29606511
1		-6.37714234
2		-6.37909915
3		-6.37914526
4		-6.37914634
5		-6.37914636
6		-6.37914636

Constructing the boosted potential from the nonrelativistic one

Table A.2 shows the convergence of the numerical solution of Eq. (2.16) concerning the iteration number. The calculations are performed using the Yamaguchi separable potential in fixed points ($p = 0.05 \text{ fm}^{-1}$, $p' = 0.10 \text{ fm}^{-1}$) for four different values of

the Jacobi momentum $k = 1, 5$, and 10 fm^{-1} . The nonrelativistic Yamaguchi separable potential $V_{nr}(p, p')$ is also given. The potential strength λ_{nr} is calculated using Eq. (2.7) with $E_d = -2.225 \text{ MeV}$.

TABLE A.2 – The convergence of the matrix elements of the boosted potential $V_k(p, p')$ (in units of MeV fm^3) as a function of iteration number calculated by Yamaguchi separable potential in the fixed points ($p = 0.05 \text{ fm}^{-1}$, $p' = 0.10 \text{ fm}^{-1}$) and for four different values of the Jacobi momentum $k = 1, 5, 10 \text{ fm}^{-1}$. The value of the nonrelativistic Yamaguchi separable potential $V_{nr}(p, p')$ is also given. Result are obtained with λ_{nr} calculated with Eq. (2.7) with $E_d = -2.225 \text{ MeV}$.

$V_{nr}(p, p')$			
-6.29691170			
$V_k(p, p')$			
Iteration #	$k = 1 \text{ fm}^{-1}$	$k = 5 \text{ fm}^{-1}$	$k = 10 \text{ fm}^{-1}$
0	-6.26160053	-5.57378393	-4.34071747
1	-6.34145948	-5.63163590	-4.36941472
2	-6.34336891	-5.63276815	-4.36977645
3	-6.34341349	-5.63278983	-4.36978093
4	-6.34341452	-5.63279024	-4.36978098
5	-6.34341454	-5.63279024	-4.36978098
6	-6.34341454	-5.63279024	-4.36978098

Relativistic and nonrelativistic dimer binding energy

TABLE A.3 – Convergence of the nonrelativistic (E_d^{nr}) and relativistic (E_d^{rel}) dimer binding energies as a function of the number of relative momentum mesh points N_p for the Yamaguchi-I potential.

N_p	$E_d^{nr} \text{ (MeV)}$	$E_d^r \text{ (MeV)}$	$\left \frac{E_d^{nr} - E_d^r}{E_d^{nr}} \right \times 100\%$
30	-2.206342	-2.207639	0.058785
40	-2.207020	-2.208319	0.058858
50	-2.207089	-2.208388	0.058856
60	-2.207088	-2.208386	0.058810
70	-2.207088	-2.208386	0.058810
80	-2.207087	-2.208386	0.058856
90	-2.207087	-2.208386	0.058856
100	-2.207087	-2.208386	0.058856

Table A.3 shows that the constructed relativistic potential accurately reproduces the binding energy obtained from the Yamaguchi-I potential, with a relative percentage difference of approximately 0.06%. In Table A.4, we show the dimer relativistic and non-relativistic binding energies for all Yamaguchi models using potential strengths listed in Table 2.1.

TABLE A.4 – Nonrelativistic and relativistic dimer binding energies for all Yamaguchi models

Yamaguchi potential type	E_d^{nr} (MeV)	E_d^r (MeV)	$\left \frac{E_d^{nr} - E_d^r}{E_d^{nr}} \right \times 100\%$
Y-I	-2.207087	-2.208386	0.058856
Y-II	-0.415328	-0.415373	0.010835
Y-III	-0.412947	-0.412992	0.010896
Y-IV	-0.331778	-0.331807	0.008741

TABLE A.5 – The boosted and nonrelativistic dimer binding energies in the unit of MeV. The nonrelativistic potentials obtained from a separable boosted potential by solving Eq. (2.16), and the boosted result are calculated directly from Eq. (2.29). The boosted potential strength λ_k is calculated by Eq. (2.30) when the dimer rest energy is $M_d = -2.225$ MeV.

Potential	β (fm ⁻¹)	$k = 0$ fm ⁻¹	$k = 1$ fm ⁻¹	$k = 10$ fm ⁻¹	$k = 100$ fm ⁻¹	$k = 1000$ fm ⁻¹
boosted	1	-2.225000	-2.225000	-2.225000	-2.225000	-2.225000
NR	1	-2.223682	-2.223682	-2.223682	-2.223682	-2.223682
boosted	10	-2.225000	-2.225000	-2.225000	-2.225000	-2.225000
NR	10	-2.223682	-2.223682	-2.223682	-2.223682	-2.223682
boosted	100	-2.225000	-2.225000	-2.225000	-2.225000	-2.225000
NR	100	-2.223682	-2.223682	-2.223682	-2.223682	-2.223682
boosted	1000	-2.224998	-2.224998	-2.224996	-2.225000	-2.225000
NR	1000	-2.223868	-2.223870	-2.223981	-2.223662	-2.223682

Three-body binding energy and expectation values

Table A.6 shows the convergency of results for the Yamaguchi-I potential, including the expectation value of the total Hamiltonian $\langle H \rangle$ calculated with the wave function, the nonrelativistic binding energies E_{nr}^{3B} of the 3B system, and the corresponding relative percentage differences between them, as presented in the last column. The calculations are performed by varying the number of mesh points for the Jacobi momenta p and q (with $N_p = N_q$) while keeping the number of mesh points for the angle between them fixed at 40 by solving Eq. (2.60). The 3D Faddeev integral equation solution requires a maximum of 6 iterations.

TABLE A.6 – The expectation value of Hamiltonian $\langle H \rangle = \langle H_0 \rangle + \langle V \rangle$ and nonrelativistic 3B binding Energy E_{nr}^{3B} , calculated for Yamaguchi-I potential, as a function of the number of mesh points for Jacobi momenta p and q ($N_p = N_q$).

$N_p = N_q$	$\langle H \rangle$ (MeV)	E_{nr}^{3B} (MeV)	$\left \frac{\langle H \rangle - E_{nr}^{3B}}{E_{nr}^{3B}} \right \%100$
30	-25.267	-25.483	0.8476
40	-25.406	-25.423	0.0669
50	-25.426	-25.413	0.0511
60	-25.403	-25.414	0.0433
70	-25.414	-25.414	0.0000
80	-25.407	-25.411	0.0157
90	-25.409	-25.410	0.0039

Similar to Table A.6, in Table A.7, we present the results using 60 mesh points for Jacobi momenta p and q , and 40 mesh points for angle variables for different Yamaguchi type potentials.

TABLE A.7 – The expectation value of Hamiltonian $\langle H \rangle = \langle H_0 \rangle + \langle V \rangle$, nonrelativistic 3B binding Energy E_{nr}^{3B} , and relative percentage difference between them, calculated for four models of Yamaguchi potential.

Potential	$\langle H \rangle$ (MeV)	E_{nr}^{3B} (MeV)	$\left \frac{\langle H \rangle - E_{nr}^{3B}}{E_{nr}^{3B}} \right \%100$
Y-I	-25.403	-25.414	0.0433
Y-II	-12.444	-12.455	0.0883
Y-III	-9.2199	-9.2329	0.1408
Y-IV	-8.499	-8.5121	0.1539

Appendix B - Analytic calculation of potential strength

Starting from the Schrödinger equation for a bound state

$$H|\psi\rangle = E|\psi\rangle, \quad (\text{B.1})$$

where H is the Hamiltonian, define as $H = H_0 + V$, the potential's separable form, i.e., $V = \lambda|\chi\rangle\langle\chi|$, permits the expression

$$(H_0 + \lambda|\chi\rangle\langle\chi|)|\psi\rangle = E|\psi\rangle. \quad (\text{B.2})$$

After applying the completeness relation and left-multiplying by $\langle p|$, we arrive at:

$$\frac{p^2}{2m}\psi(p) + 4\pi\lambda \int_0^\infty dp' g(p)g(p')\psi(p') = E\psi(p), \quad (\text{B.3})$$

simplifying further, we reach

$$\psi(p) = \lambda \frac{g(p)}{E - \frac{p^2}{2m}} \int_0^\infty dp' g(p')\psi(p'), \quad (\text{B.4})$$

multiplying by $g(p)$ and integrating over p , we find

$$\int_0^\infty g(p)\psi(p)dp = \lambda \int_0^\infty dp \frac{g^2(p)}{E - \frac{p^2}{2m}} \int_0^\infty dp' g(p')\psi(p') \quad (\text{B.5})$$

which can be simplified as

$$\frac{1}{\lambda} = 4\pi \int_0^\infty dp p^2 \frac{g^2(p)}{E_d - \frac{p^2}{m}}. \quad (\text{B.6})$$

Appendix C - Calculating the non-PW dimer binding energy and wave function

Malfliet-Tjon potential

To examine the difference between the angular-dependent equation (3.3) and the equation without angular dependence (3.4), we initially use the spin-averaged Yukawa-type Malfliet-Tjon (MT) potential (MALFLIET; TJON, 1969). To discretize the continuous momentum and angle variables, we use the Gauss-Legendre quadratures with a linear mapping $\phi = \pi(1 + x)$ for angle variables and a hyperbolic mapping $p = \frac{1+x}{1-x}$ for the magnitude of Jacobi momenta. The MT potential in the momentum space is given by

$$V(\mathbf{p}, \mathbf{p}') = \frac{1}{2\pi} \left(\frac{V_R}{\sqrt{q^2 + \mu_R^2}} + \frac{V_A}{\sqrt{q^2 + \mu_A^2}} \right), \quad \mathbf{q} = \mathbf{p} - \mathbf{p}'. \quad (\text{C.1})$$

The derivation of the Eq. (C.1) can be found in Appendix D.

In the context of the MT potential, we introduce two distinct models in our 2D calculations, as indicated in Table C.1. Model-1 is constructed by considering both the repulsive and attractive components of the potential, where V_R and V_A represent the strengths of the repulsive and attractive parts, respectively, and μ_R and μ_A denote their corresponding ranges. On the other hand, Model-2 is solely based on the attractive part of the potential.

TABLE C.1 – Parameters of two models of MT potential we use in 2D calculations.

MT-model	V_A (MeV fm)	μ_A (fm ⁻¹)	V_R (MeV fm)	μ_R (fm ⁻¹)
Model-1	-600.00	1.550	1438.7228	3.21
Model-2	-600.00	1.550	0	0

In Table C.2, we present the dimer binding energy calculated using Model-1 and Model-2 of the MT potential as a function of number of mesh points for angle variable, with the parameters listed in Table C.1. The results are shown for the angular-dependent dimer obtained by solving Eq. (3.3) (top panel), and for the dimer without angular dependence using Eq. (3.4) (bottom panel). The calculations are performed with 200 mesh points for

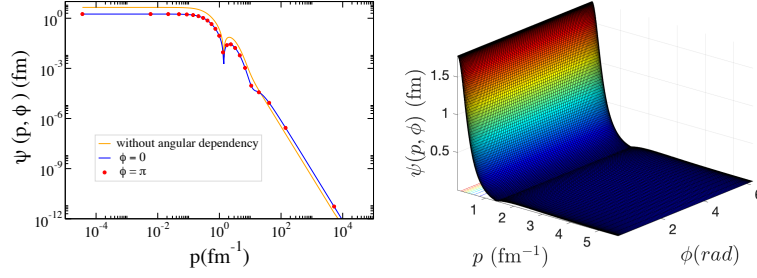
2B relative momenta.

TABLE C.2 – Convergence of 2B binding energy as a function of mesh points for angle variables N_ϕ . Upper panel is the result for angular-dependent dimer obtained by solving Eq. (3.3), bottom panel is the results for dimer without angular dependence using Eq. (3.4).

N_ϕ	E_d (MeV)	$E_d^{(0)}$ (MeV)	$E_d^{(1)}$ (MeV)
With angular dependency Eq. (3.3)			
	Model-1	Model-2	
41	−6.245	−7874	−314.2
61	−6.245	−7834	−312.3
81	−6.245	−7821	−311.8
101	−6.245	−7815	−311.6
Without angular dependency Eq. (3.4)			
101	−6.246	−7806	−312.4

Figure C.1 illustrates the angular dependence of the dimer wave function calculated using Eq. (3.3) for both Model-1 and Model-2. In addition, 2D plots present the dimer wave function calculated using Eq. (3.4). The calculations were performed using 200 mesh points for the 2B relative momenta and 101 mesh points for the angle variables.

MT Model-1



MT Model-2

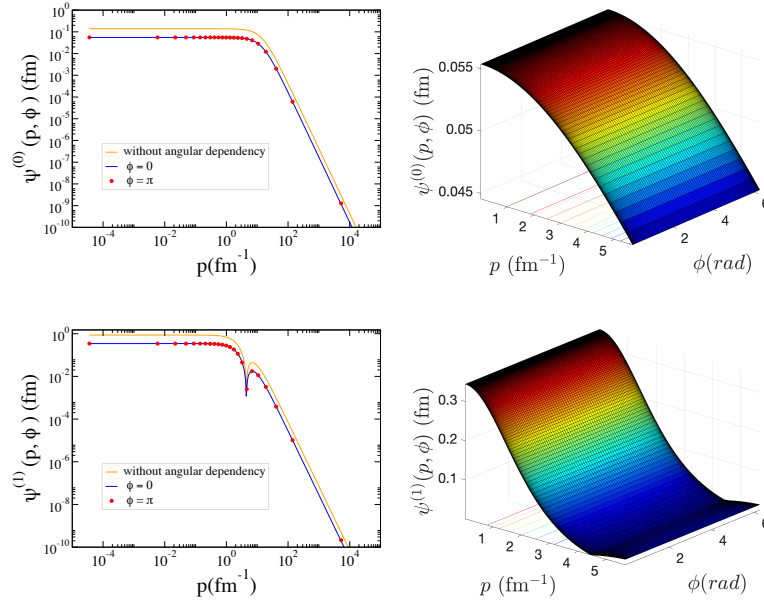


FIGURE C.1 – The dimer wave function was calculated using Model-1 and Model-2 of the MT potential, both as a function of relative momentum for a fixed angle (left panel), and as a function of relative momentum and the angle between them (right panel).

Coulomb potential

To further test the numerical accuracy of the solution of the angle-independent Eq. (3.4), we adopt Coulomb-type potentials, which have an analytical solution given by

$$V(\mathbf{p}, \mathbf{p}') = \frac{-1}{\pi |\mathbf{p} - \mathbf{p}'|}. \quad (\text{C.2})$$

For particles with mass $m = 1$, it is well known that the exact bound state energy levels are of the form (YANG *et al.*, 1991; PARFITT; PORTNOI, 2002; OLSEN *et al.*, 2016)

$$E_n = -\frac{1}{(n + 1/2)^2}, \quad n = 0, 1, 2, \dots \quad (\text{C.3})$$

where n is the principal quantum number. We use the potential given in Eq. (C.2) and the results for 2B binding energies are presented in Table C.3.

TABLE C.3 – The analytical and numerical dimer binding energies calculated for Coulomb potential Eq. (C.3). The calculations are performed with 500 mesh points for relative momenta and 40 mesh points for angle variables. Results are obtained with $\hbar c = \text{mass} = 1$.

n	E_{exact}	E_{num}	$(\frac{E_{exact}-E_{num}}{E_{exact}}) \times 100$
0	-4.00000	-3.99928	0.01800
1	-0.44444	-0.44441	0.00700
2	-0.16000	-0.16017	0.10625
3	-0.08163	-0.08193	0.36751

From Table C.3, it is evident that the calculated results obtained using Eq. (3.4) are in good agreement with the exact values provided in Eq. (C.3), which confirm the accuracy of the numerical method for solving Eq. (3.4). In Fig. C.2 we show the dimer wave functions $\psi^{(n)}(p)$ as a function of relative momentum p , corresponding to the numerical binding energies listed in Table C.3.

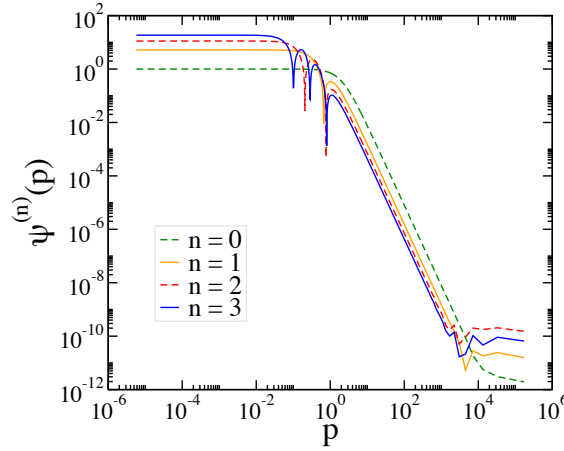


FIGURE C.2 – Dimer wave functions $\psi^{(n)}(p)$ as a function of relative momentum p for ground and excited states.

Appendix D - Fourier transformation of Malfliet-Tjon potential

To obtain the Malfliet-Tjon interaction in momentum space, we perform the following Fourier transformation.

$$\begin{aligned}
 V(\mathbf{q}) &= \frac{1}{4\pi^2} \int d^2r e^{-i\mathbf{q}\cdot\mathbf{r}} V(r); \quad \mathbf{q} \cdot \mathbf{r} = q \cdot r \cos(\phi) \\
 &= \frac{V_0}{4\pi^2} \int_0^\infty dr r \int_0^{2\pi} d\phi \frac{e^{-\mu r}}{r} e^{-iqr \cos(\phi)} \\
 &= \frac{V_0}{4\pi^2} \int_0^\infty dr e^{-\mu r} \int_0^{2\pi} d\phi e^{-iqr \cos(\phi)}; \quad \int_0^{2\pi} d\phi e^{-iqr \cos(\phi)} = 2\pi J_0(qr) \\
 &= \frac{V_0}{2\pi} \int_0^\infty dr e^{-\mu r} J_0(qr); \quad qr = t \rightarrow dr = \frac{dt}{q} \\
 &= \frac{V_0}{2\pi} \int_0^\infty \frac{dt}{q} e^{\frac{-\mu t}{q}} J_0(t); \quad \int_0^\infty dt e^{-st} J_0(t) = \frac{1}{\sqrt{1+s^2}} \\
 &= \frac{1}{2\pi} \frac{V_0}{\sqrt{q^2 + \mu^2}}.
 \end{aligned} \tag{D.1}$$

Appendix E - Exciton convergence with RK potential

TABLE E.1 – The convergence of ground state exciton binding energies (meV) as a function of the number of mesh points N_p and N_ϕ . The calculations are performed for MoS₂ substrate in s -wave. The last row shows the quadratic extrapolation of exciton energy eigenvalues to an infinite number of mesh points.

N_p	N_ϕ							
	11	41	61	81	121	161	201	301
300	-730.3	-772.8	-785.7	-795.0	-808.2	-817.7	-825.1	-838.7
400	-730.2	-765.5	-775.2	-782.1	-792.0	-799.1	-804.6	-814.7
500	-730.2	-761.8	-769.5	-775.1	-782.9	-788.6	-793.0	-801.0
600	-730.2	-759.7	-766.1	-770.7	-777.2	-781.9	-785.6	-792.2
700	-730.2	-758.4	-763.8	-767.8	-773.4	-777.4	-780.5	-786.2
800	-730.2	-757.6	-762.3	-765.7	-770.6	-774.1	-776.9	-781.8
900	-730.2	-757.0	-761.1	-764.2	-768.6	-771.7	-774.1	-778.5
1000	-730.2	-756.6	-760.3	-763.1	-767.0	-769.8	-771.9	-775.9
Quad. extrap.@ $1/N_p \rightarrow 0$	-730.29	-753.85	-753.36	-753.42	-753.52	-753.40	-753.27	-753.34

As one can see from Table E.1, the extrapolated value for the exciton binding energy with $N_\phi = 61$ is in good agreement with the expected value for the exciton binding energy. This confirms that the convergence of the exciton binding energy is achieved with $N_\phi = 61$. To check the accuracy of our results, we have also calculated the expectation values of the free Hamiltonian $\langle H_0 \rangle$, the 2B potential $\langle V \rangle$, and the total Hamiltonian $\langle H \rangle$.

In Table E.2, we present the results for the expectation values and exciton binding energy. The values are shown as a function of the number of mesh points for relative momentum (N_p), while keeping the number of mesh points for the angle variable fixed at $N_\phi = 61$. The last column of Table E.2 shows the relative percentage difference between the total Hamiltonian $\langle H \rangle$ and the binding energy E_{2B} . The results exhibit a perfect agreement, confirming the accuracy of our calculations.

TABLE E.2 – Expectation values in meV of the 2B free Hamiltonian $\langle H_0 \rangle$, pair potentials $\langle V \rangle$, 2B Hamiltonian $\langle H \rangle$, and binding energy E_{2B} in meV calculated for RK potentials. The calculations are performed for MoS₂ in s -wave channel ($m = 0$) with $N_\phi = 61$.

N_p	E_{2B}	$\langle H_0 \rangle$	$\langle V \rangle$	$\langle H \rangle$	$\left \frac{(\langle H \rangle - E_{2B})}{E_{2B}} \right \times 100\%$
300	-785.68	221.85	-1007.53	-785.68	$2.082 \cdot 10^{-6}$
400	-775.19	219.24	-994.42	-775.18	$1.457 \cdot 10^{-7}$
500	-769.53	217.89	-987.42	-769.53	$3.548 \cdot 10^{-6}$
600	-766.09	217.10	-983.19	-766.09	$1.330 \cdot 10^{-4}$
700	-763.84	216.60	-980.43	-763.83	$6.691 \cdot 10^{-5}$
800	-762.27	216.267	-978.53	-762.27	$2.478 \cdot 10^{-4}$
900	-761.13	216.038	-977.17	-761.13	$7.098 \cdot 10^{-5}$
1000	-760.29	215.88	-976.17	-760.29	$1.330 \cdot 10^{-7}$
Quad. extrap.@ $1/N_p \rightarrow 0$	-753.36	214.64	-967.96	-753.32	$5.300 \cdot 10^{-3}$

Appendix F - PW and non PW relations and calculations

F.1 Derivation of the relation between the PW and non PW potential

In this appendix, we want to define a partial wave projection of the local potential $V(r)$. for this, we have

$$V(\mathbf{p}, \mathbf{p}') = \frac{1}{(2\pi)^2} \int d^2r e^{-i\mathbf{p}\cdot\mathbf{r}} V(r) e^{i\mathbf{p}'\cdot\mathbf{r}}. \quad (\text{F.1})$$

To numerically solve Eq. (F.1) in the most general case, we define a coordinate system where the vectors \mathbf{p} , \mathbf{p}' , and \mathbf{r} are freely oriented in the 2D plane, as depicted in Fig. F.1.

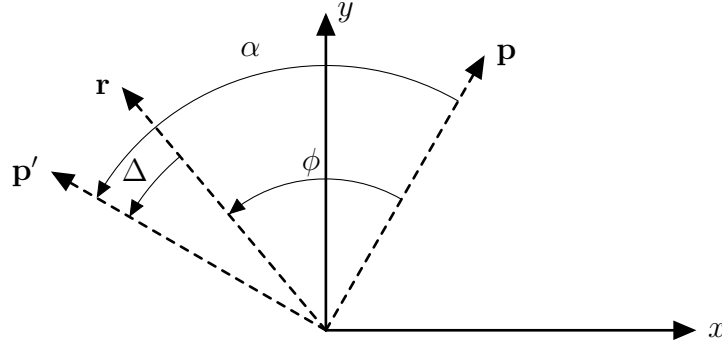


FIGURE F.1 – The coordinate system using fo fourier transformation

By expanding the exponential terms in the partial wave, using the equation (ADHIKARI, 1986)

$$e^{i\mathbf{p}\cdot\mathbf{r}} = e^{ipr \cos(\phi)} = \sum_{m=0}^{\infty} \epsilon_m i^{-m} \cos(m\phi) J_m(pr) \quad (\text{F.2})$$

we have

$$V(\mathbf{p}, \mathbf{p}') = \frac{1}{(2\pi)^2} \int d^2r V(r) \sum_{m=0}^{\infty} \epsilon_m i^{-m} \cos(m\phi) J_m(pr) \sum_{n=0}^{\infty} \epsilon_n i^n \cos(n\Delta) J_n(p'r) \quad (\text{F.3})$$

where

$$\epsilon_m = \begin{cases} 1 & m = 0, \\ 2 & m \neq 0. \end{cases} \quad (\text{F.4})$$

Eq. (F.3) can be written as

$$\begin{aligned} V(\mathbf{p}, \mathbf{p}') &= \frac{1}{(2\pi)^2} \int_0^{\infty} dr r \int_0^{2\pi} d\phi \sum_{m=0}^{\infty} \sum_{n=0}^{\infty} \epsilon_m \epsilon_n i^{n-m} \\ &\times \cos(m\phi) \cos(n(\alpha - \phi)) J_m(pr) V(r) J_n(p'r) \\ &= \frac{1}{(2\pi)^2} \sum_{m=0}^{\infty} \sum_{n=0}^{\infty} \epsilon_m \epsilon_n i^{n-m} \int_0^{\infty} dr r J_m(pr) V(r) J_n(p'r) \\ &\times \int_0^{2\pi} d\phi \cos(m\phi) \cos(n(\alpha - \phi)). \end{aligned} \quad (\text{F.5})$$

Orthogonality of the cosine is given by

$$\int_0^{2\pi} d\phi \cos(m\phi) \cos(n(\alpha - \phi)) = \cos(n\alpha) \Delta_m \delta_{mn} \quad \text{with} \quad \Delta_m = \begin{cases} 2\pi & m = 0, \\ \pi & m \neq 0, \end{cases} \quad (\text{F.6})$$

using this equation, Eq. (F.5) can be simplified as

$$\begin{aligned} V(\mathbf{p}, \mathbf{p}') &= \frac{1}{(2\pi)^2} \sum_{m=0}^{\infty} \sum_{n=0}^{\infty} \epsilon_m \epsilon_n i^{n-m} \Delta_m \delta_{mn} \int_0^{\infty} dr r J_m(pr) V(r) J_n(p'r) \\ &= \frac{1}{(2\pi)^2} \sum_{m=0}^{\infty} \epsilon_m^2 \cos(m\alpha) \Delta_m \int_0^{\infty} dr r J_m(pr) V(r) J_m(p'r). \end{aligned} \quad (\text{F.7})$$

From Eqs. (F.4) and (F.6) we have

$$\delta_m \epsilon_m = 2\pi, \quad (\text{F.8})$$

therefore Eq. (F.7) can be written as

$$V(\mathbf{p}, \mathbf{p}') = \frac{1}{2\pi} \sum_{m=0}^{\infty} \epsilon_m \cos(m\alpha) V_m(p, p') \quad (\text{F.9})$$

where

$$V_m(\mathbf{p}, \mathbf{p}') = \int_0^{\infty} dr r J_m(pr) V(r) J_m(p'r). \quad (\text{F.10})$$

By multiplying both sides of Eq. (F.9) to $\cos(n\phi)$ and integral over the angle ϕ we have

$$\int_0^{2\pi} d\phi V(\mathbf{p}, \mathbf{p}') \cos(n\phi) = \frac{1}{2\pi} \sum_{m=0}^{\infty} \epsilon_m V_m(p, p') \int_0^{2\pi} d\phi \cos(m\phi) \cos(n\phi), \quad (\text{F.11})$$

using orthogonality relation, Eq. (F.6), and Eq.(F.8) we can simplify Eq. (F.11) as

$$\int_0^{2\pi} d\phi V(\mathbf{p}, \mathbf{p}') \cos(m\phi) = V_m(p, p'), \quad (\text{F.12})$$

which is the relation between non-partial wave potential $V(\mathbf{p}, \mathbf{p}')$ and partial wave one $V_m(p, p')$.

F.2 PW wave and non PW dimer binding energy and wave function

To explore the PW relations in more detail, we consider the MT potential using both Model-1 and Model-2 with parameters defined in Table C.1, as well as the Coulomb potential defined in Appendix C.

Malfliet-Tjon potential

In Table. F.1 we present the dimer binding energies calculated with MT potential with parameters listed in Table C.1, for different PW channels using Eq. (3.5).

TABLE F.1 – Dimer binding energies calculated with two models MT potential with parameters listed in Table C.1, with $m = 0$ and $m = 1$ PW channels.

m	E_d (MeV)	$E_d^{(0)}$ (MeV)	$E_d^{(1)}$ (MeV)
	model-1	model-2	
0	−6.246	−7806	−312.4
1	—	−281.5	—

To study the structure of the non-PW and PW Malfliet-Tjon potentials calculated using Eq. (3.6), we select the defined model-1 Malfliet-Tjon potential. The 2B potential for both the non-PW and PW MT potentials is plotted in Fig. F.2 for summation over different partial wave number N_{pw} using Eq. (F.9). Furthermore, the relative difference between non-partial and constructed partial wave potential is illustrated in Fig. F.3. The calculations are performed with 200 mesh points for 2B relative momenta and 101 mesh points for angle variables.

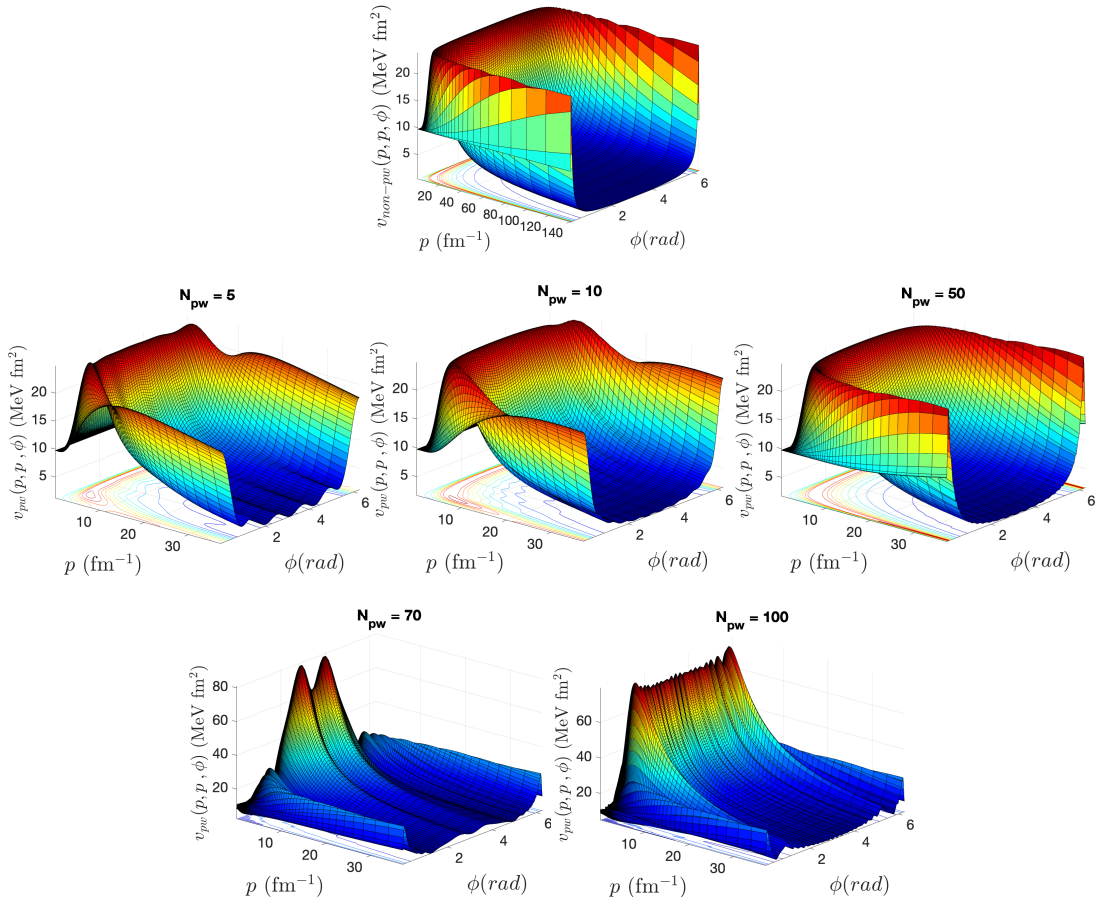


FIGURE F.2 – Angular and momentum dependencies of the diagonal matrix element of the non-PW (top panel) and PW 2B potential obtained with MT model-1, with $p = p'$ for different PW number N_{pw} .

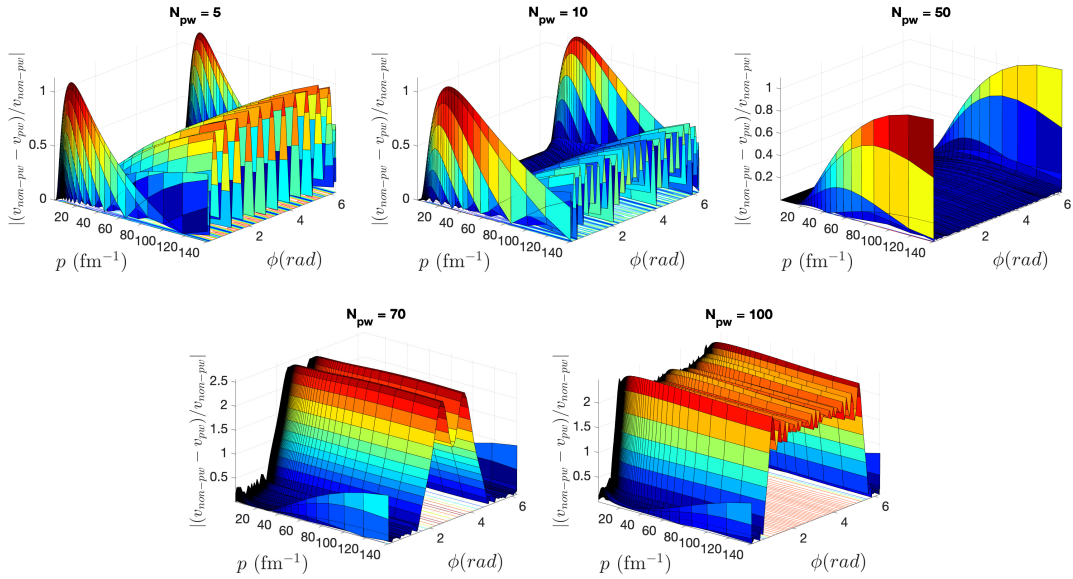


FIGURE F.3 – Angular and momentum dependencies of the relative difference of 2B potentials obtained from non-PW and the summation of PWs up to N_{pw} calculated for MT model-1 potential.

To examine the momentum dependency of the PW potential, we plot the non-PW

and PW potentials as functions of p and p' in Fig. F.4 where the angle ϕ is fixed to 0.57 radian. Additionally, in Fig. F.5, we present the difference between the non-PW and PW potentials for fixed values of ϕ . These figures provide a similar analysis to Figs. F.2 and F.3 but focus on the momentum dependency of PW potential.

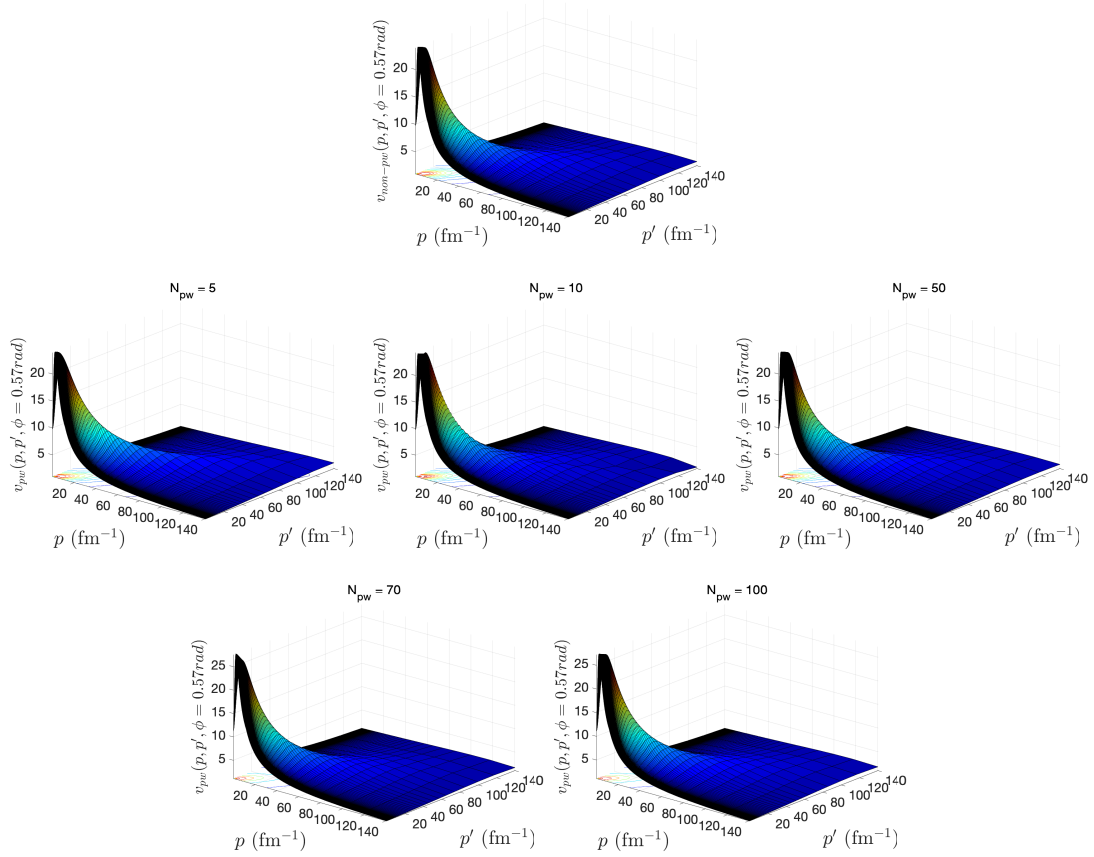


FIGURE F.4 – Similar to Fig. F.2, but for fixed angle variable as a function of p and p' .

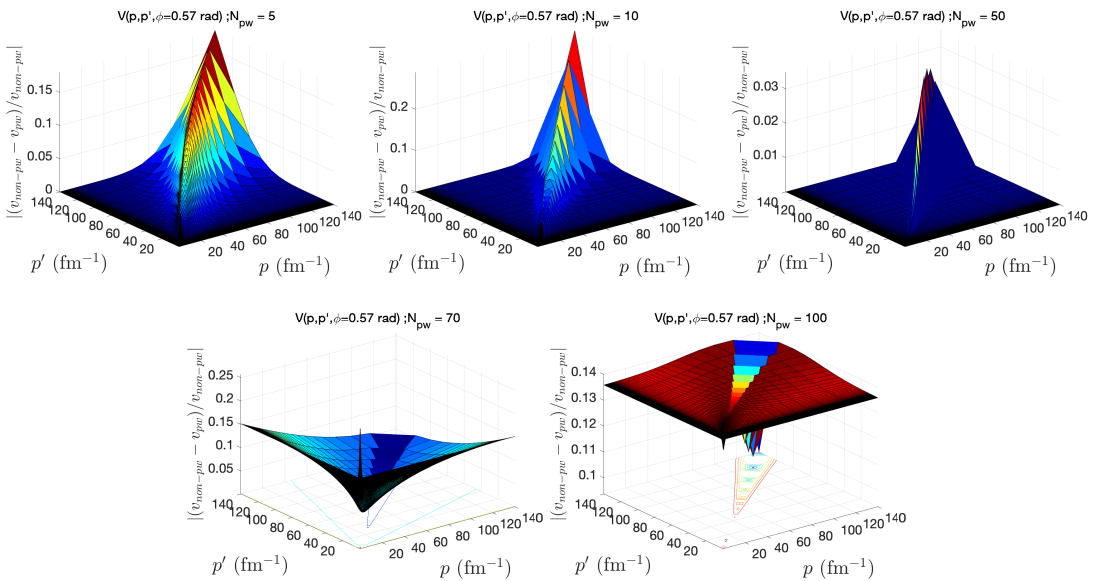


FIGURE F.5 – Similar to Fig. F.3, but for fixed angle variable as a function of p and p' .

From Figs. F.3 and F.5, it is evident that when $N_{pw} > N_\phi/2$, the structure of the PW potential undergoes a significant change.

Coulomb potential

We also consider the Coulomb potential as defined in Eq. (C.2) to investigate the partial wave LS equation, Eq. (3.5), in more detail. The corresponding PW binding energies for various partial waves are presented in Table F.2 for ground and excited states. These calculations are performed using 500 mesh points for relative momenta and 40 mesh points for angle variables.

TABLE F.2 – Dimer binding energy calculated for different partial waves channel with coulomb potential defined in Eq. (C.2).

m	$E_d^{(0)}$	$E_d^{(1)}$	$E_d^{(2)}$	$E_d^{(3)}$
0	-3.999	-0.444	-0.160	-0.082
1	-0.444	-0.160	-0.082	—
2	-0.160	-0.082	—	—
3	-0.082	—	—	—

In Fig. F.6, we show the dimer wave function for different partial waves corresponding to the results listed in Table. F.2.

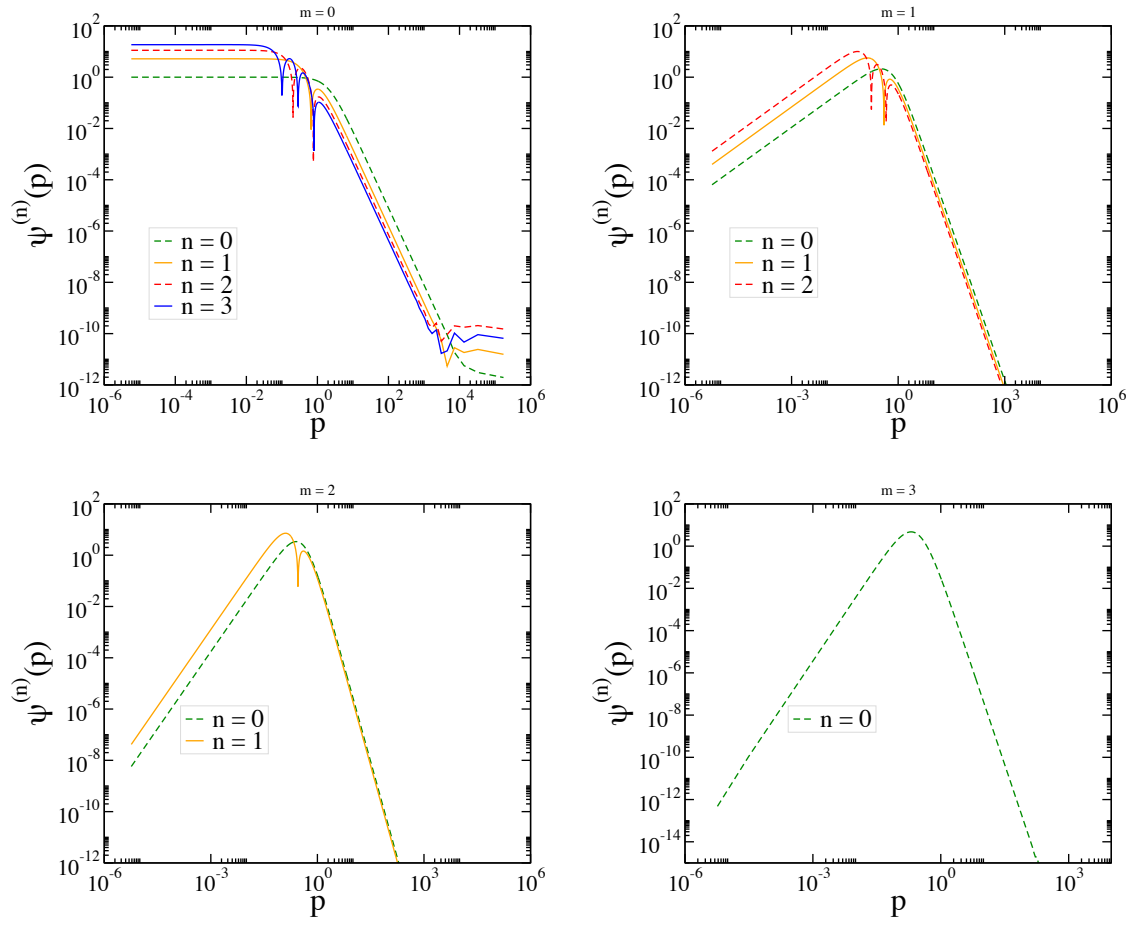


FIGURE F.6 – Dimer wave functions $\psi^{(n)}(p)$ as a function of relative momentum p , for different PW channels corresponding to the numerical binding energies listed in Table F.2.

Appendix G - t —matrix in separable form

The free propagator $G_0(E)$ is given by

$$G_0(E) \equiv \frac{1}{E - H_0}. \quad (\text{G.1})$$

Analogously, the resolvent (or Green's function) is defined as

$$G(E) \equiv \frac{1}{E - H}. \quad (\text{G.2})$$

Using the relation for Hamiltonian, i.e., $H = V + H_0$ and Eqs. (G.1) and (G.2), we can write

$$V = H - H_0 = G_0^{-1}(E) - G^{-1}(E). \quad (\text{G.3})$$

By multiplying Eq. (G.3) for G_0 from the left and G from the right, we obtain

$$G = G_0 + G_0 V G, \quad (\text{G.4})$$

Similarly, by multiplying Eq. (G.3) for G from the left and G_0 from the right, we have

$$G = G_0 + G V G_0. \quad (\text{G.5})$$

Next, we can find the two-body transition matrix $t(E)$ by inserting Eq. (G.5) into Eq. (G.4), resulting in

$$G = G_0 + G_0 [V + V G V] G_0 = G_0 + G_0 t G_0, \quad (\text{G.6})$$

where the t -matrix, $t(E)$, is defined as

$$t = V + V G V. \quad (\text{G.7})$$

Inserting Eq. (G.6) into Eq. (G.4) we have

$$G = G_0 + G_0 V (G_0 + G_0 t G_0) = G_0 + G_0 [V + V G_0 t] G_0. \quad (\text{G.8})$$

By comparing Eq. (G.8) and Eq. (G.6) we have

$$t = V + VG_0t, \quad (\text{G.9})$$

Alternatively one can obtain

$$t = V + tG_0V. \quad (\text{G.10})$$

For one term separable potential

$$V = \lambda|\chi\rangle\langle\chi|, \quad (\text{G.11})$$

we can write Eq. (G.9) as

$$t = \lambda|\chi\rangle\langle\chi| + \lambda|\chi\rangle\langle\chi|G_0t. \quad (\text{G.12})$$

multiplying Eq. (G.12) by $\langle\chi|G_0$ from the left

$$\langle\chi|G_0(E)t(E) = \frac{\lambda\langle\chi|G_0|\chi\rangle\langle\chi|}{1 - \lambda\langle\chi|G_0(E)|\chi\rangle} \quad (\text{G.13})$$

Inserting Eq. (G.13) back in Eq. (G.12), we can write t-matrix in seperable form as

$$t(E) = |\chi\rangle\tau(E)\langle\chi|, \quad (\text{G.14})$$

where

$$\tau(E) = \left(\frac{1}{\lambda^{-1} - \langle\chi|G_0(E)|\chi\rangle} \right). \quad (\text{G.15})$$

Appendix H - Relations between different fragmentation in the four-body system

In this appendix, we study the terms in the FY equation, Eq. (5.21).

Evaluating $\langle \mathbf{u}_1 \ \mathbf{u}_2 \ \mathbf{u}_3 | G_0 t P | \mathbf{u}'_1 \ \mathbf{u}'_2 \ \mathbf{u}'_3 \rangle$

For evaluating the first term, Eq. (5.22), we should insert again, a completeness relation between the two-body t -matrix operator and permutation operator P as:

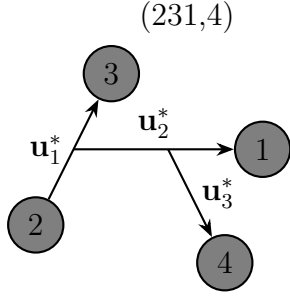
$$\begin{aligned} \langle \mathbf{u}_1 \ \mathbf{u}_2 \ \mathbf{u}_3 | G_0 t P | \mathbf{u}'_1 \ \mathbf{u}'_2 \ \mathbf{u}'_3 \rangle &= \frac{1}{E - \frac{u_1^2}{m} - \frac{3u_2^2}{4m} - \frac{2u_3^2}{3m}} \\ &\times \int D^2 u'' \langle \mathbf{u}_1 \ \mathbf{u}_2 \ \mathbf{u}_3 | t | \mathbf{u}''_1 \ \mathbf{u}''_2 \ \mathbf{u}''_3 \rangle \langle \mathbf{u}''_1 \ \mathbf{u}''_2 \ \mathbf{u}''_3 | P | \mathbf{u}'_1 \ \mathbf{u}'_2 \ \mathbf{u}'_3 \rangle \end{aligned} \quad (\text{H.1})$$

Where the matrix elements of two-body t -matrix and permutation operator P are evaluated separately as:

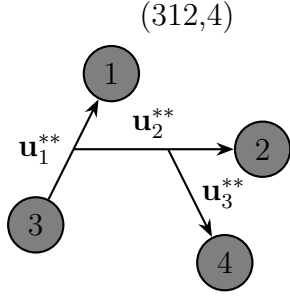
$$\begin{aligned} \langle \mathbf{u}_1 \ \mathbf{u}_2 \ \mathbf{u}_3 | t | \mathbf{u}''_1 \ \mathbf{u}''_2 \ \mathbf{u}''_3 \rangle &= \delta^2(\mathbf{u}_2 - \mathbf{u}''_2) \delta^2(\mathbf{u}_3 - \mathbf{u}''_3) \langle \mathbf{u}_1 | t(\epsilon) | \mathbf{u}''_1 \rangle \\ \epsilon &= E - \frac{3u_2^2}{4m} - \frac{2u_3^2}{3m} \end{aligned} \quad (\text{H.2})$$

$$\begin{aligned} \langle \mathbf{u}''_1 \ \mathbf{u}''_2 \ \mathbf{u}''_3 | P | \mathbf{u}'_1 \ \mathbf{u}'_2 \ \mathbf{u}'_3 \rangle &= {}_{123,4;12} \langle \mathbf{u}''_1 \ \mathbf{u}''_2 \ \mathbf{u}''_3 | \mathbf{u}'_1 \ \mathbf{u}'_2 \ \mathbf{u}'_3 \rangle_{312,4;31} + {}_{123,4;12} \langle \mathbf{u}''_1 \ \mathbf{u}''_2 \ \mathbf{u}''_3 | \mathbf{u}'_1 \ \mathbf{u}'_2 \ \mathbf{u}'_3 \rangle_{231,4;23} \\ &= \delta^2(\mathbf{u}''_3 - \mathbf{u}'_3) \left\{ \delta^2(\mathbf{u}''_1 + \frac{1}{2}\mathbf{u}'_1 - \frac{3}{4}\mathbf{u}'_2) \delta^2(\mathbf{u}''_2 + \mathbf{u}'_1 + \frac{1}{2}\mathbf{u}'_2) \right. \\ &\quad \left. + \delta^2(\mathbf{u}''_1 + \frac{1}{2}\mathbf{u}'_1 + \frac{3}{4}\mathbf{u}'_2) \delta^2(\mathbf{u}''_2 - \mathbf{u}'_1 + \frac{1}{2}\mathbf{u}'_2) \right\} \end{aligned} \quad (\text{H.3})$$

For evaluation the matrix elements of permutation operator P we have used the relation between Jacobi momenta in different two-body subsystems $(312, 4; 12)$, $(231, 4; 12)$ and $(123, 4; 12)$.



$$\begin{aligned} \mathbf{u}_1^* &= \frac{\mathbf{k}_2 - \mathbf{k}_3}{2} \equiv -\frac{1}{2}\mathbf{u}_1 - \frac{3}{4}\mathbf{u}_2, \\ \mathbf{u}_2^* &= \frac{2}{3}(\mathbf{k}_1 - \frac{\mathbf{k}_2 + \mathbf{k}_3}{2}) \equiv \mathbf{u}_1 - \frac{1}{2}\mathbf{u}_2, \\ \mathbf{u}_3^* &= \frac{3}{4}(\mathbf{k}_4 - \frac{\mathbf{k}_1 + \mathbf{k}_2 + \mathbf{k}_3}{3}) \equiv \mathbf{u}_3, \end{aligned} \quad (\text{H.4})$$



$$\begin{aligned} \mathbf{u}_1^{**} &= \frac{\mathbf{k}_3 - \mathbf{k}_1}{2} \equiv -\frac{1}{2}\mathbf{u}_1 + \frac{3}{4}\mathbf{u}_2, \\ \mathbf{u}_2^{**} &= \frac{2}{3}(\mathbf{k}_2 - \frac{\mathbf{k}_1 + \mathbf{k}_3}{2}) \equiv -\mathbf{u}_1 - \frac{1}{2}\mathbf{u}_2, \\ \mathbf{u}_3^{**} &= \frac{3}{4}(\mathbf{k}_4 - \frac{\mathbf{k}_1 + \mathbf{k}_2 + \mathbf{k}_3}{3}) \equiv \mathbf{u}_3, \end{aligned} \quad (\text{H.5})$$

Inserting Eqs. (H.2) and (H.3) into Eq. (H.1) leads to:

$$\begin{aligned} \langle \mathbf{u}_1 \mathbf{u}_2 \mathbf{u}_3 | G_0 t P | \mathbf{u}_1' \mathbf{u}_2' \mathbf{u}_3' \rangle &= \frac{\delta^2(\mathbf{u}_3 - \mathbf{u}_3')}{E - \frac{u_1^2}{m} - \frac{3u_2^2}{4m} - \frac{2u_3^2}{3m}} \\ &\quad \{ \delta^2(\mathbf{u}_2 + \mathbf{u}_1' + \frac{1}{2}\mathbf{u}_2') \langle \mathbf{u}_1 | t(\epsilon) | \frac{1}{2}\mathbf{u}_2 + \mathbf{u}_2' \rangle \\ &\quad + \delta^2(\mathbf{u}_2 - \mathbf{u}_1' + \frac{1}{2}\mathbf{u}_2') \langle \mathbf{u}_1 | t(\epsilon) | \frac{-1}{2}\mathbf{u}_2 - \mathbf{u}_2' \rangle \} \end{aligned} \quad (\text{H.6})$$

Evaluating $\langle \mathbf{v}_1 \mathbf{v}_2 \mathbf{v}_3 | G_0 t \tilde{P} | \mathbf{v}_1' \mathbf{v}_2' \mathbf{v}_3' \rangle$

Representation of the second term, Eq. (5.22), follows the similar steps:

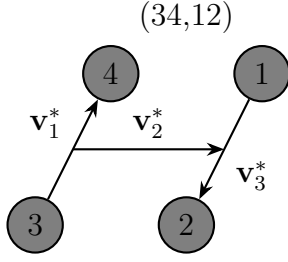
$$\begin{aligned} \langle \mathbf{v}_1 \mathbf{v}_2 \mathbf{v}_3 | G_0 t \tilde{P} | \mathbf{v}_1' \mathbf{v}_2' \mathbf{v}_3' \rangle &= \frac{1}{E - \frac{v_1^2}{m} - \frac{v_2^2}{2m} - \frac{v_3^2}{m}} \int D^2 v'' \langle \mathbf{v}_1 \mathbf{v}_2 \mathbf{v}_3 | t | \mathbf{v}_1'' \mathbf{v}_2'' \mathbf{v}_3'' \rangle \\ &\quad \times \langle \mathbf{v}_1'' \mathbf{v}_2'' \mathbf{v}_3'' | \tilde{P} | \mathbf{v}_1' \mathbf{v}_2' \mathbf{v}_3' \rangle \end{aligned} \quad (\text{H.7})$$

The matrix elements of two-body t -matrix and permutation operator \tilde{P} are evaluated as:

$$\langle \mathbf{v}_1 \mathbf{v}_2 \mathbf{v}_3 | t | \mathbf{v}_1'' \mathbf{v}_2'' \mathbf{v}_3'' \rangle = \delta^2(\mathbf{v}_2 - \mathbf{v}_2'') \delta^2(\mathbf{v}_3 - \mathbf{v}_3'') \langle \mathbf{v}_1 | t(\epsilon^*) | \mathbf{v}_1'' \rangle; \quad \epsilon^* = E - \frac{v_2^2}{2m} - \frac{v_3^2}{m} \quad (\text{H.8})$$

$$\begin{aligned} \langle \mathbf{v}_1'' \mathbf{v}_2'' \mathbf{v}_3'' | \tilde{P} | \mathbf{v}_1' \mathbf{v}_2' \mathbf{v}_3' \rangle &= {}_{12,34;12} \langle \mathbf{v}_1'' \mathbf{v}_2'' \mathbf{v}_3'' | \mathbf{v}_1' \mathbf{v}_2' \mathbf{v}_3' \rangle_{34,12;34} \\ &= \delta^2(\mathbf{v}_1'' - \mathbf{v}_3') \delta^2(\mathbf{v}_2'' + \mathbf{v}_2') \delta^2(\mathbf{v}_3'' - \mathbf{v}_1') \end{aligned} \quad (\text{H.9})$$

For evaluation the matrix elements of permutation operator \tilde{P} we have used the relation between Jacobi momenta in different two-body subsystems (12, 34; 12), (34, 12; 34).



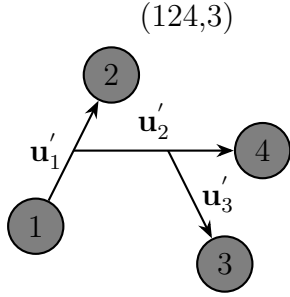
$$\begin{aligned} \mathbf{v}_1^* &= \frac{\mathbf{k}_3 - \mathbf{k}_1}{2} \equiv \mathbf{v}_3 \\ \mathbf{v}_2^* &= \frac{\mathbf{k}_3 + \mathbf{k}_4}{2} - \frac{\mathbf{k}_1 - \mathbf{k}_2}{2} \equiv -\mathbf{v}_2, \\ \mathbf{v}_3^* &= \frac{\mathbf{k}_1 - \mathbf{k}_2}{2} \equiv \mathbf{v}_1. \end{aligned} \quad (\text{H.10})$$

Inserting Eqs. (H.8) and (H.9) into Eq. (H.7) leads to:

$$\langle \mathbf{v}_1 \mathbf{v}_2 \mathbf{v}_3 | G_0 t \tilde{P} | \mathbf{v}_1' \mathbf{v}_2' \mathbf{v}_3' \rangle = \frac{\delta^2(\mathbf{v}_2 + \mathbf{v}_2') \delta^2(\mathbf{v}_3 - \mathbf{v}_1')}{E - \frac{v_1^2}{m} - \frac{v_2^2}{2m} - \frac{v_3^2}{m}} \langle \mathbf{v}_1 | t(\epsilon^*) | \mathbf{v}_3' \rangle \quad (\text{H.11})$$

Evaluating $\langle \mathbf{u}_1' \mathbf{u}_2' \mathbf{u}_3' | (1 + P_{34}) | \mathbf{u}_1'' \mathbf{u}_2'' \mathbf{u}_3'' \rangle$

For evaluation the third term, Eq. (5.22), we should use the relation between Jacobi momenta in different chains (123, 4; 12) and (124, 3; 12).

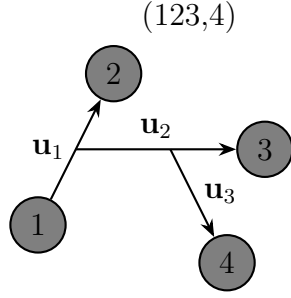


$$\begin{aligned} \mathbf{u}_1' &= \frac{\mathbf{k}_1 - \mathbf{k}_2}{2} \equiv \mathbf{u}_1, \\ \mathbf{u}_2' &= \frac{2}{3}(\mathbf{k}_4 - \frac{\mathbf{k}_1 + \mathbf{k}_2}{2}) \equiv \frac{1}{3}\mathbf{u}_2 + \frac{8}{9}\mathbf{u}_3, \\ \mathbf{u}_3' &= \frac{3}{4}(\mathbf{k}_3 - \frac{\mathbf{k}_1 + \mathbf{k}_2 + \mathbf{k}_4}{3}) \equiv \mathbf{u}_2 - \frac{1}{3}\mathbf{u}_3. \end{aligned} \quad (\text{H.12})$$

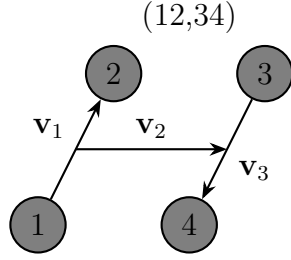
$$\begin{aligned} \langle \mathbf{u}_1' \mathbf{u}_2' \mathbf{u}_3' | (1 + P_{34}) | \mathbf{u}_1'' \mathbf{u}_2'' \mathbf{u}_3'' \rangle &= \delta^2(\mathbf{u}_1' - \mathbf{u}_1'') \\ &\times \left\{ \delta^2(\mathbf{u}_2' - \mathbf{u}_2'') \delta^2(\mathbf{u}_3' - \mathbf{u}_3'') \right. \\ &\quad \left. + \delta^2(\mathbf{u}_2' - \frac{1}{3}\mathbf{u}_2'' - \frac{8}{9}\mathbf{u}_3'') \delta^2(\mathbf{u}_3' - \mathbf{u}_2'' + \frac{1}{3}\mathbf{u}_3'') \right\} \quad (\text{H.13}) \end{aligned}$$

Evaluating $\langle \mathbf{v}_1' \mathbf{v}_2' \mathbf{v}_3' | (1 + P_{34}) | \mathbf{u}_1' \mathbf{u}_2' \mathbf{u}_3' \rangle$

Finally, for evaluation of the fourth term, Eq. (5.22), we should use the relation between Jacobi momenta in two naturally different chains (123, 4; 12) and (12, 34; 12).



$$\begin{aligned} \mathbf{u}_1 &= \frac{\mathbf{k}_1 - \mathbf{k}_2}{2} \\ \mathbf{u}_2 &= \frac{2}{3}(\mathbf{k}_3 - \frac{\mathbf{k}_1 + \mathbf{k}_2}{2}) \\ \mathbf{u}_3 &= \frac{3}{4}(\mathbf{k}_4 - \frac{\mathbf{k}_1 + \mathbf{k}_2 + \mathbf{k}_3}{3}) \end{aligned} \quad (\text{H.14})$$



$$\begin{aligned} \mathbf{v}_1 &= \frac{\mathbf{k}_1 - \mathbf{k}_2}{2} \\ \mathbf{v}_2 &= \frac{\mathbf{k}_1 + \mathbf{k}_2}{2} - \frac{\mathbf{k}_3 + \mathbf{k}_4}{2} \\ \mathbf{v}_3 &= \frac{\mathbf{k}_3 - \mathbf{k}_4}{2} \end{aligned} \quad (\text{H.15})$$

$$\begin{aligned} \langle \mathbf{v}'_1 \mathbf{v}'_2 \mathbf{v}'_3 | (1 + P_{34}) | \mathbf{u}'_1 \mathbf{u}'_2 \mathbf{u}'_3 \rangle &= \langle \mathbf{v}'_1 \mathbf{v}'_2 \mathbf{v}'_3 | \mathbf{u}'_1 \mathbf{u}'_2 \mathbf{u}'_3 \rangle + {}_{123,4;12} \langle \mathbf{v}'_1 \mathbf{v}'_2 \mathbf{v}'_3 | \mathbf{u}'_1 \mathbf{u}'_2 \mathbf{u}'_3 \rangle_{124,3;12} \\ &= \delta^2(\mathbf{u}'_1 - \mathbf{v}'_1) \\ &\times \left\{ \begin{aligned} &\delta^2(\mathbf{u}'_2 + \frac{2}{3}\mathbf{v}'_2 - \frac{2}{3}\mathbf{v}'_3) \quad \delta^2(\mathbf{u}'_3 + \frac{1}{2}\mathbf{v}'_2 + \mathbf{v}'_3) \\ &+ \delta^2(\mathbf{u}'_2 + \frac{2}{3}\mathbf{v}'_2 + \frac{2}{3}\mathbf{v}'_3) \quad \delta^2(\mathbf{u}'_3 + \frac{1}{2}\mathbf{v}'_2 - \mathbf{v}'_3) \end{aligned} \right\} \quad (\text{H.16}) \end{aligned}$$

FOLHA DE REGISTRO DO DOCUMENTO			
1. CLASSIFICAÇÃO/TIPO TD	2. DATA 31 de janeiro de 2025	3. DOCUMENTO Nº DCTA/ITA/TD-078/2024	4. Nº DE PÁGINAS 169
5. TÍTULO E SUBTÍTULO: Application of Faddeev Technique: From Three-Body Nuclear Systems to 2D Semiconductor Materials			
6. AUTOR(ES): Kamyar Mohseni			
7. INSTITUIÇÃO(ÕES)/ÓRGÃO(S) INTERNO(S)/DIVISÃO(ÕES): Instituto Tecnológico de Aeronáutica – ITA			
8. PALAVRAS-CHAVE SUGERIDAS PELO AUTOR: 1. Faddeev equation. 2. Zero range 3. Universality. 4. Two dimensions. 5. Exciton. 6. Trion. 7. Few-body.			
9. PALAVRAS-CHAVE RESULTANTES DE INDEXAÇÃO: Teoria relativística; Equações de Faddeev; Problema de poucos corpos; Fatores de forma; Frente de luz; Partículas elementares; Física nuclear; Física.			
10. APRESENTAÇÃO: (X) Nacional () Internacional ITA, São José dos Campos. Curso de Doutorado. Programa de Pós-Graduação em Física. Área de Física Atômica e Molecular. Orientador: Prof. Dr. André Jorge Carvalho Chaves. Coorientadores: Prof. Dr. Tobias Frederico, Prof. Dr. Diego Rabelo da Costa . Defesa em 13/12/2024. Publicada em 2024.			
11. RESUMO: <p>We investigate the three-boson bound-state mass and wave functions within a three-body relativistic framework in three-dimensional momentum space. We utilize Kamada, and Glöcke boosted potentials with a non-relativistic short-range separable potential characterized by Yamaguchi and Gaussian form factors. By driving these form factors towards the zero-range limit while keeping the two-body binding energy fixed, we demonstrate that the three-boson relativistic masses and wave functions become model-independent, and the Thomas collapse is avoided. Interestingly, the non-relativistic limit retains the Efimov effect. The stability in the zero-range limit is attributed to the reduction of the boosted potential with the increase of the virtual pair center of mass momentum within the three-boson system. A comparison is made with Light-Front and Euclidean calculations to validate our findings.</p> <p>Next, we develop a fundamental formalism for studying trions in semiconductor layered materials. The Faddeev equations in momentum space describe the interaction of three different particles lying in two dimensions. We solve the trion Faddeev coupled integral equations using both a short-range one-term separable Yamaguchi potential and the repulsive Rytova-Keldysh (RK) interaction, which is applied to the MoS₂ layer. Due to the challenge posed by the repulsive electron-electron RK potential, two distinct regularization methods are devised. The first method regulates the repulsive interaction in the infrared region, while the second method regulates it in the ultraviolet region. Through extrapolation of the trion energy to the situation without screening, consistent results are obtained for the MoS₂ layer, revealing a trion binding energy of $-49.5(1)$ meV for an exciton energy of -753.3 meV. The trion structure for both RK and Yamaguchi potentials is analyzed in detail, emphasizing their overall similarities and the dominant cluster structure, where a firmly bound exciton is weakly bound to an electron. This is further manifested in the dominance of two Faddeev components over the one where the hole is a spectator of the interacting electron pair.</p> <p>To investigate the trion further, we study it in real space by transforming the trion wave functions from momentum to configuration space using Fourier transforms. This approach provides insights into the spatial arrangement and correlations among trion constituent particles. We investigate the trion structure in configuration space using both Yamaguchi and RK potentials, demonstrating the importance of screening effects on the trion's spatial distribution. The correlation functions and expectation values of Jacobi coordinates are calculated, revealing the geometrical configurations and internal structure of trions. The study confirms the accuracy of the numerical methods and provides a comprehensive understanding of trions' binding properties and structures in 2D semiconductor materials.</p> <p>In addition to three-body bound states in three-dimensional and two-dimensional, we study the four-body (4B) systems in two-dimensional momentum space using the Faddeev-Yakubovsky (FY) scheme. The chapter begins with a theoretical foundation of the FY approach, followed by deriving the FY equations for a 4B system in 2D space. We present numerical results for a system of identical particles interacting through a separable potential, demonstrating the effectiveness of the iterative method in solving the FY equations. The results highlight the binding energies of the 4B system, providing insights into the interactions and stability of a 4B system in 2D materials. This work is a preparatory step for more detailed future studies, aiming to explore the physical properties and potential applications of biexcitons in condensed matter physics.</p> <p>By combining these research studies, we contribute to understanding bound states in three-boson systems and provide insights into the properties and structures of trions and biexcitons in semiconductor monolayer materials.</p>			
12. GRAU DE SIGILO: (X) OSTENSIVO () RESERVADO () SECRETO			